Bone tissue material properties are altered in Chronic Kidney Disease to lower fracture resistance-determining bone quality

by

Chelsea Marie Heveran

B.A., Lewis & Clark College, 2007

M.Eng., Boston University, 2013

A dissertation submitted to the faculty of the Graduate School of the University of Colorado in partial fulfillment of the requirements for the degree of Doctor of Philosophy

Mechanical Engineering

2017

This thesis entitled:

Bone tissue material properties are altered in Chronic Kidney Disease to lower fracture resistance-determining bone quality

written by Chelsea M. Heveran

has been approved for the Department of Mechanical Engineering

_____

Virginia L. Ferguson, Ph.D., *primary advisor*

_____

R. Dana Carpenter, Ph.D.

July 31, 2017

The final copy of this thesis has been examined by the signatories, and we find that both the content and the form meet acceptable presentation standards of scholarly work in the above mentioned discipline.

IACUC protocol #: 78314(04)IE PI King

Heveran, Chelsea Marie (Ph.D., Mechanical Engineering)

Bone tissue material properties are altered in Chronic Kidney Disease to lower fracture resistance-determining bone quality

Thesis directed by Associate Professor Virginia L. Ferguson

Chronic kidney disease (CKD) is associated with a clinically-observed increase in bone fragility, yet the specific changes to fracture resistance-determining bone quality are not understood. CKD disrupts systemic mineral homeostasis and alters bone turnover. Thus, it was hypothesized that CKD deleteriously affects tissue-scale material properties. In Aim 1, mice with surgically-induced moderate CKD had diminished tissue-scale material properties, including mineral content and nanoindentation modulus, in bone formed during CKD compared with sham mice. Heterogeneity of microscale bone material was also altered with CKD. Next, CKD occurs most often in the elderly, yet geriatric patients with CKD have higher fracture risk than age-matched individuals without CKD. Aging reduces bone quality and may affect the behavior of osteocytes, the most prevalent type of bone cell. Osteocytes are essential for maintaining bone quality, but age-related changes to osteocytes, including lacunar morphologies, are not known. We hypothesized that osteocyte lacunae would have different morphologies with increasing age in mouse cortical bone. In Aim 2, we found that osteocytes become smaller, more spherical, and sparser with advancing age. Additionally, a convenient and inexpensive method to visualize and analyze 3D osteocyte lacunar geometries from confocal laser scanning microscopy depth stacks was presented. In Aim 3, it was hypothesized that aging and CKD together reduce bone material quality for mice with moderate CKD across the hierarchical organization of the bone tissue composite. We found that aging and CKD diminish bone material properties, including mineral and collagen matrix, from the microscale to the whole bone. Additionally, CKD reduced microscale material heterogeneity. Lastly, in Aim 4, it was hypothesized that fracture toughness depends on microscale material heterogeneity. In a rat model of exercise and obesity, fracture toughness of the femur was significantly influenced by the heterogeneity of nanoindentation modulus for lamellar bone. The relationship between fracture toughness and standard deviation of modulus had a negative quadratic form, implying that too-low or too-high variability in mechanical properties is

deleterious to bone toughness. The collected work reported here provides insights into how bone material quality is diminished in CKD as well as how these changes may alter bone fracture resistance.

Dedicated to Cathie, John, and Jim

Acknowledgements

This work would not have been possible without the support and encouragement of many people over many years. First, I am grateful to my family and friends for their unwavering support of my goals.

I deeply appreciate the guidance and encouragement that I have received throughout my dissertation from Dr. Virginia Ferguson. I am also grateful to Dr. Yueping Zhang, who advised my undergraduate honors research project in Psychology at Lewis & Clark College. Though Mechanical Engineering is a far departure from my undergraduate major, my first research opportunities were transformative and shaped my current research-oriented career trajectory. Thanks also to Dr. Vinod Sarin at Boston University, who advised my first research efforts in Materials Science, and who convinced me to pursue a PhD.

Many thanks to my fantastic labmates at the Biomechanics & Biomimetics Lab. I am particularly grateful to many undergraduate students who have helped me during my dissertation research. Special thanks to Ahmed Shahid, Maddy Whetstone, Gabrielle Melli, Geya Kairamkonda, Timmy Gouin, Mick Bruce, and Adam Rauff for their many hours of hard work and assistance.

Lastly, I am extremely thankful to my husband, Alexey Dynkin. His years of encouragement and help have made my doctoral education possible.

TABLE OF CONTENTS

LIST OF FIGURES

LIST OF TABLES

CHAPTER 1

1. Introduction

1.1 Motivation and Specific Aims

Chronic Kidney Disease (CKD) is an important global public health problem that has accelerated in prevalence in recent decades alongside the growing elderly populations of developed nations [Coresh *et al.*, 2007; Levey *et al.*, 2007; Nickolas *et al.*, 2008]. CKD is associated with a clinically-observed increase in bone fragility. Individuals with CKD have a higher incidence of both fracture and fracture-related mortality than age- and sex-matched controls with normal kidney function [Nitsch *et al.*, 2009; Nickolas *et al.*, 2008]. Indeed, it is known that CKD is commonly and perniciously accompanied by renal osteodystrophy, disrupted mineral homeostasis, and extracellular calcification under the broader syndrome of Chronic Kidney Disease – Mineral and Bone Disorder (CKD-MBD) [Moe *et al.*, 2006].

Bone fragility from CKD-MBD is challenging for the clinician to detect and manage. Patients are at greatest risk of bone fracture with severe CKD, long duration of mild-moderate CKD, or the combination of CKD and advanced age [Naylor *et al.*, 2014]. Dual Energy X-Ray Absorptiometry (DEXA) is the clinical standard for identifying bone mineral loss, yet in CKD many patients present with fracture without an abnormal DEXA score [Nickolas *et al* 2008]. Currently, changes from CKD to bone material and structure that result in loss of bone fracture resistance are not known. At the same time, therapeutics used clinically to manage bone loss in CKD (*i.e.*, antiresportives such as bisphosphonates) are used with limited understanding of their specific effects on bone fragility in CKD, and may have undesired systemic repercussions. Thus, clinical decision making may benefit from an improved understanding of the material and structural determinants of skeletal fragility in CKD.

The principle objective of this thesis is to determine why CKD causes increased fracture risk in a mouse model of CKD. Bone fracture resistance is determined by bone quality – a constellation of hierarchical material and structural contributing elements that together determine bone strength and toughness [Seeman *et al.*, 2006; Donnelly *et al*, 2010]. Bone material and microarchitecture can be modified, for better or

worse, through pharmaceuticals, exercise, and diet, and thus it is imperative to for the clinician to understand the sources of bone fragility in CKD in order to appropriately direct patient care. The altered mineral homeostasis and bone turnover resulting from CKD-MBD implies that bone quality may worsen with renal dysfunction [Moe *et al.*, 2006; Wolf *et al.*, 2015]. Yet the specific effects of CKD on bone material, including mineral and matrix components, and microarchitecture have yet to be determined. **The first aim of this work is to understand whether bone quality is diminished in bone formed during CKD.** The osteocyte, which resides within bone and systemically participates in CKD, is a key regulator of bone quality. Osteocyte perilacunar remodeling changes the shape of osteocyte lacunae, which can impact bone microstructure, material properties, and mechanosensitivity. Yet osteocyte lacunae are complex three-dimensional shapes, and current methods to visualize these three-dimensional networks require prohibitively rare or expensive technologies (*e.g.*, synchrotron radiation, nanoCT). **The second aim of this work is to develop a convenient and efficient method to visualize and analyze networks of 3D osteocyte lacunae based on confocal laser scanning microscopy (CLSM), a relatively common and inexpensive tool.** The method is first applied to investigate how changes occur to osteocyte lacunar networks with aging. Next, although CKD is most common among the elderly, the combined influences of aging and CKD on bone quality are unknown. It is not understood how aging and CKD influence the osteocyte lacunar geometries, cortical and trabecular microarchitecture, tissue-scale bone material properties, and whole-bone mechanical and material properties that together influence fracture resistance. **Therefore, the third aim is to determine how aging and CKD together participate in diminishing bone quality**. In early work for this thesis studying the effects of CKD on bone material at the microscale, a compelling hypothesis emerged that kidney dysfunction may change material heterogeneity. **The fourth aim is to identify the role of bone material heterogeneity in intrinsic bone fracture toughness**, such that the altered bone tissue heterogeneity in CKD and other metabolic bone diseases can be better interpreted.

The overarching hypothesis of this work is that CKD deteriorates bone quality, including microscale material properties, to decrease bone fracture toughness. Bone quality is hypothesized to

worsen progressively with advancing kidney disease, and in addition to the bone quality reduction associated with aging. It is further hypothesized that microscale material heterogeneity specifically contributes to the fracture toughness of bone. The net effect of these worsening bone parameters lies in their contribution to bone fragility. In order to address this overarching hypothesis, the following Specific Aims are proposed.

Specific Aim 1: Determine whether microscale bone quality is reduced in bone formed following the onset of CKD.

While bone material properties in surgical models of CKD in rodents (*e.g.*, 5/6th nephrectomy) have been evaluated, disagreement exists about whether bone material quality is worsened or conserved with kidney disease [Kadokawa *et al.*, 2011, Iwasaki *et al.*, 2011, Iwasaki *et al.*, 2015]. The lack of agreement may originate from the location of microscale material property evaluation; these previous efforts have surveyed a select few microscale locations in the cortical mid-envelope although actively forming bone following 5/6 Nx in mice and rats forms along the outer periosteal and endosteal surfaces. Thus, while altered mineralization and mechanical properties at the microscale are suspected because of the pathophysiology of renal osteodystrophy, microscale material properties have not been thoroughly surveyed in either human or animal models. **The hypothesis of Aim 1 was that bone material properties are diminished in CKD, and that microscale arrays spanning cortical bone tissue established before and after nephrectomy would reveal deleterious changes to bone material properties.**

To complete Aim 1, 11-week-old C57Bl/6J mice underwent either 5/6 nephrectomy (5/6 Nx), to induce CKD, or sham surgeries and were killed at 22 weeks of age. Nanoindentation arrays were placed on a transverse section of the midshaft tibia in arrays spanning the cortical thickness. Arrays were large enough to survey indentation modulus in the newest bone located near the periosteal surface as well in extant bone in the cortical mid-envelope. Following nanoindentation, the mineral volume fraction was assessed by quantitative backscattered scanning electron microscopy (qBSE) at the indentation sites. Bones from mice with 5/6 Nx had significantly lower nanoindentation modulus and lower mineral volume fraction in newly

formed bone after the onset of CKD; this pattern was not observed in sham mice. Further, altered variance in modulus and mineral volume fraction in 5/6 Nx compared with sham implies a possible loss of tissue-scale toughening mechanisms [Tai *et al.,* 2007; Yao *et al.*, 2011]. These changes to bone material were observed in the absence of changes to bone microarchitecture from microCT and whole bone bending strength and modulus from three-point bending.

The key result of Aim 1 was that microscale bone material was observed to worsen (less mineralized and lower nanoindentation modulus) with moderate CKD. Another important observation was that heterogeneities of both modulus and mineral volume fraction were altered with CKD. The work was innovative in employing large, site-matched arrays spanning the cortical thickness that allowed assessment of microscale cortical bone properties in bone formed before and after nephrectomy. The size of these arrays enabled estimation of material heterogeneity, which had not been explored in CKD models prior to this study. The significance of Aim 1 was to resolve the previously unanswered question of whether bone material worsened in CKD, and thereby to establish an important line of inquiry into how clinically-observed loss of bone fracture resistance is associated with diminished material properties.

Specific Aim 2: Develop a method to assess 3D osteocyte lacunar geometries and evaluate changes to osteocyte lacunar networks in aging.

Osteocytes, which account for approximately 95% of bone cells, are critical for coordinating bone deposition and resorption, as well as bone mechanotransduction. They also participate systemically in disease processes *via* endocrine signaling [Bonewald 2011; Schaffler *et al.,* 2014]. In addition, the osteocyte can directly modify the local bone material environment through perilacunar remodeling. The reversible removal and deposition of bone in the perilacunar space may contribute to maintenance of bone quality and fracture resistance [Alliston 2014; Tang *et al.,* 2014; Fowler *et al.,* 2016]. Perilacunar remodeling is thought to participate in systemic mineral homeostasis, and is sensitive to extreme physiological conditions (*e.g.,* lactation, hibernation, microgravity) and some therapeutics (*e.g.,* glucocorticoids) [Qing *et al.,* 2012; Kaya *et al.,* 2015; Kwiecinski *et al.,* 1987; Lane *et al.,* 2004]. Aging may alter mineral metabolism, and is also associated with changes to osteocyte behavior (*i.e.,* expression of toxic proteins by senescent osteocytes)

[Orwoll *et al.*, 2009; Tsai *et al.*, 1984; Farr *et al.*, 2016]. Yet it is unknown if aging alters osteocyte lacunar geometries, such as volume and orientation. These changes to osteocyte lacunar geometries may affect bone structural competence, fracture properties, and mechanosensitivity.

Visualizing and measuring osteocyte lacunar geometries is necessary for understanding the role of the osteocyte in modulating bone quality. Most attempts to visualize osteocyte lacunae have involved two-dimensional (2D) approaches, which have several critical limitations. Osteocyte lacunae can appear indistinguishable from non-lacunar objects (*e.g.*, a cross-section of vasculature). Furthermore, the ellipsoidal shape that characterizes osteocyte lacunae can be sliced into many different ellipses with widely differing geometries depending on the sectioning plane. Three-dimensional (3D) images can surmount the challenges of 2D quantification of osteocyte lacunar network geometries. Yet previous efforts to visualize lacunae in 3D often utilize expensive and inaccessible technologies (*e.g.*, synchrotron-radiation microCT and submicron-resolution conventional CT 'nanoCT'). By contrast, confocal laser scanning microscopy (CLSM) is a relatively common, fast, and inexpensive technique with the ability to capture depth stacks (z-stacks) at submicron resolution of brightly stained (*e.g.*, basic fuchsin) osteocyte lacunae. Some prior work has employed CLSM for analysis of 3D lacunae [McCreadie *et al.*, 2004; Kamel El-Sayed *et al.*, 2015; Lai *et al.*, 2015; Kerschnitzki *et al.*, 2013]. These studies rely either on manual segmentation (slow and prone to user error) or construct proprietary algorithms for segmenting and reconstructing lacunae for 3D analysis. The primary purpose of Aim 2 was to develop an open-source method for automatic segmentation and reconstruction of osteocyte lacunae in 3D from CLSM images. These 3D networks of osteocyte lacunae can then be analyzed for network geometries and orientations. The secondary purpose of Aim 2 was to evaluate whether 3D osteocyte lacunar geometries change with aging. **The hypothesis of Aim 2 was that osteocyte lacunae can be reconstructed in 3D from images generated in confocal laser scanning microscopy, and that these 3D images reveal changes to osteocyte lacunar geometries with aging in mice that would be overlooked in 2D analyses of osteocyte lacunae.**

A Matlab-based program was developed that manually segments and reconstructs osteocyte lacunae from image stacks obtained from CLSM. The validity of this approach was tested with use of phantom

geometries, manual segmentation, and comparison with nanoCT. To study the effect of aging on 3D osteocyte lacunar geometries, ~200 μm thick sections of basic fuchsin-stained cortical mouse bone from the midshaft tibia were prepared from 6, 18, and 24 month old mice who served as sham controls for a study of aging and CKD.

The primary result from Aim 2 is that osteocyte lacunae can be reconstructed and analyzed in 3D from z-stacks generated during confocal laser scanning microscopy, a convenient and accessible technology. The Matlab-based program constructed during this project enables time-efficient segmentation of lacunae while minimizing user bias. The secondary goal of this project was to investigate whether aging changes 3D osteocyte lacunar geometries. It was found that lacunae from cortical mouse bone become smaller, more spherical, and sparser with aging. With the exception of diminished lacunar number density, changes with aging from 3D analyses were not evident in 2D assessments from the same mice. Instead, closest center of mass and orientation appeared to change in 2D but not 3D, revealing that 2D metrics have the potential to be misleading.

Aim 2 is innovative in providing an open-source tool to study 3D osteocyte lacunar networks from CLSM imaging. While the method was first demonstrated for studying the effects of aging on 3D osteocyte lacunar geometries, the same approach can be utilized to study osteocyte lacunae in CKD as well as in other diseases, physiological states, and interventions that affect the osteocyte.

Specific Aim 3: Determine the influence of CKD and aging on bone fragility.

The prevalence of CKD increases with age, such that the majority of patients with CKD are elderly [Nickolas *et al.*, 2008]. Aging is known to diminish bone quality with respect to microarchitecture as well as to material properties. Aging thins trabeculae and cortical bone, and increases cortical porosity [Riggs *et al.*, 2004]. Bone material also worsens; with increased age there is greater mineralization and altered mineral chemistry [Boskey *et al.*, 2002; Boskey *et al.*, 2010; Akkus *et al.*, 2003], increased accumulation of microdamage [Shaffler *et al.*, 1995], and increased non-enyzmatic crosslinking of the collagen matrix [Wang *et al.*, 2002]. It is not known how aging and CKD together reduce bone quality, and whether the effects of CKD on bone are greater in older patients. Clinicians are limited in treating the skeletal effects

of CKD in part from the unknown interaction between aging and CKD on bone quality. Human studies of these combined effects have not been conducted and are complicated by the high incidence of additional aging-related diseases known to diminish skeletal fracture resistance (*e.g.*, diabetes). Thus, studying bone outcomes in a model of CKD in young through geriatric mice may provide the first insights into the combined effects of CKD and aging on bone quality and fracture resistance. **The hypothesis of Aim 3 was that CKD and aging lower bone quality in mice, including material properties and bone microarchitecture, more than aging alone.** It was further hypothesized that reduced heterogeneity of material properties (*e.g.*, nanoindentation modulus) is significantly associated with lowered bone fracture toughness.

Bone quality spanning multiple length scales was evaluated for young (3 mo), middle-age (15 mo), and old (21 mo) C57Bl/6 male mice undergoing either 5/6 Nx or Sham procedures and aged an additional three months (final ages 6, 18, and 24 months). Whole bone mechanical properties were assessed from three-point bending of the femur. Microarchitecture of trabecular bone (proximal tibia) and cortical bone (midshaft femur) were assessed from microCT. Site-matched maps spanning the cortical thickness of the femur evaluated bone chemistry from Raman spectroscopy, modulus from nanoindentation, and mineral volume fraction from qBSE. Enzymatic and non-enzymatic collagen crosslinks were evaluated using high-performance liquid chromatography (HPLC).

The key finding of Aim 3 is that bone quality changes with both aging and CKD, such that bone quality is worst in the oldest animals with CKD. Aging reduced trabecular and cortical microarchitecture and whole-bone mechanical properties. CKD further diminished both trabecular and cortical microarchitecture and whole-bone mechanical and material properties. The effect of CKD on bone quality emerged with age. Few differences were evident between CKD and sham for young mice. At middle-age, mice with CKD compared with sham had diminished whole bone mechanical and material properties (*e.g.*, stiffness, toughness, post-yield displacement) cortical microarchitecture (*e.g.*, cortical porosity, cortical thickness), and modulus from nanoindentation. Old mice with CKD compared with sham had diminished trabecular microarchitecture (*e.g.*, trabecular number, trabecular thickness, trabecular mineral density), as

well as reduced collagen crosslinks. Though there were few significant differences in cortical bone for old mice with CKD *vs* sham, mean cortical microarchitecture was generally lowest in old mice with CKD. Both old and middle-age mice had decreased mineral, as evidenced by both trabecular and cortical mineral densities measured by microCT. Material property differences were most evident at middle-age at both the microscale (lower modulus and standard deviation, a measure of heterogeneity, from nanoindentation) and whole bone scale (toughness from three-point bending). 3D osteocyte lacunar geometries became smaller, more spherical, and sparser with age in sham mice, but were not different between ages for mice with CKD, potentially implicating the osteocyte in bone quality changes in CKD.

The innovation of Specific Aim 3 is that it is the first assessment of bone quality changes in CKD alongside aging. Aim 3 is also innovative in generating site-matched maps of cortical bone chemistry, composition, and mechanical properties spanning the cortical thickness. This Aim is further innovative in comparing the evaluating the influence of microscale material properties on whole bone structural integrity. The significance of this work is in improving the clinical understanding of how bone fracture resistance is lost with CKD as well as the role of aging in this process. Specically, knowledge of changes to mineral and collagen with aging and CKD may help the clinician consider appropriate treatment choices.

<u>Specific Aim 4: Investigate how bone material property heterogeneity contributes to whole bone fracture toughness</u>.

Bone is a hierarchical composite with material and structural elements ranging from the nanoscale to the mesoscale. Bone structure at the microscale is known to be important to bone fracture toughness; a known toughening mechanism in human bone is for cracks to deflect along relatively compliant osteonal cement lines [Koester *et al.,* 2008]. Bone material properties and their microscale spatial heterogeneity are widely thought to also be important to bone toughness, but the work supporting this theory has been largely observational [Lloyd *et al.*, 2016]. For example, work spanning a number of disease models has found that heterogeneity of bone composition (from quantitative SEM techniques) is abnormal in individuals with fragility fractures [Roschger *et al.*, 2008; Busse *et al.,* 2009; Tamminen *et al.* 2014]. Heterogeneity in nanoindentation modulus, which results in part from compositional variance, has been demonstrated using

FEA models to provide a tissue-scale toughening mechanism [Tai *et al.*, 2007; Yao *et al.*, 2011]. However, no previous report has detailed a direct evaluation of how heterogeneity of tissue-scale modulus, as well as variance in microscale bone chemistry (*e.g.*, mineral:matrix, crystallinity) and composition (*i.e.*, mineral volume fraction) contribute to bone fracture toughness. Because of this gap in understanding, it is unknown if therapies that increase or decrease material heterogeneity would influence bone fracture resistance. **The hypothesis of Aim 4 was that microscale bone heterogeneity, including variance for both tissue-scale stiffness and physical characteristics of the bone tissue composite, contributes to rat bone fracture toughness.**

To evaluate the contributions of material heterogeneity on fracture toughness, notched fracture toughness testing was conducted on rat femurs from a study of exercise and obesity. Male and female rats were fed a high-fat diet for 10 weeks, starting at 5 weeks of age, and separated into lean, middle, and obese tertiles within sex by weight. The lean and obese rats were then randomly assigned to exercised (treadmill running) or sedentary groups and were killed four weeks later. Femurs from these rats were notched and fractured to obtain a fracture toughness. Microscale material properties and their variance (*i.e.*, heterogeneity) were then assessed for both lamellar and woven bone with nanoindentation and Raman spectroscopy.

Fracture toughness was higher for exercised compared with sedentary rats. Multiple linear regression models revealed that fracture toughness for lamellar bone and woven bone depended on microscale bone heterogeneity. Fracture toughness had a negative quadratic dependence on the standard deviation of reduced modulus as well as mineral:matrix for lamellar bone regardless of exercise or obesity, implying that a "sweet spot" of material properties and their variance contributes to fracture resistance.

The significance of Aim 4 lies in evaluating the contribution of disrupted material variance to the development of bone fragility. With this knowledge, researchers and clinicians may be aided in understanding the significance of altered heterogeneity observed in bone from human fragility fractures in diseases such as CKD.

1.2 References

1. Coresh, J., Selvin, E., Stevens, L. A., Manzi, J., Kusek, J. W., Eggers, P., ... & Levey, A. S. (2007). Prevalence of chronic kidney disease in the United States. *Jama*, *298*(17), 2038-2047.

2. Levey, A. S., Atkins, R., Coresh, J., Cohen, E. P., Collins, A. J., Eckardt, K. U., ... & Powe, N. R. (2007). Chronic kidney disease as a global public health problem: approaches and initiatives–a position statement from Kidney Disease Improving Global Outcomes. *Kidney international*, *72*(3), 247-259.

3. Nickolas, T. L., Leonard, M. B., & Shane, E. (2008). Chronic kidney disease and bone fracture: a growing concern. *Kidney international*, *74*(6), 721-731.

4. Nitsch, D., Mylne, A., Roderick, P. J., Smeeth, L., Hubbard, R., & Fletcher, A. (2009). Chronic kidney disease and hip fracture-related mortality in older people in the UK. *Nephrology Dialysis Transplantation*, *24*(5), 1539-1544.

5. Moe, S., Drüeke, T., Cunningham, J., Goodman, W., Martin, K., Olgaard, K., & Eknoyan, G. (2006). Definition, evaluation, and classification of renal osteodystrophy: a position statement from Kidney Disease: Improving Global Outcomes (KDIGO). *Kidney international*, *69*(11), 1945-1953.

6. Seeman, E., & Delmas, P. D. (2006). Bone quality—the material and structural basis of bone strength and fragility. *New England Journal of Medicine*, *354*(21), 2250-2261.

7. Donnelly, E. (2011). Methods for assessing bone quality: a review. *Clinical Orthopaedics and Related Research®*, *469*(8), 2128-2138.

8. Wolf, M. (2015). Mineral (Mal) Adaptation to Kidney Disease—Young Investigator Award Address: American Society of Nephrology Kidney Week 2014. *Clinical Journal of the American Society of Nephrology*, *10*(10), 1875-1885.

9. Kadokawa, S., Matsumoto, T., Naito, H., & Tanaka, M. (2011). Assessment of trabecular bone architecture and intrinsic properties of cortical bone tissue in a mouse model of chronic kidney disease. *Journal of Hard Tissue Biology*,*20*(2), 79-86.

10. Iwasaki, Y., Kazama, J. J., Yamato, H., & Fukagawa, M. (2011). Changes in chemical composition of cortical bone associated with bone fragility in rat model with chronic kidney disease. *Bone*, *48*(6), 1260-1267.

11. Iwasaki, Y., Kazama, J. J., Yamato, H., Matsugaki, A., Nakano, T., & Fukagawa, M. (2015). Altered material properties are responsible for bone fragility in rats with chronic kidney injury. *Bone*, *81*, 247-254.

12. Tai, K., Dao, M., Suresh, S., Palazoglu, A., & Ortiz, C. (2007). Nanoscale heterogeneity promotes energy dissipation in bone. *Nature materials*, *6*(6), 454-462.

13. Yao, H., Dao, M., Carnelli, D., Tai, K., & Ortiz, C. (2011). Size-dependent heterogeneity benefits the mechanical performance of bone. *Journal of the Mechanics and Physics of Solids*, *59*(1), 64-74.

14. Allen, M. R., Newman, C. L., Chen, N., Granke, M., Nyman, J. S., & Moe, S. M. (2015). Changes in skeletal collagen cross-links and matrix hydration in high-and low-turnover chronic kidney disease. *Osteoporosis International*,*26*(3), 977-985.

15. Riggs, B. L., Melton, L. J., Robb, R. A., Camp, J. J., Atkinson, E. J., Peterson, J. M., ... & Khosla, S. (2004). Population-based study of age and sex differences in bone volumetric density, size, geometry, and structure at different skeletal sites. *Journal of Bone and Mineral Research*, *19*(12), 1945-1954.

16. Boskey, A. L. (2002). Variations in bone mineral properties with age and disease. *JOURNAL OF MUSCULOSKELETAL AND NEURONAL INTERACTIONS*, *2*(6), 532-534.

17. Boskey, A. L., & Coleman, R. (2010). Aging and bone. *Journal of dental research*, *89*(12), 1333-1348.

18. Akkus, O., Polyakova-Akkus, A., Adar, F., & Schaffler, M. B. (2003). Aging of microstructural compartments in human compact bone. *Journal of Bone and Mineral Research*, *18*(6), 1012-1019.

19. Schaffler, M. B., Choi, K., & Milgrom, C. (1995). Aging and matrix microdamage accumulation in human compact bone. *Bone*, *17*(6), 521-525.

20. Wang, X., Shen, X., Li, X., & Agrawal, C. M. (2002). Age-related changes in the collagen network and toughness of bone. *Bone*, *31*(1), 1-7.

21. Koester, K. J., Ager, J. W., & Ritchie, R. O. (2008). The true toughness of human cortical bone measured with realistically short cracks. *Nature materials*, *7*(8), 672-677.

22. Lloyd, A. A., Wang, Z. X., & Donnelly, E. (2015). Multiscale contribution of bone tissue material property heterogeneity to trabecular bone mechanical behavior. *Journal of biomechanical engineering*, *137*(1), 010801.

23. Roschger, P., Paschalis, E. P., Fratzl, P., & Klaushofer, K. (2008). Bone mineralization density distribution in health and disease. *Bone*, *42*(3), 456-466.

24. Busse, B., Hahn, M., Soltau, M., Zustin, J., Püschel, K., Duda, G. N., & Amling, M. (2009). Increased calcium content and inhomogeneity of mineralization render bone toughness in osteoporosis: mineralization, morphology and biomechanics of human single trabeculae. *Bone*, *45*(6), 1034-1043.

25. Tamminen, I. S., Misof, B. M., Roschger, P., Mäyränpää, M. K., Turunen, M. J., Isaksson, H., & Klaushofer, K. (2014). Increased heterogeneity of bone matrix mineralization in pediatric patients prone to fractures: a biopsy study. *Journal of Bone and Mineral Research*, *29*(5), 1110-1117.

26. Ritchie, R. O., Koester, K. J., Ionova, S., Yao, W., Lane, N. E., & Ager, J. W. (2008). Measurement of the toughness of bone: a tutorial with special reference to small animal studies. *Bone*, *43*(5), 798-812.

27. McCreadie, B. R., Hollister, S. J., Schaffler, M. B., & Goldstein, S. A. (2004). Osteocyte lacuna size and shape in women with and without osteoporotic fracture. *Journal of biomechanics*, *37*(4), 563-572.

28. Kamel-ElSayed, S. A., Tiede-Lewis, L. M., Lu, Y., Veno, P. A., & Dallas, S. L. (2015). Novel approaches for two and three dimensional multiplexed imaging of osteocytes. *Bone*, *76*, 129-140.

29. Lai, X., Price, C., Modla, S., Thompson, W. R., Caplan, J., Kirn-Safran, C. B., & Wang, L. (2015). The dependences of osteocyte network on bone compartment, age, and disease. *Bone research*, *3*.

30. Kerschnitzki, M., Kollmannsberger, P., Burghammer, M., Duda, G. N., Weinkamer, R., Wagermaier, W., & Fratzl, P. (2013). Architecture of the osteocyte network correlates with bone material quality. *Journal of bone and mineral research*, *28*(8), 1837-1845.

31. Qing, H., Ardeshirpour, L., Divieti Pajevic, P., Dusevich, V., Jähn, K., Kato, S., ... & Bonewald, L. F. (2012). Demonstration of osteocytic perilacunar/canalicular remodeling in mice during lactation. *Journal of bone and mineral research*, *27*(5), 1018-1029.

32. Kaya, S., Basta-Pljakic, J., Seref-Ferlengez, Z., Majeska, R. J., Cardoso, L., Bromage, T., ... & Fritton, S. P. (2016). Lactation-Induced Changes in the Volume of Osteocyte Lacunar-Canalicular Space Alter Mechanical Properties in Cortical Bone Tissue. *Journal of Bone and Mineral Research*.

33. Kwiecinski, G. G., Krook, L., & Wimsatt, W. A. (1987). Annual skeletal changes in the little brown bat, Myotis lucifugus lucifugus, with particular reference to pregnancy and lactation. *Developmental Dynamics*, *178*(4), 410-420.

34. Lane, N. E., Yao, W., Balooch, M., Nalla, R. K., Balooch, G., Habelitz, S., & Bonewald, L. F. (2006). Glucocorticoid-Treated Mice Have Localized Changes in Trabecular Bone Material Properties and Osteocyte Lacunar Size That Are Not Observed in Placebo-Treated or Estrogen-Deficient Mice. *Journal of bone and mineral research*, *21*(3), 466-476.

35. Orwoll, E. S., & Meier, D. E. (1986). Alterations in calcium, vitamin D, and parathyroid hormone physiology in normal men with aging: relationship to the development of senile osteopenia. *The Journal of Clinical Endocrinology & Metabolism*, *63*(6), 1262-1269.

36. Tsai, K. S., Heath 3rd, H., Kumar, R., & Riggs, B. L. (1984). Impaired vitamin D metabolism with aging in women. Possible role in pathogenesis of senile osteoporosis. *Journal of Clinical Investigation*, *73*(6), 1668.

37. Farr, J. N., Fraser, D. G., Wang, H., Jaehn, K., Ogrodnik, M. B., Weivoda, M. M., ... & Bonewald, L. F. (2016). Identification of senescent cells in the bone microenvironment. *Journal of Bone and Mineral Research*, *31*(11), 1920-1929.

FIGURE 1-1: OUTLINE OF SPECIFIC AIMS

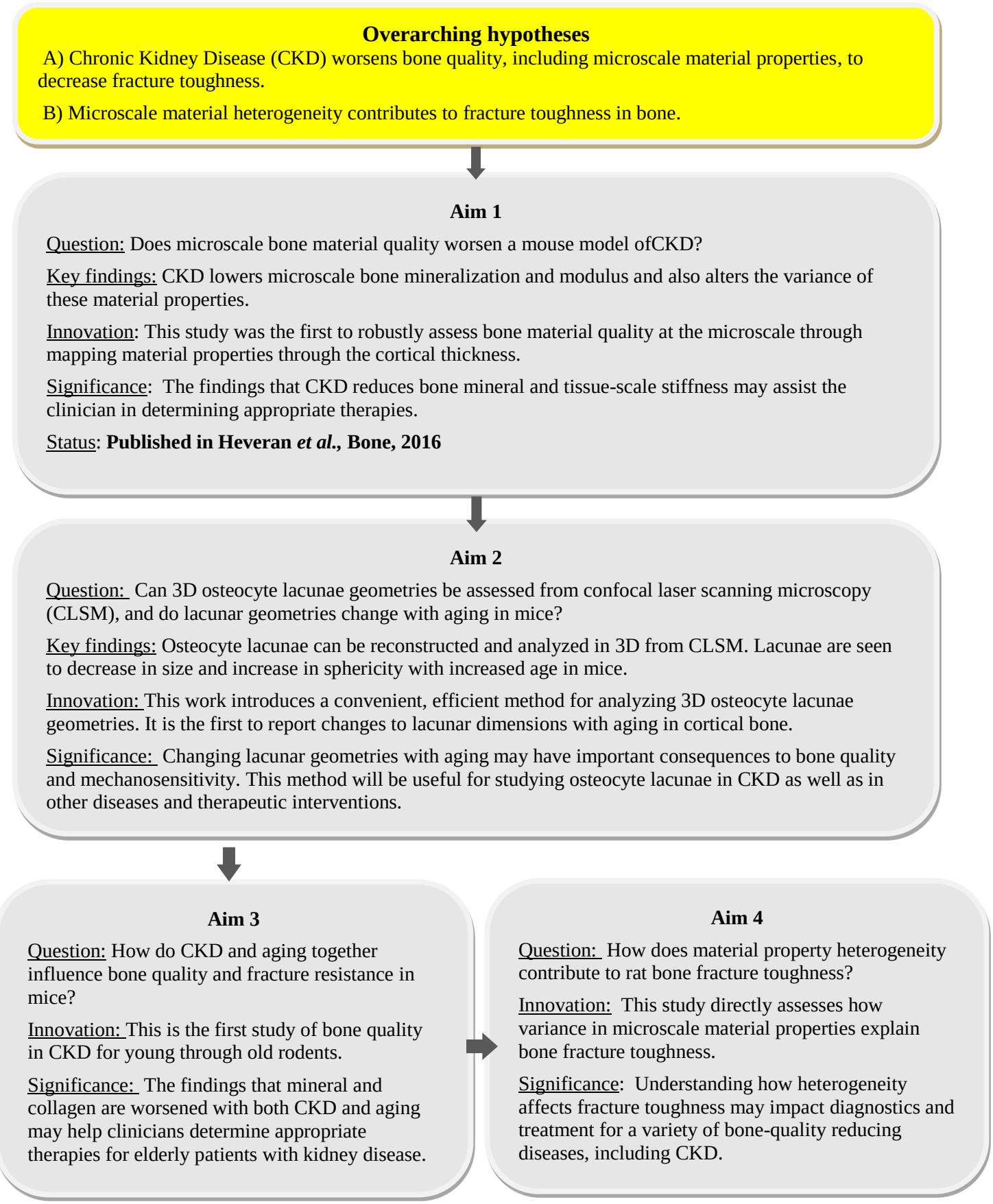

2. Background

2.1 Chronic Kidney Disease

2.1.1 Bone fragility in Chronic Kidney Disease: prevalence and clinical limitations

Bone fragility with Chronic Kidney Disease (CKD) is a growing global public health concern [Levey *et al.*, 2007; Moe *et al.*, 2006]. Primarily affecting elderly populations, the incidence of moderate to severe CKD is estimated at 24-36% of adults over 64 years [Zhang *et al.*, 2012]. Renal osteodystrophy is a common complication of CKD, now recognized as a component of the Chronic Kidney Disease – Mineral and Bone Disorder (CKD-MBD) syndrome involving disruption of mineral homeostasis, bone pathology, and extraskeletal (*e.g.*, vascular) calcification [Moe *et al.*, 2006].

CKD has been clinically associated with an increase in fracture risk [Naylor *et al.*, 2014; Nickolas *et al.*, 2008]. In a three-year cohort study conducted in Ontario, Canada, fracture prevalence in adults with CKD increased with severity of disease and age. For men and women over the age of 65, 2-4% of men and 6-8% of women with mild to moderate CKD sustained a bone fracture. These rates increase with severity of disease; this same age group experienced fracture rates of 5% and 10% for men and women with end-stage renal disease, respectively. Prevalence of fracture risk was also seen to increase with age. Men and women ages 40-65 with end-stage renal failure had lower rates of fracture, at 3% and 4%, respectively, than older patients with similarly staged kidney disease [Naylor *et al.*, 2014]. This increased fracture prevalence has been associated with mortality. Nitsch *et al* reported that men and women age 75 years and over with a hip fracture suffer a 2-fold increase in mortality compared with age- and sex- matched individuals without CKD [Nitsch *et al.*, 2009].

A lack of knowledge about the specific effects of CKD on bone fracture resistance critically limits clinicians in providing appropriate care for patients. Specifically, fracture risk in patients with CKD is difficult to predict, and appropriate treatment is uncertain. Measuring bone mass with Dual-Energy X-ray Absorptiometry (DEXA) is the clinical standard for assessing fracture risk and can identify patients with profound bone mineral loss. Yet DEXA is not predictive of fracture risk in CKD [Nickolas *et al.*, 2008]. As a low-resolution, two-dimensional technique, DEXA that can miss important changes to bone

microarchitecture and material properties. Thus, patients often present with fractures while having normal-range DEXA scores. Without understanding the effects of CKD on bone microarchitecture and material, it is difficult to address the limitations of DEXA to improve fracture prediction. Clinicians are also limited in how to treat bone fragility in CKD. Most patients with CKD are older, and bisphosphonate therapies for managing skeletal fragility in aging are predominantly focused on controlling unbalanced bone remodeling (*i.e.*, greater bone-resorbing osteoclast activity versus bone-forming osteoblast activity) through reducing osteoclast numbers or activity [Rogers *et al.*, 2000]. However, it is known that in aging (without CKD), bisphosphonate drugs can lead to adynamic bone disease and worsen bone mineral and the supporting collagen network [Gourion-Arsiquaud *et al.*, 2010; Allen *et al.*, 2008; Mashiba *et al.*, 2000]. Treatment of CKD patients with phosphate binders or calcitriol to suppress parathyroid hormone (PTH) can also lead to adynamic bone disease, and may further increase the risk of cardiovascular calcification [Malluche *et al.*, 2004]. An improved understanding of the effects of CKD on bone quality is necessary for clinicians to best choose therapeutics to manage the skeletal fragility of their patients.

Currently, the effects of CKD on bone quality to impart skeletal fragility are not known. In particular, it is not understood whether and how CKD changes bone microarchitecture and material quality. It is also important to identify how changes to bone quality in CKD occur together with deleterious changes to bone that occur in normal aging. In understanding the etiology of skeletal fragility in CKD, clinicians may gain valuable insights into which treatments are most appropriate for patients of varying ages and stages of disease. In the following sections, the pathophysiology of CKD is first discussed (2.1.2), along with an overview of rodent models available to study the effects of CKD on the skeleton (2.1.3). The physiological roles of the skeleton (2.2), as well as the complexities of bone as a hierarchical (2.3), dynamic (2.4), and heterogenous composite (2.5) are then explored, with emphasis within each section on the possible influences of CKD to disrupt the intricate functions, structure, and material of bone to impart fragility. Finally, section 2.6 summarizes what is known from experimental work involving CKD on bone quality, and highlights gaps in the current understanding of CKD-induced skeletal fragility.

2.1.2 The pathophysiology of Chronic Kidney Disease

The healthy kidneys work alongside the parathyroid, intestine, and bone to regulate mineral homeostasis. The definition of CKD is based on a glomerular filtration rate (GFR, ml/min per 1.73 m^2) of less than 60 ml/min for three or more months. The level of reduction determines the stage of disease (stage 1: > 60 ml/min, stage 2: 59-45 ml/min, stage 3: 44-30 ml/min, stage 4: 29– 16 ml/min, stage 5 (end stage renal disease requiring dialysis): < 15) [Levey *et al.*, 2012]. Because GFR is difficult to measure, calculating an estimated GFR (eGFR) from serum creatinine is common. The failing kidney can be managed by dialysis or transplant, thus morbidity instead commonly results from cardiovascular disease (CVD), acute kidney infection, or complications related to bone fracture [Moe *et al.*, 2006; Levey *et al.*, 2012].

The healthy kidney excretes phosphorus and calcium and thus participates along with the intestine, where minerals are absorbed, and the bone, where minerals are stored, to maintain mineral homeostasis [Moe *et al.*, 2006]. When kidney function is compromised and glomerular filtration rate decreases, the serum concentration of phosphate and calcium increase. The elevated phosphate directly and indirectly, through masking serum calcium, trigger an increase in parathyroid hormone (PTH) expression. PTH acts on the kidney to reduce reabsorption of phosphate while also increasing the absorption of calcium through upregulating an enzyme responsible for conversion of vitamin D to its active form, calcitriol [Quarles *et al.*, 2008]. Bone is also affected; PTH acts on the OPG/RANK pathway to increase osteoclastic resorption and elevate bone turnover, which in turn increases serum phosphate and calcium [Moe *et al.*, 2006]. Fibroblast growth factor 23 (FGF23) is also active in phosphate metabolism, and is secreted by osteocytes very early in CKD progression [Fang *et al.*, 2014]. As with PTH, FGF23 also works to decrease phosphate re-absorption at the kidney, but FGF23 activity decreases calcitriol and thus may interfere with the self-regulating feedback loop between PTH and vitamin D [Quarles *et al.*, 2012]. FGF23 and PTH work together in early kidney disease to compensate for hyperphosphatemia and are largely effective in controlling systemic (*i.e.*, circulating) phosphate levels, but secondary hyperparathyroidism (SHPT) develops as CKD progresses [Quarles *et al.*, 2012; Komaba *et al.*, 2010]. The onset of SHPT is characterized by high bone turnover as the bone is removed in response to sustained elevated PTH and then re-established as newly

deposited bone tissue [Kazama *et al.,* 2015]. The net bone mass is not profoundly impaired, thus the use of DEXA as a screening tool for low bone mass in CKD is insufficient [Nickolas *et al.,* 2008]. The overexpression of PTH over time appears to impair osteoblast performance and may eventually lead to the low-turnover adynamic bone disease that is common in end stage renal disease [Moe *et al.*, 2006].

The dysregulation of phosphate and calcium in CKD is likely to impair bone material properties and microarchitecture. Healthy cortical bone matures in the span of weeks to months from osteoid to bone tissue with increased mineral content, crystal size, perfection, and orientation, substitution of carbonate into the hydroxyapatite mineral lattice, and crosslinking throughout the collagen matrix [Donnelly *et al.,* 2009]. Because bone remodeling is temporally staggered, healthy cortical tissue of the whole bone has a range of maturities. The various degrees of mineralization, range of crystal sizes and orientations, and amount of crosslinking may all contribute to a heterogeneous, fracture-resistant bone [Seeman *et al.,* 2006; Gourion-Arsiquaud *et al.,* 2013; Boskey *et al.,* 2003; Saito *et al.,* 2010]. The frequent removal of mature cortical bone and replacement with newly-deposited osteoid as occurs in CKD may result in a less mature, less heterogeneous bone tissue composite. Bone microarchitecture could also be impaired; cortical and trabecular microarchitectures have been shown to negatively correlate with increased biochemical markers of bone turnover [Chaitou *et al.,* 2010]. It is unknown how loss of bone quality in CKD would participate with normal decrease in bone quality, including both material and microarchitecture, with aging. The potential effects of altered mineral homeostasis and abnormal bone turnover in CKD on specific aspects of bone material and microarchitecture are discussed in depth in sections 2.2 - 2.6.

The deleterious changes to bone from CKD clinically correspond with the development of vascular calcification. The concurrence of bone and vascular changes are now recognized as Chronic Kidney Disease – Metabolic Bone Disorder [Moe *et al.,* 2008]. Calcium and phosphate liberated into serum from increased bone turnover can cause vascular smooth muscle cells to mineralize [Moe *et al.,* 2006]. Identifying appropriate treatments to restore bone quality could therefore potentially improve cardiovascular outcomes as well as manage bone fragility. Treatment of CKD-MBD has been attempted with bisphosphonates, which diminish osteoclastic activity and thereby slow bone turnover [Moe *et al.,* 2008; Moe *et al.,* 2015].

Bisphosphonates are prescribed to preserve bone mass in osteoporosis, but are known to diminish bone material properties including altered bone mineral content and chemistry [Gourion-Arsiquaud *et al.*, 2010], increased collagen crosslinking [Allen *et al.*, 2008], and accumulation of microdamage [Mashiba *et al.*, 2000]. Because the specific changes to bone material and structure in CKD are poorly understood, clinicians are critically lacking information when prescribing bisphosphonates or other bone-affecting therapies to manage skeletal fragility or related cardiovascular disease. These fundamental questions about the effects of the complex pathophysiology of CKD on bone quality and fracture resistance motivate the use of carefully designed preclinical rodent models of kidney disease.

2.1.3 Rodent models of Chronic Kidney Disease

Chronic Kidney Disease is highly co-morbid with aging and other diseases such as diabetes and hypertension [Levey *et al.*, 2007]. In order to study the isolated effects of CKD on bone, rodent models have been employed. These models span chemical, surgical, and genetic induction of either spontaneous or progressive kidney disease [Yang *et al.*, 2010]. Chemical induction of CKD includes the spontaneous CKD that results from injection of a nephrotoxin or high doses of adenine delivered through diet [Yang *et al.*, 2010; Ferrari *et al.*, 2014]. Surgical models, such as uninephrectomy (UNx) and 5/6th nephrectomy (5/6 Nx), gradually produce chronic kidney disease [Chanutin & Ferris, 1932]. Unlike the severe CKD, and confounding malnutrition, caused by oral adenine administration, UNx and 5/6 Nx produce mild and moderate CKD, respectively, that mimic many aspects of human disease [Ferrari *et al.*, 2014; Yang *et al.*, 2010; Gava *et al.*, 2012]. The 5/6 Nx model induces high turnover renal osteodystrophy unless paired with thyroparathyroidectomy, in which low-bone turnover results [Iwasaki *et al.*, 2015]. The primary disadvantage of 5/6 Nx is that consistent ablation of the mouse kidney is difficult, and thus some variation in the severity of kidney disease achieved through surgery is likely. Though 5/6 Nx has been commonly employed to since the 1930s to study CKD in renal and cardiovascular systems [*e.g.*, Chanutin & Ferris, 1932; Gava *et al.*, 2012, Moe *et al.*, 2008], few studies have considered bone outcomes [Iwasaki *et al.*, 2011; Iwasaki *et al.*, 2015; Kadokawa *et al.*, 2011].

Genetic models have also been employed to study CKD. The Cy/+ model involves autosomal dominant polycystic kidney disease produced by a mutation in a gene that codes for the SamCystin protein. When employed in male Han:SPRD rats, Cy/+ model produces high-turnover CKD in young adults [Newman *et al.*, 2014; Moe *et al.*, 2014; Allen *et al.*, 2015]. An alternate approach used in mice is the genetic induction of Alport Syndrome. In both rodents and humans, Alport Syndrome involves the progressive onset of CKD (alongside loss of hearing and other complications) because of a deficiency in Type IV collagen, affecting basement membranes and thus kidney glomeruli [Rheault *et al.*, 2004]. In a model of Alport Syndrome (*Col4a3* knockout) on the 129 background, 10-week old mice with severe CKD had high-turnover renal osteodystrophy. However, in this context, mice have severe CKD by 9 weeks of age [Stubbs *et al.*, 2012]. Growth of the immature skeleton during the entirety of disease progression complicates the longitudinal assessment of renal osteodystrophy. A separate model of Alport Syndrome, the Col4a5 knockout on a C57Bl/6 background, is more promising for the temporal characterization of CKD on the murine skeleton [Rheault *et al.*, 2004]. In the Col4a5 model, male C57Bl/6 mice with the x-linked knockout experience a slowly progressive renal disease. Moderate kidney disease and proteinuria develops by age 75-100 days, and severe disease (glomerular filtration rate 10-20% of normal) manifests by 200 days of life [Rheault *et al.*, 2004]. Bone outcomes have not been characterized for this model. A limitation of the genetic models is that all lead to severe CKD in either skeletally immature or young adult rodents. Thus, genetic models are not currently appropriate for studying the combined effects of CKD and aging on the skeleton.

2.2. Physiological functions of bone

Bone provides the structural framework for the body's soft tissues. However, the skeleton serves several additional critical roles. Red blood cells are created within the marrow of long bones. Bone is also a mineral reservoir; the resorption or deposition of mineralized bone tissue helps to facilitate serum homeostasis of calcium and phosphate. Bone participates in mineral homeostasis through activities coordinated by the osteocyte. The osteocyte orchestrates the absorption of bone by osteoclasts and the deposition of bone by osteoblasts [Bonewald 2011]. It has recently been established that the osteocyte can

also directly engage in mineral homeostasis through removing the material volume surrounding the osteocyte lacuna in reversible process called perilacunar remodeling [Teti *et al*., 2009]. The surface area available for resorbing mineral *via* the osteocyte lacunar-canalicular system is immense relative to surfaces available for osteoclastic resorption [Bonewald 2011]. Changes to bone material and microarchitecture occur as the skeleton dynamically responds to systemic mineral requirements through osteoclast- and osteocyte-mediated resorption. Pathological changes to osteocyte behavior, including altered bone turnover from osteoclasts and osteoblasts, and potentially perilacunar remodeling, could occur with the altered mineral homeostasis of CKD.

Bone also has paracrine and endocrine functions through the actions of the osteocyte. For example, the osteocyte can secrete sclerostin to decrease differentiation of osteoblasts [Quarles *et al.,* 2008]. FGF23, secreted by the osteocyte, has a role in down-regulating vitamin D and affecting both PTH and serum phosphate [Quarles *et al.,* 2012]. These paracrine and endocrine functions are known to be disrupted in CKD. FGF23 is secreted early in CKD progression, preceding detectable changes to circulating phosphate, PTH, and vitamin D [Fang *et al.,* 2014]. Sclerostin is also elevated in both mouse and human bones [Sabbagh *et al.,* 2012].

While participating in many physiological processes, bone maintains fracture resistance as a strong, tough, and relatively lightweight composite. The hierarchical, heterogeneous, and dynamic characteristics that impart fracture resistance to healthy bone and their potential disruptions through CKD are explored in depth in sections 2.3-2.5.

2.3 Bone is a hierarchical composite

Bone tissue has a hierarchical organization, with length-scales of structural importance ranging from the whole bone down to the nanoscale [Weiner & Traub, 2002; Seeman *et al.,* 2006]. The basic structural unit of bone is carbonated hydroxyapatite mineral embedded within type I collagen fibers. Bone mineral shares many similarities with geologic hydroxyapatite ($Ca_{10}(PO_4)_3(OH)$). Both contain calcium, phosphate, and hydroxyl groups. However, while tremendous heat and pressure cause geologic hydroxyapatite to form large, relatively perfect hexagonal crystals, the physiological environment of the

body constrains the size of bone mineral. The hydroxyapatite comprising bone mineral is actually carbonated hydroxyapatite. Carbonate favorably substitutes at body temperatures for phosphate groups in "B" sites (and also for hydroxyl groups in "A" sites, but less commonly in biological apatites) [Wopenka & Pasteris, 2005]. Generally forming plates (but sometimes rods), bone mineral crystals have a very high surface area relative to volume and are thus easily dissolved when necessary to liberate calcium for physiologic demands. Indeed, dimensions of bone mineral crystals are on the order of 50 nm x 25 nm x 2 nm [Weiner & Traub, 1992].

The other primary constituent of the bone tissue composite is type I collagen. The ~300 nm length collagen molecule is comprised of a left-handed triple helix of collagen proteins. These molecules are held together into fibrils by crosslinks, some of which are enzymatically formed and others (advanced glycation end-products (AGEs) are formed spontaneously in response to glycation or oxidation. A gap zone between the ends of collagen molecules provides a binding site for bone mineral. The staggering of neighboring collagen molecules by 67 nm creates a characteristic banded look of the mineralized fibrils (~0.5 μm thick). Collagen fibrils in turn pack together to create collagen fibers. Collagen fibers arrange into dense lamellae in a given orientation to constitute cortical bone. These lamellae form layers of bone that replace the disordered "woven bone" common to growing animals, including rodents. In large animals, cortical bone can form osteonal structures. Within an osteon, lamellae form concentric rings around Haversion canals, containing blood vessels and nerves. Each ring of lamellar bone (thickness 3-7 μm) has a different orientation, taking a "twisted plywood" structure. The osteon is surrounded by a cement line with a less mineral-dense, tough material able to dissipate crack energy through deflection. Cancellous, or "spongy" bone, is formed from thin plates of mineralized collagen. The bridge-like trabeculae within cancellous bone form at the end of the long bones and align toward the principal directions of load [Seeman *et al.*, 2006].

The bone mineral-collagen composite may be expected to change in CKD. The disrupted mineral homeostasis that accompanies kidney disease could change the amount of mineralization, the perfection of crystals, and their chemistry. These types of changes have been observed in other metabolic bone diseases, including osteomalacia and hypophosphatemic rickets [Faibesh *et al.*, 2005; Karunaratne *et al.*, 2012].

Collagen crosslinking could also change with CKD. In particular, CKD increases oxidative stress and elevates AGEs [Linden *et al.,* 2008]. This increased non-enzymatic collagen crosslinking could pathologically stiffening bone and lowering toughness [Allen *et al.,* 2008]. Increased AGEs have been proposed as a mechanism by which bone can lose tissue-scale toughness. In SAXS-WAXS experiments of diabetic tissue, the increased crosslinking of aging tissue led to less plasticity in mineralized collagen fibrils [Zimmerman *et al.,* 2011]. Indeed, increased non-enzymatic crosslinks have been observed in clinical studies of patients with end-stage renal failure [Malluche *et al.,* 2012]. Thus, bone material, including mineral and collagen, is expected to change in CKD due to altered mineral homeostasis and oxidative stress. Additional changes to bone quality in CKD are expected from changes to bone turnover and related tissue maturation. These changes are detailed in the next section.

2.4 Bone is a dynamic structure: tissue maturation, remodeling, and aging

Bone is not a static tissue structure and can change in both microarchitecture and material properties. During skeletal expansion of the growing organism, changes to bone are referred to as modeling. Following skeletal maturity and the cessation of skeletal growth, bone continues to change by the process of remodeling. Osteocytes direct remodeling through coordinating bone deposition by osteoblasts and resorption by osteoclasts. During remodeling, osteoclasts dissolve bone to cut a cone into the existing tissue. The osteoblasts which follow then establish a new osteon, while embedded osteoblasts in the bone matrix become osteocytes [Hadjidakis *et al*., 2006]. Rodents and other small animals that lack osteonal bone can only model bone tissue, optimizing bone geometry through depositing bone on forming surfaces and remove bone from other surfaces. This process is most active during skeletal growth in mice, and tapers markedly after skeletal maturity [Ferguson *et al.,* 2003].

Bone remodeling can occur for several reasons, including maintenance of bone material. When bone microdamage or tissue-scale material properties change the local strain profile, osteoclasts are recruited to begin remodeling, ultimately establishing new bone free of damage and with immature material properties [Burr *et al.,* 1985; Robling *et al.,* 2006]. Bone remodeling can also take place in response to systemic physiological demand for mineral. The osteocyte can also directly participate in mineral

homeostasis through perilacunar remodeling. Osteocytes and their interconnecting canaliculi network form a surface area in contact with mineralized bone that greatly exceeds the area available for conventional remodeling [Teti *et al.,* 2009]. Thus, osteocytes can directly dissolve bone mineral in the perilacunar space surrounding osteocytes to quickly respond to physiological needs for mineral. This effect has been observed in lactation, where osteocytes reversibly repair their perilacunar environments, as well as in irreversibly in hibernation, spaceflight, and glucocorticoid therapy [Qing *et al.,* 2012; McGee-Lawrence *et al.,* 2011; Blaber *et al.,* 2013; Lane *et al.,* 2006]. Perilacunar remodeling has recently been suggested to be essential to bone quality maintenance. In one study, MMP13 knockout mice unable to undergo perilacunar remodeling had diminished bone quality and fracture toughness [Tang *et al.,* 2012]. These bone quality changes (hypermineralization, disorganized collagen, increased non-enzymatic crosslinks) in MMP13-null male mice were consistent with the hypothesis that perilacunar remodeling is essential for maintenance of tissue-scale bone quality. Gardinier and coworkers found that perilacunar bone has lower mineral:matrix from Raman spectroscopy and mineral content from SEM after exercise, and that these changes to osteocyte behavior may be mediated by PTH signaling [Gardinier *et al.,* 2016].

The maturation of newly deposited bone occurs over the span of days to weeks. Bone tissue is first deposited as unmineralized osteoid. Within days, a collagen network develops and mineral deposition begins. The majority of hydroxyapatite mineral crystals establish during this primary nucleation phase. These crystals contain little carbonate and are poorly organized. Over the next weeks to months, these bone crystals gradually grow and mature. Bone hydroxyapatite crystals become larger and more aligned. Collagen crosslinking also increases during tissue maturation. Enzymatic crosslinks mature over the course of primary mineralization, while non-enzymatic crosslinks establish as the tissue ages and is exposed to glycation and oxidation [Saito & Marumo, 2010]. These increases in mineral content and size as well as collagen crosslinking all contribute to stiffening of bone tissue with maturation [Donnelly *et al.,* 2009]. The higher carbonate content of mature bone tissue is not known to have a biomechanical effect, but does increase the local solubility of bone mineral and may therefore facilitate remodeling of mature bone [Wopenka & Pasteris, 2005]. The course of tissue maturation can be witnessed through surveying

microscale bone chemistry, composition, and mechanical properties in bone deposited over a span of time [Donnelly *et al.,* 2009].

Aging changes tissue material properties in part because of less-frequent bone remodeling. With decreased bone turnover, the average tissue age increases. Thus, aged bone has more mineral with larger crystals and more substituted carbonate [Boskey *et al.,* 2002; Currey *et al.,* 1996]. Older bone also has more mature enzymatic and non-enzymatic crosslinks [Nyman *et al.,* 2006]. With less frequent remodeling, the aging skeleton also has more microdamage [Schaffler *et al.,* 2005]. Aging also commonly results in disruptions between osteoclastic resorption and osteoblastic deposition. With unmatched deposition compared to absorption, bone mass is lost and the microarchitectures of cortical and trabecular bone worsen [Parfitt *et al.,* 1983]. These deleterious changes to material properties, microarchitecture, and bone mass together contribute to the loss of bone fracture resistance with aging [Currey *et al.,* 1996; Zioupos *et al.,* 1998].

The effects of CKD on bone quality are uncertain, yet abnormal bone turnover implicates changes to bone tissue maturation. In high-turnover CKD, the average tissue age would be expected to be reduced. The amounts of mineral and enzymatic collagen crosslinking may also be lower, and crystals smaller and less substituted with carbonate. However, non-enzymatic crosslinking could still increase. The uremic environment of CKD introduces bone to oxidative stress, which may promote formation of AGEs. While diminished mineral and enzymatic crosslinks could reduce bone stiffness, increased non-enzymatic crosslinks would be expected to have an opposite effect. Changes to osteocyte perilacunar remodeling could also potentially occur, which could further affect how and where bone material is changed in CKD. Meanwhile, even if net bone mass is constant in CKD, increased turnover could result in changes to cortical and trabecular microarchitecture. Though changes to bone material and microarchitecture from high turnover could all plausibly occur in CKD, it is unclear which of these changes would contribute most to loss of fracture resistance. Altered turnover could also lead to changes in microscale heterogeneity of material properties. The potential influence of bone heterogeneity on skeletal fragility in CKD is detailed in the following section.

2.5 Bone is a heterogeneous composite: contributions of compositional and structural variation to fracture toughness

The dynamic remodeling of the hierarchical bone-mineral composite results in characteristically heterogenous bone tissue. Bone has variable tissue age and maturation, and thus heterogeneous microscale mineralization, collagen crosslinking, and stiffness. Structural variation also exists. Osteocyte lacunae are varied in their shape and orientation. In human and other large animal bone, the lamellar boundaries within osteons as well as the cement lines surrounding osteons introduce structural variability. For small animal bone, the largest structural variation occurs with lamellar boundaries.

Bone heterogeneity may contribute to fracture resistance, though important questions remain about how variance in material and structure actively toughen bone [Lloyd *et al.,* 2015, Tai *et al.,* 2011; Koester *et al.,* 2008]. The influence of structural heterogeneity on bone fracture toughness is currently more understood than contributions to toughness from material variance. In work from the Ritchie group, osteonal bone is seen to have increasing fracture toughness with length of crack (*i.e.,* a rising R-curve). That is, cracks can propagate relatively easily when approximately 100 μm or shorter. Longer transverse cracks begin to interact with bone structure, such as cement lines, and dissipate energy through deflection [Koester *et al.,* 2008].

The role of material heterogeneity on fracture toughness is less clear. Abnormally high or low variance in mineral volume fraction has been noted in backscatter SEM studies comparing bone samples with and without fragility fractures. The coefficient of variance of bone mineralization was lower in iliac crest biopsies from women with vertebral fractures versus healthy cadaveric controls [Ciarelli *et al.,* 2009]. Yet in another study of bone mineralization at the iliac crest, cadaveric trabeculae from women with osteoporotic vertebral fractures had a wider distribution of bone mineral content than healthy trabeculae [Busse *et al.,* 2009]. Increased heterogeneity in mineralization has also been reported in both trabecular and cortical bone for fracture-prone children [Tamminen *et al.,* 2014].

The specific impairments to bone tissue toughening mechanisms from altered mineral heterogeneity are not well understood. Microscale bone mineralization is moderately predictive of

nanoindentation modulus, although there is considerable scatter in this composite-law relationship within normal ranges of mineral content [Oyen *et al.*, 2008]. Nonetheless, potential toughening mechanisms related to mineral heterogeneity could include crack energy dissipation at interfaces between material domains with dissimilar tissue-scale stiffness, as indicated by FEA populated with spatial variance in modulus measured by AFM [Tai *et al.*, 2011]. Locally stiff regions may also facilitate microcracking, a toughening mechanism observed to increase the fracture toughness of bone [Vashishth *et al.*, 1997; Ziupos *et al.*, 1998]. In addition to variability in mineral content, other aspects of bone material heterogeneity could influence fracture toughness. Variation in mineral size and orientation could potentially influence crack initiation and propagation. Further, variability in collagen properties may also be important. Tissue-scale bone stiffness determined in part by collagen integrity and crosslinking. Additionally, intermolecular sliding of collagen molecules allows bone to undergo substantial plastic strains [Launey *et al.*, 2010]. Ultimately, the contributions of variation in mineral content, mineral size and orientation, and collagen integrity to bone fracture toughness are not understood.

Very limited experimental work has considered how microscale material heterogeneity influences fracture toughness. Makowski and coworkers considered how bone chemistry measured from Raman spectroscopy contributes to fracture toughness in human cortical bone spanning a range of ages [Makowski *et al.*, 2015]. Mineral:matrix, crystallinity, and carbonate:phosphate had poor correlations with fracture toughness, though principal components of whole spectra were somewhat predictive of fracture toughness [Makowski *et al.*, 2015]. In another study, Granke and coworkers assessed clinically-measurable parameters of bone quality (stiffness from reference point indentation, bound and free water from NMR) as well as more traditional measures of bone quality (cortical porosity and total mineral density from microCT) as well a fracture toughness from human cortical bone spanning several decades of age [Granke *et al.*, 2015]. Multiple linear regression (MLR) showed that the initiation fracture toughness decreased with age and pore water, and increased with bound water and loading stiffness from reference point indentation. In a second MLR model within the same study, initiation fracture toughness decreased with cortical porosity and pentosidine content [Granke *et al.*, 2015]. These findings demonstrate that fracture toughness does have

measurable dependency on bone quality characteristics. However, neither of these studies comprehensively assessed how variability in physical characteristics of the bone-tissue composite (*e.g.,* chemistry and composition) as well as the microscale modulus affect fracture resistance. The paucity of experimental studies on this topic limits the interpretation of observed abnormal microscale material heterogeneity in bone fragility-causing diseases such as CKD.

CKD has the potential to change bone heterogeneity. The increased turnover associated with hyperparathyroidism lowers the average tissue maturation. Locally, this may increase heterogeneity of mineral content as bone undergoes rapid turnover and re-mineralization. However, tissue-scale elastic properties are influenced by mineral content, crystal maturity, and also collagen crosslinking. To date, no studies have evaluated how CKD influences bone material heterogeneity.

2.6 Review of studies of bone outcomes in CKD: current knowledge and gaps in understanding

The effects of CKD on bone quality have been studied in a limited number of prior efforts. Very few works have involved human bone, likely because of the comorbidity of CKD with diabetes and other conditions, the prevalence of patient treatment with bone-affecting therapies such as corticosteroids or estrogen-replacement therapy, as well as the challenges involved in obtaining human biopsy samples [Nickolas *et al.,* 2008; Malluche *et al.,* 2012]. In a study of trabecular bone from iliac crest biopsies obtained from patients with end-stage renal disease, bone demonstrating high-turnover characteristics from histomorphometry had 10% lower mineral:matrix (assessed with Fourier-transformed infrared spectroscopy, FTIR) and 12% lower nanoindentation modulus compared with biopsies from healthy volunteers of similar age. No differences were observed in crystallinity or the ratio of mature to immature enzymatic matrix crosslinks from FTIR. Altered bone turnover affected bone quality outcomes. Patients with low-turnover bone did not demonstrate material changes, but did have lowered trabecular bone volume and thickness than controls [Malluche *et al.,* 2012]. Additional studies of bone quality in human studies of CKD are sparse. Case study evidence presented in a review article described “island-like” hypomineralized regions of human trabecular bone [Kazama *et al.,* 2015]. Mitome and coworkers evaluated iliac bone biopsies from patients on dialysis with severe secondary hyperthyroidism and high-turnover bone. Bone

outcomes were compared with cadaveric controls. Analysis of crosslinks with HPLC revealed that the CKD group had relatively more immature enzymatic crosslinks compared with controls, and a 10-fold increase in pentosidine [Mitome *et al.*, 2012]. Important evidence has been gathered from these human studies about how bone material may change in CKD. However, these few studies have not answered numerous clinically-relevant questions. In particular, it is unknown how CKD affects bone quality outcomes in the cortical as well as trabecular compartments, how CKD and aging together reduce bone quality, and how bone quality may be affected in kidney disease preceding end-stage renal failure.

Studies of bone outcomes in rodent models of CKD are relatively more frequent than human studies, but results from these efforts still create confusion about the changes to bone material and microarchitecture occurring with kidney disease. Whether and how CKD affects microscale bone material has been a particular source of disagreement between studies. Kadokawa and co-workers reported on bone outcomes from male Crlj:CD1 mice subjected to moderate CKD *via* 5/6th nephrectomy (5/6th of kidney volume removed, '5/6 Nx') at 5-6 weeks of age. At 26 weeks of age, mice had diminished trabecular thickness and increased trabecular spacing, as well as lower trabecular number, bone volume / total volume, and connectivity density. Meanwhile, measurements at the center of the midshaft cortical tibia with FTIR and nanoindentation did not evidence differences in microscale material properties with CKD, leading the authors to conclude that bone fragility in CKD originates from diminished bone microarchitecture and not impairment of bone material [Kadokawa *et al.*, 2006]. Findings from this study were in disagreement with a later study of CKD in 12-week old male Sprague-Dawley rats, where high-turnover CKD was induced with 5/6 Nx and compared with low-turnover CKD (5/6 Nx + thyroparathyroidectomy (TPTx)), low-turnover control (TPTx), or sham groups. After 16 weeks of CKD, both high- and low- turnover groups had reduced storage modulus and tan delta for the whole femur, as well as diminished microscale material properties. Raman measures of Pentosidine:matrix were increased and crystallinity was decreased for both high-turnover and low-turnover groups. Meanwhile, mineral:matrix decreased in high-turnover CKD and increased with low-turnover CKD. The degree of orientation of hydroxyapatite bone crystals (alignment of c-axis) was also decreased in both high- and low-turnover CKD. As with the Kadokawa *et al.* report,

material properties in this study were measured in the middle of the cortical thickness at the sectioned mid-shaft diaphysis. While there were differences in the bone studied (tibia *vs* femur), and method of microscale material assessment (FTIR *vs* Raman), a potentially more significant reason for discrepancies between these studies is the location of material property assessment. In rodents, bone forms predominantly on periosteal and endosteal surfaces. Newly formed bone following 5/6 Nx may be expected to demonstrate an effect of CKD, while extant tissue in the interior bone cortex would be less likely to change. Both studies reported surveying the interior bone tissue; differences from one study to another in distance of the evaluation sites from the forming surfaces could influence the interpretation of bone material quality measurements.

Progressive genetic models are also employed to study bone quality changes in CKD. In a genetic polycystic CKD model in male Cy/+ rats, there were no differences in bone quality at 30 weeks (moderate disease) between rats with CKD and their wild-type littermates [Newman *et al.*, 2014]. Neither AFM-measured elastic modulus nor Raman chemistry (mineral:matrix, carbonate:phosphate, crystallinity) measured at the cortical surface of whole bones worsened with CKD. Enzymatic and non-enzymatic (pentosidine) crosslinks measured by HPLC were also similar between CKD and wild-type groups. Initial indentations from reference point indentation (RPI) were 20% deeper with CKD, suggesting a possible change in bone mechanical properties. Meanwhile, 35-week old Cy/+ rats with severe renal dysfunction and high-turnover or low-turnover (through administration of calcium to drinking water) bone had increased pentosidine [Allen *et al.*, 2015]. High-bone turnover rats had significantly higher cortical porosity and lower ultimate stress from four-point bending than controls, while low-turnover rats had significantly lower toughness. Tissue-scale material property measurements analogous to the earlier study in younger rats were not reported. Thus, current rodent studies depict an incongruous picture of whether material properties should change in moderate CKD, and whether these changes are likely to involve the mineral, the collagen matrix, or both.

Several studies have also considered the effects of therapeutic agents on bone outcomes in CKD. Iwasaki *et al* administered an oral adsorbent of the ureac toxin indoxyl sulfate to rats with 5/6 Nx and TPTx [Iwasaki *et al.*, 2013]. The AST-120 drug rescued the increased pentosidine, mineral:matrix ratio, and

carbonate:phosphate resulting from CKD, but did not have a different effect from vehicle on whole bone storage modulus or tan delta. Several other studies have considered treatment effects in the Cy/+ model of genetic CKD. Rats were treated with zoledronic acid, an anti-resportive bisphosphonate, calcium in the drinking water to serve as a phosphate binder and lower PTH, or both [Moe *et al.*, 2014]. These therapies were administered at 25 weeks, and bone outcomes evaluated at 35 weeks in rats with severe CKD. Both zoledronic acid and calcium increased trabecular bone volume measured by microCT. However, while calcium lessened cortical porosity and increased ultimate load and stiffness from three-point bending, zoledronic acid did not. Calcium meanwhile lead to increased calcification at the aortic arch. Another study compared zoledronic acid, an anti-sclerostin antibody, and vehicle on bone outcomes in Cy/+ rats [Moe *et al.*, 2015]. Rats were additionally stratified into high- and low-PTH groups through administration of calcium in their drinking water. The anti-sclerostin antibody only increased bone volume / total volume and trabecular mineralization surface in animals with low PTH. Cortical porosity was not affected by either treatment, nor were biomechanical properties from four-point bending. None of these studies have thoroughly evaluated how candidate treatments impact microscale material properties or fracture toughness. The effects of bisphosphonates and anti-sclerostin antibody on bone material in CKD are likely complex, and a more complete understanding of the effects of CKD on bone material is necessary to evaluate whether a therapy can rescue diminished bone quality and fracture resistance.

In summary, previous studies of bone outcomes in human CKD as well as rodent analogues present evidence that changes to bone material properties and microarchitecture may be important for understanding the development of bone fragility with kidney disease. However, several gaps currently exist in the understanding of how bone quality is diminished with CKD. First, rodent studies are necessary for the careful study of bone outcomes in CKD, but are in disagreement about whether and how microscale bone material may change. Studying bone formed after the onset of CKD as opposed to extant tissue may serve to clarify these discrepancies. It is also important to understand whether the osteocyte may contribute to changes to bone quality in CKD. The osteocyte is implicated in the pathophysiology of CKD, and a growing body of work suggests that the osteocyte regulates local bone material and structure. Yet changes

to three-dimensional osteocyte lacunar geometries have not been investigated in CKD. Next, previous animal models have all involved young rodents. It is unknown how aging and CKD together influence bone outcomes. This is an essential question considering that most patients with CKD are elderly. Lastly, though effects of CKD on microscale bone heterogeneity could contribute to loss of fracture toughness, this hypothesis has not been evaluated. These gaps in the clinical understanding of how CKD affects bone quality and fracture resistance motivate the work described within this thesis.

2.7 References

1. Levey, A. S., Atkins, R., Coresh, J., Cohen, E. P., Collins, A. J., Eckardt, K. U., ... & Powe, N. R. (2007). Chronic kidney disease as a global public health problem: approaches and initiatives–a position statement from Kidney Disease Improving Global Outcomes. *Kidney international*, *72*(3), 247-259.

2. Moe, S., Drüeke, T., Cunningham, J., Goodman, W., Martin, K., Olgaard, K., & Eknoyan, G. (2006). Definition, evaluation, and classification of renal osteodystrophy: a position statement from Kidney Disease: Improving Global Outcomes (KDIGO). *Kidney international*, *69*(11), 1945-1953.

3. Zhang, Q. L., & Rothenbacher, D. (2008). Prevalence of chronic kidney disease in population-based studies: systematic review. *BMC public health*,*8*(1).

4. Naylor, K. L., McArthur, E., Leslie, W. D., Fraser, L. A., Jamal, S. A., Cadarette, S. M., ... & Garg, A. X. (2014). The three-year incidence of fracture in chronic kidney disease. *Kidney international*, *86*(4), 810-818.

5. Nickolas, T. L., Leonard, M. B., & Shane, E. (2008). Chronic kidney disease and bone fracture: a growing concern. *Kidney international*, *74*(6), 721-731.

6. Nitsch, D., Mylne, A., Roderick, P. J., Smeeth, L., Hubbard, R., & Fletcher, A. (2009). Chronic kidney disease and hip fracture-related mortality in older people in the UK. *Nephrology Dialysis Transplantation*, *24*(5), 1539-1544.

7. Rogers, M. J., Gordon, S., Benford, H. L., Coxon, F. P., Luckman, S. P., Monkkonen, J., & Frith, J. C. (2000). Cellular and molecular mechanisms of action of bisphosphonates. *Cancer*, *88*(S12), 2961-2978.

8. Gourion-Arsiquaud, S., Allen, M. R., Burr, D. B., Vashishth, D., Tang, S. Y., & Boskey, A. L. (2010). Bisphosphonate treatment modifies canine bone mineral and matrix properties and their heterogeneity. *Bone*, *46*(3), 666-672.

9. Allen, M. R., Gineyts, E., Leeming, D. J., Burr, D. B., & Delmas, P. D. (2008). Bisphosphonates alter trabecular bone collagen cross-linking and isomerization in beagle dog vertebra. *Osteoporosis international*, *19*(3), 329-337.

10. Mashiba, T., Hirano, T., Turner, C. H., Forwood, M. R., Johnston, C. C., & Burr, D. B. (2000). Suppressed bone turnover by bisphosphonates increases microdamage accumulation and reduces some biomechanical properties in dog rib. *Journal of Bone and Mineral Research*, *15*(4), 613-620.

11. Malluche, H. H., Mawad, H., & Monier-Faugere, M. C. (2004). The importance of bone health in end-stage renal disease: out of the frying pan, into the fire?. *Nephrology Dialysis Transplantation*, *19*(suppl 1), i9-i13.

12. Quarles, L. D. (2008). Endocrine functions of bone in mineral metabolism regulation. *The Journal of clinical investigation*, *118*(12), 3820-3828.

13. Fang, Y., Ginsberg, C., Sugatani, T., Monier-Faugere, M. C., Malluche, H., & Hruska, K. A. (2014). Early chronic kidney disease–mineral bone disorder stimulates vascular calcification. *Kidney international*, *85*(1), 142-150.

14. Quarles, L. D. (2012). Role of FGF23 in vitamin D and phosphate metabolism: implications in chronic kidney disease. *Experimental cell research*, *318*(9), 1040-1048.

15. Sabbagh, Y., Graciolli, F. G., O'Brien, S., Tang, W., dos Reis, L. M., Ryan, S., ... & Liu, S. (2012). Repression of osteocyte Wnt/β-catenin signaling is an early event in the progression of renal osteodystrophy. *Journal of Bone and Mineral Research*, *27*(8), 1757-1772.

16. Komaba, H., & Fukagawa, M. (2010). FGF23–parathyroid interaction: implications in chronic kidney disease. *Kidney international*, *77*(4), 292-298.

17. Kazama, J. J., Matsuo, K., Iwasaki, Y., & Fukagawa, M. (2015). Chronic kidney disease and bone metabolism. *Journal of bone and mineral metabolism*, *33*(3), 245-252.

18. Gourion-Arsiquaud, S., Faibish, D., Myers, E., Spevak, L., Compston, J., Hodsman, A., ... & Boskey, A. L. (2009). Use of FTIR spectroscopic imaging to identify parameters associated with fragility fracture. *Journal of bone and mineral research*, *24*(9), 1565-1571.

19. Boskey, A. (2003). Bone mineral crystal size. *Osteoporosis international*, *14*, S16-S21.

20. Saito, M., & Marumo, K. (2010). Collagen cross-links as a determinant of bone quality: a possible explanation for bone fragility in aging, osteoporosis, and diabetes mellitus. *Osteoporosis international*, *21*(2), 195-214.

21. Chaitou, A., Boutroy, S., Vilayphiou, N., Munoz, F., Delmas, P. D., Chapurlat, R., & Szulc, P. (2010). Association between bone turnover rate and bone microarchitecture in men: the STRAMBO study. *Journal of Bone and Mineral Research*, *25*(11), 2313-2323.

22. Seeman, E., & Delmas, P. D. (2006). Bone quality—the material and structural basis of bone strength and fragility. *New England Journal of Medicine*, *354*(21), 2250-2261.

23. Donnelly, E, Boskey, AL, Baker SP, van der Meulen MCH (2009). Effects of tissue age on bone tissue material composition and nanomechanical properties in the rat cortex. Journal of Biomedical Materials Research, Part A; (92): 1048-1056.

24. Moe, S. M., & Chen, N. X. (2008). Mechanisms of vascular calcification in chronic kidney disease. *Journal of the American Society of Nephrology*,*19*(2), 213-216.

25. Moe, S. M., Chen, N. X., Newman, C. L., Organ, J. M., Kneissel, M., Kramer, I.. & Allen, M. R. (2015). Anti-sclerostin antibody treatment in a rat model of progressive renal osteodystrophy. *Journal of Bone and Mineral Research*, *30*(3), 499-509.

26. Yang, H. C., Zuo, Y., & Fogo, A. B. (2010). Models of chronic kidney disease. *Drug Discovery Today: Disease Models*, *7*(1), 13-19.

27. Ferrari, G. O., Ferreira, J. C., Cavallari, R. T., Neves, K. R., dos Reis, L. M., Dominguez, W. V., ... & Moysés, R. M. (2014). Mineral bone disorder in chronic kidney disease: head-to-head comparison of the 5/6 nephrectomy and adenine models. *BMC nephrology*, *15*(1), 1.

28. Chanutin, A., & Ferris, E. B. (1932). Experimental renal insufficiency produced by partial nephrectomy: I. Control diet. *Archives of Internal Medicine*, *49*(5), 767-787.

29. Gava, A. L., Freitas, F. P., Balarini, C. M., Vasquez, E. C., & Meyrelles, S. S. (2012). Effects of 5/6 nephrectomy on renal function and blood pressure in mice. *International journal of physiology, pathophysiology and pharmacology*, *4*(3), 167.

30. Iwasaki, Y., Kazama, J. J., Yamato, H., Matsugaki, A., Nakano, T., & Fukagawa, M. (2015). Altered material properties are responsible for bone fragility in rats with chronic kidney injury. *Bone*, *81*, 247-254.

31. Iwasaki, Y., Kazama, J. J., Yamato, H., & Fukagawa, M. (2011). Changes in chemical composition of cortical bone associated with bone fragility in rat model with chronic kidney disease. *Bone*, *48*(6), 1260-1267.

32. Kadokawa, S., Matsumoto, T., Naito, H., & Tanaka, M. (2011). Assessment of Trabecular Bone Architecture and Intrinsic Properties of Cortical bone Tissue in a Mouse Model of Chronic Kidney Disease. *Journal of Hard Tissue Biology*, *20*(2), 79-86.

33. Newman, C. L., Moe, S. M., Chen, N. X., Hammond, M. A., Wallace, J. M., Nyman, J. S., & Allen, M. R. (2014). Cortical bone mechanical properties are altered in an animal model of progressive chronic kidney disease. *PloS one*,*9*(6), e99262.

34. Moe, S. M., Chen, N. X., Newman, C. L., Gattone, V. H., Organ, J. M., Chen, X., & Allen, M. R. (2014). A comparison of calcium to zoledronic acid for improvement of cortical bone in an animal model of CKD. *Journal of Bone and Mineral Research*, *29*(4), 902-910.

35. Allen, M. R., Newman, C. L., Chen, N., Granke, M., Nyman, J. S., & Moe, S. M. (2014). Changes in skeletal collagen cross-links and matrix hydration in high-and low-turnover chronic kidney disease. *Osteoporosis International*, *26*(3), 977-985.

36. Rheault, M. N., Kren, S. M., Thielen, B. K., Mesa, H. A., Crosson, J. T., Thomas, W., ... & Segal, Y. (2004). Mouse model of X-linked Alport syndrome. *Journal of the American Society of Nephrology*, *15*(6), 1466-1474.

37. Stubbs, J. R., He, N., Idiculla, A., Gillihan, R., Liu, S., David, V., ... & Quarles, L. D. (2012). Longitudinal evaluation of FGF23 changes and mineral metabolism abnormalities in a mouse model of chronic kidney disease.*Journal of Bone and Mineral Research*, *27*(1), 38-46.

38. Bonewald, L. F. (2011). The amazing osteocyte. *Journal of Bone and Mineral Research*, *26*(2), 229-238.

39. Teti, A., & Zallone, A. (2009). Do osteocytes contribute to bone mineral homeostasis? Osteocytic osteolysis revisited. *Bone*, *44*(1), 11-16.

40. Weiner, S., & Traub, W. (1992). Bone structure: from angstroms to microns.*The FASEB journal*, *6*(3), 879-885.

41. Wopenka, B., & Pasteris, J. D. (2005). A mineralogical perspective on the apatite in bone. *Materials Science and Engineering: C*, *25*(2), 131-143.

42. Faibish, D., Gomes, A., Boivin, G., Binderman, I., & Boskey, A. (2005). Infrared imaging of calcified tissue in bone biopsies from adults with osteomalacia. *Bone*, *36*(1), 6-12.

43. Karunaratne, A., *et al*. (2012). Significant deterioration in nanomechanical quality occurs through incomplete extrafibrillar mineralization in rachitic bone: Evidence from in-situ synchrotron X-ray scattering and backscattered electron imaging. *Journal of Bone and Mineral Research*, *27*(4), 876-890.

44. Linden, E., Cai, W., He, J. C., Xue, C., Li, Z., Winston, J., ... & Uribarri, J. (2008). Endothelial dysfunction in patients with chronic kidney disease results from advanced glycation end products (AGE)-mediated inhibition of endothelial nitric oxide synthase through RAGE activation. *Clinical Journal of the American Society of Nephrology*, *3*(3), 691-698.

45. Zimmermann, E. A., Schaible, E., Bale, H., Barth, H. D., Tang, S. Y., Reichert, P., ... & Ritchie, R. O. (2011). Age-related changes in the plasticity and toughness of human cortical bone at multiple length scales. *Proceedings of the National Academy of Sciences*, *108*(35), 14416-14421.

46. Malluche, H. H., Porter, D. S., Monier-Faugere, M. C., Mawad, H., & Pienkowski, D. (2012). Differences in bone quality in low-and high-turnover renal osteodystrophy. *Journal of the American Society of Nephrology*, *23*(3), 525-532.

47. Hadjidakis, D. J., & Androulakis, I. I. (2006). Bone remodeling. *Annals of the New York Academy of Sciences*, *1092*(1), 385-396.

48. Ferguson, V. L., Ayers, R. A., Bateman, T. A., & Simske, S. J. (2003). Bone development and age-related bone loss in male C57BL/6J mice. *Bone*, *33*(3), 387-398.

49. Burr, D. B., Martin, R. B., Schaffler, M. B., & Radin, E. L. (1985). Bone remodeling in response to in vivo fatigue microdamage. *Journal of biomechanics*, *18*(3), 189-200.

50. Robling, A. G., Castillo, A. B., & Turner, C. H. (2006). Biomechanical and molecular regulation of bone remodeling. *Annu. Rev. Biomed. Eng.*, *8*, 455-498.

51. Qing, H., Ardeshirpour, L., Divieti Pajevic, P., Dusevich, V., Jähn, K., Kato, S., ... & Bonewald, L. F. (2012). Demonstration of osteocytic perilacunar/canalicular remodeling in mice during lactation. *Journal of bone and mineral research*, *27*(5), 1018-1029.

52. McGee-Lawrence, M. E., Stoll, D. M., Mantila, E. R., Fahrner, B. K., Carey, H. V., & Donahue, S. W. (2011). Thirteen-lined ground squirrels (Ictidomys tridecemlineatus) show microstructural bone loss during hibernation but preserve bone macrostructural geometry and strength. *Journal of Experimental Biology*, *214*(8), 1240-1247.

53. Blaber, E. A., Dvorochkin, N., Lee, C., Alwood, J. S., Yousuf, R., Pianetta, P., ... & Almeida, E. A. (2013). Microgravity induces pelvic bone loss through osteoclastic activity, osteocytic osteolysis, and osteoblastic cell cycle inhibition by CDKN1a/p21. *PloS one*, *8*(4), e61372.

54. Lane, N. E., Yao, W., Balooch, M., Nalla, R. K., Balooch, G., Habelitz, S., ... & Bonewald, L. F. (2006). Glucocorticoid-Treated Mice Have Localized Changes in Trabecular Bone Material Properties and Osteocyte Lacunar Size That Are Not Observed in Placebo-Treated or Estrogen-Deficient Mice.*Journal of bone and mineral research*, *21*(3), 466-476.

55. Boskey, A. L. (2002). Variations in bone mineral properties with age and disease. *JOURNAL OF MUSCULOSKELETAL AND NEURONAL INTERACTIONS*, *2*(6), 532-534.

56. Currey, J. D., Brear, K., & Zioupos, P. (1996). The effects of ageing and changes in mineral content in degrading the toughness of human femora.*Journal of biomechanics*, *29*(2), 257-260.

57. Nyman, J. S., Roy, A., Acuna, R. L., Gayle, H. J., Reyes, M. J., Tyler, J. H., ... & Wang, X. (2006). Age-related effect on the concentration of collagen crosslinks in human osteonal and interstitial bone tissue. *Bone*, *39*(6), 1210-1217.

58. Schaffler, M. B., Choi, K., & Milgrom, C. (1995). Aging and matrix microdamage accumulation in human compact bone. *Bone*, *17*(6), 521-525.

59. Parfitt, A. M., Mathews, C. H., Villanueva, A. R., Kleerekoper, M., Frame, B., & Rao, D. S. (1983). Relationships between surface, volume, and thickness of iliac trabecular bone in aging and in osteoporosis. Implications for the microanatomic and cellular mechanisms of bone loss. *Journal of clinical investigation*, *72*(4), 1396.

60. Zioupos, P., & Currey, J. D. (1998). Changes in the stiffness, strength, and toughness of human cortical bone with age. *Bone*, *22*(1), 57-66.

61. Lloyd, A. A., Wang, Z. X., & Donnelly, E. (2015). Multiscale contribution of bone tissue material property heterogeneity to trabecular bone mechanical behavior. *Journal of biomechanical engineering*, *137*(1), 010801.

62. Tai, K., Dao, M., Suresh, S., Palazoglu, A., & Ortiz, C. (2007). Nanoscale heterogeneity promotes energy dissipation in bone. *Nature materials*, *6*(6), 454-462.

63. Koester, K. J., Ager, J. W., & Ritchie, R. O. (2008). The true toughness of human cortical bone measured with realistically short cracks. *Nature materials*, *7*(8), 672-677.

64. Ciarelli, T. E., Tjhia, C., Rao, D. S., Qiu, S., Parfitt, A. M., & Fyhrie, D. P. (2009). Trabecular packet-level lamellar density patterns differ by fracture status and bone formation rate in white females. *Bone*, *45*(5), 903-908.

65. Busse, B., Hahn, M., Soltau, M., Zustin, J., Püschel, K., Duda, G. N., & Amling, M. (2009). Increased calcium content and inhomogeneity of mineralization render bone toughness in osteoporosis: mineralization, morphology and biomechanics of human single trabeculae. *Bone*, *45*(6), 1034-1043.

66. Tamminen, I. S., Misof, B. M., Roschger, P., Mäyränpää, M. K., Turunen, M. J., Isaksson, H., & Klaushofer, K. (2014). Increased heterogeneity of bone matrix mineralization in pediatric patients prone to fractures: a biopsy study. *Journal of Bone and Mineral Research*, *29*(5), 1110-1117.

67. Oyen, M. L., Ferguson, V. L., Bembey, A. K., Bushby, A. J., & Boyde, A. (2008). Composite bounds on the elastic modulus of bone. *Journal of biomechanics*, *41*(11), 2585-2588.

68. Vashishth, D., Behiri, J. C., & Bonfield, W. (1997). Crack growth resistance in cortical bone: concept of microcrack toughening. *Journal of biomechanics*,*30*(8), 763-769.

69. Nalla, R. K., Kinney, J. H., & Ritchie, R. O. (2003). Mechanistic fracture criteria for the failure of human cortical bone. *Nature materials*, *2*(3), 164-168.

70. Launey, M. E., Buehler, M. J., & Ritchie, R. O. (2010). On the mechanistic origins of toughness in bone. *Annual review of materials research*, *40*, 25-53.

71. Mitome, J., Yamamoto, H., Saito, M., Yokoyama, K., Marumo, K., & Hosoya, T. (2011). Nonenzymatic cross-linking pentosidine increase in bone collagen and are associated with disorders of bone mineralization in dialysis patients. *Calcified tissue international*, *88*(6), 521-529.

72. Iwasaki, Y., Kazama, J. J., Yamato, H., Shimoda, H., & Fukagawa, M. (2013). Accumulated uremic toxins attenuate bone mechanical properties in rats with chronic kidney disease. *Bone*, *57*(2), 477-483.

73. Gardinier, J. D., Al-Omaishi, S., Morris, M. D., & Kohn, D. H. (2016). PTH signaling mediates perilacunar remodeling during exercise. *Matrix Biology*, *52*, 162-175.

74. Farr, J. N., Fraser, D. G., Wang, H., Jaehn, K., Ogrodnik, M. B., Weivoda, M. M., ... & Bonewald, L. F. (2016). Identification of senescent cells in the bone microenvironment. *Journal of Bone and Mineral Research*, *31*(11), 1920-1929.

75. Tang, S. Y., Herber, R. P., Ho, S. P., & Alliston, T. (2012). Matrix metalloproteinase–13 is required for osteocytic perilacunar remodeling and maintains bone fracture resistance. *Journal of Bone and Mineral Research*, *27*(9), 1936-1950

76. Makowski, A. J., Granke, M., Uppuganti, S., Mahadevan-Jansen, A., & Nyman, J. S. (2015, February). Bone tissue heterogeneity is associated with fracture toughness: a polarization Raman spectroscopy study. In *SPIE BiOS* (pp. 930341-930341). International Society for Optics and Photonics.

77. Granke, M., Makowski, A. J., Uppuganti, S., Does, M. D., & Nyman, J. S. (2015). Identifying novel clinical surrogates to assess human bone fracture toughness. *Journal of Bone and Mineral Research*, *30*(7), 1290-1300.

3. Bone quality characterization

3.1 Nanoindentation

3.1.1 Contact mechanics

The contact mechanics underlying nanoindentation analysis originate from Hertzian mechanics for elastic contact. For frictionless, elastic contact of a rigid spherical indenter with a homogeneous material, Hertz found that the contact radius (a) is related to the radius of the indenter (R) and the deflection of the specimen free surface (h) as [Fisher-Cripps 2002]:

$Equation$ 3.1.1 $$a^2 = Rh$$

Hertz showed that for spherical contact, the surface deflection is related to the applied load as [Fischer-Cripps 2002]:

$Equation$ 3.1.2 $$P = \frac{4\,E_R\sqrt{R}}{3}h^{3/2}$$

Half a century later, Sneddon further determined that for a cone of angle 2α, the relationship between load and displacement could be modified as [Sneddon 1948]:

$Equation$ 3.1.3 $$P = \frac{2\,E_R tan(\alpha)}{\pi}h^2$$

In the 1970s, the Russian scientists Bulychev *et al* published a method to determine Young's modulus from the unloading curve of an indentation test [Bulychev *et al*, 1976]. A relationship between the unloading slope, max load, and contact area was derived from Sneddon's equation for conical contact (Equation 3.1.3), by taking the derivative of P with respect to h and setting $h=h_{max}$, $a = h_c\tan(\alpha)$, and $h_c/h = 2/\pi$, and $A = \pi a^2$. The resulting equation, now utilized in most conventional elastic-plastic nanoindentation analyses is:

$Equation$ 3.1.4 $$E_R = \frac{dP}{dh}\frac{\sqrt{\pi}}{\sqrt{A}} = S\frac{\sqrt{\pi}}{\sqrt{A}}$$

This approach assumes elastic unloading, and thus dP/dh is taken from the initial portion of the unloading curve. Pharr, Oliver, and Brotzen demonstrated that Equation 3.1.4 can be applied to all axially symmetric indenters geometries instead of just conical tips [Pharr *et al*., 1992]. This relationship applies well to elastic

and also elastic-plastic contact [Oliver & Pharr, 2004] and is robust to small geometric deviations from axisymmetry [Gao & Wu, 1993].

3.1.2 Oliver - Pharr analysis

Oliver and Pharr pioneered an analytic approach to nanoindentation in the early 1990s by providing a method to estimate contact area and contact depth from indentation without the need to directly image the residual indents as had been required in earlier hardness testing [Oliver & Pharr, 2004]. In the Oliver-Pharr method, testing with a known tip geometry (through calibration) makes measurement of modulus and hardness possible from the load-displacement curves. Oliver and Pharr expanded upon work by Sneddon to calculate the contact depth, h_c, knowing only the maximum depth, maximum load, and stiffness, all of which are easily measurable properties:

Equation 3.1.5
$$h_c = h_{max} - \varepsilon \frac{P_{max}}{S}$$

The constant ε is given as 0.75 for a paraboloid of revolution.

Tip calibration to calculate $A = A(h_c)$ is achieved by placing an array of indents at varying loads in a known reference standard (*e.g.* fused quartz or single crystal aluminum). Using a known value for E_r for the calibration material, A is calculated for each point using Equation 3.1.4 and then regressed against h_c to give a calibration curve. The curve is fit with the relation:

Equation 3.1.6
$$A = C_0 h_c^2 + C_1 h_c + C_2 h_c^{1/2} + C_3 h_c^{1/4} \ldots$$

Having established $A = A(h_c)$ from tip calibration, the reduced modulus for the material under investigation is calculated from Equation 3.1.4.

This reduced modulus is a combination of both sample and tip mechanical properties (E_{tip} = 1140 GPa, ν_{tip}= 0.17), according to:

Equation 3.1.7
$$\frac{1}{E_r} = \frac{1}{E'} + \frac{(1 - \nu_{tip}^2)}{E_{tip}}$$

The plane strain elastic modulus, *E'*, is a function of the sample elastic modulus as well as Poisson's ratio. Thus, in calculating and reporting *E'*, assumptions are avoided about the sample Poisson's ratio.

Equation 3.1.8 $$E'_{sample} = \frac{E_{sample}}{(1 - v^2_{sample})}$$

The contact hardness can be calculated from:

Equation 3.1.9 $$H = \frac{P_{max}}{A}$$

However, it should be noted that contact hardness scales with total deformation upon loading, because at P_{max} both elastic and plastic contributions to deformation have occurred. Thus, contact hardness is highly correlated to elastic modulus for materials with considerable elastic response, such as bone, and is not an independent measure [Olesiak *et al*, 2010; Ferguson *et al* 2009; Oyen & Ko 2007].

3.1.3 Special considerations for nanoindentation of bone

Nanoindentation is useful for understanding how age [*e.g.*, Donnelly *et al.*, 2011; Rho *et al.*, 2002], disease [*e.g.*, Heveran *et al.*, 2016; Nyman *et al.*, 2011; Fratzl-Zelman 2009], and other physiologically relevant factors influence bone tissue mechanical properties. However, the standard triangular load-unload curve sufficient for analyzing metals and ceramics is troublesome for the nanoindentation of viscoelastic materials, including bone. The viscoelasticity of bone has contributions from multiple length-scales: collagen fibers, cement lines, and fluid flow together generate the time-dependent mechanical response of bone tissue [Garner *et al.*, 2000]. When indenting a viscoelastic material with a triangular load-unload function, the unloading curve bows outward due to the creep rate exceeding the unloading rate [Ebenstein *et al.*, 2006; Olesiak *et al.*, 2010; Bushby *et al.*, 2004], preventing analysis of stiffness from the unloading curve slope. Viscoelastic energy can be dissipated with a hold period as the central segment in a trapezoidal load function [Ebenstein *et al.*, 2006, Olesiak *et al*, 2010]. Alternatively, viscoelasticity of bone can be directly analyzed from the hold period [Olesiak *et al*, 2010].

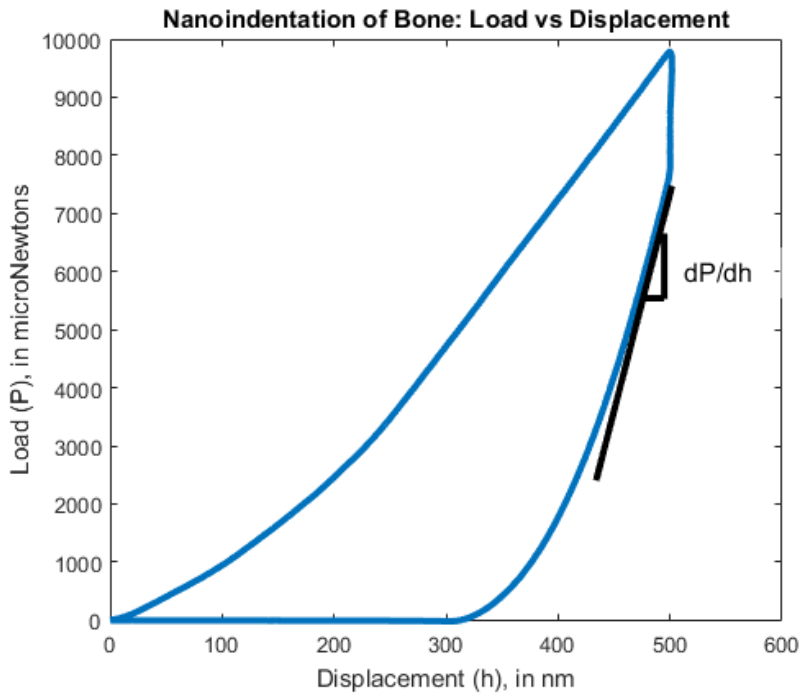

Figure 3-1: Nanoindentation of cortical mouse bone

Another important consideration for the nanoindentation of bone is porosity. The pores in bone can crush and compact during indentation, leading to an artificial stiffening under the indenter tip [Vanstreels *et al.*, 2013]. Embedding the bone with an infiltrating polymer, such as poly(methyl)methacrylate (PMMA) stabilizes the pore volumes and also allows for the surface to be polished to a fine finish [Bushby *et al.*, 2004]. The embedding process does change mechanical properties of bone; dehydration and embedding results in significantly increased nanoindentation modulus and thus results following this method require careful comparison with bone prepared differently [Bushby *et al.*, 2004].

3.1.4 Assessment of microscale heterogeneity using nanoindentation

The spatial heterogeneity of mechanical properties at the nano- to microscales corresponds to chemical, structural, and compositional variation in the material [Ulm *et al.*, 2007]. Nanoindentation has been employed to assess heterogeneity of modulus in shales [Wilkinson *et al.*, 2015; Ulm *et al.*, 2007], concrete [Ulm *et al.*, 2007], polymers [Bedoui *et al*, 2008], battery electrode materials [Baranowski *et al*,

2016; Amanieu *et al*, 2014], and bone [*e.g.*, Heveran *et al.*, 2016; Paietta *et al.*, 2011, Ulm *et al* 2007, Rho *et al.*, 2002; Tai *et al.*, 2007; Yao *et al.*, 2011; Hoffler *et al.*, 2000]. From finite element analyses generated from spatially-surved nanoindentation modulus in bovine bone, it is expected that heterogeneity in mechanical properties measured with nanoindentation can contribute to energy dissipation at crack tips and therefore improved fracture toughness [Tai *et al.*, 2007; Yao *et al.*, 2011].

Properly evaluating heterogeneity in nanoindentation modulus requires careful tip selection and well as choice of indentation depth. In bone, the smallest structural features, such as individual lamellae and the interlamellar transition zones between them, occur at in the order of single micrometers [Gupta *et al.*, 2006]. Tips small enough to survey bone microstructure include Berkovich and small (*e.g.*, 5 μm radius) conicospherical geometries. Small conicospherical tips have the additional advantage of promoting elastic contact [Bushby *et al.*, 2001]. Though loading-unloading curves from nanoindentation of bone demonstrate hysteresis and therefore inelastic energy dissipation, this plasticity is not explained by dislocation motion as with metals. Instead, inelasticity in bone is often achieved by microcracking [Ritchie *et al.*, 2008]. Depth of indentation is also an important consideration for assessing material heterogeneity. Shallow indentations are overly influenced by surface roughness, while increasing depth inevitably volume-averages material response. For bone embedded in PMMA, indentations between 200-500 micrometers in depth avoid surface roughness without substantial compromise in resolution of material heterogeneity [Paietta *et al.*, 2011].

3.2 Raman spectroscopy

3.2.1 Theory

Raman spectroscopy is a vibrational spectroscopic technique based on the inelastic scattering of laser light. In a typical Raman test, an approximately micrometer-sized beam of monochromatic light from a laser source is focused on the study sample (spot size = $1.22\,\lambda$ / numerical aperture). Though most photons elastically interact with the sample (Rayleigh scattering), a small fraction of the incident light (~ 1 in 10^7 photon) is inelastically scattered from molecular vibrations of the sample (Raman scattering). By exchanging energy with the sample, photons either lose (Stokes shift) or gain (anti-Stokes shift) energy, and therefore change frequency. Raman shifts occur at characteristic energies depending on the sample

chemistry. Molecular vibrations depend on the mass of the atoms and the strength of the bonds between them. Thus, weak bonds and heavy atoms lead to small Raman shifts while strong bonds and light atoms result in large Raman shifts. When intensity is plotted against the Raman shift in frequency (usually the stronger Stokes signal), bands emerge at characteristic frequency shifts to form the chemical "signature" of a material. Raman spectra can be collected in approximately micrometer-resolution maps; because of the non-destructive nature of the technique, spacing can be reduced to the resolution limit to deliver a two-dimensional map of sample chemistry [Colthup 2012].

3.2.2 Bone chemistry assessment with Raman spectroscopy

Raman spectroscopy delivers information about the carbonated hydroxyapatite mineral as well as the supporting collagen matrix. The major peaks pertaining to bone mineral include ν_1 Phosphate (960 cm^{-1}), ν_2 Phosphate (430 cm^{-1}), proline (855 cm^{-1}), and B-type carbonate (1070 cm^{-1}). The collagen matrix is primarily assessed from the amide I, amide III, proline, and CH_2 peaks. The amide I peak (1670 cm^{-1}) corresponds to C=O bonds perpendicular to the collagen backbone, while the amide III peak (1270 cm^{-1}) results from C-N vibrations along the backbone [Kazanci *et al.*, 2006]. The CH_2 peak is generated by collagen side groups and, to an extent, noncollageneous proteins. Yeni *et al* posited that changes to collagen secondary structure from dehydration should affect backbone amide peaks more than the side-group CH_2 signal [Yeni *et al.*, 2006]. Some peaks are also known to be polarization dependent. The collagen amide I and v_1 phosphate in particular are known to vary in intensity according to the polarization direction of incident laser light. This effect can be exploited with appropriate polarization optics to interpret collagen orientation, as has been shown in osteonal bone [Makowski *et al.*, 2013]. However, without additional optics, $v_1$phosphate:amide I demonstrates substantial polarization phase mismatch and thus is dependent on not only mineral content but also tissue organization [Gamsjaeger *et al.*, 2010]. Better alternatives include $v_2$phosphate:amide III and $v_1$phosphate:proline, which are each phase-matched to avoid polarization dependence [Gamsjaeger *et al.*, 2010; Makowski *et al.*, 2013].

3.2.3 Data acquisition and analysis

The acquisition of Raman spectra begins with determining appropriate excitation parameters. Although red and green lasers are both common in Raman spectroscopy systems, utilization of red laser light has the advantage of minimizing fluorescence from bone matrix proteins [Carden *et al.*, 2000]. Longer exposures and repeated acquisitions can improve signal to noise ratio for generated spectra. From the acquired Raman data, analysis starts with removal of background fluorescence, where a fitted polynomial subtracts the baseline from the spectra. The spectral contributions from embedding media can also be subtracted [*e.g.*, McCreadie *et al.*, 2006, Carden *et al.*, 2000, Donnelly *et al.*, 2009], although as previously mentioned, the process of bone dehydration and embedding with an infiltrating polymer can alter the secondary structure of collagen and thus affect backbone amide vibrations [Yeni *et al.*, 2006]. Following baseline subtraction and correction for embedding media, peak areas and intensities are quantified.

Results from Raman spectroscopy are typically compared in terms of peak ratios. Raman spectroscopy is exquisitely sensitive to topography, and so differences in beam focus from topographic gradients or surface roughness greatly affect peak intensities. Thus, normalized peak intensity or area ratios allow comparison of compositional information across samples [Carden *et al.*, 2000]. Commonly reported ratios for bone include mineral:matrix and carbonate:phosphate. The mineral:matrix ratio is commonly reported as ν_1 phosphate / amide I, but either ν_1 or ν_2 phosphate can be normalized to any of the collagen peaks: amide I, amide III, proline, or CH_2 [Carden *et al.*, 2000]. The carbonate:phosphate ratio can be reported as the 1070 cm^{-1} carbonate peak / ν_1 or ν_2 phosphate. Both mineral:matrix and carbonate:phosphate ratios are expected to increase with bone tissue maturation and the consequent increase in collagen mineralization as well as carbonate substitution into the hydroxyapatite crystal lattice [Donnelly *et al.*, 2009].

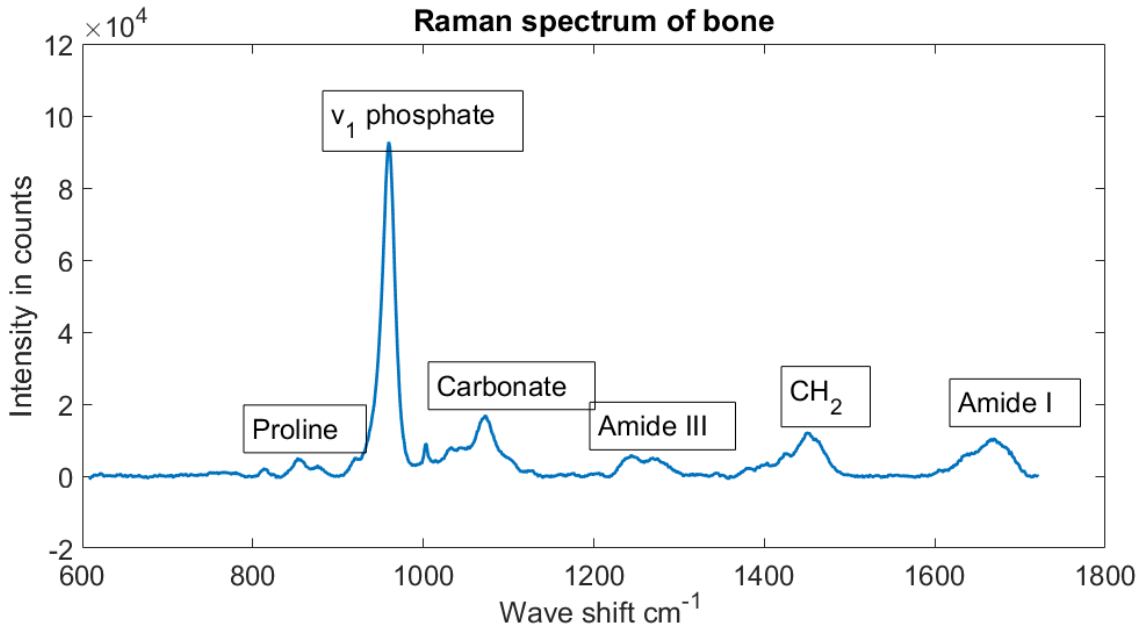

Figure 3-2: The Raman spectrum of bone

Some groups interpret the ratio of 1660/1690 sub peaks within the amide I envelope as representing the ratio of immature to mature crosslinks. This interpretation originated in FTIR work where band signals corresponding to standards for immature and mature crosslinks were determined at 1660 and 1690 cm^{-1} [Paschalis *et al.*, 2001]. Further work has revealed that care is required in the interpretation of the 1660/1690 ratio for Raman spectroscopy [McNerny *et al* 2014]. In particular, changes to the amide I envelope are produced by sample dehydration or denaturation [Yeni *et al.*, 2006]. However, even for samples without substantial damage from dehydration or embedding, the 1660:1690 ratio does not necessarily relate to changes to immature and mature crosslinks. For instance, in a study of lathyritic rats, the 1660:1690 did not correspond with immature and mature collagen crosslinks measured by gold-standard technique of high performance liquid chromatography [McNerny *et al.*, 2014]. For these reasons, the 1660:1690 ratio is not interpreted in the studies comprising this thesis, where the amide I band has likely been modified from sample dehydration and embedding.

Crystallinity can also be measured from Raman spectra. Yeramshetty *et al* demonstrated that crystallinity, defined as the inverse of the half-width of the ν_1 phosphate peak at the half-maximum intensity,

correlates well to the c-length of the carbonated hydroxyapatite crystal measured from the [002] reflection in X-Ray Diffraction for a range of biomineralized tissues [Yeramshetty *et al*, 2006]. As with mineral:matrix and carbonate:phosphate ratios, crystallinity is expected to increase with tissue maturation, although over a comparatively narrow spatial region [Donnelly *et al.*, 2009].

3.2.4. Raman spectroscopy measurements co-located with nanoindentation

Raman spectroscopy is well-suited for matched testing with nanoindentation. Raman spectra can be obtained under a range of preparation and environmental conditions, and are thus compatible with requirements for specimen thickness, stability, and hydration for nanoindentation. Unlike other spectroscopy techniques (*e.g.*, Fourier-Transformed Infrared Spectroscopy), Raman spectra can be obtained from thick specimens, which are generally more appropriate for nanoindentation testing [Carden *et al.*, 2000]. Samples are sometimes embedded in stabilizing media for nanoindentation (*e.g.*, PMMA, epoxy, acrylic); the contributions of an infiltrating polymer can be readily subtracted from Raman spectra [*e.g.* Donnelly *et al.*, 2009, McCreadie *et al.*, 2006]. Raman spectroscopy can also be performed for wet or submerged specimens [Carden *et al.*, 2000]. Maintaining sample hydration can be important for retaining sample microstructure (*e.g.*, biological materials), or for preserving the relationship between material chemistry and a time-dependent mechanical response (*e.g.*, viscoelastic or poroelastic materials).

Raman spectroscopy and nanoindentation are especially complementary because the microscale resolution of Raman spectroscopy is similar to the radii of the smallest indenter tips (*i.e.*, Berkovich or small conicospherical geometries). The matched length scales of Raman Spectroscopy and nanoindentation allows the generation of spatially matched two-dimensional maps of sample chemistry and mechanical properties (Figure 3-3).

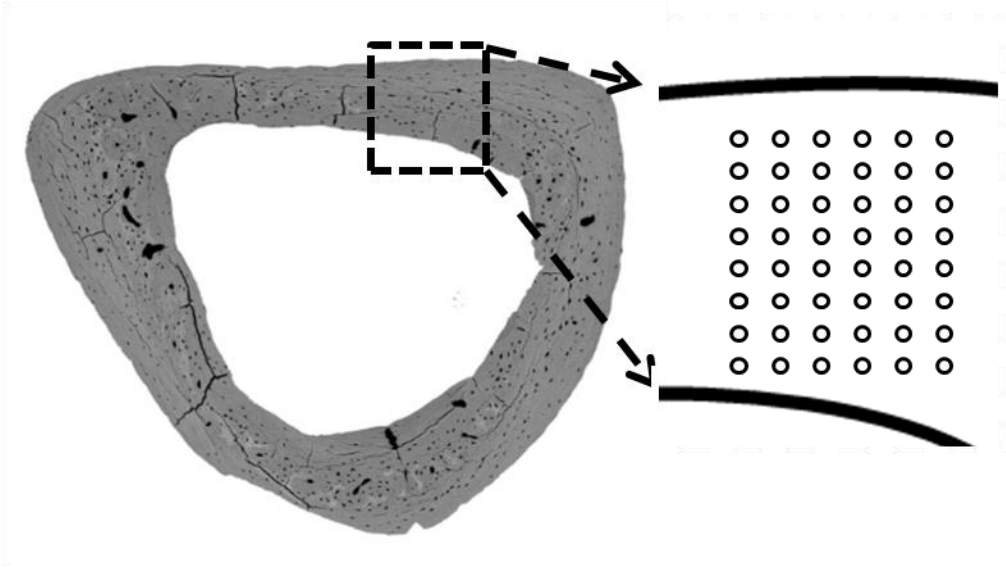

Figure 3-3: Site-matched measurement of bone material properties

Using this technique, the dependency of mechanical performance on microscale material heterogeneity has been assessed for bone tissue [Donnelly *et al.*, 2009; Hofmann *et al.*, 2006] However, because Raman spectroscopy must be assessed prior to nanoindentation in order to preserve sample structure, co-locating Raman spectroscopy and nanoindentation maps on separate instruments, as has been required with conventional Raman spectroscopy and nanoindentation platforms, is time-consuming and introduces the opportunity for spatial error. Using a novel co-located Raman Spectroscopy – Nanoindentation system facilitates mapping sample chemistry and mechanical properties efficiently and accurately [Tomaschke *et al.*, – in preparation].

3.3 Quantitative backscattered SEM

Secondary electron microscopy (SEM) techniques can probe the topography and composition of bone tissue. In SEM, electrons are emitted from a filament and directed towards the sample surface. The filament is typically tungsten, and emits electrons thermionically when voltage is applied and the filament consequently heats. The electron beam is focused onto the sample surface with condenser and objective lenses. The beam rasters across the sample surface under the control of electromagnetic coils, and the resulting spatial image is viewed on the computer monitor [Goldstein *et al.*, 2003].

The interaction of the electron beam with the sample produces secondary, Auger, and backscattered electrons. Secondary electrons form when an electron from the incident beam inelastically interacts with sample valence electrons, causing a sample atom to ionize and eject an electron. Some of the electrons emitted by the sample through this mechanism have enough energy to travel to the sample surface and escape towards the detector. The secondary electron mode detector is typically positively biased to help direct these electrons for collection. In this mode, bright areas on the image correspond to areas on the sample that generate a larger number of secondary electrons. Thus, secondary mode imaging is dominated by topographical contrast and is relatively unaffected by sample composition. Auger electrons are generated when an electron from an inner shell is ejected. An outer shell electron must radiate energy in order to fill the lower-energy inner shell vacancy, and necessarily emits x-ray radiation. The x-rays produced by these shell transitions have characteristic energies associated with the emitting element, and thus this signal can be used for compositional analysis [Goldstein *et al.*, 2003].

The backscattered signal is generated from elastic interactions between the incident beam and the nuclei of sample atoms. Backscattered electrons necessarily have higher energy (> 50 eV) than secondary electrons. These backscattered electrons travel linearly towards the backscatter detector. The secondary detector is sometimes positively biased during backscattered SEM imaging in order to avoid collection of the relatively stronger secondary mode signal [Goldstein *et al*, 2003]. Backscatter and secondary modes probe different interaction volumes; backscattered electrons can be generated several micrometers into the sample, while secondary electrons have a shallow escape depth close to the surface [Howell *et al.*, 2003]. The proportion of backscattered electrons to the number of incident electrons is referred to as the backscatter coefficient. The larger nuclei of heavier elements are more likely to backscatter incident electrons, and thus a strong compositional dependence exists between the backscatter coefficient and the atomic number [Goldstein *et al.*, 2003]. The backscatter coefficient, η, is related to the atomic number, Z, as in Equation 3.3.1:

Equation 3.3.1 $$\eta = 2^{-9/\sqrt{Z}}$$

Brightness in grey level is related linearly to the backscatter coefficient [Campbell *et al.*, 2012]. Therefore, measuring grey level in backscatter mode can be used to explore material composition. The backscatter coefficient is sensitive to working distance, beam current, accelerating voltage, and spot size. In order to obtain quantitative information (quantitative backscattered SEM, or qBSE) about sample composition that can be compared between imaging sessions, reference standards are used that bracket the expected compositional variation of bone. Carbon, aluminum, and magnesium reference standards are often used but have major drawbacks. Carbon, with an atomic number of 6, has a much lower atomic number than bone, which has a range of approximately 9-14 [Campbell *et al.*, 2012], and often lies below the lower end of the range of many commercially available backscatter detectors. Meanwhile, as metals, aluminum and magnesium both suffer some amount of tunneling contrast and also oxidize over time, adding experimental uncertainty to analyses [Campbell *et al.*, 2012]. An alternate approach involves using tunable reference materials made of glass. Borosilicate glass doped with lithium and rubidium creates compositions bracketing the expected range of bone. These glasses are amorphous, are therefore exempt from tunneling contrast, and are also stable over time [Campbell *et al.*, 2012]. Moreover, these standards (in our lab) have been developed to bracket the range of atomic numbers observed in biologic mineralized tissues.

The above method can measure a calibrated mean grey level for a sample. This mean grey level can be converted to a mineral volume fraction for bone, assuming atomic numbers and densities of 6.833 and 1.285 g/cm^3 for the organic matrix and 14.06 and 3.18 g/cm^3 for bone hydroxyapatite mineral [Campbell *et al.*, 2015]. From the measured mean grey levels, a bone-equivalent mineral volume fraction can therefore be calculated from each of the reference standards. These known mineral volume fractions for the reference standards are then mapped to mean grey level = 0 for the brightest standard and mean grey level = 255 for the darkest standard in order to calibrate imaging data for each session.

3.4 Notched fracture toughness testing

3.4.1 Theory

Fracture toughness testing can assess the resistance of bone tissue to crack initiation and also crack propagation. The consideration of fracture toughness in material assessment and design is relatively recent, following unexpected structural failures in the early through mid 20th century of storage containers (*e.g.*, a tank containing 2 million gallons of molasses fractured in Boston, MA in 1919, leading to a devastating flood), welded ship hulls, and airliners. In the early 1920s, the British scientist A.A. Griffith made the founding contributions to fracture mechanics through studying glass, which he observed failed at much lower stress in tension than would be theoretically predicted from molecular bonding strengths. Description of Griffith's findings and the following discussion of fracture mechanics are restricted to mode-I opening cracks, versus mode II sliding in plane or mode III sliding out of plane.

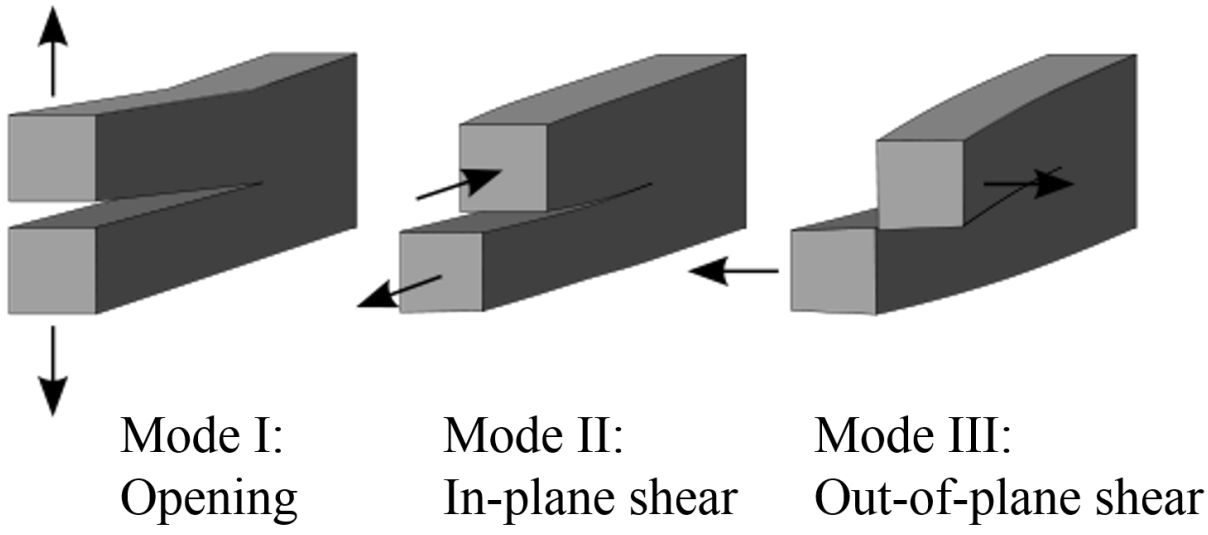

Figure 3-4: Modes of fracture. Fracture can occur in three different modes: opening, in-plane shear, and out-of-plane shear. The first of these modes is the focus of the fracture toughness theory and discussion in this dissertation. Figure credit 'Twisp', Wikimedia Commons. Licensed under Public Domain.

Griffith considered that for a mode I crack to propagate, the external work dW must be equal to at least the change in surface energy from crack growth ($d\Gamma_0$) and also potential energy (dU) from crack opening displacement (Equation A.4.1) [Rosler *et al.*, 2010].

Equation 3.4.1 $$dW = dU + d\Gamma_0$$

The strain energy release rate, G, is the energy per crack area to extend the two new surfaces associated with crack propagation. G is calculated by considering the change in energy balance with crack propagation, da, as shown in Equation 3.4.2 [Rosler *et al.*, 2010].

Equation 3.4.2 $$G = \frac{1}{t}\left(\frac{dW}{da} - \frac{dU}{da}\right) = \frac{1}{t}\frac{\Gamma_0}{da} = 2\gamma_0$$

For the situation of negligible external work, Griffith assumed that the potential energy released by crack propagation was available for the formation of new crack surfaces. In the 1950s, Irwin updated this understanding by considering the effects of plasticity at the crack tip in metals. Irwin determined that energy from crack propagation could also be dissipated at the "process zone" around the tip through dislocation motion, microcracking, or other non-linear elastic mechanisms. Among other contributions, Irwin found that linear elastic fracture mechanics (LEFM) could still be employed if the process zone was relatively small compared with the crack length and also located far from specimen edges. Irwin also related Griffith's energy criterion to intrinsic material properties through defining the stress intensity factor, K, a measure of intensity of stresses resulting from crack size, geometry, and applied force. The stress intensity factor is related to the strain energy release rate, G, and the plane-strain elastic modulus as in Equation 3.4.3.

Equation 3.4.3 $$G = \frac{K^2}{E'}$$

In linear elastic fracture mechanics, there exists a relatively simple relationship between the stress intensity factor, K, applied load, and crack length. The relationship between K, applied stress (S), and crack length (a) is:

Equation 3.4.4 $$K = FS\sqrt{\pi a}$$

The factor F is a dimensionless geometry factor that depends on the context of shape and position of crack in the specimen, as well as the crack length and specimen dimensions (*i.e.,* thickness or half-width). K_c is

the critical value at which fracture will happen, and is affected by loading rate, temperature, and the dimensions of the specimen. If the specimen is thick enough for plane strain conditions, K_c becomes K_{IC}, the mode-I plane strain fracture toughness. K_{IC} is considered a material property describing the material's ability to resist fracture in the presence of a crack. When analyzing fracture toughness from applied load, Equation 3.4.5 is employed. Here, P is the applied load, F_p is another dimensionless geometry factor and function of crack length and specimen half-width, t is the specimen thickness, and b is the specimen half-width.

Equation 3.4.5 $$K = F_P \frac{P}{t\sqrt{b}}$$

LEFM requires small-scale yielding such that the process zone around the crack tip is small relative to the crack, the remaining unbroken ligament, and the distance from the sample boundaries. In order to employ LEFM for a material with a process zone, such as bone, the sample must either meet plane strain conditions per ASTM 399-90, or have dimensions approximately 8 times the radius of the process zone. This radius can be calculated from Equation 3.4.6, where. σ_0 is the yield stress.

Equation 3.4.6 $$2r_0 = \frac{1}{\pi}\left(\frac{K}{\sigma_0}\right)^2$$

Accordingly, the requirements for LEFM to apply to a plane stress sample are that the crack length, remaining ligament, and sample width all exceed $\frac{1}{4\pi}\left(\frac{K}{\sigma_0}\right)^2$. Otherwise, the observed fracture behavior has too much of a contribution from yielding [Dowley *et al.*, 2013].

A fracture toughness test requires an initially sharp crack exceeding the dimensions of any internal flaw in the specimen. For metals, a pre-crack is established through cyclic loading. For softer materials and also for bone, the initial notch is instead introduced with a razor [Ritchie *et al.*, 2008]. In an ASTM standard fracture toughness test, the sample is machined into a single edge notch bend or compact tension specimen, notched, and broken in three point bending [ASTM E399]. K_Q is calculated from Equation 3.4.5 with P = P_Q, the load at which a line 95% of the initial stiffness extending from the origin intersects the loading

curve. If LEFM is satisfied, the small-small yielding criteria limits the sample plasticity and thus the decrease in slope is due to crack growth. For a valid K_C, the P_{max} must be less than 10% greater than P_Q. This K_C is considered K_{IC} and considered a material property if plane strain conditions are met [ASTM E399].

Alternative approaches exist for analyzing the fracture toughness of an elastic-plastic material for which the geometric demands of LEFM are not possible. One such approach is the J-integral. The definition of the J-integral is the line integral around a path that encloses the crack tip. Indeed, J is the equivalent of G, the strain energy release rate, for a nonlinear-elastic situation. J can be used to calculate fracture toughness per ASTM E1820. This method allows the calculation of J_{IC} for small samples that would fail linear elastic assumptions in traditional fracture toughness testing. J_{IC} can then be used to estimate K_{IC}:

Equation 3.4.7 $$K_{IC} = \sqrt{(J_{IC}\, E')}$$

In the J method, crack growth cannot easily be monitored by the loading curve, as changes in stiffness occur from both crack growth and plasticity. Thus, partial unloading can be employed to monitor changes in compliance per ASTM E1820 specifications for single edge notch bend or compact tension samples; the slopes of the unloading curves decrease as the crack increases length [ASTM E1820].

J is calculated as:

Equation 3.4.8 $$J = J_{el} + J_{pl}$$

The elastic component of J is calculated as:

Equation 3.4.9 $$J_{el} = K^2 \frac{(1-\nu^2)}{E}$$

J_{el} is evaluated for each crack length increment of the partial unload regime; K at each of these increments is calculated according to equations appropriate to the sample geometry per ASTM E1820. J_{pl} is calculated from A_{pl}, which is given from the area under the curve associated with crack extension. Then, for standard

specimen configurations, J_{pl} is calculated as in Equation 3.4.10, where n is a geometric factor, t is thickness, and b-a is the uncracked ligament:

Equation 3.4.10 $$J_{pl} = n \frac{A_{pl}}{t(b-a)}$$

J is then plotted versus the crack extension in order to generate an "R curve" and evaluate crack resistance. From this curve, J_Q is the value of J where the crack extension is 0.20 mm. The crack propagation toughness can also be assessed. Materials such as bone have no true K_{IC}; K_c increases with critical crack length because the growing cracks begin to interact with bone microstructure such as cement lines [Koester *et al.*, 2008]. K_c (from J_c) can be plotted versus crack extension. The slope of this R curve describes the crack propagation toughness.

3.4.2 Evaluation of fracture toughness for small animal bones

Fracture toughness testing for small animal bones such as from mice and rats is challenging because these specimens are too small to be machined into single edge notch bend or compact tension specimens. The Ritchie group described a protocol for determining fracture toughness of mouse and rat bones, which has since been adopted by the bone quality community [Ritchie *et al.*, 2008; McNerny *et al.*, 2015; Makowski *et al.*, 2014; Ionova-Martin *et al.*, 2011]. A small cylindrical rodent bone, typically the femur, is notched with a razor blade on the anterior aspect to a depth achieving a consistent notch angle less than 110° (Figure 3-4). Bones are broken in three-point bending, with the notched surface in tension. The broken surface is then studied in backscatter mode in SEM, allowing measurement of the initial notch and instability angles. The initial notch angle (Θ_{notch}) is measured from clearly visible razor grooves. The instability angle ($\theta_{instability}$) is evaluated from the zone of stable crack propagation. Stable crack propagation appears as a darker, grooved surface immediately following the initial notch. Not all bones are sufficiently ductile to produce stable crack propagation.

Measurement of the initial notch and instability angles, in combination with the force-displacement curves from three-point bending, allow the calculation of $K_{initial,}$ K_{max}, and $K_{instability}$ fracture toughnesses from Equation 3.4.11.

Equation 3.4.11 $$K_c = F_b \frac{P_s S R_o}{\pi(R_o^4 - R_i^4)} \sqrt{\pi R_m \theta_c}$$

In Equation 3.4.11, R_o and R_i are the outer and inner radii of the cortical bone cross-section, respectively. P_s is the applied load, θ_c is the half-crack angle, and S is the outer loading span. F_b is a lengthy geometrical factor developed for a thick-walled cylindrical pipe with an edge crack, as is reported in Ritchie *et al.*, 2008. $K_{initial}$ is a function of the initial notch angle as well as the yield load, P_Q, determined by the intersection of the loading curve and a secant line drawn from the origin with a slope of 95% of the initial stiffness. As mentioned previously, a valid K_c result requires limited plasticity and thus $P_{max}/P_Q < 1.1$. Importantly, rodent bones often fail this criterion, and thus $K_{initial}$ is infrequently reported. As an alternative to the 5% secant method, the maximum load and initial notch angle can be used to calculate K_{max}. This measure is straightforward to analyze but inherently limited because stable crack growth cannot be included. A third measure, $K_{instability}$, incorporates stable crack growth through measuring an instability angle from SEM (3-1-4). This latter measure has the advantage of including crack propagation toughness, which for larger samples would be calculated from a K_c *vs* crack extension "R curve."

Table 3-1: Fracture toughness measurements for small animal bones

K_c Measure	P_s	θ_c
$K_{initial}$	P_Q	Θ_{notch}
K_{max}	P_{max}	Θ_{notch}
$K_{instability}$	P_{final}	$\theta_{instability}$

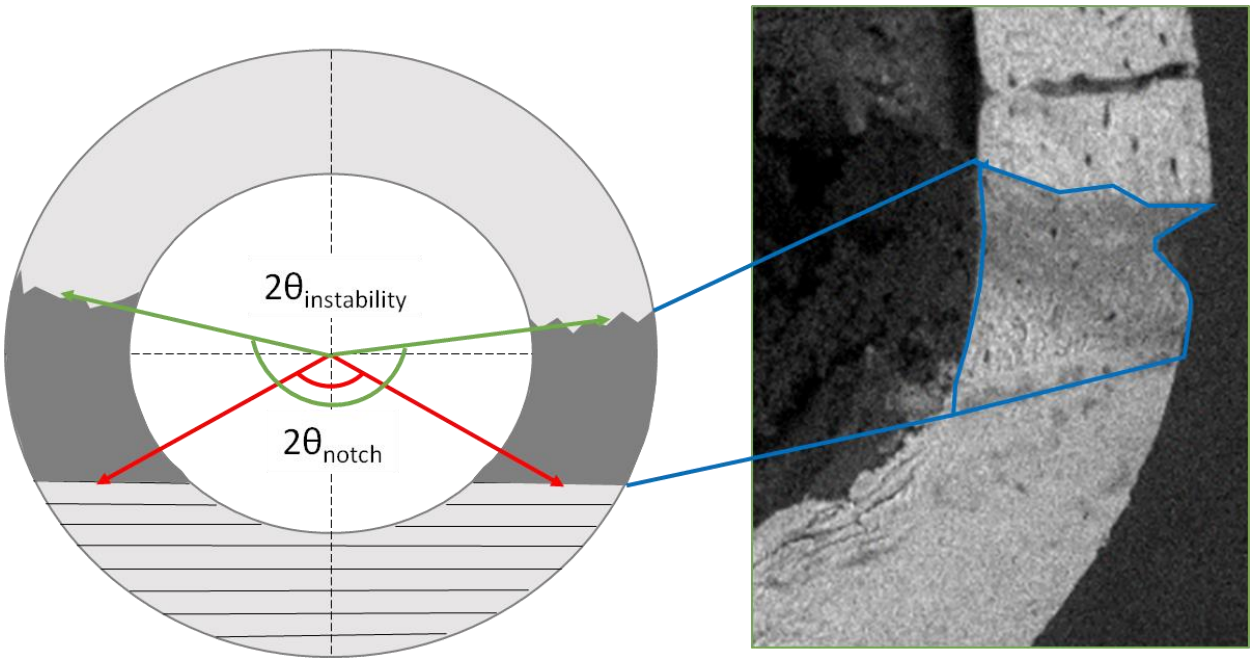

Figure 3-5: Measurement of fracture toughness for small animal bones SEM image on right collected by Chelsea Heveran. Figure adapted from Ritchie *et al*., Bone, 2008. Fracture toughness is evaluated for femurs through measuring the notch half-angle in SEM and equation 3.4.11.

The J-integral method would be enticing for fracture toughness testing of rodent bone given the geometrical limitations of small bones and their elastic-plastic behavior. However, the method is currently limited by numerical relationships between J and sample geometry. A solution for thin-walled cylinders

from the nuclear piping industry has been employed (Equation 3.4.11), but is invalid for samples, including most rat and mouse bones, with a mean radius:thickness ratio below 5. Furthermore, the length of the uncracked ligament is typically insufficiently large for mice and barely sufficient for rats [Ritchie *et al.*, 2008].

3.5 High-performance liquid chromatography

The bone tissue composite contains several types of collagen, of which type I collagen is most prevalent. Type I collagen molecules are comprised of a central triple helical region as well as two nonhelical telopeptide regions at the amino- and carboxyl- terminals. Intramolecular and intermolecular crosslinking facilitate the organization of collagen molecules into fibrils. The collagen matrix derives its strength from these crosslinks, which in turn contributes to whole bone mechanical properties [Saito *et al.*, 2010].

Collagen crosslinks occur in enzymatic and non-enzymatic varieties. Enzymatic crosslinks form *via* the activity of the enzymes lysine hydroxylase and lysyl oxidase. There are seven major enzymatic crosslinks: dehydrodihydroxylysinonorleucine (deH-DHLNL), (2) dehydrohydroxylysinonorleucine (deH-HLNL), (3) dehydrohistidinohydroxymerodesmosine (deH-HHMD), (4) hydroxylysylpyridinoline (HP), also known as pyridinoline, (5) deoxypyridinoline lysylpyridinoline (LP)), also known as deoxypyridinoline, (6) pyrrole, and (7) histidinohydroxylysinonorleucine (HHL). Of these, the first three are immature, divalent crosslinks, which are reducible in $NaBH_4$. The latter four are mature, trivalent, and irreducible. Over time, the immature crosslinks mature into the mature crosslinks; specifically, deH-DHLNL matures into HP or pyrrole while deH-HLNL matures into LP [Saito *et al.*, 2010]. Mature crosslinks are important for bone mechanical properties. In rodent studies of lathyrism, where lysyl oxidase is inhibited and thus quantities of enzymatic collagen crosslinks are reduced, bone fracture toughness, strength and stiffness are impaired [McNernie *et al.*, 2015; Oxlund *et al.*, 1995].

Non-enzymatic crosslinks are instead induced by glycation or oxidation and are thus referred to as "advanced glycation end-products" (AGEs). Pentosidine is one such AGE, with concentration in bone determined by rate of formation and removal *via* bone tissue turnover. Higher concentrations of pentosidine

have been observed in advanced age [Wang *et al.*, 2002], as well as in diseases such as diabetes [Oren *et al.*, 2011], and are associated with reduced fracture toughness [Granke *et al.*, 2015].

Collagen crosslink content for bone can be assessed using High-Performance Liquid Chromatography (HPLC). This technique is utilized in order to separate components in a mixture. The sample mixture is pressurized and pumped through a column containing either polar media and a non-polar mobile phase ("normal-phase HPLC"), or, more commonly, non-polar media and a polar mobile phase ("reversed-phase HPLC"). Components in the sample have different affinities with the polar and non-polar phases, and thus these components separate in the column. The mobile phase for reversed-phase HPLC often contains water and may also contain organic solvents (*e.g.*, acetonitrile or methanol) or acids. The mobile phase composition is changed over the course of the experiment to encourage the elution of particular sample components.

An HPLC experiment to characterize bone collagen crosslinks begins with hydrolyzing the bone tissue with HCl to break down bone collagen matrix into smaller peptides. The resuspended hydrolysate is then injected into the HPLC system. The collagen crosslinks of interest (*e.g.*, HP, LP, pentosidine) are fluorescent and thus their elution from the column can be detected at characteristic retention times. The peak areas or intensities associated with each component can be translated into a quantitative measure of crosslink concentration in the bone sample through the use of calibration standards [Bank *et al.*, 1997]. These crosslink concentrations are then normalized to the concentration of collagen in the sample. Because the amino acid hydroxyproline has a constant concentration within collagen (14% per collagen weight), measuring hydroxyproline concentration provides a reference for collagen content. Thus, following the measurement of crosslink concentration, the same samples can be derivatized and then evaluated with HPLC for amino acid concentration, including hydroxyproline [Banks *et al.*, 1996].

3.6 References

1. Fisher-Cripps, A. Nanoindentation, 2002. *New York, Springer Verlag*.

2. Sneddon, I. N. (1948, October). Boussinesq's problem for a rigid cone. In *Mathematical Proceedings of the Cambridge Philosophical Society* (Vol. 44, No. 04, pp. 492-507). Cambridge University Press.

3. Bulychev, S. I., Alekhin, V. P., Shorshorov, M. K., & Ternovskii, A. P. (1976). Mechanical properties of materials studied from kinetic diagrams of load versus depth of impression during microimpression. *Strength of Materials*,*8*(9), 1084-1089.

4. Pharr, G. M., Oliver, W. C., & Brotzen, F. R. (1992). On the generality of the relationship among contact stiffness, contact area, and elastic modulus during indentation. *Journal of materials research*, *7*(03), 613-617.

5. Oliver, W. C., & Pharr, G. M. (2004). Measurement of hardness and elastic modulus by instrumented indentation: Advances in understanding and refinements to methodology. *Journal of materials research*, *19*(01), 3-20.

6. Gao, H., & Wu, T. W. (1993). A note on the elastic contact stiffness of a layered medium. *Journal of materials research*, *8*(12), 3229-3232.

7. Olesiak, S. E., Oyen, M. L., & Ferguson, V. L. (2010). Viscous-elastic-plastic behavior of bone using Berkovich nanoindentation. *Mechanics of Time-Dependent Materials*, *14*(2), 111-124.

8. Oyen, M. L., & Ko, C. C. (2007). Examination of local variations in viscous, elastic, and plastic indentation responses in healing bone. *Journal of Materials Science: Materials in Medicine*, *18*(4), 623-628.

9. Donnelly, E, Boskey, AL, Baker SP, van der Meulen MCH (2009). Effects of tissue age on bone tissue material composition and nanomechanical properties in the rat cortex. Journal of Biomedical Materials Research, Part A; (92): 1048-1056.

10. Rho, J. Y., Zioupos, P., Currey, J. D., & Pharr, G. M. (2002). Microstructural elasticity and regional heterogeneity in human femoral bone of various ages examined by nano-indentation. *Journal of biomechanics*, *35*(2), 189-198.

11. Heveran, C. M., Ortega, A. M., Cureton, A., Clark, R., Livingston, E. W., Bateman, T. A., & Ferguson, V. L. (2016). Moderate chronic kidney disease impairs bone quality in C57Bl/6J mice. *Bone*, *86*, 1-9.

12. Nyman, J. S., Even, J. L., Jo, C. H., Herbert, E. G., Murry, M. R., Cockrell, G. E., ... & Thrailkill, K. M. (2011). Increasing duration of type 1 diabetes perturbs the strength–structure relationship and increases brittleness of bone. *Bone*, *48*(4), 733-740.

13. Fratzl-Zelman, N., Roschger, P., Gourrier, A., Weber, M., Misof, B. M., Loveridge, N., ... & Fratzl, P. (2009). Combination of nanoindentation and quantitative backscattered electron imaging revealed altered bone material properties associated with femoral neck fragility. *Calcified tissue international*, *85*(4), 335-343.

14. Garner, E., Lakes, R., Lee, T., Swan, C., & Brand, R. (2000). Viscoelastic dissipation in compact bone: implications for stress-induced fluid flow in bone. *Journal of biomechanical engineering*, *122*(2), 166-172.

15. Ebenstein, D. M., & Pruitt, L. A. (2006). Nanoindentation of biological materials. *Nano Today*, *1*(3), 26-33.

16. Bushby, A. J., Ferguson, V. L., & Boyde, A. (2004). Nanoindentation of bone: comparison of specimens tested in liquid and embedded in polymethylmethacrylate. *Journal of Materials Research*, *19*(01), 249-259.

17. Vanstreels, K., Wu, C., Gonzalez, M., Schneider, D., Gidley, D., Verdonck, P., & Baklanov, M. R. (2013). Effect of pore structure of nanometer scale porous films on the measured elastic modulus. *Langmuir*, *29*(38), 12025-12035.

18. Ulm, F. J., Vandamme, M., Bobko, C., Alberto Ortega, J., Tai, K., & Ortiz, C. (2007). Statistical indentation techniques for hydrated nanocomposites: concrete, bone, and shale. *Journal of the American Ceramic Society*, *90*(9), 2677-2692.

19. Wilkinson, T. M., Zargari, S., Prasad, M., & Packard, C. E. (2015). Optimizing nano-dynamic mechanical analysis for high-resolution, elastic modulus mapping in organic-rich shales. *Journal of Materials Science*, *50*(3), 1041-1049.

20. Bedoui, F., Sansoz, F., & Murthy, N. S. (2008). Incidence of nanoscale heterogeneity on the nanoindentation of a semicrystalline polymer: Experiments and modeling. *Acta Materialia*, *56*(10), 2296-2306.

21. Baranowski, L. L., Heveran, C. M., Ferguson, V. L., & Stoldt, C. R. (2016). Multi-Scale Mechanical Behavior of the Li3PS4 Solid-Phase Electrolyte. *ACS Applied Materials & Interfaces*, *8*(43), 29573-29579.

22. Amanieu, H. Y., Rosato, D., Sebastiani, M., Massimi, F., & Lupascu, D. C. (2014). Mechanical property measurements of heterogeneous materials by selective nanoindentation: application to LiMn 2 O 4 cathode. *Materials Science and Engineering: A*, *593*, 92-102.

23. Paietta, R. C., Campbell, S. E., & Ferguson, V. L. (2011). Influences of spherical tip radius, contact depth, and contact area on nanoindentation properties of bone. *Journal of biomechanics*, *44*(2), 285-290.

24. Tai, K., Dao, M., Suresh, S., Palazoglu, A., & Ortiz, C. (2007). Nanoscale heterogeneity promotes energy dissipation in bone. *Nature materials*, *6*(6), 454-462.

25. Yao, H., Dao, M., Carnelli, D., Tai, K., & Ortiz, C. (2011). Size-dependent heterogeneity benefits the mechanical performance of bone. *Journal of the Mechanics and Physics of Solids*, *59*(1), 64-74.

26. Hoffler, C. E., Moore, K. E., Kozloff, K., Zysset, P. K., Brown, M. B., & Goldstein, S. A. (2000). Heterogeneity of bone lamellar-level elastic moduli. *Bone*, *26*(6), 603-609.

27. Gupta, H. S., Stachewicz, U., Wagermaier, W., Roschger, P., Wagner, H. D., & Fratzl, P. (2006). Mechanical modulation at the lamellar level in osteonal bone. *Journal of materials research*, *21*(08), 1913-1921.

28. Bushby, A. J. (2001). Nano-indentation using spherical indenters. *Nondestructive testing and evaluation*, *17*(4-5), 213-234.

29. Ritchie, R. O., Koester, K. J., Ionova, S., Yao, W., Lane, N. E., & Ager, J. W. (2008). Measurement of the toughness of bone: a tutorial with special reference to small animal studies. *Bone*, *43*(5), 798-812.

30. Colthup, Norman. Introduction to infrared and Raman spectroscopy. Elsevier, 2012.

31. Kazanci, M., Roschger, P., Paschalis, E. P., Klaushofer, K., & Fratzl, P. (2006). Bone osteonal tissues by Raman spectral mapping: orientation–composition. *Journal of structural biology*, *156*(3), 489-496.

32. Yeni, Y. N., Yerramshetty, J., Akkus, O., Pechey, C., & Les, C. M. (2006). Effect of fixation and embedding on Raman spectroscopic analysis of bone tissue. *Calcified tissue international*, *78*(6), 363-371.

33. Makowski, A. J., Patil, C. A., Mahadevan-Jansen, A., & Nyman, J. S. (2013). Polarization control of Raman spectroscopy optimizes the assessment of bone tissue. *Journal of biomedical optics*, *18*(5), 055005-055005.

34. Gamsjaeger, S., Masic, A., Roschger, P., Kazanci, M., Dunlop, J. W. C., Klaushofer, K., ... & Fratzl, P. (2010). Cortical bone composition and orientation as a function of animal and tissue age in mice by Raman spectroscopy. *Bone*, *47*(2), 392-399.

35. Carden A & Morris MD (2000). Application of vibrational spectroscopy to the study of mineralized tissues (review). Journal of Biomedical Optics; 5(3):259-268.

36. McCreadie BR, Morris MD, Chen T, *et al* (2006). Bone tissue compositional differences in women with and without osteoporotic fracture. Bone; 39:1190-1195.

37. Paschalis, E. P., Verdelis, K., Doty, S. B., Boskey, A. L., Mendelsohn, R., & Yamauchi, M. (2001). Spectroscopic characterization of collagen cross-links in bone. *Journal of Bone and Mineral Research*, *16*(10), 1821-1828.

38. McNerny, E., Gong, B., Morris, M. D., & Kohn, D. H. (2015). Bone Fracture Toughness and Strength Correlate with Collagen Cross-Link Maturity in a Dose-Controlled Lathyrism Mouse Model. *Journal of Bone and Mineral Research*, *30*(3), 455-464.

39. Yerramshetty, J. S., Lind, C., & Akkus, O. (2006). The compositional and physicochemical homogeneity of male femoral cortex increases after the sixth decade. *Bone*, *39*(6), 1236-1243.

40. Hofmann, T., Heyroth, F., Meinhard, H., Fränzel, W., & Raum, K. (2006). Assessment of composition and anisotropic elastic properties of secondary osteon lamellae. *Journal of biomechanics*, *39*(12), 2282-2294.

41. Goldstein, J., Newbury, D. E., Echlin, *et al* (2003). *Scanning electron microscopy and X-ray microanalysis*. Springer Science & Business Media.

42. Howell, P. G. T., & Boyde, A. (2003). Volumes from which calcium and phosphorus X-rays arise in electron probe emission microanalysis of bone: Monte Carlo simulation. *Calcified tissue international*, *72*(6), 745-749.

43. Boyde, A., & Jones, S. J. (1996). Scanning electron microscopy of bone: instrument, specimen, and issues. *Microscopy research and technique*,*33*(2), 92-120.

44. Campbell, S. E., Geiss, R. H., Feller, S. A., & Ferguson, V. L. (2012). Tunable glass reference materials for quantitative backscattered electron imaging of mineralized tissues. *Journal of Materials Research*, *27*(19), 2568-2577.

45. Rösler, J., Harders, H., & Baeker, M. (2010). *Mechanical behaviour of engineering materials: metals, ceramics, polymers, and composites*. Springer Science & Business Media.

46. Dowling, N. E. (2013). *Mechanical behavior of materials: engineering methods for deformation, fracture, and fatigue*. Prentice hall.

47. Makowski, A. J., Uppuganti, S., Wadeer, S. A., Whitehead, J. M., Rowland, B. J., Granke, M., ... & Nyman, J. S. (2014). The loss of activating transcription factor 4 (ATF4) reduces bone toughness and fracture toughness. *Bone*, *62*, 1-9.

48. Ionova-Martin, S. S., Wade, J. M., Tang, S., Shahnazari, M., Ager III, J. W., Lane, N. E., ... & Ritchie, R. O. (2011). Changes in cortical bone response to high-fat diet from adolescence to adulthood in mice. *Osteoporosis international*, *22*(8), 2283-2293.

49. Standard, A. S. T. M. (2001). Standard test method for measurement of fracture toughness. *ASTM, E1820-01*, 1-46.

50. ASTM E399-90, (2002). Annual Book of ASTM Standards, Vol. 03.01. American Society for Testing and Materials, West Conshohocken, PA.

51. Saito, M., & Marumo, K. M. S. K. M. (2010). Collagen cross-links as a determinant of bone quality: a possible explanation for bone fragility in aging, osteoporosis, and diabetes mellitus. *Osteoporosis international*, *21*(2), 195-214.

52. Oxlund, H., Barckman, M., Ørtoft, G., & Andreassen, T. T. (1995). Reduced concentrations of collagen cross-links are associated with reduced strength of bone. Bone, 17(4), S365-S371.

53. Wang, X., Shen, X., Li, X., & Agrawal, C. M. (2002). Age-related changes in the collagen network and toughness of bone. *Bone*, *31*(1), 1-7.

54. Oren, T. W., Botolin, S., Williams, A., Bucknell, A., & King, K. B. (2011). Arthroplasty in veterans: analysis of cartilage, bone, serum, and synovial fluid reveals differences and similarities in osteoarthritis with and without comorbid diabetes. *Journal of rehabilitation research and development*, *48*(10), 1195.

55. Granke, M., Makowski, A. J., Uppuganti, S., Does, M. D., & Nyman, J. S. (2015). Identifying novel clinical surrogates to assess human bone fracture toughness. Journal of Bone and Mineral Research, 30(7), 1290-1300.

56. Bank, R. A., Beekman, B., Verzijl, N., de Roos, J. A., Sakkee, A. N., & TeKoppele, J. M. (1997). Sensitive fluorimetric quantitation of pyridinium and pentosidine crosslinks in biological samples in a single high-performance liquid chromatographic run. *Journal of Chromatography B: Biomedical Sciences and Applications*, *703*(1), 37-44.

57. Bank, R. A., Jansen, E. J., Beekman, B., & te Koppele, J. M. (1996). Amino acid analysis by reverse-phase high-performance liquid chromatography: improved derivatization and detection conditions with 9-fluorenylmethyl chloroformate. *Analytical biochemistry*, *240*(2), 167-176.

4. Moderate Chronic Kidney Disease Impairs Bone Quality in C57Bl/6J Mice

This chapter is published in full as:

Heveran, C. M., Ortega, A. M., Cureton, A., Clark, R., Livingston, E. W., Bateman, T. A., Levi, M, King, K.B. & Ferguson, V. L. (2016). Moderate chronic kidney disease impairs bone quality in C57Bl/6J mice. *Bone*, *86*, 1-9.

Abstract

Chronic kidney disease (CKD) increases bone fracture risk. While the causes of bone fragility in CKD are not clear, the disrupted mineral homeostasis inherent to CKD may cause material quality changes to bone tissue. In this study, 11-week old male C57Bl/6J mice underwent either 5/6th nephrectomy (5/6 Nx) or sham procedures. Mice were fed a normal chow diet and euthanized 11 weeks post-surgery. Moderate CKD with high bone turnover was established in the 5/6 Nx group as determined through serum chemistry and bone gene expression assays. We compared nanoindentation modulus and mineral volume fraction (assessed through quantitative backscattered scanning electron microscopy) at matched sites in arrays placed on the cortical bone of the tibia mid-diaphysis. Trabecular and cortical bone microarchitecture (μCT) and whole bone strength were also evaluated. We found that moderate CKD minimally affected bone microarchitecture and did not influence whole bone strength. Meanwhile, bone material quality decreased with CKD; a pattern of altered tissue maturation was observed with 5/6 Nx whereby the newest 60 micrometers of bone tissue adjacent to the periosteal surface had lower indentation modulus and mineral volume fraction than more interior, older bone. The variance of modulus and mineral volume fraction were also altered following 5/6 Nx, implying that tissue-scale heterogeneity may be negatively affected by CKD. The observed lower bone material quality may play a role in the decreased fracture resistance that is clinically associated with human CKD.

4. 1 Introduction

Chronic kidney disease (CKD) is recognized as a global health problem [Levey *et al.,* 2007]. An estimated 7.2% of adults over age 30 and 23-36% of persons aged 64+ have at least moderate kidney dysfunction [Zhang & Rothenbacher, 2008]. Bone fragility is an important consequence of CKD. In a three-year study, patients with moderate CKD had a 1.6 - 2.4 fold increase in fracture prevalence compared with age-matched controls having mild or no disease. With severe CKD, fracture rate increases by 3.1 – 5.1 fold [Naylor *et al.,* 2014]. Moreover, the presence of moderate CKD increases fracture-related mortality by two fold in patients over 70 years of age [Nitsch *et al.,* 2009]. The mechanisms by which bone fragility develops in CKD are incompletely understood.

Although bone mineral density is used clinically to diagnose fracture risk, bone fragility in CKD cannot be explained by declines in bone mineral density alone [Nitsch *et al.,* 2009]. However, a growing body of work across several models of bone disease demonstrates that bone strength and fracture resistance also depend on bone quality. Bone quality is the comprehensive state of tissue microarchitecture and bone material properties including mechanical response, mineralization, collagen cross-linking, and accumulation of microdamage [Donnelly 2011, Seeman & Delmas, 2006]. CKD is a disease of profoundly dysregulated mineral homeostasis, and thus, changes in bone mineralization and other parameters of bone quality may be expected [Moe *et al.,* 2006, Wolf 2015].

Few previous studies have investigated bone quality in CKD. Some of these prior works employed 5/6th nephrectomy (5/6 Nx), which is well-established to produce moderate CKD with high-turnover osteodystrophy that mimics key aspects of human kidney dysfunction [Fleck *et al.,* 2006, Gava *et al.,* 2012]. Bone quality has been observed to decrease after 5/6 Nx; diminished bone microarchitecture (BV/TV, Tb.N, Conn.D, and increased Tb.Sp) was observed for tibial trabecular bone in Crlj:CD1 mice 16 weeks following 5/6 Nx [Kadokawa *et al.,* 2011]. Microscale cortical bone material properties have been assessed after 5/6 Nx, but results for these studies are in disagreement about whether bone material quality is diminished or preserved. In a complex model of CKD (5/6 Nx with additional thyroparathyroidectomy (TPTx) in rats), bone developed a low-turnover response while Raman Spectroscopy revealed higher mineral to matrix

ratio, carbonate to phosphate ratio, collagen maturity, and pentosidine to amide ratio in cortical bone compared with TPTx alone [Iwasaki *et al.*, 2011]. In a subsequent study by the same group, rats were given either 5/6 Nx alone or alongside TPTx. 5/6 Nx produced high-turnover bone response as well as increased mineral to matrix ratio, while 5/6 Nx and TPTx resulted in low-turnover and decreased mineral to matrix ratio. Increased pentosidine to matrix ratio, decreased crystallinity and degree of orientation of the c-axis of bone mineral crystals were general to both uremic models [Iwasaki *et al.*, 2015]. Meanwhile, Kadokawa *et al.* did not observe changes in FTIR-observed mineral to matrix ratio, mineral maturity, collagen maturity, or indentation modulus in mice after 5/6 Nx compared with sham. Critically, these studies all employed microscale materials characterization techniques (*e.g.*, nanoindentation, FTIR, Raman Spectroscopy) within the middle of the cortical thickness [Iwasaki 2011 *et al.*, Iwasaki *et al.*, 2015, Kadokawa *et al.*, 2011]. Yet new rodent bone is apposited primarily on periosteal and endosteal surfaces [Ferguson *et al.*, 2003, Donnelly *et al.*, 2010]. It is possible that the inconsistent observation of bone material changes after 5/6 Nx results from surveying bone that predominantly existed prior to nephrectomy; that is, material property assessment regions of interest were not necessarily placed on bone actively forming under the influence of CKD.

Bone material quality has not been studied in rodent cortical bone for tissue apposited after nephrectomy. In this study, we evaluate the influence of moderate CKD established *via* 11 weeks of 5/6 Nx in C57Bl/6J mice, a low bone density, well-characterized inbred mouse strain. We seek to characterize how bone microscale material properties may diminish in bone established during CKD, and together with microarchitecture and whole bone strength describe bone quality in a mouse model of moderate CKD with high bone turnover.

4.2 Materials and Methods

4.2.1 Specimens

Eight-week-old male C57Bl/6J mice (n = 26) were obtained from Jackson Laboratories (Catalog number 000664, Bar Harbor, ME). Mice were maintained on a 12-h light / 12-h dark cycle and housed (n = 5 max) in polycarbonate cages with standard bedding. Mice were fed a normal rodent chow diet with

water freely available. We randomly assigned mice to sham (n = 12) or 5/6 Nx (n = 14) groups. The 5/6 Nx group underwent a two-stage nephrectomy procedure; at 10 weeks of age, 2/3 of the right kidney was ablated, followed by complete ablation of the left kidney one week later. The control group received sham operations with the same timeframe. Mice were anesthetized using 1.5% isoflurane during procedures. A post-operative dose of buprenorphine (0.5 mg/kg) was administered after surgeries and prior to recovery and every 12 hours for the following 2 days. Calcein (10 mg/kg) and tetracycline (20 mg/kg) were administered *via* intraperitoneal injection two weeks and two days before euthanasia, respectively. Mice were euthanized at 11 weeks following the second procedure by exsanguination and midline thoracotomy. Following euthanasia, femurs, tibiae, and humeri were harvested. The right femur diaphysis was cleaned of soft tissue and marrow, and then snap-frozen and stored at -80° C for gene expression. Other harvested bones were stored in phosphate buffered saline (PBS) soaked gauze at -20° C until analyses or embedding. All animal procedures were approved by the Institutional Animal Use and Care Committee at the University of Colorado Denver. Investigators were blinded to specimen treatment status for methods described in §2.2-§2.6. For methods described in §2.7 – §2.9, specimens were randomly selected from each treatment group.

4.2.2 Serum chemistry

Serum biochemistry analyses were performed on blood drawn at sacrifice. Plasma creatinine concentrations were determined using kits from BioAssay System (Hayward, CA). Blood urea nitrogen (BUN), plasma phosphate and plasma calcium levels were measured with kits from Stanbio Laboratory (Boerne, TX). Intact plasma parathyroid hormone (PTH) level was measured with kits from Immutopics (San Clemente, CA). Phosphate, calcium, and creatinine assays were performed for sixteen samples each (5/6 Nx: n = 8, sham: n = 8). BUN and PTH were assessed for twelve samples (5/6 Nx: n = 6, sham: n = 6), and eleven samples (5/6 Nx: n = 5, sham: n = 6), respectively.

4.2.3 qPCR

Relative gene expression was performed using quantitative real-time polymerase chain reaction (qPCR). Frozen femurs were powdered with two 30-second pulses 2600 rpms per manufacturer's instructions (Sartorious mikro-dismembrator S). RNA was extracted and cDNA prepared as previously

described by King *et al.* [King *et al.*, 2009]. The fast SYBR green qPCR method (Bio-Rad CFX connect real-time system) was used with the primer sequences listed in Table 4-1.

Table 4-1. Primer sequences used for mRNA analysis.

Gene	Forward Sequence	Reverse Sequence
18s	CGCCGCTAGAGGTGAAATTCT	CGAACCTCCGACTTTCGTTCT
Alpl	GAGGGACGAATCTCAGGGTA	TTTCAAGGTCTCTTGGGCTT
Ibsp	CTTACCGAGCTTATGAGGATGAAT	AAATGGTAGCCAGATAAGACAG
Bglap	AGACAAGTCCCACACAGCAG	TTGGACATGAAGGCTTTGTC
Col1a1	GCTCCTCTTAGGGGGCACT	CCACGTCTCACCATTGGGG

Alpl = gene for alkaline phosphatase; *Ibsp* = gene for bone sialoprotein; *Bglap* = gene for osteocalcin; *Col1a1* = gene for type I collagen α1 chain.

All primers were designed and then individually validated to the MIQE guidelines of amplification efficiency between 90% and 110% [Bustin *et al.*, 2009]. Conditions were set at an initiation temperature of 95° C for 20 seconds, followed by 40 cycles of denaturing at 95° C for 3 seconds and annealing at 60° C for 30 seconds. Following this DNA amplification, a melting temperature sequence was used to determine size of amplicon. Data were analyzed using the $\Delta\Delta C_q$ method for relative fold change (equations 2.3.1 – 2.3.3) with 18s as the reference gene. For this method, C_q is defined as the number of cycles necessary to reach the threshold cycle of target amplification, and ΔC_q is the difference between the number of cycles to threshold for the gene of interest and the reference gene. Smaller values for ΔC_q indicates the presence of more copies of RNA, because less time is necessary to reach the peak of the reverse transcription reaction. $\Delta\Delta C_q$ is the difference between ΔC_q for 5/6 Nx and sham, and its value has reverse orientation of the fold change.

Equation 4.2.3.1 $$\Delta Cq = Cq_{gene\ of\ interest} - Cq_{18s}$$

Equation 4.2.3.2 $$\Delta\Delta Cq = \Delta Cq_{5/6Nx} - \Delta Cq_{Sham}$$

Equation 4.2.3.3 $$Fold\ change = 2^{-\Delta\Delta Cq}$$

4.2.4 µCT

Left tibiae were cleaned of non-osseous tissue and stored in 70% ethanol at 4°C. Left femurs were cleaned and fresh frozen in PBS soaked gauze at -20°C. The femurs were defrosted at 4°C overnight before micro-computed tomography imaging (µCT). Microarchitecture was evaluated *via* µCT for all 26 study specimens (10 µm voxel size; MicroCT 80, Scanco Medical AG, Basserdorf, Switzerland). For the tibiae, scans extended in the distal direction from immediately below the proximal growth plate. The scans were acquired using a 70-kVp peak X-ray tube potential, a 0.5 mm Al filter, and an integration time of 800 ms to minimize beam hardening effects and optimize the signal-to-noise ratio. Each sample was contoured semi-automatically and subjected to Gaussian filtration. Thresholding was site-specific, using values of 450 and 723 mg HA/cm^3 for tibial and femoral analyses, respectively. The proximal tibia was evaluated for parameters including trabecular bone volume fraction (BV/TV), trabecular number (Tb.N), trabecular spacing (Tb.Sp), trabecular thickness (Tb.Th), and connectivity density (Conn.D). Femurs were scanned at the mid-diaphysis, with µCT cortical bone parameters including total mineral density (TMD), cortical thickness (Ct.Th), cortical bone area (BA), total area (TA), cortical porosity (Ct.Po), moment of inertia about the anterior-posterior axis (I_{max}), moment of inertia about the medial-lateral axis (I_{min}), and the distance between the centroid and bone surface in the anterior-posterior direction (C_{min}) [Bouxsein *et al.*, 2010]. Contours for cortical bone were fit tightly to the periosteal and endosteal surfaces, without gaps, so as to minimize measurement variance. Contours for trabecular bone were drawn a distance away from the endocortical surface to avoid erroneously including cortical bone.

4.2.5 Ashing

Humeri from all 26 mice were first oven-dried at 105° C for 24 hours and weighed to obtain dry bone mass. The bones were then oven-dried at 800° C for 24 hours to obtain the bone mineral mass. Percent mineralization was calculated from the ratio of bone mineral mass to dry bone mass.

4.2.6 Whole Bone Mechanical Testing

Following µCT, all left femurs underwent three-point bending and femoral neck testing (Insight II Material Testing System, 250 N load cell, MTS Systems Corporation, Eden Prairie, MN). We removed

bones from the PBS-soaked gauze and placed them on fixtures for mechanical testing while taking care to maintain their hydration levels. Femurs were first tested to failure in three-point bending using a deflection rate of 5 mm/min on a custom anvil with an 8-mm span. The proximal femur fragment was then placed in a pencil vise fixture mounted in-line with the main compressive direction, with the femoral head pointing up [Jämsa *et al.*, 1998]. The femoral neck was tested to failure using a deflection rate of 5 mm/min.

For both three-point bending and femoral neck tests, load-displacement curves were analyzed for mechanical properties including stiffness, maximum load, displacement at maximum load, energy at maximum load, load at yield, displacement at yield, energy at yield, post-yield displacement, load at fracture, displacement at fracture, and energy at fracture. The yield point was defined as the intersection of a secant line drawn with a 10% reduction in slope from the initial tangent stiffness and the load-displacement curve [Jepsen *et al.*, 1996]. Using I_{min} and C_{min} from μCT, we estimated material properties including bending modulus, maximum stress, and toughness from the three-point bending data using standard beam bending equations as applied to the mouse femur [Turner & Burr, 1993].

4.2.7 Mineral Apposition Rate

Fluorescent labels administered in this study were too diffuse to allow reliable dynamic histomorphometry, including an estimate of mineral apposition rate (MAR). In order to calculate MAR for the purposes of estimating the amount of bone tissue formed following nephrectomy, we employed published femoral mid-diaphysis periosteal mineral apposition rates for the same strain, sex, and age range of mice [Ferguson *et al.*, 2003]. In that study, bone formation was characterized for femurs from male C57Bl/6 mice at 18 time points between 4 and 104 weeks of age. Mice killed at 10, 12, 15, 18, and 22 weeks of age and administered tetracycline labels at 6-day intervals permit characterization of MAR relevant to the current study. Periosteal MAR was calculated as the bone formation rate (bone area / time between labels) divided by the linear extent of the mineralizing perimeter. Using this calculated periosteal MAR for the age of mice in the present study, mean linear apposition (calculated from a crescent-shaped area) was estimated to be 80 μm.

4.2.8 Nanoindentation

Subsequent to μCT analysis, tibiae were histologically dehydrated in ethanol and embedded in poly(methyl)methacrylate (PMMA). Embedded bones were sectioned at 0.8 mm proximal to the tibia-fibula junction using a low speed diamond saw (Isomet, Buehler, Lake Bluff, IL). Specimens were ground using wet silicon carbide paper (600 and 1200 grit), and then polished using aluminum oxide pastes (9, 5, 3, 1, 0.1, 0.05 μm) and Rayon fine clothes (South Bay Technologies, San Clemente, CA) to a final finish of 0.05 μm. Samples were sonicated between each polishing step.

Nanoindentation was performed for twelve randomly selected samples (5/6 Nx: n = 6, sham: n = 6) using a Hysitron TI 950 Triboindenter (Hysitron Inc., Minneapolis, MN) and 5 μm diamond spherical tip. The nanoindentation array was situated on the posterior-lateral quadrant of the cortical tibia mid-diaphysis (Figure 4-1).

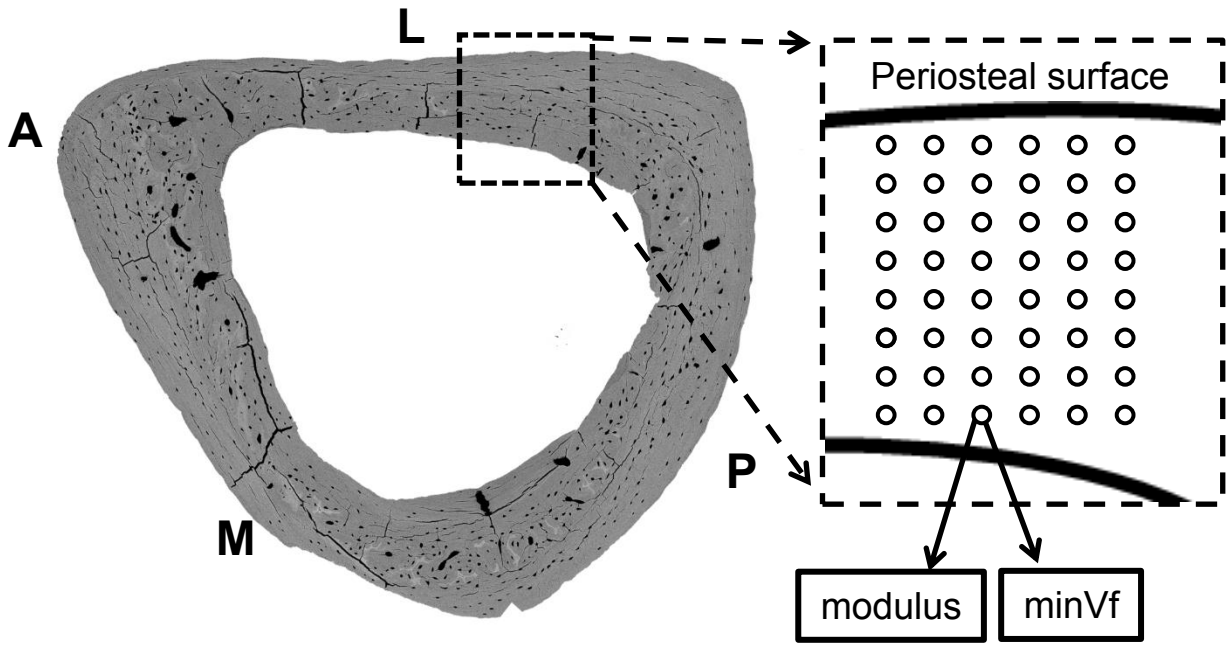

Figure 4-1: Microscale material property assessment. Modulus and minVf were measured at matched micrometer-scale sites in arrays placed on the posterior-lateral mid-diaphysial tibia, with points spaced 20 µm in x & y. Arrays extended through the cortical thickness, sampling bone tissue of varying age, including bone likely to have been established either before or after CKD.

Arrays had a minimum of six points in each row, and eight rows such that material properties were evaluated throughout the cortical thickness. The first row was parallel to, and within 20 µm from, a tangent line to the periosteal surface. Spacing in both x and y directions between indents was 20 µm. The load function was depth controlled; indentation rate was 31 nm/s until a max depth of 500 nm. Max depth was maintained for 120 s to allow dissipation of viscoelastic energy. Indentation modulus was calculated using Oliver-Pharr analysis considering the first 45% of the unloading curve [Bushby *et al.,* 2004].

4.2.9 Quantitative Backscattered Scanning Electron Microscopy

Following nanoindentation, samples were sputter coated with carbon in preparation for scanning electron microscopy using backscattered electron imaging (qBSE, JEOL JASM6490 LV, 20 kV, aperture

60 µm, 14-mm working distance) [Boyde *et al.*, 1999, Campbell *et al.*, 2012]. Images were acquired at 300x to include the nanoindentation array using both backscatter compositional and shadow modes. Raw grey levels of compositional images were calibrated using borosilicate glass reference standards [Campbell *et al.*, 2012]. Custom Matlab code was employed to measure the mean grey level in circular regions of interest (ROI) situated over the nanoindentation indents, and convert mean grey level to corresponding mineral volume fraction (minVf) based on a previously published calibration curve [Campbell *et al.*, 2012]. The ROI radius was selected to be 2.5 times the indent contact radius (*R*) after performing a sensitivity analysis with ROI ranging from 1-3*;* minVf was observed to stabilize at and beyond 2.5*R*. The indent impression was excluded from the ROI for analysis to reduce error from topographic shadowing. Black pixels were not included in mean grey level calculation, as post-calibration pixel values of 0 indicate regions without mineral content, such as cracks, lacunae, or PMMA. If an ROI overlapped with a crack, lacuna, or the bone/PMMA interface, the ROI and its corresponding indent were excluded from minVf and indentation modulus datasets, respectively. The distance of indents from the periosteal surface was measured using the shadow-mode images and the ImageJ measurement tool [Rasband 1997]. Endosteal perimeter (Endo.P), periosteal perimeter (Peri.P), endosteal area (Endo.A), periosteal area (Peri.A) and cortical area (Cort.A, the difference between periosteal and endosteal areas) were also calculated from qBSE images using ImageJ.

4.2.10 Data Analysis

Data are presented as mean ± standard error of the mean. The average and variance for modulus and minVf were calculated per row (eight rows spaced at 20 µm, with 6-9 points each). The average modulus and minVf at each row were compared between 5/6 Nx and sham groups using repeated-measures ANOVA. Post-hoc testing was conducted between row means within each treatment group, and for each row between treatments. A modified Bonferroni procedure was employed to control family-wise error at alpha = 0.05. Variance in modulus and minVf was compared between treatment groups at each indentation row for all indents *via* Levene's method.

All other measures were compared for 5/6 Nx and sham groups utilizing unpaired t-tests, with significance set *a priori* to $p < 0.05$. Data sets were examined for both normality and equal variance. All statistical analyses were performed with Minitab (v.17).

4.3 Results

4.3.1 Kidney Function

Moderate CKD following 11 weeks of 5/6 Nx was confirmed with significantly higher BUN (sham = 7.42 mg/mL, 5/6 Nx = 44.68 mg/mL, $p < 0.001$) and creatinine levels (sham = 0.37 mg/mL, 5/6 Nx = 0.50 mg/mL, $p = 0.042$) in 5/6 Nx than sham [Levey *et al.*, 2003]. Mean PTH was not statistically different between groups (sham = 211.12 pg/mL, 5/6 Nx = 359.27 pg/mL, $p = 0.120$). Serum calcium and phosphate did not change with treatment status.

4.3.2 Gene Expression

The expression of genes coding for mouse alkaline phosphatase (*Alpl*) and mouse bone sialoprotein (*Ibsp*) were significantly higher in mice that received nephrectomy (Table 4-2). The expression of osteocalcin was nearly 5-fold higher with nephrectomy, but was not significant, potentially due to variation among the control mice (as indicated by a higher standard deviation in ΔC_q data). Type I collagen showed no difference.

Table 4-2. Expression of bone matrix and mineralization genes in the femurs of sham and 5/6 Nx treated C57Bl\6J male mice (n = 11 / group).

Gene	Treatment	$\Delta C_q \pm$ StdError	$\Delta\Delta C_q \pm$ StdError	Fold-change (significance)
Alpl				
	Sham	19.4 ± 0.5	0 ± 0.5	0
	5/6 Nx	17.5 ± 0.5	−1.9 ± 0.5	6.1 (p = 0.020)
Ibsp				
	Sham	17.4 ± 0.6	0 ± 0.6	0
	5/6 Nx	15.7 ± 0.5	−1.7 ± 0.5	5.4 (p = 0.031)
Bglap				
	Sham	16.5 ± 0.6	0 ± 0.6	0
	5/6 Nx	14.5 ± 0.5	−1.5 ± 0.5	4.8 (*p* = 0.067)
Col1a1				
	Sham	13.5 ± 0.5	0 ± 0.5	0
	Nephrectomy	12.6 ± 0.5	−0.9 ± 0.5	2.3 (*p* = 0.206)

Alpl = gene for alkaline phosphatase; *Ibsp* = gene for bone sialoprotein; *Bglap* = gene for osteocalcin; *Col1a1* = gene for type I collagen α1 chain; C_q = quantification cycle (also known as quantification threshold, C_t).

4.3.3 Bone microarchitecture

μCT of the tibia revealed significantly decreased Tb.N (-5.87%, p = 0.016) and increased Tb.Sp (7.74%, p = 0.008) with 5/6 Nx. For the femur, TMD was lower after 5/6 Nx (-1.89%, p < 0.001) (Table 4-3). Cortical porosity was higher following 5/6 Nx (+107.90%, p =0.139), but this difference was not significant because of high variance. No other μCT measures of the tibia (BV/TV, Tb.Th, vBMD) or femur (pMOI, Bone Area, Total Area, BA/TA) differed between sham and 5/6 Nx. No differences were found in Endo.P, Peri.P, Endo.A, Peri.A, or Cort.A as measured from qBSE images of the tibial midshaft.

Table 4-3. Cortical and trabecular microarchitecture assessed by µCT (mean ± standard error)

	Cortical bone								*Trabecular bone*				
	TMD (mg HA / cm^3)	Ct.Th (mm)	BA (mm^2)	TA (mm^2)	Ct.Po (%)	I_{max} (mm^4)	I_{min} (mm^4)	C_{min} (mm)	BV/TV (%)	Tb.Th (mm	Tb.N	Tb.Sp (mm)	Conn.D
Sham (n = 12)	1043.70 ± 3.57	0.17 ± 0.00	0.77 ± 0.03	0.77 ± 0.03	0.19 ± 0.04	0.29 ± 0.02	0.13 ± 0.01	0.66 ± 0.01	15.41 ± 0.72	0.05 ± 0.00	4.81 ± 0.08	0.20 ± 0.00	126.32 ± 7.89
5/6 Nx (n = 14)	1023.98 ± 3.23 * p < 0.001	0.16 ± 0.00	0.71 ± 0.01	0.71 ± 0.01	0.40 ± 0.13	0.26 ± 0.01	0.12 ± 0.00	0.67 ± 0.02	15.35 ± 0.46	0.05 ± 0.00	4.53 ± 0.07* p = 0.016	0.22 ± 0.00* p = 0.008	136.52 ± 7.90

. Cortical and trabecular microarchitecture were assessed at the femur mid-shaft and proximal tibia, respectively. Significant differences ($p < 0.05$) between treatment groups are noted with *. TMD = total mineral density; Ct.Th = cortical thickness; BA = bone area; TA = total area; Ct.Po = cortical porosity; I_{max} = moment of inertia about the anterior-posterior axis, I_{min} = moment of inertia about the medial-lateral axis, C_{min} = distance from the centroid to the surface in the anterior-posterior direction; BV/TV = trabecular bone volume fraction, Tb.Th = trabecular thickness, Tb.N = trabecular number; Tb.Sp = trabecular spacing; Conn.D = connectivity density.

4.3.4 Ashing

No differences were observed between sham and 5/6 Nx for dry mass (sham = 21.22 ± 0.67; 5/6 Nx: 21.74 ± 0.34), mineral mass (sham = 12.53 ± 0.37; 5/6 Nx: 12.46 ± 0.14), or percent mineral (sham = 59.81 ± 2.85; 5/6 Nx: 57.39 ± 0.55).

4.3.5 Whole Bone Mechanical Properties

Sham and 5/6 Nx groups did not differ in mechanical properties at maximum load, yield, or fracture as measured by three-point bending and femoral neck testing (Tables 4-4 and 4-5). Material properties (bending modulus, maximum stress, toughness) calculated from three-point bending were also unchanged with 5/6 Nx.

Table 4-4: Femur mechanical properties determined by three-point bending (mean ± standard error).

Parameter	Sham (n = 12)	5/6 Nx (n = 14)
Stiffness (N/mm)	115.63 ± 4.29	114.54 ± 5.39
Load at Yield (N)	15.64 ± 0.90	15.58 ± 0.77
Displacement at Yield (mm)	0.15 ± 0.01	0.15 ± 0.01
Energy at Yield (mJ)	1.30 ± 0.11	1.29 ± 0.10
Post-Yield Displacement (mm)	0.34 ± 0.03	0.33± 0.06
Max load (N)	18.46 ± 0.59	17.75 ± 0.61
Displacement at Max Load (mm)	0.25 ± 0.018	0.25 ± 0.020
Energy at Max Load (mJ)	2.99 ± 0.32	2.97 ± 0.32
Load at Fracture (N)	15.51 ± 0.68	15.27 ± 0.86
Displacement at Fracture (mm)	0.49 ± 0.02	0.48 ± 0.06
Energy at Fracture (mJ)	6.99 ± 0.49	6.48 ± 0.78
Bending Modulus (GPa)	8.89 ± 0.99	9.42 ± 0.81
Maximum stress (MPa)	189.36 ± 8.22	195.60 ± 8.16
Toughness (N/mm^2)	8.87 ± 0.54	8.94 ± 1.07

No significant differences were observed between sham and 5/6 Nx for any measure.

Table 4-5: Femur mechanical properties determined by femoral neck fracture test (mean ± standard error).

Parameter	Sham (n = 12)	5/6 Nx (n = 14)
Stiffness (N/mm)	175.54 ± 5.58	170.35 ± 5.25
Max load (N)	21.46 ± 0.89	22.25 ± 0.67
Displacement at Max Load (mm)	0.16 ± 0.01	0.19 ± 0.02
Energy at Max Load (mJ)	1.97 ± 0.13	2.53 ± 0.29
Load at Yield (N)	19.05 ± 1.01	17.86 ± 0.94
Displacement at Yield (mm)	0.12 ± 0.01	0.12 ± 0.00
Energy at Yield (mJ)	1.26 ± 0.11	1.14 ± 0.10
Post-Yield Deflection (mm)	0.07 ± 0.15	0.09 ± 0.02
Load at Fracture (N)	18.30 ± 1.43	20.71 ± 0.86
Displacement at Fracture (mm)	0.19 ± 0.01	0.20 ± 0.02
Energy at Fracture (mJ)	2.57 ± 0.26	2.84 ± 0.37

No significant differences were observed between sham and 5/6 Nx for any measure.

4.3.5 Microscale Mechanical Properties

Repeated measures ANOVA found a significant main effect of row away from the periosteal surface, as well as a significant interaction between treatment and row. Sham mice had the lowest modulus in the first 20 μm from the periosteal surface, but no row means were significantly different for this treatment group (Figure 4-2).

A

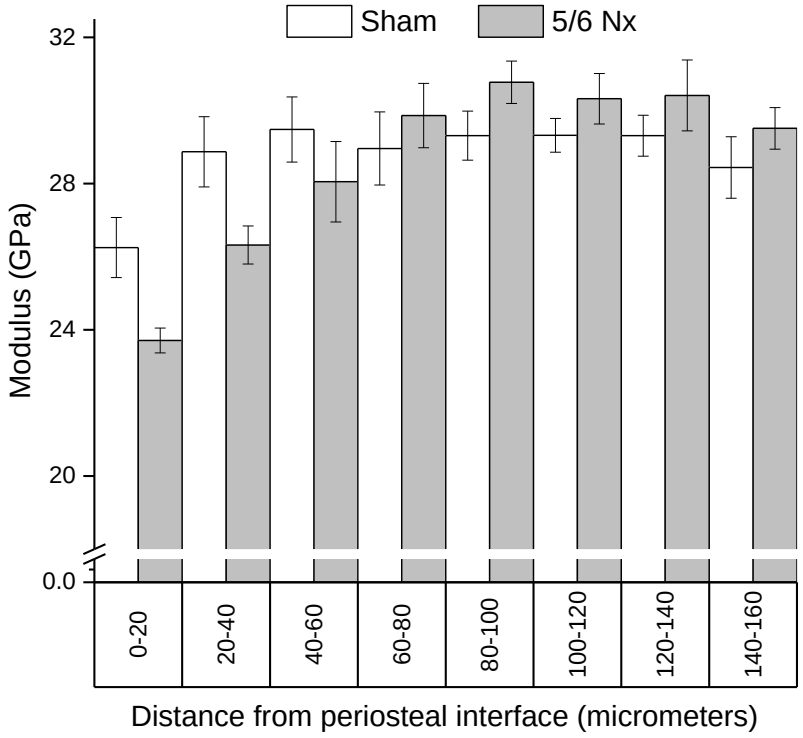

B

Distance (μm)	Indentation modulus (GPa)	
	Sham	5/6 Nx
0-20	26.25 ± 0.82^{A}	23.71 ± 0.34^{C}
20-40	28.87 ± 0.96^{A}	$26.32 \pm 0.52^{B,C}$
40-60	29.48 ± 0.89^{A}	$28.05 \pm 1.10^{B,A}$
60-80	28.96 ± 1.00^{A}	29.86 ± 0.88^{A}
80-100	29.31 ± 0.67^{A}	30.77 ± 0.58^{A}
100-120	29.32 ± 0.46^{A}	30.32 ± 0.69^{A}
120-140	29.31 ± 0.56^{A}	30.41 ± 0.97^{A}
140-160	28.44 ± 0.84^{A}	$29.51 \pm 0.57^{B,A}$

Figure 4-2: Indentation modulus measured at 20 μm increments from the periosteal surface. A) Indentation modulus increases with distance from the periosteal surface. Modulus increases with distance in sham mice as bone tissue matures until a plateau is reached 20 μm from the periosteal surface. Modulus is initially lower and matures more slowly with 5/6 Nx. B) Mean and standard error for indentation modulus at each row. Within each treatment group, measures that do not share a letter subscript are

significantly different. Significance was set at family-wise α of 0.05. Error bars indicate standard error of the mean.

Nephrectomized mice had a larger region of lower modulus tissue than observed in sham. Modulus was significantly lower in rows 1 and 2 (0-40 μm) than in rows 4 – 7 (80-140 μm). Row 2 (20-40 μm) and row 3 (40-60 μm) also did not differ, indicating that the zone of lower modulus tissue from 5/6 Nx extends through the first 60 μm of tissue. Row 8 had a similar modulus to Rows 2 and 3, which may indicate altered material properties in newly apposited endosteal bone. Comparing each row between treatments, modulus was lower in 5/6 Nx than sham for row 1 ($p = 0.028$) and row 2 ($p = 0.042$). These between-group comparisons reveal noteworthy trends, but p-values were higher than the critical α adjusted for family-wise error. Variance was also compared for all points between treatment groups by row using Levene's test (Table 4-6).

Table 4-6: Variance in microscale material properties calculated at each array row.

	Modulus		minVf	
Row	Sham	5/6 Nx	Sham	5/6 Nx
1	6.58	2.24*	3.23	8.54
2	7.34	3.17*	2.01	4.03*
3	7.52	5.97	3.81	8.72*
4	7.59	5.72	4.26	6.00
5	5.30	2.71	4.20	4.84
6	3.51	4.49	4.09	3.30
7	2.62	6.99	3.03	5.58
8	4.81	2.51	3.30	2.55

Variance calculated from points pooled across specimens within each treatment group per row.
Significant differences ($p < 0.05$) between 5/6 Nx and sham are indicated by *.

For row 1 (0-20 μm), variability in modulus was significantly lower (-65.96%) in 5/6 Nx than sham, indicating decreased heterogeneity of tissue-scale stiffness with kidney disease. Row 2 (20-40 μm) also had significantly lower variance (-56.81%) in 5/6 Nx than in sham. All other rows had variance that did not significantly differ between treatments.

4.3.6 Microscale bone mineralization

Sham mice had similar minVf throughout cortical bone; no differences in minVf were seen with distance from the periosteal surface. By contrast, in 5/6 Nx, a periosteal band of undermineralized tissue was clearly visible in bone expected to have apposited post-nephrectomy (Figure 4-3).

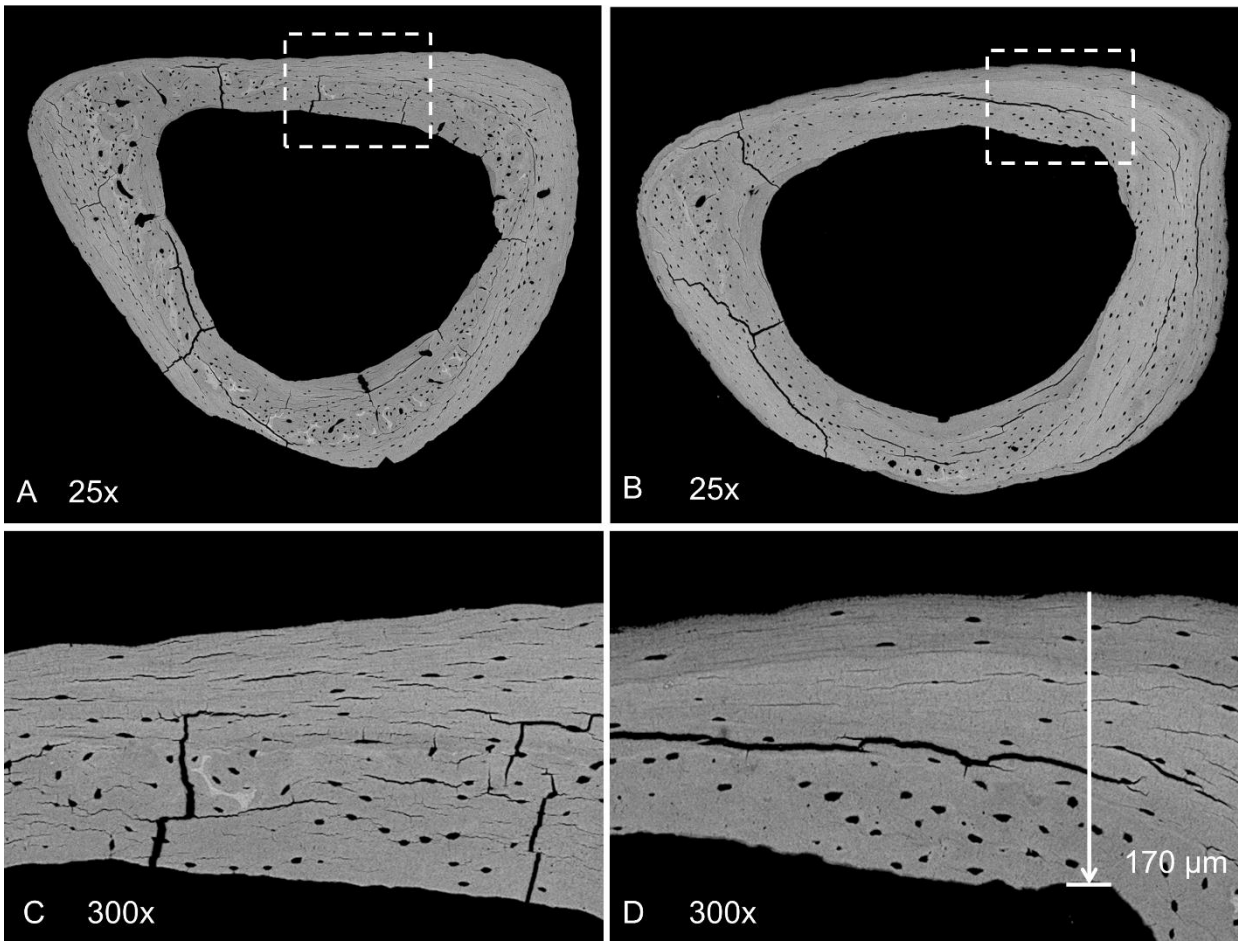

Figure 4-3. Quantitative Backscattered SEM images of the cortical tibia for sham and 5/6 Nx. Mineral volume fraction was assessed with qBSE at the cortical mid-diaphysis of the tibia for A) sham and B) 5/6 Nx mice. Images used for analyses were captured at 300x for regions of interest (dotted lines). Mineral volume fraction does not differ with distance from the periosteal surface for C) sham, but is lower in the newest (*i.e,* most recently apposited) periosteal bone for D) 5/6 Nx.

In repeated measures ANOVA with factors of row and treatment, the main effect of row was significant as was the interaction between row and treatment. There were no differences in minVf between any rows for sham mice. A markedly different mineralization profile was evident with 5/6 Nx (Figure 4-3). Row 1 (0-20 µm) had significantly lower minVf than more interior rows 5-7 (80-140 µm). The area of undermineralized tissue with 5/6 Nx was observed to extend through row 4, as the first four rows (0-80 µm) did not significantly differ in minVf (Figure 4-4).

A

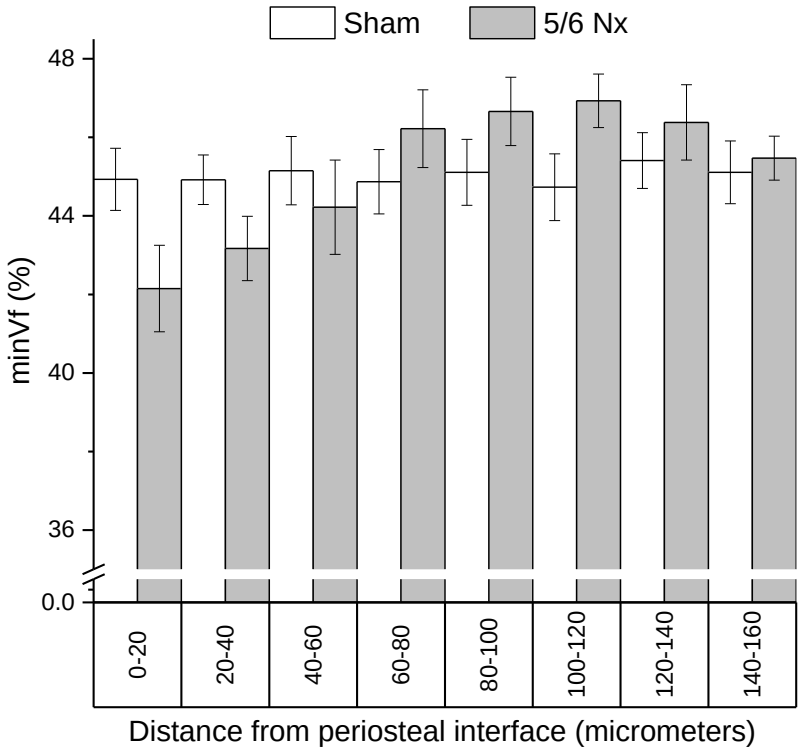

B

Distance (μm)	minVf (%)	
	Sham	5/6 Nx
0-20	44.93 ± 0.79^{A}	42.15 ± 1.13^{B}
20-40	44.92 ± 0.63^{A}	$43.17 \pm 0.82^{A,B}$
40-60	45.15 ± 0.87^{A}	$44.22 \pm 1.17^{A,B}$
60-80	44.87 ± 0.82^{A}	$46.22 \pm 0.99^{A,B}$
80-100	45.11 ± 0.84^{A}	46.66 ± 0.87^{A}
100-120	44.73 ± 0.85^{A}	46.93 ± 0.68^{A}
120-140	45.41 ± 0.71^{A}	46.38 ± 0.96^{A}
140-160	45.11 ± 0.80^{A}	$45.47 \pm 0.56^{A,B}$

Figure 4-4: Mineral volume fraction measured at 20 μm increments from the periosteal surface. A) Mineral volume fraction (minVf) increases with distance from the periosteal surface for 5/6 Nx, but not for sham. B) Mean and standard error for minVf at each row. Within each treatment group, measures that do not share a letter subscript are significantly different. No row means differ between treatment groups. Significance was set at family-wise α of 0.05. Error bars indicate standard error of the mean.

Row 8, which on some bones approached the endosteal surface, was similar to rows 2-4; this last row may be influenced by newly apposited endosteal bone. Variance in minVf was also compared between treatment groups for each row (Table 4-6). For bone 0-20 μm from the periosteal surface, variability in minVf was 122.98% higher in 5/6 Nx than sham, but variances for the two groups were not significantly different. Bone 20-40 μm in distance had significantly higher variability (+100.50%) in mineral for 5/6 Nx than for sham. At 40-60 μm, variance in minVf also significantly higher (+128.87%) for 5/6 Nx than for sham. All other rows had variance that was not significantly different between treatments.

4.4 Discussion

The purpose of this investigation was to evaluate bone quality alterations, including tissue microarchitecture and material properties, in a mouse model of high-turnover chronic kidney disease (CKD). Kidney disease was induced at 11 weeks of age *via* 5/6th nephrectomy (5/6 Nx) in male C57Bl/6J mice. The significantly elevated BUN and creatinine were observed without concomitantly increased PTH, and thus without evidence of secondary hyperparathyroidism, suggesting that CKD was moderate in severity [Joy *et al.,* 2007, Levey *et al.*, 2003]. We observed markedly altered maturation of bone material properties with distance from the periosteal surface for 5/6 Nx compared with sham. These deleterious alterations occurred despite only minimal changes to bone microarchitecture and without significant differences in whole bone mechanical response or material properties derived from three-point bending. Our findings of altered microscale mineral volume fraction and modulus may provide new insight into the clinically observed increase in bone fragility that accompanies human CKD.

Our work fills a critical gap by assessing microscale bone material properties in arrays extending through newer and into older bone tissue, including bone close to the periosteal surface that is likely established after 5/6 Nx. While previous studies of rodent bone quality in simple (i.e, 5/6 Nx) and complex (*i.e.*, 5/6 Nx compounded with thyroparathyroidectomy) surgical models of CKD have surveyed cortical bone for material properties, each study evaluated bone material quality at interior cortical bone that likely formed prior to CKD [Iwasaki *et al.*, 2011, Iwasaki *et al.*, 2015, Kadokawa *et al.*, 2011]. In our study, bone

material quality was similar in the oldest, most interior bone for CKD and sham groups, indicating that previously established bone was not affected by kidney dysfunction. In contrast to sham, 5/6 Nx was characterized by a 40-60 μm band of bone with both lower modulus and lower mineral volume fraction compared with more interior, older bone. In other words, older, more mineral-dense cortical bone was preceded by a zone of newer, lower quality bone tissue for 5/6 Nx (Figure 4-3). These observations underscore the importance of assessing microscale material properties in newly formed as opposed to pre-existing bone in nephrectomy models of CKD.

It was necessary to assess whether the reduced indentation modulus and mineral volume fraction observed in new bone apposited after 5/6 Nx were caused by CKD, or were instead explained by normal bone mineral maturation, *i.e.,* the temporal mineralization of osteoid. Because mice in this study were not skeletally mature at the time of 5/6 Nx, substantial bone formation and cortical expansion were concurrent with CKD [Ferguson *et al.,* 2003, Glatt *et al.,* 2007]. It is known that newly deposited osteoid increases in mineral content, crystallite size, and stiffness over time until achieving the chemistry, structure, and mechanical response of mature bone [Donnelly 2010]. We therefore compared bone maturation patterns between sham and CKD groups. We observed a normal pattern of bone tissue maturation in new cortical bone for sham mice. This maturation was exhibited by increasing indentation modulus values, measured within micrometer-sized regions of bone, within the first ~20 μm distance from the periosteal surface and then a plateau in modulus values at distances > 20 μm. Sham mice did not evidence differences in mineral volume fraction with distance from the periosteal surface. By contrast, tissue maturation was altered with CKD; the region of less-stiff tissue extended to 40-60 μm from the periosteal surface and was also undermineralized.

While our fluorescent labels confirmed periosteal apposition at the site of our nanoindentation arrays, they were too diffuse to allow calculation of mineral apposition rate or clearly distinguish sites of newly formed bone tissue. Consequently, it was not possible to determine the exact boundary between bone tissue apposited before and after nephrectomy. However, a zone of new, lower-quality bone tissue 60 μm in width is quite possible; from mineral apposition rates measured for the femur for the same strain, sex,

and age range of mice, an estimated 80 micrometers of periosteal apposition may be expected [Ferguson *et al.*, 2003]. Because the periosteal and endosteal perimeters (and cortical area) were not different for 5/6 Nx and sham, mineral apposition is comparable between groups. Furthermore, gene expression indicates significantly raised *Alpl* and *Ibsp*, both of which are related to matrix mineralization. While we cannot determine if these changes were due to a change in osteoblast/osteocyte activity or number, because osteocalcin and collagen gene expression were not greater in the CKD group, change in activity as opposed to number seems more likely. These increased markers of matrix mineralization do not necessarily imply a greater content of mineral in new bone tissue; indeed, we observe that mineral volume fraction is decreased in new bone with CKD. Instead, increased expression of *Alpl* and *Ibsp* likely corresponds with high-turnover bone response and the deposition of a substantial quantity of new tissue following 5/6 Nx. The exact boundary of new and pre-existing bone within these 160 μm wide arrays is less important than the observation of altered tissue mineral and modulus maturation with CKD in arrays that include both new tissue and bone established before nephrectomy. Indeed, abnormal mineral maturation kinetics have been observed in other diseases where bone quality is reduced and fracture risk increased, such as osteoporosis and osteogenesis imperfecta [Roschger *et al.*, 2008].

Our observations may also imply a reduction in bone toughness with CKD. The marked increase in mineralization and modulus between new and extant bone potentially introduces a dissimilar material interface with CKD; abnormal interfaces in bone can reduce tissue toughness [Wagermaier *et al.*, 2015]. Microscale bone tissue heterogeneity is altered for bone apposited during CKD, which may also imply a reduction of bone tissue toughness. Specifically, variance was decreased for indentation modulus and increased for mineral volume fraction. Lowered heterogeneity in indentation modulus has not been directly related to fracture risk [Lloyd *et al.*, 2015], yet has been experimentally observed in bones where fracture has occurred [Tjhia *et al.*, 2011]. Cortical bone in atypical bone fracture with severely suppressed bone turnover had reduced variance in indentation modulus measured at 500 nm, the same depth as assessed in our study, when compared with an age-matched group without fracture [Tjhia *et al.*, 2011]. Variance in indentation modulus may serve to increase tissue-scale toughening mechanisms. Fratzl *et al.* analytically

established that periodically varying elastic and inelastic regions should increase toughness [Fratzl *et al.*, 2007]. Additionally, experimentally-measured heterogeneous indentation modulus was seen to promote energy dissipation in a finite element model when compared with homogenous modulus [Tai *et al.*, 2011]. While the Tai *et al.* study assessed heterogeneity in elastic properties from indents at 40 nm of depth, we indented to 500 nm in order to minimize the effects of surface roughness while maintaining the same coefficient of variance as indents as shallow as 100 nm [Paietta *et al.*, 2011]. It is beyond the scope of the present study to evaluate if the energy-dissipation mechanisms proposed by Tai *et al*. extend to this greater length scale. Meanwhile, altered heterogeneity in mineral volume fraction may also contribute to bone fragility. Abnormally high or low variance in mineral volume fraction has been noted in backscatter SEM studies comparing bone samples with and without fragility fractures. The coefficient of variance of bone mineralization was lower in iliac crest biopsies from women with vertebral fractures versus healthy cadaveric controls [Ciarelli *et al.*, 2009]. Yet in another study of bone mineralization at the iliac crest, cadaveric trabeculae from women with osteoporotic vertebral fractures had a wider distribution of bone mineral content than healthy trabeculae [Busse *et al.*, 2009]. Increased heterogeneity in mineralization has also been reported in both trabecular and cortical bone for fracture-prone children [Tamminen *et al.*, 2014]. Thus, abnormal variance in mineral volume fraction, whether too high or too low, may be indicative of lower tissue toughness and reduced fracture resistance. Tissue toughness was not directly evaluated in this study; however, the emergence of a materials interface, less variable indentation modulus, and more variable mineral volume fraction are characteristic of less-tough bone. This potential reduction of bone toughness, along with lower stiffness and mineralization, may comprise important factors influencing skeletal fragility in CKD.

The decrease in indentation modulus variance concurrent with increase in mineral volume fraction variance was unexpected. From tissue composite theory, it is expected that the infilling of stiff mineral within a softer matrix should substantially increase the overall bone tissue modulus. However, in considering the dependence of modulus on mineral volume fraction as published in prior works, the variance in mineral volume fraction only poorly explains that of modulus within the range of mineral

volume fraction data observed in our study [Currey 1998, Oyen *et al.*, 2008]. An alternate explanation is that lowered mineral volume fraction observed in CKD has a minor influence on tissue stiffness, and that the variance in modulus may be better explained by coincident changes related to mineral deposition or growth, such as mineral crystal size and distribution, mineral chemistry, or modifications to the underlying collagen matrix.

The length-scale of observation is important for identifying bone quality changes in bone-affecting metabolic diseases [Roschger *et al.*, 2008, Karunaratne, *et al.*, 2012], and appears to be particularly crucial in CKD. At the micrometer length scale, bone material quality was worse with CKD. Yet lowered material quality did not impair mechanical or resulting material properties at the whole bone scale. How and to what degree whole bone properties change with CKD remains unclear. Iwasaki *et al.* observed changes in whole bone storage modulus and tan delta in rats after 16 weeks with 5/6 Nx and a high-phosphate diet [Iwasaki *et al.*, 2015]. Meanwhile, in a Cy/+ genetic CKD model in rats, diseased bones had significantly lower ultimate stress, a trend towards lowered toughness, and no change in modulus as measured from three-point bending [Allen *et al.*, 2014]. In another study with Cy /+ rats, CKD significantly reduced ultimate stress and stiffness, while energy to failure was not changed [Moe *et al.*, 2014]. That whole bone mechanical properties were not compromised in our study could result from a lesser quantity of diseased bone or less severe CKD. To gain insight into the influences of poor bone quality on whole bone properties, we performed a first order approximation of flexural load at the yield point for either sham or diseased cases. The load at yield for a whole long bone can be estimated by calculating whole bone modulus in three point bending [Turner & Burr, 1993]. For this calculation, moments of inertia were taken from microCT, moduli were chosen to be the mean of the three closest nanoindentation rows to the periosteal surface for either sham or 5/6 Nx groups (from Figure 4-2), mean displacement at yield was 0.15 mm (from Table 4-4), and span length was maintained at 8-mm. Since load scales linearly with whole bone modulus, the load at yield for bones consisting entirely of diseased tissue was predicted to decrease by -16.6% as compared to healthy bones. However, we observed from qBSE that on average 21% of cortical bone area had apparently diminished minVf following 11 weeks of 5/6 Nx, therefore the expected reduction in load at yield should

be substantially less than the aforementioned extreme example of a fully diseased bone. Thus, the 10-20% standard deviation observed around max, yield, and fracture loads exceeds the magnitude of the estimated effect size of 5/6 Nx. While whole bone strength is one important part of the suite of bone quality assessments, the uncertainty inherent in mouse bone flexural testing may limit the ability to resolve important changes in bone quality in moderate CKD [Ferguson *et al.,* 2003, Jämsa *et al.,* 1998]. Instead, the use of microscale techniques such as nanoindentation and qBSE may more reliably reveal changes to bone quality that could contribute towards fracture risk.

Our study had several limitations. The primary limitation was that dynamic bone histomorphometric measurements were not possible because of prohibitively diffuse fluorescent labels. Dynamic histomorphometry would have provided additional insight into how bone formation and resorption are altered with CKD and will be implemented wherever possible in future studies. Also limiting was the single time-point for gene expression assessment. Longitudinal analysis of serum markers of bone would aid in interpretation of bone material changes and should be performed in future analyses. Furthermore, in our study and others, rodents were skeletally immature at the time of nephrectomy [Kadokawa *et al.,* 2011, Iwasaki *et al.,* 2011, Iwasaki *et al.,* 2015]. The tendency of bone microarchitecture and whole bone mechanical properties to diminish with CKD may have been overshadowed by substantial bone growth as mice underwent skeletal maturation. The confounding influences of age and CKD could be clarified with a study of young, middle-aged, and mature mice.

In summary, microscale material properties of the cortical bone within the tibia diaphysis were impaired for mice that experienced surgically-induced CKD concurrent with skeletal maturation. Bone apposited between 11 weeks of age (time of 5/6 Nx) and 22 weeks (euthanasia) possessed lower and less variable indentation modulus, as well as lower and more variable mineral volume fraction, compared with bone from sham mice. The current work addressed an important inconsistency in whether microscale material properties change with CKD; namely, through placing arrays in a location of actively forming bone, lower bone material quality was readily observed. A preponderance of evidence collected from this study and others now suggests that CKD does affect bone material properties, and that these properties may

involve the quantity of mineral or its maturation (*e.g.*, current work, Iwasaki *et al.*, 2011, Iwasaki *et al.*, 2015), or the collagen network supporting mineralization [Allen *et al.*, 2014]. Looking ahead, a site-matched approach employing nanoindentation alongside Raman Spectroscopy may reveal greater detail about how formation and maturation of bone mineral and matrix are specifically altered with CKD, and how these changes contribute to diminished microscale mechanical properties.

Acknowledgements:

We are grateful to Joseph Walquist for helpful discussions about bone mechanical analyses. This work was supported by the NIH/NIA T32AG000279, NIH/NIA AG026529, and NIH/NCATS Colorado CTSA Grant UL1 TR001082. Contents are the authors' sole responsibility and do not necessarily represent official NIH views.

4.5 References

1. Levey, A.S., Atkins, R., Coresh, J., Cohen, E.P., Collins, A.J., Eckardt, K.U., *et al*. (2007). Chronic kidney disease as a global public health problem: approaches and initiatives – a position statement from Kidney Disease Improving Global Outcomes. *Kidney International*, 72(3), 247-259.
2. Zhang, Q. L., & Rothenbacher, D. (2008). Prevalence of chronic kidney disease in population-based studies: systematic review. *BMC public health*, *8*(1), 117.
3. Naylor, K. L., McArthur, E., Leslie, W. D., Fraser, L. A., Jamal, S. A., Cadarette, S. M., *et al*. (2014). The three-year incidence of fracture in chronic kidney disease. *Kidney international*, *86*(4), 810-818.
4. Nitsch, D., Mylne, A., Roderick, P. J., Smeeth, L., Hubbard, R., & Fletcher, A. (2009). Chronic kidney disease and hip fracture-related mortality in older people in the UK. *Nephrology Dialysis Transplantation*, *24*(5), 1539-1544.
5. Donnelly, E. (2011). Methods for assessing bone quality: a review. *Clinical Orthopaedics and Related Research*, *469*(8), 2128-2138.
6. Seeman, E., & Delmas, P. D. (2006). Bone quality—the material and structural basis of bone strength and fragility. *New England Journal of Medicine*, *354*(21), 2250-2261.
7. Moe, S., Drüeke, T., Cunningham, J., Goodman, W., Martin, K., Olgaard, K., *et al*. (2006). Definition, evaluation, and classification of renal osteodystrophy: a position statement from Kidney Disease: Improving Global Outcomes (KDIGO). *Kidney international*, *69*(11), 1945-1953.
8. Wolf, M. (2015). Mineral maladaptation to kidney disease – young investigator award address: American Society of Nephrology Kidney Week 2014. *Clinical journal of american society of nephrology*, *10*(10), 1875-1885.
9. Fleck, C., Appenroth, D., Jonas, P., Koch, M., Kundt, G., Nizze, H., *et al*. (2006). Suitability of 5/6 nephrectomy (5/6NX) for the induction of interstitial renal fibrosis in rats–Influence of sex, strain, and surgical procedure. *Experimental and Toxicologic pathology*, *57*(3), 195-205.
10. Gava, A. L., Freitas, F. P., Balarini, C. M., Vasquez, E. C., & Meyrelles, S. S. (2012). Effects of 5/6 nephrectomy on renal function and blood pressure in mice. *International journal of physiology, pathophysiology and pharmacology*, *4*(3), 167.
11. Kadokawa, S., Matsumoto, T., Naito, H., & Tanaka, M. (2011). Assessment of Trabecular Bone Architecture and Intrinsic Properties of Cortical bone Tissue in a Mouse Model of Chronic Kidney Disease. *Journal of Hard Tissue Biology*, *20*(2), 79-86.
12. Iwasaki, Y., Kazama, J. J., Yamato, H., & Fukagawa, M. (2011). Changes in chemical composition of cortical bone associated with bone fragility in rat model with chronic kidney disease. *Bone*, *48*(6), 1260-1267.
13. Iwasaki, Y., Kazama J.J., Yamato H., Matsugaki A., Nakano T. & Fukagawa M. (2015). Altered material properties are responsible for bone fragility in rats with chronic kidney injury. *Bone*, *81*, 247-254.
14. Ferguson, V. L., Ayers, R. A., Bateman, T. A., & Simske, S. J. (2003). Bone development and age-related bone loss in male C57BL/6J mice. *Bone*, *33*(3), 387-398.
15. Donnelly, E., Boskey, A. L., Baker, S. P., & Van der Meulen, M. C. (2010). Effects of tissue age on bone tissue material composition and nanomechanical properties in the rat cortex. *Journal of biomedical materials research Part A*, *92*(3), 1048-1056.
16. King, K., Davidson, B., Zhou, B. H., Lu, Y., & Solomonow, M. (2009). High magnitude cyclic load triggers inflammatory response in lumbar ligaments. *Clinical Biomechanics*, *24*(10), 792-798.

17. Bustin, S. A., Benes, V., Garson, J. A., Hellemans, J., Huggett, J., Kubista, M., *et al*. (2009). The MIQE guidelines: minimum information for publication of quantitative real-time PCR experiments. *Clinical chemistry*, *55*(4), 611-622.

18. Bouxsein, M. L., Boyd, S. K., Christiansen, B. A., Guldberg, R. E., Jepsen, K. J., & Müller, R. (2010). Guidelines for assessment of bone microstructure in rodents using micro–computed tomography. *Journal of Bone and Mineral Research*, *25*(7), 1468-1486.

19. Jämsä, T., Tuukkanen, J., & Jalovaara, P. (1998). Femoral neck strength of mouse in two loading configurations: method evaluation and fracture characteristics. *Journal of biomechanics*, *31*(8), 723-729.

20. Jepsen, K. J., Goldstein, S. A., Kuhn, J. L., Schaffler, M. B., & Bonadio, J. (1996). Type-I collagen mutation compromises the post-yield behavior of Mov13 long bone. *Journal of orthopaedic research*, *14*(3), 493-499.

21. Turner, C. H., & Burr, D. B. (1993). Basic biomechanical measurements of bone: a tutorial. *Bone*, *14*(4), 595-608.

22. Bushby, A. J., Ferguson, V. L., & Boyde, A. (2004). Nanoindentation of bone: comparison of specimens tested in liquid and embedded in polymethylmethacrylate. *Journal of Materials Research*, *19*(01), 249-259.

23. Boyde, A., Travers, R., Glorieux, F. H., & Jones, S. J. (1999). The mineralization density of iliac crest bone from children with osteogenesis imperfecta. *Calcified tissue international*, *64*(3), 185-190.

24. Campbell, S. E., Geiss, R. H., Feller, S. A., & Ferguson, V. L. (2012). Tunable glass reference materials for quantitative backscattered electron imaging of mineralized tissues. *Journal of Materials Research*, *27*(19), 2568-2577.

25. Rasband, W.S., ImageJ, U. S. National Institutes of Health, Bethesda, Maryland, USA, http://imagej.nih.gov/ij/, 1997-201.

26. Joy, M. S., Karagiannis, P. C., & Peyerl, F. W. (2007). Outcomes of secondary hyperparathyroidism in chronic kidney disease and the direct costs of treatment. *Journal of Managed Care Pharmacy*, *13*(5), 397.

27. Levey, A. S., Coresh, J., Balk, E., Kausz, A. T., Levin, A., Steffes, M. W., *et al*. (2003). National Kidney Foundation practice guidelines for chronic kidney disease: evaluation, classification, and stratification. *Annals of internal medicine*, *139*(2), 137-147.

28. Glatt, V., Canalis, E., Stadmeyer, L., & Bouxsein, M. L. (2007). Age-related changes in trabecular architecture differ in female and male C57BL/6J mice. *Journal of Bone and Mineral Research*, *22*(8), 1197-1207.

29. Roschger, P., Paschalis, E. P., Fratzl, P., & Klaushofer, K. (2008). Bone mineralization density distribution in health and disease. *Bone*, *42*(3), 456-466.

30. Wagermaier, W., Klaushofe, K. & Fratzl, P. (2015). Fragility of bone is controlled by internal interfaces. *Calcif Tissue Int, 97,* 201-212.

31. Lloyd, A. A., Wang, Z. X., & Donnelly, E. (2015). Multiscale contribution of bone tissue material property heterogeneity to trabecular bone mechanical behavior. *Journal of biomechanical engineering*, *137*(1), 010801.

32. Tjhia, C. K., Odvina, C. V., Rao, D. S., Stover, S. M., Wang, X., & Fyhrie, D. P. (2011). Mechanical property and tissue mineral density differences among severely suppressed bone turnover (SSBT) patients, osteoporotic patients, and normal subjects. *Bone*, *49*(6), 1279-1289.

33. Fratzl, P., Gupta, H.S., Fischer, F.D. & Kolednik, O. (2007). Hindered crack propagation in materials with periodically varying Young's modulus – lessons from biological materials. *Advanced Materials*, 19 (18), 2657-2661.

34. Tai, K., Dao, M., Suresh, S., Palazoglu, A., & Ortiz, C. (2007). Nanoscale heterogeneity promotes energy dissipation in bone. *Nature materials*, *6*(6), 454-462.

35. Paietta, R. C., Campbell, S. E., & Ferguson, V. L. (2011). Influences of spherical tip radius, contact depth, and contact area on nanoindentation properties of bone. *Journal of biomechanics*, *44*(2), 285-290.

36. Ciarelli, T.E., Tjhia C., Rao, D.S., Qiu, S., Parfitt, A.M., & Fyhrie, D.P. (2009). Trabecular packet-level lamellar density patterns differ by fracture status and bone formation rate in white females. *Bone*, *45*(5), 903-908.

37. Busse, B., Hahn, M., Soltau. M., Zustin, J., Puschel., K., *et al*. (2009). Increased calcium content and inhomogeneity of mineralization render bone toughness in osteoporosis: Mineralization, morphology, and biomechanics of human single trabeculae. *Bone*, *45*(6), 1034-1043.

38. Tamminen, I. S., Misof, B. M., Roschger, P., Mäyränpää, M. K., Turunen, M. J., Isaksson, H., *et al*., (2014). Increased heterogeneity of bone matrix mineralization in pediatric patients prone to fractures: a biopsy study. *Journal of Bone and Mineral Research*, *29*(5), 1110-1117.

39. Currey, J. D. (1988). The effect of porosity and mineral content on the Young's modulus of elasticity of compact bone. *Journal of biomechanics*, *21*(2), 131-139.

40. Oyen, M. L., Ferguson, V. L., Bembey, A. K., Bushby, A. J., & Boyde, A. (2008). Composite bounds on the elastic modulus of bone. *Journal of biomechanics*, *41*(11), 2585-2588.

41. Karunaratne, A., *et al*. (2012). Significant deterioration in nanomechanical quality occurs through incomplete extrafibrillar mineralization in rachitic bone: Evidence from in-situ synchrotron X-ray scattering and backscattered electron imaging. *Journal of Bone and Mineral Research*, *27*(4), 876-890.

42. Allen, M. R., Newman, C. L., Chen, N., Granke, M., Nyman, J. S., & Moe, S. M. (2014). Changes in skeletal collagen cross-links and matrix hydration in high-and low-turnover chronic kidney disease. *Osteoporosis International*, *26*(3), 977-985.

43. Moe, S. M., Chen, N. X., Newman, C. L., Gattone, V. H., Organ, J. M., Chen, X., & Allen, M. R. (2014). A comparison of calcium to zoledronic acid for improvement of cortical bone in an animal model of CKD. *Journal of Bone and Mineral Research*, *29*(4), 902-910.

5. Aging causes significantly altered 3D lacunar geometries in mouse cortical bone

Chelsea M. Heveran[1], Adam Rauff[2], Karen B. King[3], R. Dana Carpenter[4b] & Virginia L. Ferguson[1b]

[b]VL Ferguson and RD Carpenter contributed equally as last authors.

[1]Department of Mechanical Engineering, University of Colorado at Boulder; [2]Department of Bioengineering, University of Colorado at Denver, [3]Department of Orthopaedics, University of Colorado School of Medicine, [4]Department of Mechanical Engineering, University of Colorado at Denver

Abstract

Osteocytes can participate in systemic mineral homeostasis through perilacunar remodeling. Changes to osteocyte lacunae may affect bone quality, tissue strains, and mechanosensitivity. Though aging is associated with both decreased bone quality and altered mineral metabolism, it is not known if osteocyte lacunae undergo age-related changes in geometry. In order to survey lacunar changes with age, we developed an open-source method whereby 3D osteocyte lacunae are automatically segmented and then reconstructed from confocal laser scanning microscopy (CLSM) depth stacks and then analyzed for geometries and orientation. This method takes advantage of the availability and speed of CLSM while avoiding time-consuming and bias-prone manual segmentation. We report that 3D osteocyte lacunae measured by confocal laser scanning microscopy become smaller, more spherical, and more sparsely populated with increased age in cortical mouse bone in groups spanning 6 – 24 months of age. Critically, these age-related changes are not seen in 2D analyses from the same samples. These results motivate further inquiry into how changes to osteocyte lacunar geometries and perilacunar material contribute to diminished bone quality in aging.

5.1. Introduction

Osteocytes, which account for approximately 95% of bone cells, are critical for coordinating bone deposition and resorption, as well as bone mechanotransduction. Osteocytes also participate systemically in disease processes *via* endocrine signaling [Bonewald 2011; Schaffler *et al.*, 2014]. In addition, the osteocyte can more directly modify the local bone material environment. This effect was first observed in extreme physiological conditions, including lactation, hibernation, and glucocorticoid therapy, where the

osteocyte resorbs perilacunar bone to maintain systemic mineral homeostasis in a process known as osteocytic osteolysis [Qing *et al.,* 2012; Kaya *et al.,* 2015; Kwiecinski *et al.,* 1987; Lane *et al.,* 2004]. These perilacunar bone changes can be reversible, as observed after weaning in previously lactating mice [Qing *et al.,* 2012; Kaya *et al.,* 2015]. Indeed, recent findings suggest that osteocytic osteolysis may be a special case of perilacunar remodeling, which occurs in healthy bone and may contribute to maintenance of bone quality and fracture resistance [Alliston 2014; Tang *et al.,* 2014; Gardinier *et al.,* 2016; Fowler *et al.,* 2016]. The lacunar-canalicular network is large, accounting for an estimated 1-14% of cortical bone volume [Schaffler *et al.,* 2014]. Not surprisingly, changes to lacunar geometries can substantially affect bone quality. Enlargement of lacunae with lactation has been shown to reduce cortical bone modulus from microindentation [Kaya *et al.,* 2015]. In addition, changes to osteocyte lacunar geometries could affect bone tissue strains, fracture properties, and mechanosensitivity.

Bone quality and fracture resistance are decreased with aging [Ferguson *et al.,* 2003; Halloran *et al.,* 2002; Raghaven *et al.,* 2012; Nalla *et al.,* 2004]. Perilacunar remodeling has been shown to contribute to fracture resistance-determining bone quality, but changes to perilacunar remodeling and resulting osteocyte lacunar geometries with aging are unknown. Aging is associated with changes to mineral metabolism, including lower levels of circulating calcidiol in older men and impaired conversion of calcidiol to calcitriol, the physiologically active form of vitamin D, in elderly women [Orwoll *et al.,* 2009; Tsai *et al.,* 1984]. Calcitriol facilitates intestinal absorption of calcium, osteoclastic resorption, and osteoblast activity [Lips 2006]. Thus, changes in vitamin D metabolism with aging could increase the burden of the skeleton and particularly the lacunar-canalicular network to maintain systemic calcium homeostasis. Perilacunar remodeling could change with aging for other reasons as well. Aging is also known to increase the prevalence of senescent osteocytes, which express toxic factors into the local bone tissue environment [Farr *et al.,* 2016]. Several groups have observed in 3D and 2D that the number density of lacunae (number of lacunae per volume of bone) decreases with advancing age, for both humans and rodents [Vashisth *et al.,* 2000; Busse *et al.,* 2010; Lai *et al.,* 2015; Mullender *et al.,* 1996]. Changes to

perilacunar geometries could potentially compensate for age-related declines in bone strength. However, how osteocyte lacunar geometries change with aging is uncertain.

Very few studies have evaluated the effects of aging on osteocyte lacunar geometries. Mullender and coworkers, using 2D histomorphometry, found that osteocyte lacunae from trabecular bone of the iliac crest had smaller mean lacunar area for men and women aged 55 years or older, compared with individuals less than 55 years of age [Mullender *et al.*, 1996]. However, these age-related differences in lacunar area were not significant. Two-dimensional imaging may contribute to the uncertainty about whether osteocyte lacunae change in aging. 2D imaging has several critical limitations. Osteocyte lacunae can appear indistinguishable from non-lacunar objects (*e.g.*, a vascular cross-section in bone). Furthermore, the ellipsoidal shape that generally characterizes osteocyte lacunae can yield a range of 2D shapes depending on the sectioning plane (Figure 5-1). It is possible that 2D methods are sufficient for detecting large changes to osteocyte lacunae as occur with lactation, but that 2D techniques have insufficient resolution to capture more subtle changes in lacunar morphologies that could result from aging.

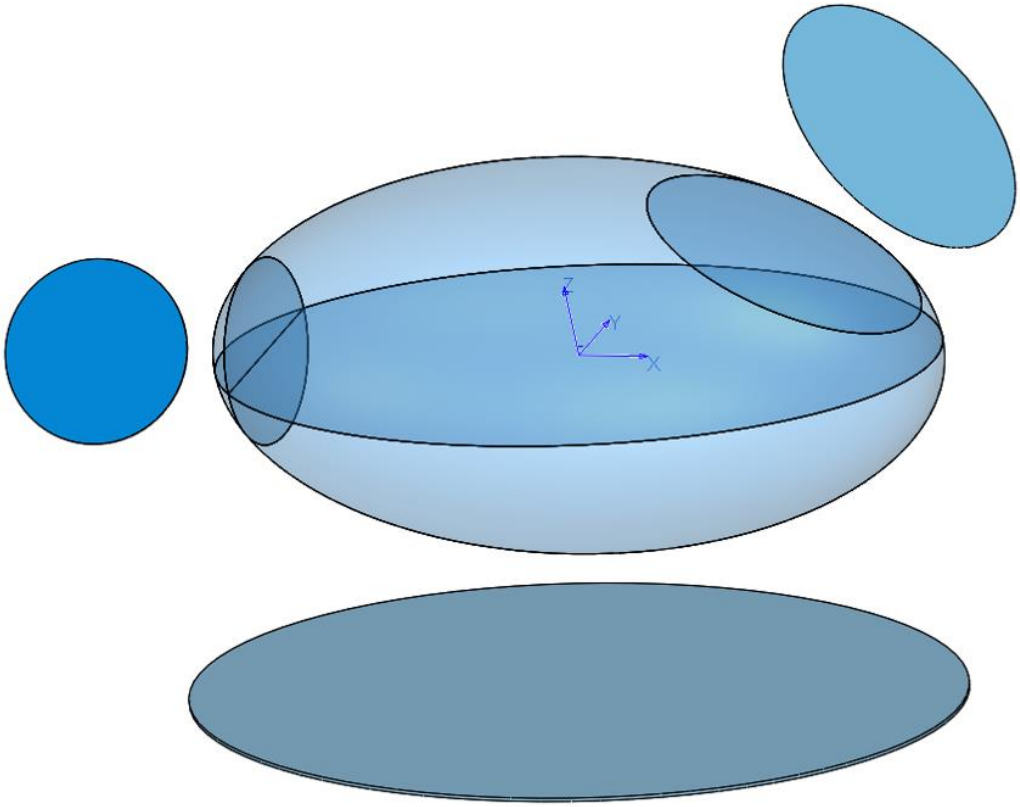

Figure 5-1: A 3D ellipsoid can be sliced into many different 2D shapes. Different 2D cross-sections of a 3D ellipsoid produce very different geometries. Accordingly, 3D methods are most appropriate for comparing osteocyte lacunar geometries between samples.

Three-dimensional (3D) images can surmount the challenges of 2D quantification of osteocyte lacunar geometries. Previous efforts have utilized synchrotron-radiation microCT to generate 3D images of osteocyte lacunae and surrounding canaliculi [Carter *et al.*, 2013; Dong *et al.*, 2014; Hesse *et al.*, 2015; Fowler *et al.*, 2016]. Submicron-resolution conventional microCT ('nanoCT') could also be employed for osteocyte lacunae visualization. However, both of these technologies are prohibitively expensive and unavailable for many researchers. By contrast, confocal laser scanning microscopy (CLSM) provides a relatively common, fast, and inexpensive technique with the ability to capture depth stacks (z-stacks) of osteocyte lacunae at submicron resolution. Some prior work has considered CLSM for the purpose of studying 3D osteocyte network geometries [McCreadie *et al.*, 2004; Kamel El-Sayed *et al.*, 2015; Lai *et*

al., 2015]. However, this technique has not been widely utilized, perhaps because of the necessity of either manually segmenting osteocytes, which is both time intensive and prone to user bias, or constructing algorithms to appropriately segment 2D osteocyte lacunae slices and then reconstruct and analyze 3D osteocyte geometries. An open-source tool for analyzing 3D osteocyte lacunar geometries from CLSM z-stacks would enable facile and time-efficient analysis of how lacunae change with aging, disease, and therapeutic interventions.

CLSM has only been sparingly employed to characterize 3D age-related changes to osteocyte lacunae. Lai *et al* reported that osteocyte lacunae from trabecular and cortical bone of male C57Bl/6 mice had smaller mean lacunar volume and surface area at 32 weeks of age than 15 weeks, but these differences were not significant. However, only three mice were studied at each age, and only 10 lacunae were analyzed for each cortical and trabecular compartment per study animal [Lai *et al.*, 2015]. In addition to 3D assessment of osteocyte lacunae, assessing rigorously large numbers of lacunae in studies with greater statistical power are needed to evaluate effects of aging on osteocyte geometries.

In this study, we employ CLSM to evaluate how 3D osteocyte lacunar geometries change with aging in large arrays of lacunae imaged from cortical mouse bone. We present an open-source automatic segmentation method for convenient and time-efficient analysis of 3D osteocyte lacunae, as well as metrics for analyzing 3D osteocyte geometries. The validity and limits of our approach are considered by analysis of phantom ellipsoidal objects and comparison with manual segmentation.

5.2. Methods

5.2.1 **Visualization and quantification of 3D osteocyte lacunar geometries**

A Matlab-based process to segment osteocyte lacunae from 2D images within z-stacks from CLSM to generate 3D osteocyte lacunae is described in 5.2.1.1. Parameters to describe 3D osteocyte lacunae geometries are then defined in 5.2.1.2. In section 5.2.1.3, several strategies are presented to understand the limitations and validity of our method. Finally, in section 5.2.2, we describe an experiment in which cortical bone from young through old mice were imaged using CLSM to quantify the effects of age on osteocyte lacunar morphology.

5.2.1.1 3D osteocyte lacunae segmentation and reconstruction

The process of segmenting and reconstructing osteocyte lacunae from confocal z-stacks is outlined in Figure 5-2.

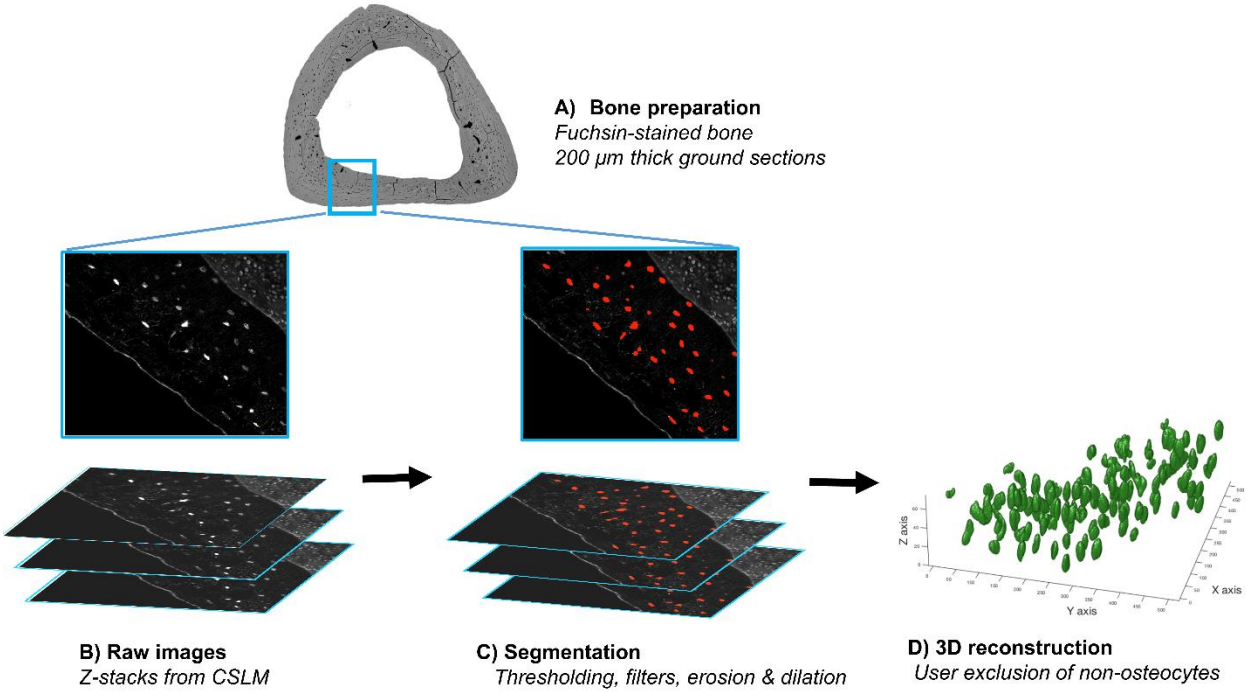

Figure 5-2: Method to reconstruct 3D osteocyte lacunae from CLSM z-stacks. A) Cortical bone is stained with basic fuchsin, dehydrated, and embedded in PMMA. Ground sections 200 µm thick are prepared for imaging. B) Z-stacks of images are acquired with CLSM. C) The 3D Osteocyte Lacunae Analysis program is used to segment osteocytes from raw images, using thresholding, filtering, and erosion / dilation steps. D) Potential osteocytes are reconstructed in 3D. The user can select non-osteocytes (*e.g.*, vasculature) for exclusion. This final 3D matrix is analyzed for osteocyte lacunar geometries.

The following process constitutes the 3D Osteocyte Lacunae Analysis program:

1) Thresholding: images are first stored as individual 2D image slices. Each image within a z-stack first undergoes smoothing *via* Gaussian filter and then thresholding. The image is filtered with a 2D smoothing kernel specified by sigma, (0.65 in our program). The mean of the smoothed image is obtained and used for the thresholding parameter. Thus, each image slice has a different threshold which is proportional to the mean intensity of that slice. The thresholding parameter is the mean of the Gaussian smoothed image multiplied by 1.9. This value, as well as sigma, worked well with our mouse

bone image data, and could be easily modified to better fit other data sets. The binarized 2D images within each stack are then stored in a 3D matrix, referred to here as '3D_Segmented_Image'.

2) Holes are filled for objects within the 3D matrix using the Matlab function imfill(3DSegmentedImage, 'holes'). Specifically, black pixels within the white outlines of the 3D lacunar edges are converted to white pixels so that each lacuna becomes a filled volume. The resulting image is called '3D_Segmented_Image_Filled.'
3) Erosion and dilation: These imaging processing operations are commonly used to eliminate small, unwanted objects remaining from thresholding. The functions used in the program operate on 3D volumes. A spherical (radius = 5 pixels) structuring element (SE) is chosen for the erosion and dilation procedure. Objects in the 3D matrix are eroded with reference to the structuring element to remove osteocyte lacunae processes and canaliculi and are then dilated back to their original volumes. The Matlab function imopen(3D_Segmented_Image_Filled, SE) achieves the erosion and dilation procedure, using the same SE for each step.
4) Edge filter: segmented objects are removed if any portion of the object touches an image boundary. This prevents incomplete objects from inclusion in the final analysis.
5) Volume filter: segmented objects smaller than 100 μm^3 or larger than 2000 μm^3 are removed, as osteocyte lacunae observed in this study generally have volumes between 200-600 μm^3.
6) User selection and removal of non-osteocyte lacuna objects: following steps 1-5, the segmented and filtered 3D image is visualized in a custom Graphical User Interface (GUI) named Visualize Lacunae GUI. Users can visualize the segmentation results and select objects (*e.g.,* vasculature) for exclusion.
7) Analysis: 3D osteocyte lacunae geometries and orientation metrics are analyzed from the final 3D matrix according to the parameters outlined in section 5.2.1.2.

5.2.1.2 Osteocyte lacunae network parameters

Osteocyte network parameters in 3D and 2D are summarized in Figure 5-3.

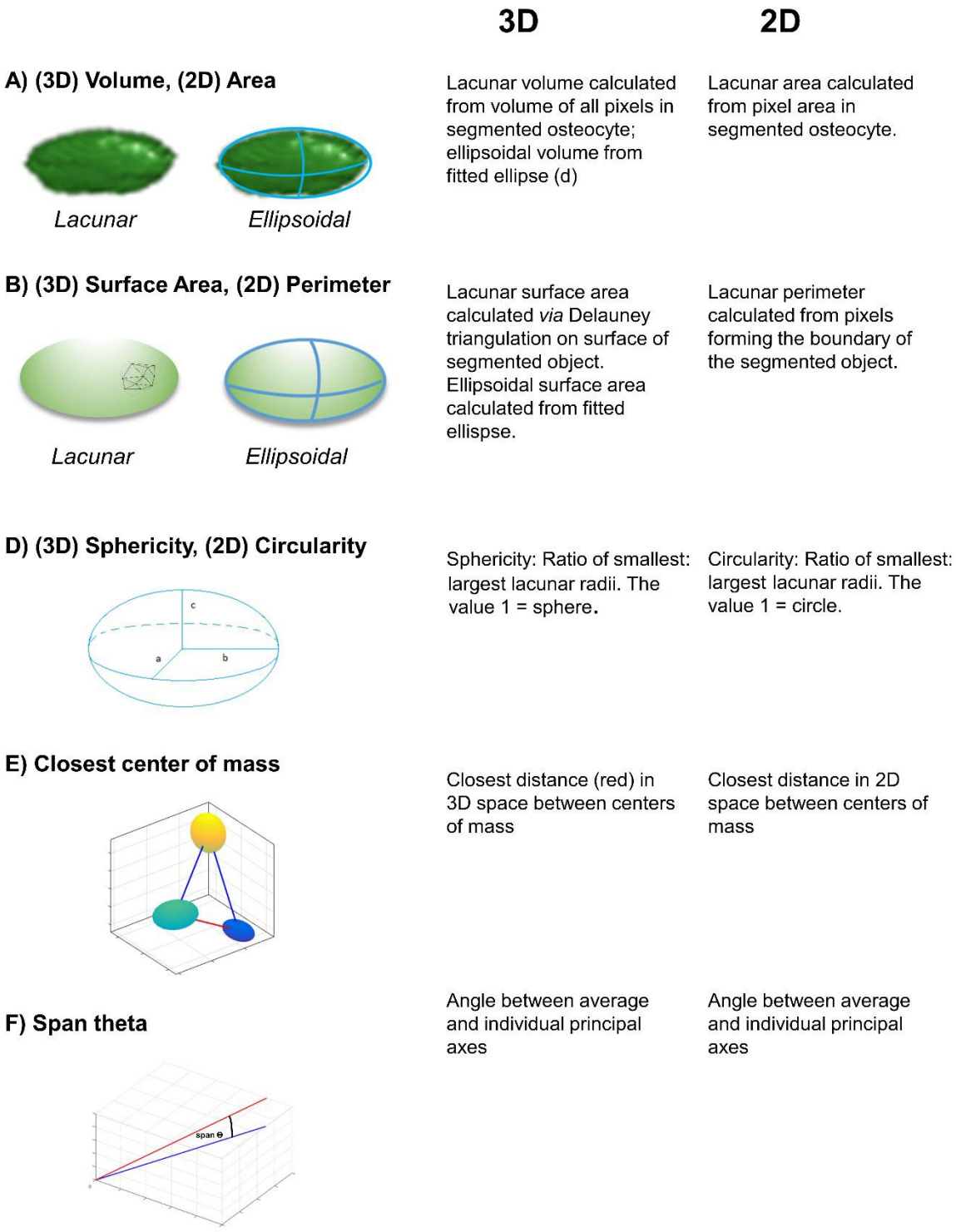

Figure 5-3: Definitions of osteocyte lacunar geometries.

Our work employs “ellipsoidal” and “lacunar” definitions of ellipsoidal objects for calculation of volume and surface area. Previous work (*e.g.,* McCreadie *et al.,* 2004; Lai *et al.,* 2015) described the geometry of 3D osteocyte lacunae objects based upon a best-fit ellipsoid. We calculate *ellipsoidal volume* and *ellipsoidal surface area* using the same approach. Briefly, the eigenvalues and eigenvectors of the inertia matrix were calculated to yield the principle moments of inertia and principle directions, respectively From the principle moments of inertia, a best-fit ellipsoid and its corresponding surface area and volume can be calculated. We also calculate *lacunar volume* from the number of pixels that comprise the 3D osteocyte lacunar object volume. *Lacunar surface area* is calculated by performing a Delauney triangulation of the pixels forming the object surface, and summing the area of the triangles.

Sphericity is the ratio of the smallest to largest radii. For the ellipsoidal approach, radii are calculated from the principle moments of inertia. For the lacunar approach, radii are calculated directly from the center of mass along the principle directions to the object edge. A value of 1 indicates a perfect sphere, with decreasing values indicating a more elongated geometry.

Closest center of mass is defined as the shortest distance in 3D space between osteocyte lacunae centers of mass. This value is calculated for each osteocyte lacunae within the sample and provides a measure of how far apart the lacunae are spaced.

Span theta is defined as the angle difference (in degrees) between the average of all lacunar principle axes and the principal axes of individual osteocyte lacunae. This parameter estimates the degree of alignment of a group of osteocyte lacunae in 3D space. The name of this variable was chosen as it only exists on the plane that spans the vectors of the individual principal axes and the average principle axis.

A slice from each z-stack (5^{th} from the imaging surface) was analyzed for 2D analogs of the 3D metrics. *Lacunar area* measures the area filled by the pixels of the segmented 2D osteocyte lacunae. *Lacunar perimeter* is evaluated from the pixels forming the object edge. *Circularity* is the ratio of major to minor axes, where a value of 1 indicates a perfect circle. *Closest center of mass* is the shortest distance between centers of mass in 2D space. The 2D equivalent of *span theta* is the standard deviation of angles between the major axis and an arbitrary x axis for all lacunae.

5.2.1.3 Validation

We first verified that the program appropriately quantifies 3D osteocyte lacunar geometries through analyzing phantom objects. These 3D ellipsoids were created with known dimensions and orientations and are available as open-source files along with the 3D Osteocyte Lacunae Analysis program (Figure 5-4).

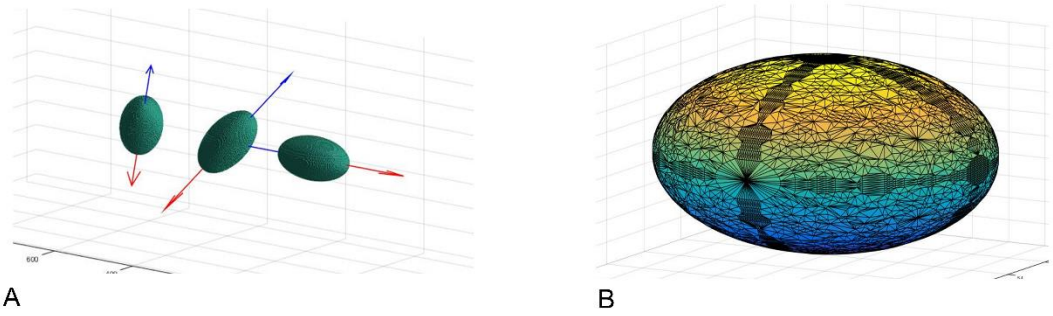

Figure 5-4: 3D ellipsoidal phantoms. The program accurately calculates A) orientation and B) surface area for ellipsoidal phantoms.

We next estimated the percentage of osteocytes present in bone that are segmented by the 3D Osteocyte Lacunae Analysis program and included in the 3D reconstruction for analysis of lacunar network geometries. Some loss of lacunae in an automatic segmentation protocol is expected, as segmentation is affected by inhomogeneity in stain penetration and the presence of bright objects such as bone marrow within the image. In order to estimate an expected number of lacunae to compare with results from automatic segmentation, manual segmentation was performed for three cortical mouse bone z-stacks (one randomly chosen sample from each of the three age groups described in 2.2) using ScanIP (version 7.0, Simpleware, Synopsys Inc). The manually segmented lacunae were subjected to a volume filtration step

analogous to volume filtering within the automatic 3D Osteocyte Lacunae Analysis program (objects with volumes less than 100 μm^3 or more than 2000 μm^3 were excluded). Manually segmented lacunae were not further modified (*i.e.*, no dilation / erosion or smoothing) before analysis of lacunar geometries. The number of osteocyte lacunae segmented by the 3D Lacunar Analysis program was compared with the number obtained through manual segmentation. Lacunar geometries obtained from automatic and manual segmentation for the same samples were then compared.

5.2.2 **Demonstration of technique**

We applied the protocol presented in Section 5.2.1 for visualization and quantification of 2D and 3D osteocyte lacunar geometries to evaluate osteocyte lacunae in cortical bone from skeletally mature young adult, middle-age, and old mice.

5.2.2.1 Cortical bone sample preparation and imaging

C57Bl/6J male mice at three ages (3 months, n =6; 15 months, n = 7; 21 months, n = 6) underwent sham (*i.e.*, placebo surgery) abdominal procedures as a control for a separate study. Mice were aged for 3 months following sham surgeries on Harlan Teklad 2920X chow diet and killed. At the study endpoint, mice were 6, 18, and 24 months of age. Six-month old mice are skeletally mature young adults, 18 month-old mice are middle-age and beyond peak for most mechanical properties, and 24 month mice are considered geriatric [Ferguson *et al.*, 2003].

The left tibia was cleaned of non-osseous tissue and simultaneously histologically dehydrated and stained with 1% basic fuchsin [Burr & Hooser, 1995]. Tibias were then cleared with acetone and embedded in PMMA. Embedded samples were transversely sectioned 1 mm proximal to the tibia-fibula junction with a low-speed saw (Buehler Isomet, Buehler, Lake Bluff, IL). A ground section was prepared from the distal section with target thickness of 200 μm (Exakt 400 CS, Exakt Technologies Inc, Oklahoma City, OK). Final sections had thicknesses of 195 μm ± 3 μm. Additional samples were prepared with a variety of thicknesses in order to assess the dependence of measures on specimen thickness and number of visualized osteocyte lacunae.

Confocal imaging of ground sections was performed in transmission with a Zeiss LSM 710 confocal laser scanning microscope, with 555 nm excitation, 568-1000 nm bandpass filter, and 40x oil-immersion objective. Stacks were obtained through the visible range of osteocyte lacunae (~50-100 μm of imaging depth) with 0.484 μm between slices. All imaging was performed blinded to specimen age.

5.2.2.2 Comparison of 2D and 3D osteocyte lacunar geometries

Three-dimensional osteocyte lacunar geometries were analyzed as described in 5.2.1. In addition, 2D osteocyte lacunar geometries were evaluated from a single slice of the same z-stack for each mouse. The fifth image from the top surface was chosen to take advantage of high contrast lacunae while minimizing effects of surface roughness. The 2D images were saved in .tif format and analyzed with custom Matlab code. The Gaussian blur was the same as for the 3D analysis. An area filter excluded objects less than 10 pixels and greater than 1000 pixels. The erosion-dilation scheme was modified such that the structuring object was a disk instead of a sphere. Lastly, objects that were not osteocytes (*e.g.*, bone marrow) were excluded by user specification. From each image, the following 2D geometric parameters were obtained: *lacunar area*, *lacunar perimeter*, *circularity* (ratio of smallest to largest radii), *closest center of mass*, *lacunar density* (number of lacunae / image area), and *span theta*. In 2D, the interpretation of span theta is the difference in angle between the direction of the major axis for each osteocyte and the average direction of all lacunae major axes.

5.2.2.3 Data analysis

The effect of age on 3D and 2D osteocyte lacunar parameters was evaluated using one-way ANOVA (Minitab v.17). Residuals were checked for normality and heteroscedasticity; the dependent variable was transformed when necessary to satisfy ANOVA model assumptions. The Tukey post-hoc procedure was utilized to compare means between ages. For all analyses, alpha was set *a priori* to $p = 0.05$. In addition, correlations for image depth *vs* number of lacunae, ellipsoidal *vs* lacunar metrics, and 3D *vs* 2D metrics were performed with OriginPro 2016.

5.3. Results

5.3.1 Validation

The program succeeded in evaluating expected geometries for phantom ellipsoids using the approach outlined in 5.2.1.3. A comparison of manual segmentation (ScanIP) and automatic segmentation (3D Osteocyte Lacunae program) demonstrates that 77.1 – 97.8% of the lacunae that are manually segmented are captured with the automatic approach described herein (Table 5-1).

Table 5-1: Comparison of osteocyte lacunar geometries between manually and automatically segmented lacunae.

Age	**6 mo**		**18 mo**		**24 mo**	
Segmentation procedure	*Manual*	*Automatic*	*Manual*	*Automatic*	*Manual*	*Automatic*
Lacunar Volume (μm^3)	265.90 ± 88.50	416.83 ± 193.23	268.42 ± 139.62	433.10 ± 233.61	242.04 ± 107.94	320.86 ± 121.72
Lacunar surface area (μm^2)	323.87 ± 90.95	339.10 ± 124.23	343.19 ± 102.16	330.81 ± 186.72	274.96 ± 79.11	279.32 ± 74.21
Sphericity	0.13 ± 0.06	0.23 ± 0.06	0.14 ± 0.05	0.25 ± 0.07	0.19 ± 0.06	0.25 ± 0.06
Closest Center of Mass (µm)	18.88 ± 4.00	19.08 ± 5.39	20.23 ± 4.19	21.61 ± 4.68	19.36 ± 3.92	19.71 ± 3.71
Span theta (degrees)	11.13 ± 22.08	11.56 ± 23.93	5.50 ± 34.81	11.98 ± 35.69	11.52 ± 31.32	8.22 ± 36.08
Number of lacunae	126	107	105	81	90	88
Lacunar density (μm^3 x 10^{-5})	3.11	2.64	2.16	1.66	2.23	2.18

Osteocyte lacunae geometries were calculated from manual (ScanIP) and automatic (3D Osteocyte Lacunar Analysis) procedures for a randomly-selected bone from each age group. Data represent the mean and standard deviation of each sample's lacunar geometries.

5.3.2. Stability of osteocyte lacunae geometries with respect to number of osteocytes

3D osteocyte lacunar geometries were observed to depend on number of osteocyte lacunae for small numbers of segmented lacunae (Figure 5-5). *Lacunar surface area* and *lacunar volume* (Figures 5-5a and 5-5b) only weakly depend on number of osteocyte lacunae. *Closest center of mass* appears to be biased towards larger values when measuring small numbers of lacunae. However, this bias is minimized when measuring larger numbers of lacunae (*i.e.,* greater than 50 per 3D image). This observation is not unexpected. Lacunae are heterogeneous with regards to size and spatial arrangement. Small volumes of bone would not be expected to capture as many unusually close or distant lacunae as larger volumes of bone. *Sphericity* (Figure 5-5c) may also be higher for small numbers of lacunae, suggesting that oblong lacunae can be prone to undersampling. We chose to analyze samples with 50 or more lacunae to ensure adequate sampling of lacunae size, shape, and orientation. The necessary imaging depth (the depth of the z-stack from CLSM imaging) to obtain 50 or more segmented lacunae was approximately 60 μm (Figure 5-6).

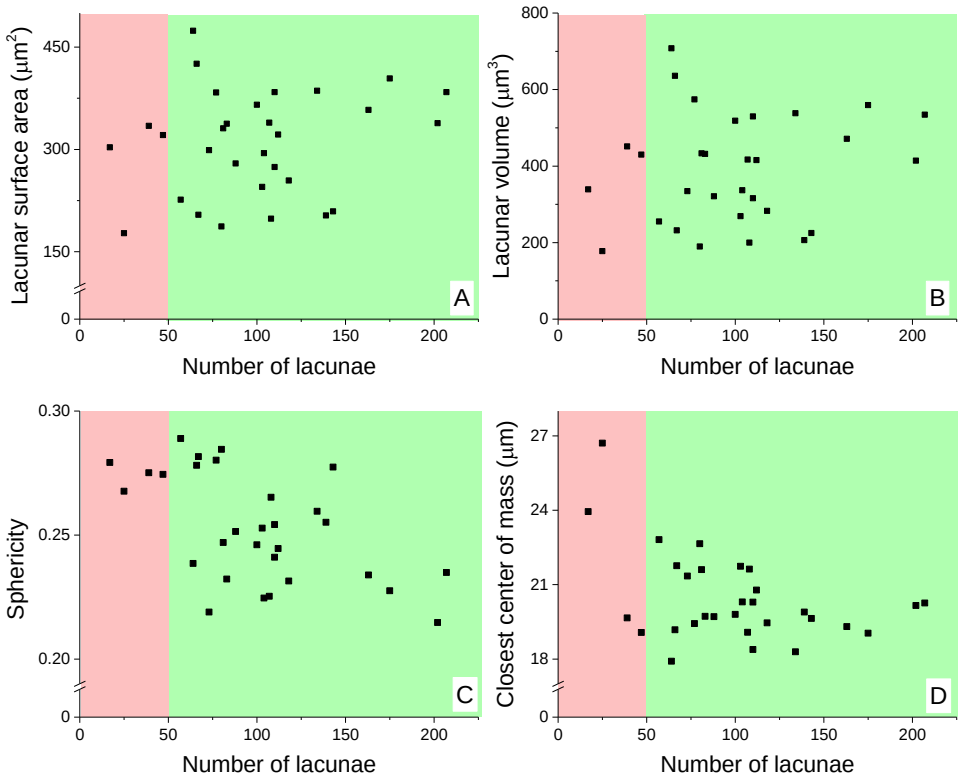

Figure 5-5: Stability of 3D osteocyte lacunar geometries with respect to number of lacunae. 3D measures of osteocyte lacunar geometries, especially sphericity (C) and closest center of mass (D), may be sensitive to number of lacunae for approximately 50 or fewer osteocytes.

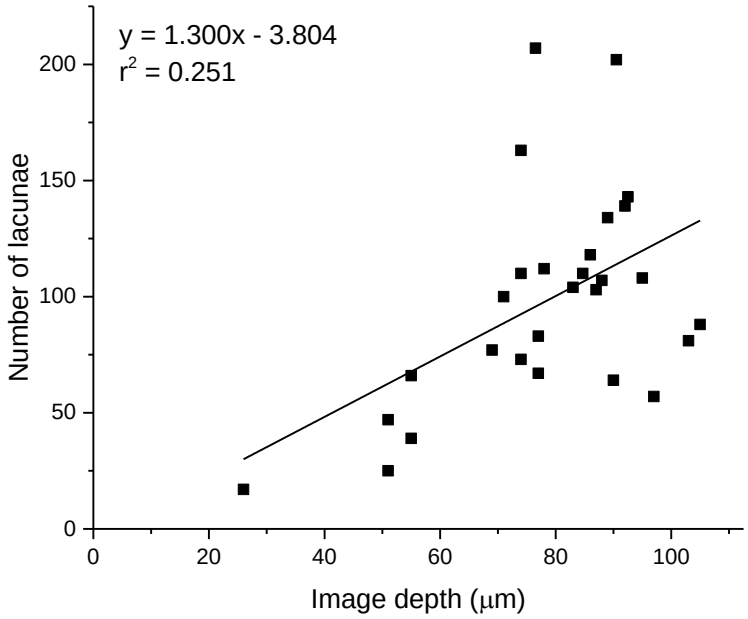

Figure 5-6: Number of osteocyte lacunae versus image depth. Image depth from CLSM of approximately 60 micrometers or greater is adequate for achieving 50 or greater lacunae.

5.3.3 Comparison of ellipsoidal and lacunar metrics

Ellipsoidal and lacunar metrics demonstrated excellent agreement (Figure 5-7), with the correlation coefficient r^2 approaching 1 for both volume and surface area. We proceeded with lacunar definitions of volume and surface area for the study of aging on osteocyte lacunar geometries, but this choice was arbitrary (Figure 5-2).

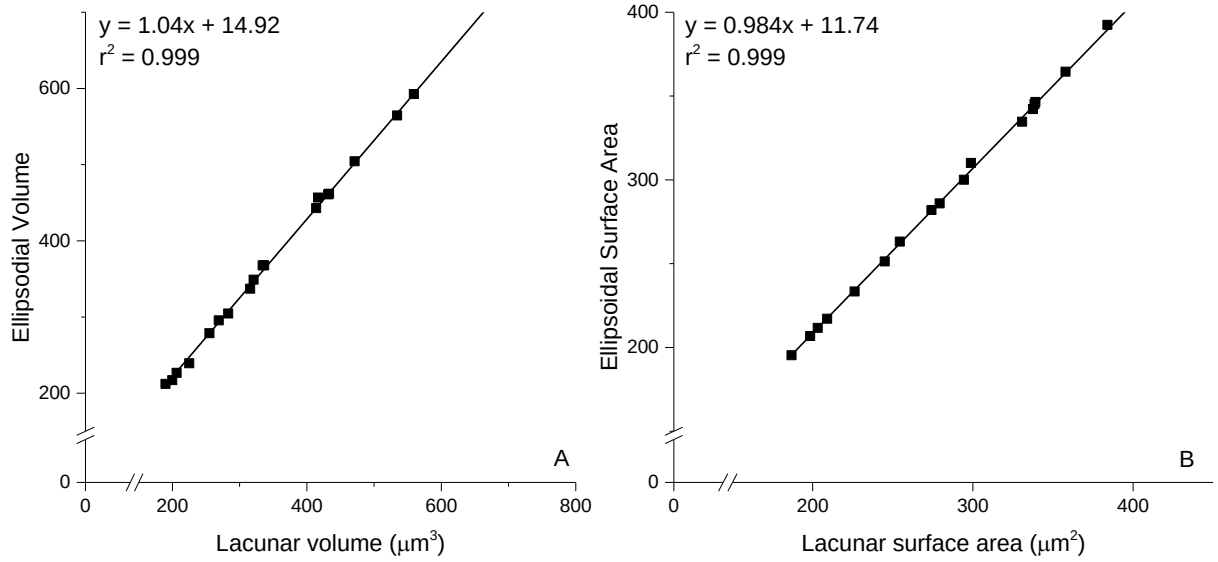

Figure 5-7: Ellipsoidal versus lacunar geometries. Ellipsoidal and lacunar calculations demonstrate excellent agreement for A) volume and B) surface area, with correlation coefficients approaching 1. Best-fit ellipsoids have been employed to describe osteocyte lacunar geometries in previous efforts [Lai *et al.*, 2015; McCreadie *et al.*, 2004], but yield essentially equivalent information as a pixel-fill lacunar approach.

5.3.4 Comparison of 2D and 3D osteocyte lacunar geometries

3D geometric measures were regressed against 2D analogous generated from an in-focus slice of the same z-stack (Figure 5-8). In general, 2D measurements poorly predict 3D outcomes from the same lacunae. *Lacunar area (2D)* was modestly predictive of *lacunar (3D) volume*, with $r^2 = 0.264$. *Lacunar perimeter (2D)* was poorly predictive of *lacunar surface area (3D)*, with $r^2 = 0.0883$. *Closest center of mass* (2D) was also poorly predictive of *closest center of mass* (3D), with $r^2 = 0.197$. Circularity was not predictive of sphericity, with $r^2 = 0.0154$. *Span theta* (2D) was not predictive of *span theta* (3D), with $r^2 = 0.0469$.

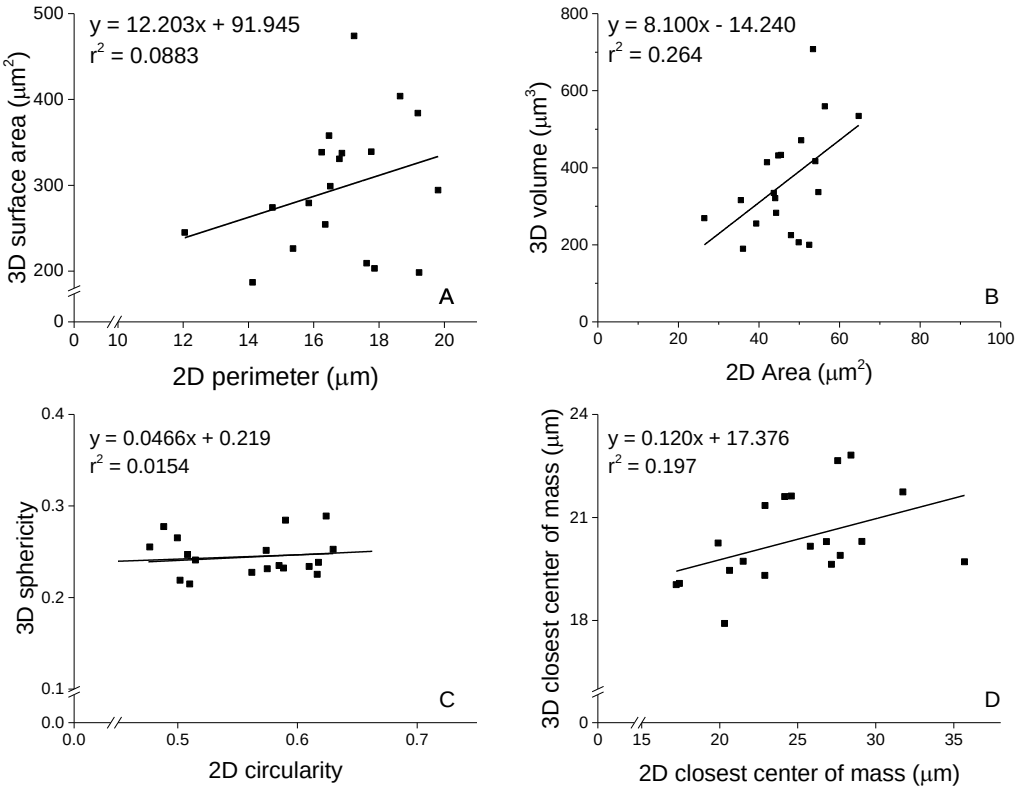

Figure 5-8: 3D versus 2D lacunar geometries. 3D parameters of osteocyte lacunae are poorly predicted by 2D analogs measured from a single in-focus slice of the same z-stack.

5.3.5 Effect of age on osteocyte lacunar geometries

Age was seen to influence 3D *lacunar volume*, *lacunar surface area*, and *sphericity*, with $p < 0.05$ for the main effect of age (Table 5-2, Figures 5-9 and 5-10). The following post-hoc comparisons between ages are adjusted by the Tukey procedure for family-wise error. *Lacunar volume* and *lacunar surface area* were reduced by -40.7% ($p = 0.028$) and -31.2% ($p = 0.022$), respectively, in old mice compared with young mice. *Sphericity* was +14.8% higher ($p = 0.013$) for old mice than young mice. Properties from middle-age (18 month) mice were intermediate between those of old and young mice, and not significantly different from either group. Age did not affect 3D *center of mass* or *span theta*. The lacunar number density, the number of osteocytes per volume of segmented bone, was reduced by -37.7% ($p = 0.010$) for old mice compared with young mice.

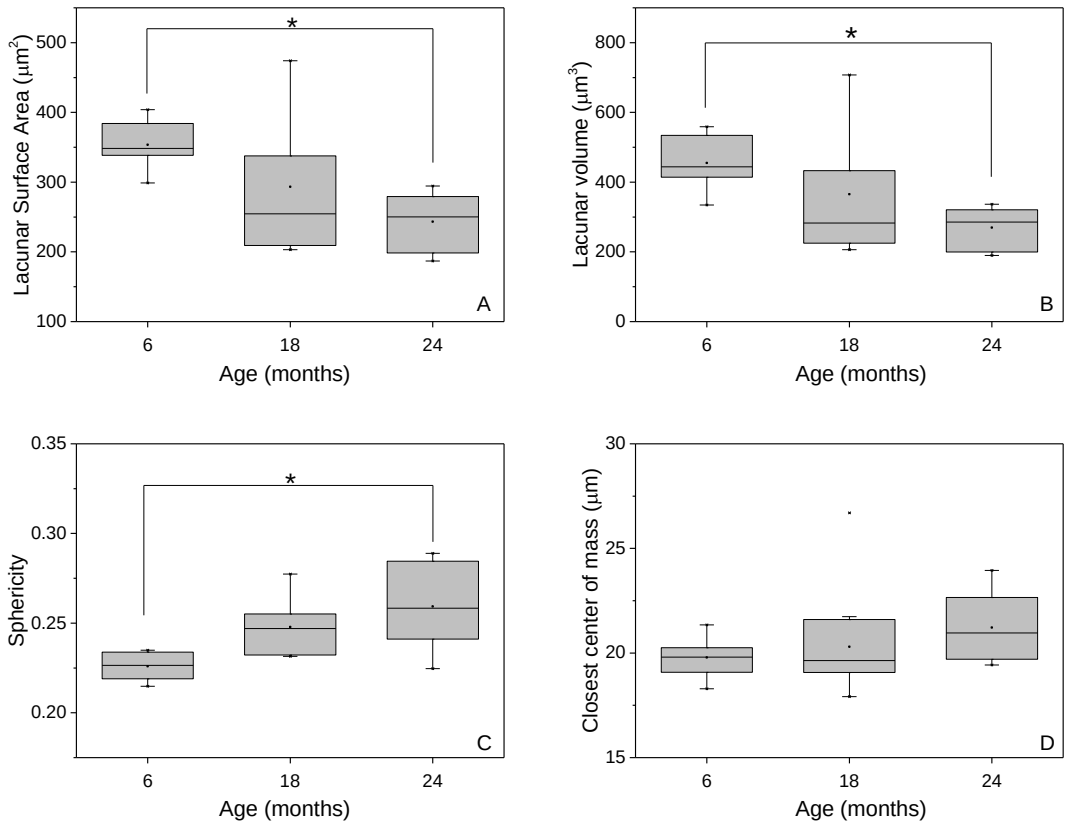

Figure 5-9: 3D osteocyte lacunar geometries change with age for cortical mouse bone. 3D osteocyte lacunar geometries change with age. Compared with young mice, lacunae from old mice have A) smaller surface area, B) smaller volume, and c) higher sphericity. The distance between lacunae, given by D) closest center of mass, does not change with age.

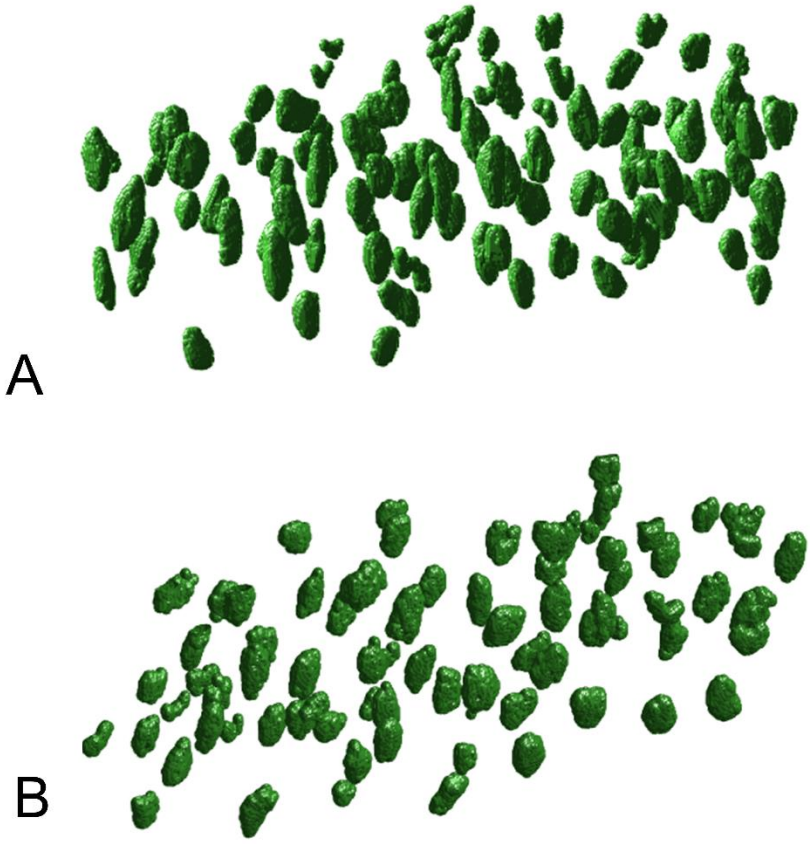

Figure 5-10: Osteocyte lacunae become smaller, more spherical, and sparser with age. 3D osteocyte lacunar geometries change with age. Compared with young mice (A), old mice (B) have smaller, more spherical, and sparser lacunae.

Table 5-2: Comparison of osteocyte lacunar geometries in 3D and 2D for cortical bone from young through old mice

	3D metrics				2D metrics		
	6 mo	*18 mo*	*24 mo*		*6 mo*	*18 mo*	*24 mo*
Lacunar Volume (μm^3) p = 0.035	454.94 ± 34.21	365.12 ± 66.74	269.67 ± 26.25*	**Lacunar Area (μm^2)** p > 0.05	51.87 ± 3.45	44.61 ± 3.26	43.70 ± 3.39
Lacunar surface area (μm^2) p = 0.028	353.72 ± 15.18	293.46 ± 36.20	243.27 ± 18.57*	**Lacunar perimeter (μm)** p > 0.05	17.47 ± 0.51	16.40 ± 0.75	16.52 ± 0.98
Sphericity p = 0.015	0.23 ± 0.00	0.25 ± 0.01	0.26 ± 0.01*	**Circularity** p > 0.05	0.57 ± 0.02	0.56 ± 0.02	0.54 ± 0.03
Closest center of mass (μm) p > 0.05	19.86 ± 0.37	20.00 ± 0.50	21.23 ± 0.54	**Closest center of mass (μm)** p = 0.012	21.02 ± 1.40	24.75 ± 1.62	28.70 ± 1.53
Span theta (degrees) p > 0.05	11.18 ± 0.65	12.01 ± 0.80	11.71 ± 0.97	**Span theta (degrees)** p = 0.055	21.33 4.52	15.72 3.09	8.52 1.07*
Lacunar density ($1/\mu m^3$ x10^{-5}) p = 0.012	3.06 ± 0.28	2.30 ± 0.24	1.91 ± 0.16*	**Lacunar density ($1/\mu m^2$ x10^{-4})** p = 0.011	6.36 ± 0.96	4.20 ± 0.46	3.25 ± 0.39*

Data are presented as mean ± standard error. For each geometric parameter, the p-value for the main effect of age is reported. *Indicates $p < 0.05$ in Tukey post-hoc comparison between young and old mice.

Meanwhile, age did not significantly affect 2D *lacunar area*, *lacunar perimeter*, or *circularity* (Table 2). In two-dimensions, *closest center of mass* changed with age. Old mice had +36.6% greater (p = 0.009) *closest center of mass* than young mice. By contrast, *closest center of mass* did not change with age in 3D (p = 0.134). 2D *span theta* did not show a significant main effect of age (p = 0.055), but lacunae from old mice did have significantly smaller angular difference from mean osteocyte orientation than younger mice (-60.1%, p = 0.045). As with *closest center of mass*, differences in *span theta* with age were not seen in 3D. *Lacunar density* was the one measure significantly affected by aging in both 3D and 2D. In 2D, lacunar density was significantly reduced from old to young mice (-49.0%, p = 0.010).

5.4. Discussion

We sought to characterize changes to osteocyte lacunae occurring with aging. In order to analyze osteocyte lacunar geometries in 3D, we developed a facile and open-source method segmentation and analysis method based on confocal laser scanning microscopy (CLSM). In this method, depth-stacks of 2D images acquired with CLSM are first segmented into 3D osteocyte lacunae and then analyzed for lacunar geometries using the open-source, Matlab-based '3D Osteocyte Lacunae Analysis' program described here. This method pairs common CLSM imaging with time-efficient segmentation and analysis procedure, while avoiding the bias and user error intrinsic to manual segmentation. Our approach avoids pitfalls inherently associated with 2D imaging including difficulty distinguishing osteocytes from non-osteocyte objects and variance in geometries due to sectioning planes that lie off of the major ellipsoid axes.

Two aspects of our method were validated. First, we analyzed geometries of ellipsoidal "phantoms" and achieved agreement between measured and expected dimensions. Next, we compared the number of segmented lacunae for automatic and manual segmentation for one randomly-selected sample from each age group. The time-intensive nature of manual segmentation (approximately 10 hours per sample) precluded a comparison of manual and automatic segmentation for every specimen. It was found that 77-98% of manually segmented lacunae were automatically segmented with the 3D Osteocyte Lacunae Analysis program. It was expected that inhomogeneity in stain penetration and contrast from bone marrow would preclude 100% automatic segmentation of lacunae. While ideal to segment and analyze all lacunae, the limitations of automatic segmentation are expected to similarly affect all samples in the present study. Automatic and manual segmentation yielded somewhat different osteocyte lacunar geometries. Lacunae were larger and more spherical from automatic than from manual segmentation (Table 5-1). Manual segmentation is prone to user error and bias, and in our experience may be particularly prone to exclusion of low-contrast pixels on the edge of lacunar cross-sections. Additionally, the manually segmented lacunar objects were not subjected to the erosion and dilation procedures that are present in the automatic procedure. Erosion and dilation would be expected to result in somewhat smoother and more spherical lacunar objects.

Nonetheless, for both segmentation strategies, cortical bone from the 24-month mouse bone had smaller and more spherical lacunae than from the 6-month mouse.

We applied the automatic segmentation and analysis method introduced herein to study the effects of age on osteocyte lacunar geometries from cortical mouse bone. Lacunae were seen to become smaller with age and also more spherical (Figures 5-9 and 5-10). These effects were large; from 6-24 months osteocyte lacunae decrease in volume by 40.7% and become 14.8% more spherical. Consistent with reports from other studies, aging also reduced the number density of lacunae [Busse *et al.*, 2010; Vashishth *et al.*, 2000; Lai *et al.*, 2015]. In our study, old mice had 37.7% fewer lacunae per volume than young mice.

The effects of aging were largely not discernable from 2D analyses of the same images. In 2D, the mean *lacunar area* and *lacunar perimeter* decreased from young to old mice, but these changes were not significant. *Circularity*, the 2D analog of *sphericity*, also did not reproduce the age dependence seen in 3D. The only measure demonstrating a significant effect of age for both 2D and 3D was *lacunar number density*, which was reduced with age. *Lacunar number density* is not sensitive to the size, shape, or alignment of lacunae. It is therefore not surprising that our study and others, spanning 2D and 3D metrics and several imaging modalities, have found agreement of decreasing number density of lacunae with aging. Interestingly, 2D imaging may also generate misleading results. In 2D, osteocyte lacunae appeared to be farther apart and more similarly oriented for old compared with young mice. Notably, with the addition of the z (depth) direction, *closest center of mass (3D)* and *span theta (3D)* do not differ with age. Osteocyte lacunae are anisotropic, with their major axis generally aligned along the long axis of the tibia. Thus, a 2D analysis, particularly for transverse sections, does not adequately survey anisotropy and cannot be relied on to discern osteocyte spatial arrangement.

Our observations highlight the limitations of 2D analysis and also reveal instances where 2D metrics could be misleading. Specifically, 2D analysis of osteocyte lacunae is inherently limited by assuming that cross-sectional geometries represent the complex ellipsoidal shapes of lacunae. A 2D section cannot reliably capture the largest dimensions of a network of lacunae, or their true orientations in space. Variance in 2D sample cutting and preparation could potentially yield quite different results for the same

samples. In addition, 2D analyses may include cross-sections of non-osteocyte objects, such as vasculature, that are difficult to distinguish from osteocyte lacunae unless visualized in 3D. Further, as demonstrated by the *closest center of mass* and *span theta* measurements in this study, changes to osteocyte spatial arrangement observed in 2D do not necessarily extend into the third dimension and could be misleading. For the above reasons, we recommend that 3D analyses are employed to assess the geometries and orientations of osteocyte lacunae.

It is important to consider whether our findings of changing osteocyte lacunar geometries with age could be confounded with age-related differences in bone tissue organization or stain penetration. Mouse cortical bone is known to have an increasing proportion of lamellar bone, as opposed to less-organized central or woven bone, with increasing age [Ferguson *et al.*, 2003]. However, in a 3D synchrotron-radiation study of osteocyte lacunae in cortical rat bone, lamellar lacunae were significantly more oblong (*i.e.*, less spherical) than lacunae from less-organized central bone [Bach-Gansmo *et al.*, 2015]. Lacunar volumes may be higher in lamellar versus non-lamellar bone, but these differences were not significant [Bach-Gansmo *et al.*, 2015]. Therefore, an increasing proportion of lamellar bone in cortical mouse bone, as would occur with aging, is not expected to explain our results of smaller and more spherical lacunae in older mice. Another possibility is that age-dependent changes to osteocyte lacunar geometry could be explained by older animals having more mineral-dense bone that decreases penetration of histological stain. In this case, the autofluorescence of cell nuclei, which are smaller and more spherical than lacunae, could dominate the contrast and lead to segmentation of nuclei instead of lacunae. However, this effect is unlikely for the current study. Bone from older mice typically stained with similar brightness as younger mice. Furthermore, the lower limit of the volume filter during segmentation (100 μm^3) would exclude nuclei. Thus, age-related changes to osteocyte lacunae observed in this study are not expected to be trivially explained by differences in bone composition or staining that may occur with age.

The decreasing lacunar volume and increasing lacunar sphericity with age likely represents bone infilling. Osteocytes are long-lived cells, and originate as osteoblasts that become trapped within forming bone matrix. Therefore, it is unlikely that aging causes new, smaller and more spherical lacunae to form,

and more plausible that existing lacunae infill with changes to perilacunar remodeling activity. However, we are unable to determine from this study whether perilacunar remodeling rate is decreased or increased, and note that a change in activity in either direction could result in the observed infilling.

This study had several limitations. The automatic segmentation process identified many but not all lacunae, due to inhomogeneity in lacunar contrast and also bright bone marrow influencing thresholding. Additionally, we did not assess changes to perilacunar remodeling activity with age. We also did not survey changes to bone quality near osteocyte lacunae. These data will be important for understanding how changes to osteocyte lacunar geometries observed with increased age influence bone strength and toughness.

The changing osteocyte lacunar geometries with aging observed in this study are novel. Though others have observed non-significant trends of decreased lacunar size with aging, 2D assessment or small sample sizes potentially obscured the effects of age on lacunar geometries [Mullender *et al.,* 1996; Lai *et al.,* 2015]. This is potentially the first description of age-related changes to lacunar spatial arrangement. Our findings fit into an emerging story where aging changes mineral metabolism, and altered mineral metabolism changes perilacunar remodeling and therefore osteocyte lacunar geometries. In support of this claim, we note that Busse and coworkers studied 3D osteocyte lacunae using synchrotron-radiation CT from iliac crest biopsies of patients who were either vitamin D sufficient or deficient [Busse *et al.,* 2013]. Lacunae were larger with vitamin D deficiency, and perilacunar material chemistry assessed by Fourier-transformed infrared spectroscopy had elevated measures of bone maturity. These data are consistent with a reduction of osteoclastic bone resorption in vitamin D, and an increased burden on osteocyte lacunae to participate in systemic mineral homeostasis. Though vitamin D deficiency does frequently occur with aging, it is not necessarily the cause of age-related changes to osteocyte lacunae reported here. The combination of 3D analysis of osteocyte lacunae and mechanistic studies may elucidate the reasons for age-related changes to osteocyte lacunae.

Our work points to the exciting possibility that osteocyte geometries may change in aging bone. In addition to aging, changes to osteocyte lacunae may occur with metabolic diseases [Bonucci *et al.,* 1977;

Busse *et al.*, 2013], osteoporosis [Mullender *et al.*, 1996], drug therapies (*e.g.*, glucorticoid therapy) [Lane *et al.*, 2004; Yao *et al.*, 2008; Fowler *et al.*, 2016], exercise [Gardinier *et al.*, 2016], and microgravity [Burger & Klein-Nulend, 1998; Blaber *et al.*, 2013]. Thus, measuring 3D osteocyte lacunar geometries is important for understanding the effects of age, disease, and therapeutic interventions. It is anticipated that the efficiency and accessibility of our 3D Osteocyte Lacunae Analysis method will assist with these investigations.

Acknowledgments:

We thank Dr. Aaron Johnson (Department of Biology, University of Colorado Denver) for use of the Zeiss 710 confocal laser scanning microscope. We also thank William Schroeder for his excellent care of study animals.

5.5. References

1. Bonewald, L. F. (2011). The amazing osteocyte. *Journal of Bone and Mineral Research*, *26*(2), 229-238.
2. Schaffler, M. B., Cheung, W. Y., Majeska, R., & Kennedy, O. (2014). Osteocytes: master orchestrators of bone. *Calcified tissue international*, *94*(1), 5-24.
3. Qing, H., Ardeshirpour, L., Divieti Pajevic, P., Dusevich, V., Jähn, K., Kato, S., ... & Bonewald, L. F. (2012). Demonstration of osteocytic perilacunar/canalicular remodeling in mice during lactation. *Journal of bone and mineral research*, *27*(5), 1018-1029.
4. Kaya, S., Basta-Pljakic, J., Seref-Ferlengez, Z., Majeska, R. J., Cardoso, L., Bromage, T., ... & Fritton, S. P. (2016). Lactation-Induced Changes in the Volume of Osteocyte Lacunar-Canalicular Space Alter Mechanical Properties in Cortical Bone Tissue. *Journal of Bone and Mineral Research*.
5. Kwiecinski, G. G., Krook, L., & Wimsatt, W. A. (1987). Annual skeletal changes in the little brown bat, Myotis lucifugus lucifugus, with particular reference to pregnancy and lactation. *Developmental Dynamics*, *178*(4), 410-420.
6. Lane, N. E., Yao, W., Balooch, M., Nalla, R. K., Balooch, G., Habelitz, S., ... & Bonewald, L. F. (2006). Glucocorticoid-Treated Mice Have Localized Changes in Trabecular Bone Material Properties and Osteocyte Lacunar Size That Are Not Observed in Placebo-Treated or Estrogen-Deficient Mice. *Journal of bone and mineral research*, *21*(3), 466-476.
7. Alliston, T. (2014). Biological regulation of bone quality. *Current osteoporosis reports*, *12*(3), 366-375.
8. Tang, S. Y., Herber, R. P., Ho, S. P., & Alliston, T. (2012). Matrix metalloproteinase–13 is required for osteocytic perilacunar remodeling and maintains bone fracture resistance. *Journal of Bone and Mineral Research*, *27*(9), 1936-1950.
9. Gardinier, J. D., Al-Omaishi, S., Morris, M. D., & Kohn, D. H. (2016). PTH signaling mediates perilacunar remodeling during exercise. *Matrix Biology*, *52*, 162-175.
10. Fowler, T. W., Acevedo, C., Mazur, C. M., Hall-Glenn, F., Fields, A. J., Bale, H. A., ... & Alliston, T. (2017). Glucocorticoid suppression of osteocyte perilacunar remodeling is associated with subchondral bone degeneration in osteonecrosis. *Scientific Reports*, *7*, 44618.
11. Ferguson, V. L., Ayers, R. A., Bateman, T. A., & Simske, S. J. (2003). Bone development and age-related bone loss in male C57BL/6J mice. *Bone*, *33*(3), 387-398.
12. Halloran, B. P., Ferguson, V. L., Simske, S. J., Burghardt, A., Venton, L. L., & Majumdar, S. (2002). Changes in bone structure and mass with advancing age in the male C57BL/6J mouse. *Journal of Bone and Mineral Research*, *17*(6), 1044-1050.
13. Raghavan, M., Sahar, N. D., Kohn, D. H., & Morris, M. D. (2012). Age-specific profiles of tissue-level composition and mechanical properties in murine cortical bone. *Bone*, *50*(4), 942-953.
14. Nalla, R. K., Kruzic, J. J., Kinney, J. H., & Ritchie, R. O. (2004). Effect of aging on the toughness of human cortical bone: evaluation by R-curves. *Bone*, *35*(6), 1240-1246.
15. Orwoll, E., Nielson, C. M., Marshall, L. M., Lambert, L., Holton, K. F., Hoffman, A. R., ... & Cauley, J. A. (2009). Vitamin D deficiency in older men. *The Journal of Clinical Endocrinology & Metabolism*, *94*(4), 1214-1222.
16. Tsai, K. S., Heath 3rd, H., Kumar, R., & Riggs, B. L. (1984). Impaired vitamin D metabolism with aging in women. Possible role in pathogenesis of senile osteoporosis. *Journal of Clinical Investigation*, *73*(6), 1668.

17. Lips, P. (2006). Vitamin D physiology. *Progress in biophysics and molecular biology*, *92*(1), 4-8.

18. Farr, J. N., Fraser, D. G., Wang, H., Jaehn, K., Ogrodnik, M. B., Weivoda, M. M., ... & Bonewald, L. F. (2016). Identification of senescent cells in the bone microenvironment. *Journal of Bone and Mineral Research*, *31*(11), 1920-1929.

19. Vashishth, D., Verborgt, O., Divine, G., Schaffler, M. B., & Fyhrie, D. P. (2000). Decline in osteocyte lacunar density in human cortical bone is associated with accumulation of microcracks with age. *Bone*, *26*(4), 375-380.

20. Busse, B., Djonic, D., Milovanovic, P., Hahn, M., Püschel, K., Ritchie, R. O., ... & Amling, M. (2010). Decrease in the osteocyte lacunar density accompanied by hypermineralized lacunar occlusion reveals failure and delay of remodeling in aged human bone. *Aging cell*, *9*(6), 1065-1075.

21. Lai, X., Price, C., Modla, S., Thompson, W. R., Caplan, J., Kirn-Safran, C. B., & Wang, L. (2015). The dependences of osteocyte network on bone compartment, age, and disease. *Bone research*, *3*.

22. Mullender, M. G., Van Der Meer, D. D., Huiskes, R., & Lips, P. (1996). Osteocyte density changes in aging and osteoporosis. *Bone*, *18*(2), 109-113.

23. Carter, Y., Thomas, C. D. L., Clement, J. G., Peele, A. G., Hannah, K., & Cooper, D. M. (2013). Variation in osteocyte lacunar morphology and density in the human femur—a synchrotron radiation micro-CT study. *Bone*, *52*(1), 126-132.

24. Dong, P., Haupert, S., Hesse, B., Langer, M., Gouttenoire, P. J., Bousson, V., & Peyrin, F. (2014). 3D osteocyte lacunar morphometric properties and distributions in human femoral cortical bone using synchrotron radiation micro-CT images. *Bone*, *60*, 172-185.

25. Hesse, B., Varga, P., Langer, M., Pacureanu, A., Schrof, S., Männicke, N., ... & Raum, K. (2015). Canalicular Network Morphology Is the Major Determinant of the Spatial Distribution of Mass Density in Human Bone Tissue: Evidence by Means of Synchrotron Radiation Phase-Contrast nano-CT. *Journal of Bone and Mineral Research*, *30*(2), 346-356.

26. McCreadie, B. R., Hollister, S. J., Schaffler, M. B., & Goldstein, S. A. (2004). Osteocyte lacuna size and shape in women with and without osteoporotic fracture. *Journal of biomechanics*, *37*(4), 563-572.

27. Kamel-ElSayed, S. A., Tiede-Lewis, L. M., Lu, Y., Veno, P. A., & Dallas, S. L. (2015). Novel approaches for two and three dimensional multiplexed imaging of osteocytes. *Bone*, *76*, 129-140.

28. Burr, D. B., & Hooser, M. (1995). Alterations to the en bloc basic fuchsin staining protocol for the demonstration of microdamage produced in vivo. *Bone*, *17*(4), 431-433.

29. Bach-Gansmo, F. L., Weaver, J. C., Jensen, M. H., Leemreize, H., Mader, K. S., Stampanoni, M., ... & Birkedal, H. (2015). Osteocyte lacunar properties in rat cortical bone: differences between lamellar and central bone. *Journal of structural biology*, *191*(1), 59-67.

30. Busse, B., Bale, H. A., Zimmermann, E. A., Panganiban, B., Barth, H. D., Carriero, A., ... & Püschel, K. (2013). Vitamin D deficiency induces early signs of aging in human bone, increasing the risk of fracture. *Science translational medicine*, *5*(193), 193ra88-193ra88.

31. Bonucci, E., & Gherardi, G. (1977). Osteocyte ultrastructure in renal osteodystrophy. *Virchows Archiv*, *373*(3), 213-231.

32. Yao, W., Cheng, Z., Pham, A., Busse, C., Zimmermann, E. A., Ritchie, R. O., & Lane, N. E. (2008). Glucocorticoid-induced bone loss in mice can be reversed by the actions of parathyroid hormone and risedronate on different pathways for bone formation and mineralization. *Arthritis & Rheumatism*, *58*(11), 3485-3497.

33. Burger, E. H., & Klein-Nulend, J. (1998). Microgravity and bone cell mechanosensitivity. *Bone*, *22*(5), 127S-130S.

34. Blaber, E. A., Dvorochkin, N., Lee, C., Alwood, J. S., Yousuf, R., Pianetta, P., ... & Almeida, E. A. (2013). Microgravity induces pelvic bone loss through osteoclastic activity, osteocytic osteolysis, and osteoblastic cell cycle inhibition by CDKN1a/p21. *PloS one*, *8*(4), e61372.

6. Chronic kidney disease and aging diminish quality from the microscale to the macroscale

Chelsea M. Heveran[1], Adam Rauff[2], Eric L. Livingston[3], Moshe Levi[4], R. Dana Carpenter[5], Ted Bateman[3], Karen B. King[6] & Virginia L. Ferguson[1]

[1]Department of Mechanical Engineering, University of Colorado, Boulder, CO; [2]Department of Bioengineering, University of Colorado, Denver, CO; [3]Department of Mechanical Engineering, University of North Carolina, Chapel Hill, NC; [4]Department of Medicine, Division of Renal Diseases and Hypertension, University of Colorado School of Medicine, Aurora, CO; [5]Department of Mechanical Engineering, University of Colorado, Denver, CO; [6]Department of Orthopaedics, University of Colorado School of Medicine, Aurora, CO

Abstract

Chronic kidney disease (CKD) increases fracture risk and is most prevalent in the elderly. Yet the changes to fracture-resistance determining bone quality with aging together with CKD are unknown. We compared bone quality from the whole bone to the microscale for young (6 month), middle-age (18 month), and old (24 month) male C57Bl/6 mice with CKD induced *via* 5/6th nephrectomy or sham surgeries. Deleterious changes to bone quality with CKD emerged with increased age such that old mice with CKD had the worst bone quality by most measures. CKD affected both collagen and mineral, and diminished bone quality from the whole bone to the microscale. CKD also lowered tissue-scale material properties, including heterogeneity of modulus from nanoindentation and crystallinity from Raman spectroscopy. These reductions to bone quality with CKD, which especially occur in middle-age and old mice, may help explain clinically-observed bone fragility.

6.1 Introduction

Chronic kidney disease (CKD) increases clinically-observed fracture risk and is most prevalent in the elderly [Nickolas et al., 2008]. Age also increases the fragility associated with CKD. Older patients are more likely to fracture than younger patients with the same stage of kidney disease [Naylor et al., 2014]. Yet the bone quality changes underlying this loss of fracture resistance with CKD together with advanced age are not understood.

Previous work in rodent models, all of which involve young adult animals, have found loss of bone material quality in CKD. Specifically, CKD has been observed to lower mineral content, tissue-scale

modulus, mineral chemistry, and collagen crosslinking [Heveran *et al.*, 2016; Iwasaki *et al.*, 2015; Allen *et al.*, 2015]. Whether CKD diminishes bone microarchitecture is uncertain, with one study finding progressive loss of trabecular microarchitecture at 16 weeks following 5/6th nephrectomy (5/6 Nx) in male Crlj:CD1 mice [Kadokawa *et al.*, 2011], and another reporting no loss of cortical or trabecular microarchitecture at 11 weeks following 5/6 Nx in male C57Bl/6 mice [Heveran *et al.*, 2016]. Meanwhile, the loss of bone quality with aging and without CKD has been relatively well described. Bone material is worsened with aging. Older bone is more mineralized and has altered mineral chemistry [Boskey *et al.*, 2002; Boskey *et al.*, 2010; Akkus *et al.*, 2003], increased microdamage [Schaffler *et al.*, 1995], and increased non-enzymatic collagen crosslinking [Wang *et al.*, 2002]. Aging worsens bone trabecular and cortical microarchitecture. Older bone has fewer and thinner trabeculae, as well as thinner and more porous cortical bone [Riggs *et al.*, 2004]. It is not known how CKD and aging together influence bone quality, including bone material and also microarchitecture.

An intriguing question is whether aging and CKD alter bone material heterogeneity, and whether changes to microscale material property heterogeneity correspond with whole bone structural integrity (*e.g.*, toughness). Heterogeneity of mineral content from quantitative backscattered SEM techniques has been shown to be altered (*i.e.*, either too low or too high) in bone from patients with fragility fractures [Roschger *et al.*, 2008]. Additionally, computational works have reported that increased heterogeneity of tissue-scale modulus and plastic work from AFM and nanoindentation may correspond with increased energy dissipation [Tai *et al.*, 2005; Yao *et al.*, 2011]. Lowered variance in nanoindentation modulus was observed in bone formed during CKD following 5/6 Nx [Heveran *et al.*, 2016]. Yet it is not known whether aging and CKD individually or together reduce cortical bone heterogeneity of mechanical (*e.g.*, modulus) or chemical (*e.g.*, mineral:matrix, crystallinity) parameters, and whether these changes would correspond to changes in whole bone toughness. This is a relevant question in part because bisphosphonate therapies, which are sometimes administered to patients with CKD, can result in adynamic bone disease and worsened material properties [Gourion-Arsiquaud *et al.*, 2010; Allen *et al.*, 2008, Mashiba *et al.*, 2000].

The purpose of this study was to investigate how CKD and aging together reduce fracture resistance-determining bone quality. To consider the influences of CKD and aging on bone quality, we employed a model of CKD induced *via* 5/6 Nx in young (6 mo), middle-age (18 mo), and old (24 mo) male C57Bl/6 mice. Bone quality was evaluated from the whole bone to the nanoscale in order to ascertain the influences of aging and CKD on bone mineral, collagen, and structural integrity. Site-matched microscale mapping of material properties allowed assessment of microscale material heterogeneity. The hypothesis of this study was that bone quality is worsened by CKD and aging together such that the worst bone quality occurs in advanced age and CKD. It was further hypothesized that altered bone material heterogeneity would occur in CKD and correspond with diminished whole bone toughness.

6.2 Methods

6.2.1 Animal model and sample preparation

Male C57Bl/6J mice were obtained from Jackson Laboratories at the ages of 3, 15, and 21 months. Mice were maintained on a 12-h light / 12-h dark cycle and housed individually in polycarbonate cages with standard bedding. Mice were fed Harlan Teklad 2920X chow and allowed free access to water. We randomly assigned mice to CKD or sham groups within each age. The CKD group underwent two-stage nephrectomy. At 3 months of age, the left kidney was removed, followed by resection of 2/3 of the right kidney one week later. The control group received sham operations with the same timeframe. Mice were anesthetized using 1.5% isoflurane during procedures. A post-operative dose of buprenorphine (0.5 mg/kg) was administered after surgeries and prior to recovery, as well as every 12 hours for the next two days. Mice were killed three months after study surgeries *via* CO_2 and cervical dislocation. At the study endpoint, mice were 6 (young; sham: n = 6, CKD: n = 7), 18 (middle-age; sham: n = 8; CKD: n = 10), and 24 (old; sham: n = 8; CKD: n = 9) months of age. All animal procedures were approved by the Institutional Animal Use and Care Committee at the University of Colorado Denver.

The left femur, tibia, humerus, and ulnae were reserved for bone quality analyses. The left tibia was preserved in 70% ethanol at stored at 4° C. All other bones were wrapped with phosphate-dampened gauze and stored at -20° C until analysis.

6.2.2. Serum and urine chemistries

Serum biochemistry analyses were performed on blood drawn three times at one-month intervals following study surgeries for all mice. Urine was also collected at euthanasia. Blood urea nitrogen (BUN), phosphate (Pi) concentration, and calcium (Ca) concentration were measured with kits from Stanbio Laboratory (Boerne, TX).

6.2.3 microCT

Microarchitecture was assessed for the cortical bone of the midshaft femur and trabecular bone of the proximal tibia using microCT for all study mice (μCT, Scanco 80, Scanco AG, Basserdorf, Switzerland). Femurs were defrosted overnight at 4˚C before scanning. Scanning was performed with 10 μm voxel size, following acquisition and analysis methods described previously [Heveran *et al.,* 2016]. Cortical parameters included bone volume / total volume (BV/TV), bone area / total area (BA/TA), cortical porosity (Ct.Po), cortical thickness (Ct.Th), total mineral density (TMD), moment of inertia about the medial-lateral axis (I_{ML}), distance between the centroid and bone surface in the anterior-posterior direction (C), and polar moment of inertia (pMOI) [Bouxsein *et al.*, 2010]. Trabecular parameters included trabecular number (Tb.N), trabecular spacing (Tb.Sp), trabecular thickness (Tb.Th), bone volume (BV), total volume (TV), bone volume / total volume (BV/TV), volumetric bone mineral density (vBMD), and connectivity density (Conn.D). Following microCT, femurs were again wrapped in phosphate-dampened gauzed and stored at -20 C for subsequent whole bone mechanical characterization.

6.2.4 Whole bone mechanical and material properties

Following microCT, left femurs underwent three-point bending (Insight II Material Testing System, 250 N load cell, MTS Systems Corporation, Eden Prairie MN) (6 mo / sham: n = 5 ; 6 mo / CKD: n = 7; 18 mo / sham: n = 8; 18 mo / CKD: n = 9; 24 mo / sham: n = 8; 24 mo / CKD: n = 8). Femurs were removed from PBS-soaked gauze and placed on fixtures for mechanical testing while taking care to maintain their hydration levels. Femurs were tested to failure using a deflection rate of 5 mm/min on a custom anvil with an 8-mm span. Load-displacement curves were analyzed for mechanical properties including stiffness, maximum load, displacement at maximum load, energy at maximum load, load at yield,

displacement at yield, energy at yield, post-yield displacement, load at fracture, displacement at fracture, and energy at fracture. The yield point was defined as the intersection of a secant line drawn with a 10% reduction in slope from the initial tangent stiffness and the load-displacement curve [Jepsen *et al.,* 1996].

Using I_{ML} and C from μCT, we estimated material properties including bending modulus, yield stress, ultimate stress, and toughness from the three-point bending data using standard beam bending equations as applied to the mouse femur [Turner & Burr, 1993].

6.2.6 3D osteocyte lacunar geometries

The left tibia was histologically dehydrated in a graded series of ethanol and stained with 1% basic fuchsin [Burr & Hooser, 1995] (6 mo / sham: n = 6 ; 6 mo / CKD: n = 5; 18 mo / sham: n = 7; 18 mo / CKD: n = 6; 24 mo / sham: n = 6; 24 mo / CKD: n = 5). Tibias were then cleared with acetone and embedded in poly(methyl)methacrylate (PMMA). Embedded samples were transversely sectioned 1 mm proximal to the tibia-fibula junction with a low-speed saw (Buehler Isomet, Buehler, Lake Bluff, IL). A ground section was prepared from the distal section with target thickness of 200 um (Exakt 400 CS, Exakt Technologies Inc, Oklahoma City, OK).

Imaging of ground sections was performed in transmission with a Zeiss LSM 710 confocal laser scanning microscope, with 555 nm excitation, 568-1000 nm bandpass filter, and 40x oil-immersion objective. Resolution in x-y and z was 0.447 and 0.493 μm, respectively. Depth stacks (z-stacks) were obtained through the visible range of osteocyte lacunae (60-100 μm of imaging depth).

3D images of osteocyte lacunae were constructed and analyzed for lacunar geometries using the open-source 3D Osteocyte Lacunae Analysis program and Matlab v17 [Heveran *et al.,* in preparation]. Briefly, each 2D image within a z-stack was automatically segmented to define lacunae. These lacunae were reconstructed in 3D. A graphical user interface allowed the user to exclude non-lacunae objects (*e.g.*, vasculature). The 3D osteocyte lacunar network was analyzed for lacunar volume, lacunar surface area, closest center of mass, sphericity (ratio of smallest to largest lacunar radii, where 1 = sphere), span theta (the difference of the 3D vector describing the major axis direction from the average direction of all lacunae), and lacunar density (number of osteocytes / image volume).

6.2.7 Site-matched assessment of microscale bone chemistry and modulus

Following three-point bending, femurs were histologically dehydrated in a graded series of ethanol, cleared in acetone, and embedded in PMMA. Embedded bones were sectioned at the femoral midshaft using a low speed diamond saw (Isomet, Buehler, Lake Bluff, IL). Specimens were ground using wet silicon carbide paper (600 and 1200 grit), and then polished with alumina pastes (9, 5, 3, 1, 0.1, 0.05 µm) and Rayon fine clothes (South Bay Technologies, San Clemente, CA) to a final finish of 0.05 µm. Samples were sonicated between each polishing step.

Raman spectroscopy was performed in maps spanning the cortical thickness with a Renishaw inVia (Renishaw, Wotton-under-Edge, Gloucestershire, UK) with 785 nm wavelength laser light routed through fiberoptics to a nanoindenter stage (TI 950, Hysitron, Minneapolis, MN). Rows of three indents spaced 15 µm apart extended every 10 µm through the cortical thickness (Figure 6-1).

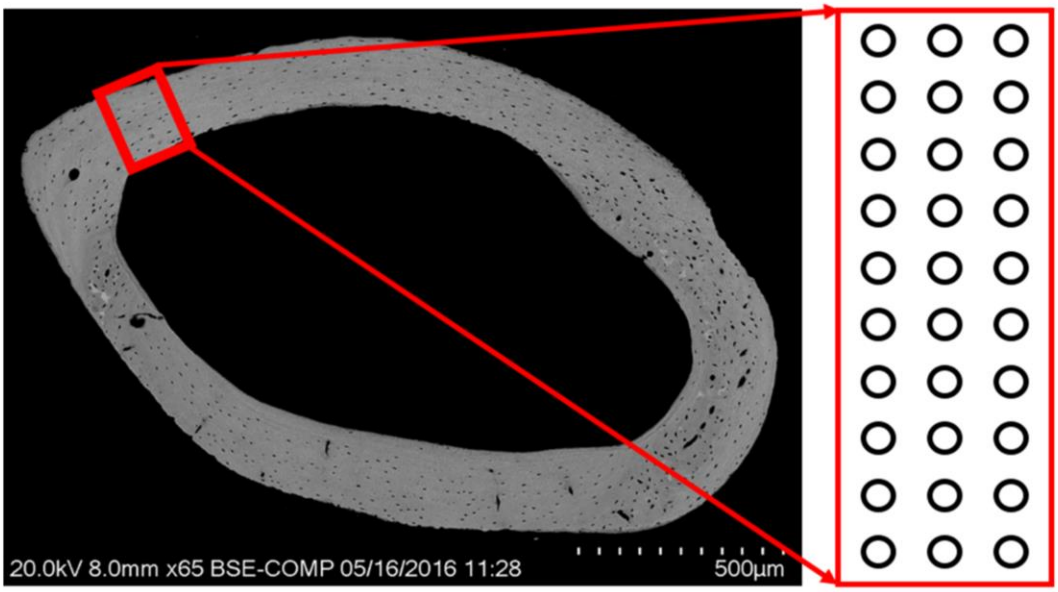

Figure 6-1: Site-matched mapping of microscale material properties. Microscale material properties are evaluated at matched sites for bone chemistry (Raman spectroscopy) and modulus (nanoindentation).

The fluorescent baseline was subtracted using Renishaw WIRE software. A reference PMMA sample was subtracted from each point, using custom Matlab code. These corrected spectra were then

analyzed for mineral:matrix (ν_1 phosphate:proline), carbonate:phosphate, and crystallinity (inverse of half-width at full maximum height of the ν_1 phosphate peak).

Nanoindentation was then performed at the same locations as Raman maps using the shared stage. A 5 µm spherical tip indented the bone at 30 nm/s until a max depth of 500 nm was obtained. Max depth was maintained for 120 s to allow dissipation of viscoelastic energy. Reduced modulus (E_r) was calculated using Oliver-Pharr analysis, considering the first 45% of the unloading curve [Bushby *et al.*, 2004].

6.2.8 High-performance liquid chromatography

The humerus was dissected of all non-osseous tissue and bone marrow was flushed (6 mo / sham: n = 4 ; 6 mo / CKD: n = 7; 18 mo / sham: n = 6; 18 mo / CKD: n = 9; 24 mo / sham: n = 7; 24 mo / CKD: n = 8). Humeri were then hydrolyzed in 6N HCl for 18 h at 110° C, and then centrifuged to evaporate excess HCl. Filtered samples were diluted 1:5 in 10 percent acetonitrile and 0.05 percent heptafluorobutyric acid (HFBA), loaded into a reverse-phase Gemini-NX C-18 column (Phenomenex, Torrance, CA) and analyzed for crosslinks hydryoxylysylpyridinoline (HP), lysyl pyridinoline (LP), and pentosidine consistent with methods described by Bank et al [Bank *et al.*, 1997]. Details of the HPLC system (model 126, Beckman-Coulter, Fullerton, CA) are described at length in Oren *et al* [Oren *et al.*, 2011]. Separation of collagen crosslinks involved the following protocol: 15 minutes of solvent containing 24% methanol and 0.15% HFBA, 10 minutes of solvent containing 40% methanol and 0.05% HFBA, and 10 minutes of solvent containing 75% acetonitrile and 0.1% HFBA. The column was equilibrated in 24% methanol and 0.15% HFBA for at least 10 minutes between sample runs. Collagen crosslink peaks were measured with a fluorescence detector (FP1520, JASCO; Easton, ML). Excitation and emission wavelengths were 295 nm and 400 nm, respectively, for HP and LP. Pentosidine was detected with 328 nm excitation and 378 nm emission. Calibration curves were generated from the measured intensities of five dilutions of a calibrator containing purified HP and LP (Quidel Corportation) and pentosidine (L. Sayre, Case Western Reserve University, Cleveland, OH).

Crosslink concentrations were then normalized to concentration of concentration. Collagen was estimated from the concentration of hydroxyproline within the sample analyzed for crosslinks. An aliquot

of the sample analyzed for crosslinks was diluted 1:50 and derivatized with 9-fluoronylmethyl chloroformate [Bank *et al.,* 1996]. The following solutions were used for the amino acid protocol (1) 20 mM citric acid, 5 mM tetramethylammonium chloride, and 0.01% sodium azide, pH 2.85; (2) 20 mM sodium acetate, 5 mM tetramethylammonium chloride, and 0.01% sodium azide, pH 4.5, and (3) 100% acetonitrile. The gradient elution profile follows: from 0-11.5 minutes a gradient of 75% (1) / 25 % (3) to 60% (1)/40% (3), at 13 minutes switch to 64% (2) / 36% (1), from 13.1 -18 minutes a gradient of 64% (2) / 36% (3) to 62% (2) / 38%(3), then at 18 minutes a switch to 25% (2) / 75% (3) until the end of the run at 23 minutes. The column was equilibrated in 75% (1) / 25% (3) for at least 10 minutes between sample runs. Amino acid peaks were monitored at 254 nm excitation and 630 nm emission. A calibration curve was generated from five dilutions of an amino acid standard prepared from collagen hydrolysate (Sigma-Aldrich #A9531, St. Louis, Missouri). Collagen has a constant concentration of hydroxyproline, thus hydroxyproline concentration was converted to concentration of collagen (285 mol hydroxyproline per mol collagen).

6.2.10 Data analysis

The effects of aging and CKD, as well as their interaction, were tested with two-way ANOVA for all parameters. The dependent variable was transformed if necessary to satisfy assumptions of residual normality and homoscedasticity. Family-wise error was controlled for these analyses using Bonferroni-adjusted alpha. For most analysis, post-hoc testing was restrained to the interaction of CKD and age (*i.e.*, testing effects of CKD within each age), which resulted in a critical alpha of 0.05 / 3 = 0.017. For analyses involving osteocyte lacunae, where the effect of aging on osteocyte morphology is generally not understood, post-hoc testing was applied to within-age and within-treatment comparisons. For these analyses, critical alpha was set as 0.05 / 9 = 0.006.

Multiple linear regression was performed with the dependent variables as whole bone material properties (toughness, modulus, ultimate stress), and the independent variables as means and standard deviations from nanoindentation modulus and Raman chemistry from maps generated for each bone. The interactions between these microscale measures and both age and CKD status were also included. Site-

matched measures were first checked for correlations using Spearman's rank-order correlation. To avoid multicollinearity, only measures with correlations less than r = 0.5 were included in multiple linear regression models. Backward elimination was employed to select to model terms. Minitab (v17) was used for all analyses.

6.3 Results

6.3.1 Confirmation of kidney disease

CKD status was confirmed with measurement of serum blood urea nitrogen (BUN), calcium, and phosphate three times at one-month intervals following 5/6 Nx or sham surgeries, and also urine collected at euthanasia. For simple effects comparisons, the critical alpha was set as 0.05 / 9 = 0.006 (comparisons for three ages at three time points) for serum measurements, and 0.05 / 3 = 0.017 (comparisons for three ages at one time point) for urine measurements. BUN was significantly increased with the main effects of CKD status ($p < 0.001$) and time from surgery ($p < 0.001$). There was a significant interaction between CKD status and time from surgery ($p = 0.001$) such that mice with 5/6 Nx had increasing BUN with time from surgery, but sham mice did not. BUN status was not significantly different between 5/6 Nx and sham at one month after surgery. There was a trend towards increased BUN for 5/6 Nx compared with sham at two months from surgery for middle-age (+108.2%, $p = 0.035$) and old (+101.3%, $p = 0.019$) mice. At three months from surgery, mice with 5/6 Nx all had significantly elevated BUN (young: +152.0%, $p = 0.004$; middle-age: +177.2%, $p < 0.001$; old: +102.3%, $p = 0.003$). BUN measured from urine at the study endpoint was significantly lower with the main effect of CKD ($p < 0.001$). Urine BUN was lower for 5/6 Nx *vs* sham at every age (young: -50.5%, $p = 0.003$, middle-age: -52.1%, $p < 0.001$; old: -56.2%, $p < 0.001$), consistent with impaired kidney function. Serum calcium was not significantly affected by age, CKD, or time from surgeries, and there were no differences between CKD and sham at any age. Meanwhile, calcium in urine was significantly reduced with the main effect of CKD ($p = 0.012$). Urine calcium was significantly reduced for CKD *vs* sham for middle-age (-58.5%, $p = 0.004$) and old mice (-67.3%, $p = 0.007$). Serum phosphate was increased with time from surgery ($p = 0.003$), and there was a significant interaction between CKD status and time from surgery ($p = 0.008$). One serum phosphate outlier (values greater than mean + three

standard deviations) was excluded from measurements. There was a trend of significantly increased serum phosphate for CKD *vs* sham at 3 post surgeries for young (+37.9%, p = 0.017), middle-age (+25.9%, p = 0.041), and old mice (+25.0%, p = 0.079). Urine phosphate was not different with main effects of CKD status or age, and was not different for CKD *vs* sham at any age.

6.3.2 microCT

One outlier (value greater than 3 standard deviations of the mean) was excluded from 24 month old sham and 24 month old CKD groups for all cortical microarchitecture analysis. Aging reduced cortical (Table 6-1, Figure 6-2) and trabecular microarchitecture (Table 6-2, Figure 6-3). For cortical bone, aging significantly decreased BV/TV, BA/TA, and Ct.Th, and increased Ct.Po, TMD, I_{ML}, and pMOI. Aging also significantly reduced trabecular BV/TV, Conn.D, Tb.N., Tb.Th, vBMD, and increased Tb.Sp.

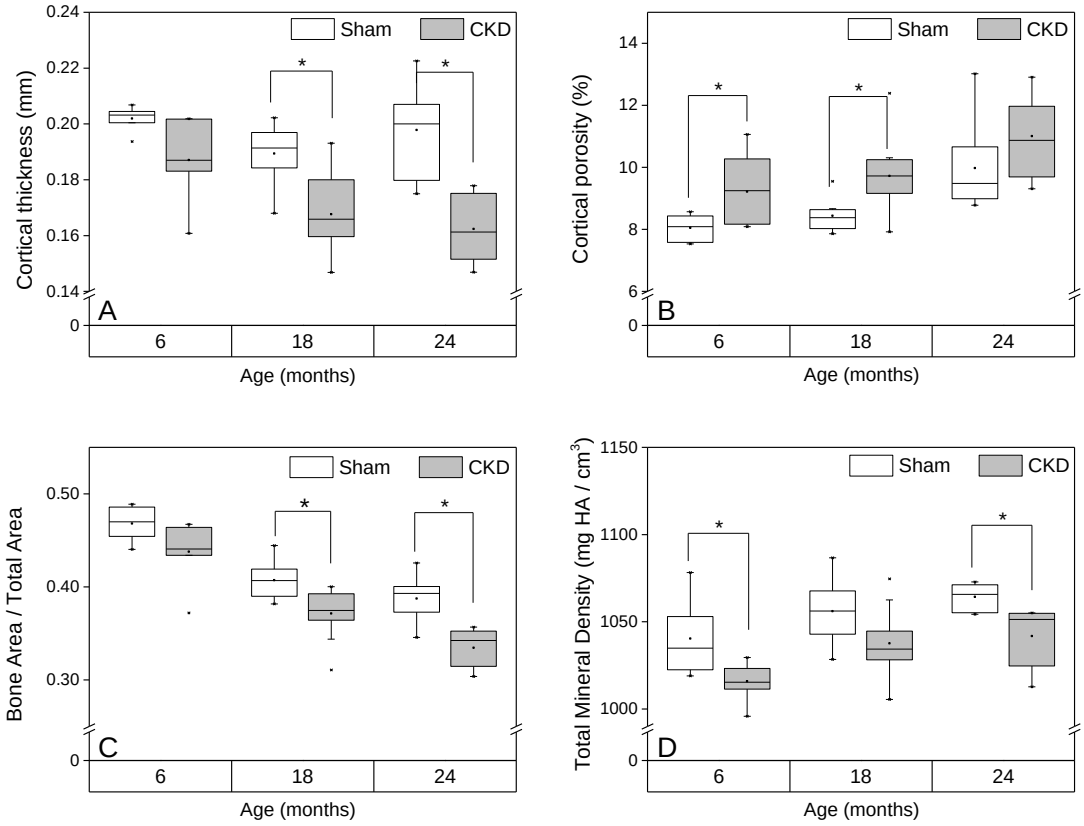

Figure 6-2: Cortical microarchitecture is diminished by aging and CKD. Cortical microarchitecture is reduced by aging and also with CKD. All measures are diminished for CKD *vs* sham beginning at either 6 months or 18 months.

Table 6-1: Cortical microarchitecture from microCT

	6 mo		18 mo		24 mo	
	Sham	*CKD*	*Sham*	*CKD*	*Sham*	*CKD*
BV/TV (%) ***Age: p < 0.001*** ***CKD*: p < 0.001** Age x CKD: p > 0.05	0.92 ± 0.0019	0.91± 0.0043	0.91 ± 0.0019	0.90 ± 0.0038 p = 0.017	0.90 ± 0.0056	0.89 ± 0.0047
BA/TA (%) ***Age: p < 0.001*** ***CKD: p < 0.001*** Age x CKD: p > 0.05	0.47± 0.0082	0.45 ± 0.0056 p = 0.034	0.41 ± 0.0075	0.37 ± 0.0087 p = 0.004	0.39 ± 0.0094	0.33 ± 0.0074 p < 0.001
Ct.Po (%) ***Age: p < 0.001*** ***CKD: p < 0.01*** Age x CKD: p > 0.05	8.05 ± 0.19	9.21 ± 0.43 p = 0.006	8.44 ± 0.19	9.72 ± 0.38 p = 0.004	9.98 ± 0.56	11.00 ± 0.472
Ct. Th (mm) ***Age: p < 0.01*** ***CKD: p < 0.001*** Age x CKD: p > 0.05	0.20 ± 0.0019	0.19 ± 0.0053 p = 0.043	0.19 ± 0.0039	0.17 ± 0.0047 p = 0.001	0.20 ± 0.0061	0.16 ± 0.0043 p < 0.001
TMD (mg HA /cm^3) ***Age: p < 0.01*** ***CKD: p < 0.001*** Age x CKD: p > 0.05	1040.40 ± 9.13	1015.90 ± 4.08 p = 0.013	1056.01 ± 6.58	1037.70 ± 6.16 p = 0.027	1064.30 ± 2.82	1041.80 ± 6.42 p = 0.017
I_{ML}(mm^4) ***Age: p < 0.001*** ***CKD: p < 0.001*** ***Age x CKD: p < 0.05***	0.13 ± 0.01	0.13 ± 0.01	0.18 ± 0.01	0.14 ± 0.01 p = 0.004	0.24 ± 0.01	0.17 ± 0.01 p = 0.001
C ***Age: p < 0.001*** CKD: p > 0.05 Age x CKD: p > 0.05	0.66 ± 0.02	0.67 ± 0.01	0.73 ± 0.01	0.72 ± 0.01	0.81 ± 0.01	0.79 ± 0.02
pMOI ***Age: p < 0.001*** ***CKD: p < 0.001*** Age x CKD: p > 0.05	0.45 ± 0.02	0.40 ± 0.02	0.54 ± 0.04	0.43 ± 0.02 p = 0.004	0.68 ± 0.03	0.53 ± 0.04 p = 0.001

Data are presented as mean +/- standard error of the mean. P-values for main effects of age and CKD as well as their interaction are reported in the left column. P-values elsewhere are for comparisons between CKD and sham at the same age.

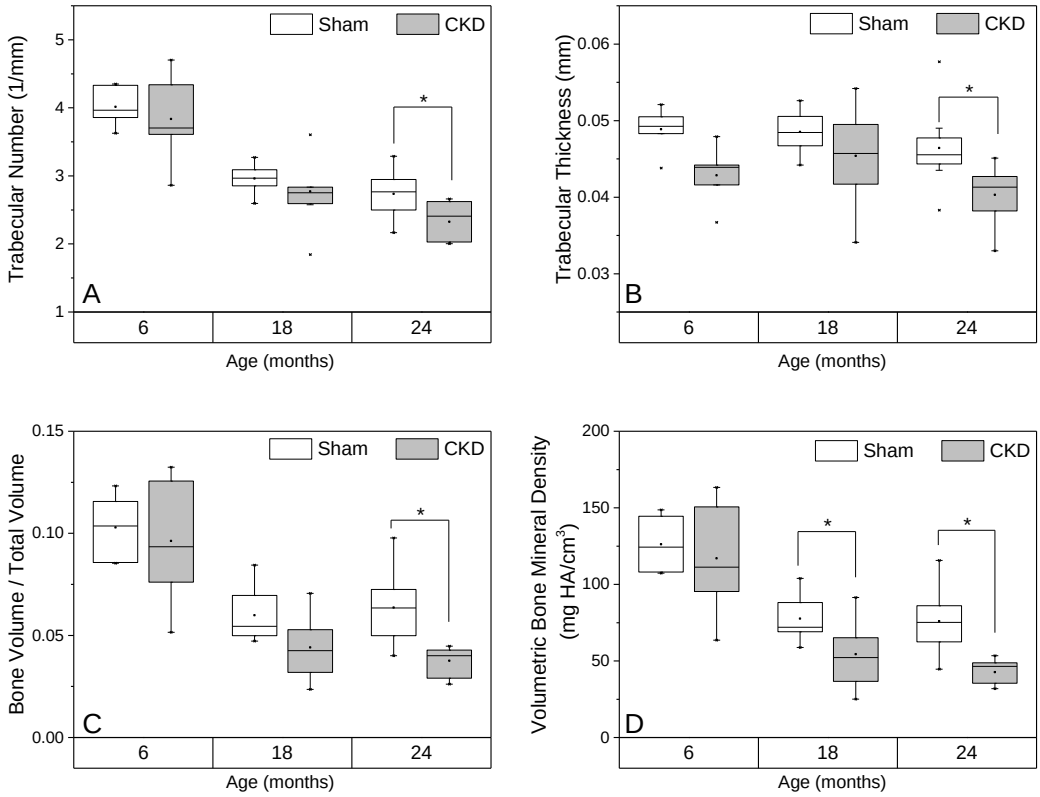

Figure 6-3: Trabecular microarchitecture is diminished by aging and CKD. Trabecular microarchitecture is diminished by both aging and CKD. Reduced trabecular microarchitecture with CKD compared with sham emerges in middle-age or old age for all measures.

Table 6-2: Trabecular microarchitecture from microCT

	6 mo		18 mo		24 mo	
	Sham	*CKD*	*Sham*	*CKD*	*Sham*	*CKD*
BV/TV (%) ***Age: p < 0.001*** ***CKD: p = 0.001*** Age x CKD: p > 0.05	0.10 ± 0.0068	0.096 ± 0.011	0.060 ± 0.0047	0.046 ± 0.0051 p = 0.034	0.064 ± 0.0065	0.038 ± 0.0027 p = 0.002
Conn.D (1/mm^3) ***Age: p < 0.001*** CKD: p > 0.05 Age x CKD: p > 0.05	54.24 ± 6.14	69.3 ± 13.1	20.35 ± 4.11	17.65 ± 6.23	28.36 ± 5.48	22.98 ± 2.49
Tb.N (1/mm) ***Age: p < 0.001*** ***CKD: p = 0.025*** Age x CKD: p > 0.05	4.02 ± 0.12	3.84 ± 0.22	2.96 ± 0.074	2.88 ± 0.11	2.74 ± 0.13	2.33 ± 0.11 p = 0.012
Tb.Sp (mm) ***Age: p < 0.001*** ***CKD: p = 0.017*** Age x CKD: p > 0.05	0.24 ± 0.0083	0.26 ± 0.017	0.34 ± 0.0090	0.35 ± 0.013	0.37 ± 0.020	0.44 ± 0.022 p = 0.009
Tb.Th (mm) ***Age: p = 0.049*** ***CKD: p = 0.001*** Age x CKD: p > 0.05	0.049 ± 0.0012	0.043 ± 0.0013 p = 0.018	0.049 ± 0.001	0.046 ± 0.0019	0.046 ± 0.0019	0.040 ± 0.0015 p = 0.010
vBMD (mg HA/cm^3) ***Age: p < 0.001*** ***CKD: p < 0.001*** Age x CKD: p > 0.05	126.19 ± 7.79	117.00 ± 13.01	77.61 ± 5.16	57.67 ± 6.75 p = 0.013	75.97 ± 7.58	42.71 ± 3.03 p < 0.001

Data are presented as mean +/- standard error of the mean. P-values for main effects of age and CKD as well as their interaction are reported in the left column. P-values elsewhere are for comparisons between CKD and sham at the same age.

CKD also affected cortical and trabecular microarchitecture. CKD significantly decreased cortical BV/TV, BA/TA, Ct.Th, TMD, I_{mL}, and pMOI, and increased Ct.Po. Of all cortical microarchitecture measures, only I_{mL} had a significant interaction between CKD and aging. CKD significantly decreased trabecular BV/TV, Tb.N, Tb.Th, vBMD, and increased Tb.Sp.

Microarchitecture was compared between CKD and sham at each age. We report comparisons that were smaller than the adjusted alpha of p = 0.05/3 = 0.017, but all p-values lower than 0.05 are shown in Tables 6-1 and 6-2. Changes to cortical microarchitecture emerged at either 6 months or 18 months for each measure. BA/TA was lower for CKD *vs* sham at 18 months (-8.79%, p = 0.004) and 24 months (-13.6%, p < 0.001). Ct.Th was also lower for CKD *vs* sham at 18 months (-11.47%, p = 0.001) and 24 months (-

17.9%, $p < 0.001$). TMD was reduced for CKD *vs* sham at 6 months (-2.35%, $p = 0.013$) and 24 months (-2.11%, $p = 0.017$). Ct.Po increased for CKD *vs* sham at 6 months (+14.49%, $p = 0.006$) and 18 months (+15.2%, $p = 0.004$). Femurs had smaller I_{ML} and pMOI for CKD *vs* sham at 18 months and 24 months. I_{mL} decreased in CKD *vs* sham at 18 months (-22.48%, $p = 0.004$) and 24 months (-27.18%, $p = 0.001$). pMOI was also lower for CKD *vs* sham at 18 months (-20.01%, $p = 0.004$) and 24 months (-21.67%, $p = 0.001$). Trabecular microarchitecture was mostly diminished in old mice. BV/TV was reduced by 40.9% ($p = 0.001$) at 24 months for CKD *vs* sham. Tb.N and Tb.Th were also lower at 24 months for CKD *vs* sham, by 15.0% ($p = 0.012$) and 13.1% ($p = 0.010$), respectively. Tb.Sp increased for CKD vs sham at 24 months (+19.1%, $p = 0.009$). vBMD was the only measure to significantly affect trabecular properties for both middle-age and old mice with CKD. At 18 months and 24 months, vBMD was decreased by 25.7% ($p = 0.013$) and 44.4% ($p < 0.001$) for CKD vs sham, respectively.

6.3.3 Whole bone mechanical and material properties

Whole bone properties were affected by aging and CKD (Table 6-3, Figure 6-4). Aging significantly reduced stiffness, yield load, displacement at yield, energy at yield, maximum load, energy at maximum load, and fracture load. Aging also significantly reduced modulus, yield stress, and ultimate stress, but did not affect toughness.

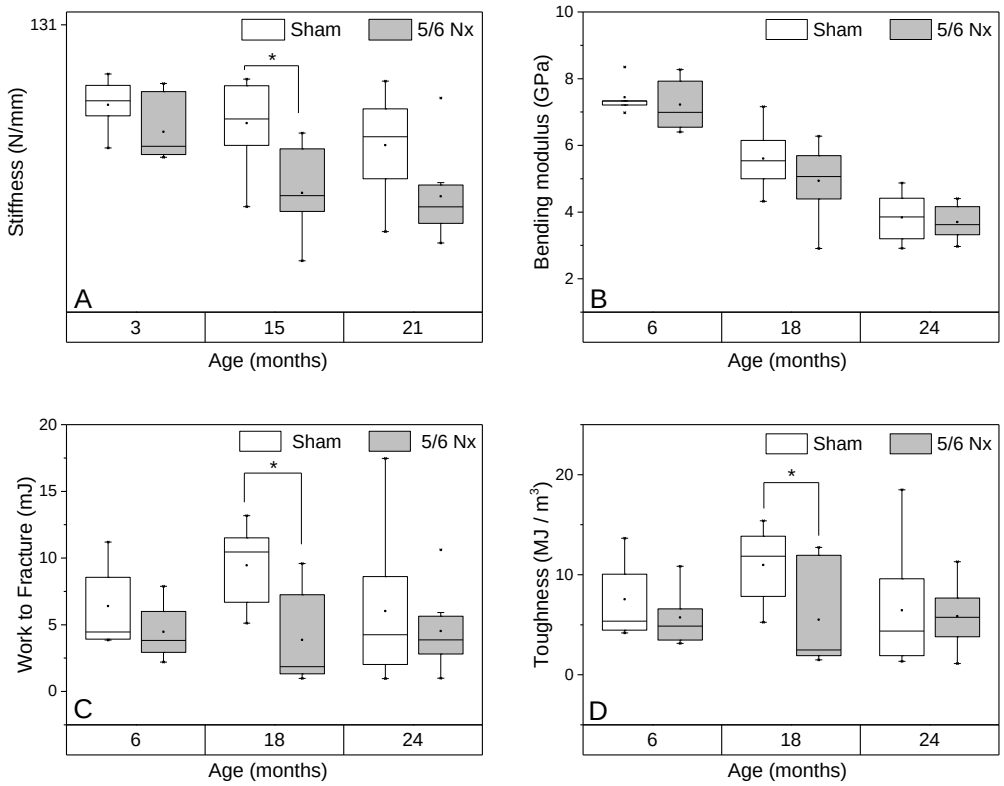

Figure 6-4: Whole bone mechanical and material properties are diminished by aging and CKD. Stiffness (A) from three-point bending is significantly reduced with aging and CKD, but modulus (B) is only diminished with aging. There is a trend of lower modulus at middle-age for CKD *vs* sham ($p = 0.091$). However, work to fracture and toughness (C-D) are more influenced by CKD than aging. Both work to fracture and toughness are significantly reduced at middle-age for CKD *vs* sham.

Table 6-3: Whole-bone mechanical and material properties from three-point bending

	6 mo		18 mo		24 mo	
	Sham	*CKD*	*Sham*	*CKD*	*Sham*	*CKD*
Modulus (GPa) ***Age: p < 0.001*** CKD: p > 0.05 Age x CKD: p > 0.05	7.44 ± 2.37	7.22 ± 0.26	5.606 ± 0.316	4.938 ± 0.355	3.841 ± 0.261	3.70 ± 0.185
Yield Stress (MPa) ***Age: p < 0.001*** CKD: p > 0.05 Age x CKD: p > 0.05	132.10 ± 10.70	127.04 ± 4.74	82.12 ± 6.55	76.20 ± 10.10	66.96 ± 7.20	65.87 ± 4.83
Ultimate Stress (MPa) ***Age: p < 0.001*** CKD: p > 0.05 Age x CKD: p > 0.05	163.12 ± 3.55	154.31 ± 3.88	110.23 ± 3.62	111.98 ± 6.53	97.41 ± 5.99	90.50 ± 4.81
Toughness (MJ/m^3) Age: p > 0.05 CKD: p = 0.053 Age x CKD: p > 0.05	7.54 ± 1.86	5.72 ± 0.99	10.97 ± 1.29	5.51 ± 1.73 p = 0.013	6.45 ± 2.09	5.86 ± 1.10
Stiffness (N/mm) ***Age: p < 0.01*** ***CKD: p < 0.001*** Age x CKD: p > 0.05	99.21 ± 5.11	88.54 ± 4.68	91.90 ± 6.04	64.28 ± 6.32 p = 0.002	83.19 ± 6.86	62.88 ± 6.25 p = 0.021
Yield Load (N) ***Age: p < 0.001*** ***CKD: p < 0.05*** Age x CKD: p > 0.05	14.26 ± 1.50	12.54 ± 0.93	9.72 ± 0.66	7.26 ± 1.02	9.50 ± 1.21	7.60 ± 0.89
Displacement at Yield (mm) ***Age: p < 0.05*** CKD: p > 0.05 Age x CKD: p > 0.05	0.16 ± 0.01	0.15 ± 0.01	0.12 ± 0.01	0.12 ± 0.02	0.13 ± 0.01	0.13 ± 0.01
Energy at Yield (mJ) ***Age: p < 0.001*** CKD: p > 0.05 Age x CKD: p > 0.05	1.25 ± 0.21	1.08 ± 0.12	0.65 ± 0.08	0.55 ± 0.11	0.71 ± 0.15	0.60 ± 0.12
Post-Yield Displacement (mm) Age: p > 0.05 CKD: p > 0.05 Age x CKD: p > 0.05	0.34 ± 0.10	0.26 ± 0.06	1.04 ± 0.20	0.54 ± 0.23 p = 0.006	0.48 ± 0.12	0.51 ± 0.19
Max Load (N) ***Age: p < 0.001*** ***CKD: p < 0.01*** Age x CKD: p > 0.05	17.46 ± 0.54	15.16 ± 0.80	13.26 ± 0.82	10.71 ± 0.82 p = 0.048	13.99 ± 1.42	10.23± 0.67 p = 0.006
Displacement at Max Load (mm) Age: p > 0.05 CKD: p > 0.05 Age x CKD: p > 0.05	0.27 ± 0.013	0.26 ± 0.0063	0.31 ± 0.027	0.24 ± 0.019	0.31 ± 0.029	0.30 ± 0.036

Energy at Max Load (mJ) Age: p > 0.05 ***CKD: p < 0.01*** Age x CKD: p > 0.05	3.14 ± 0.20	2.61 ± 0.23	2.88 ± 0.32	1.58 ± 0.20 p = 0.003	2.91 ± 0.45	2.05 ± 0.30 p = 0.050
Fracture Load (N) ***Age: p < 0.05*** CKD: p > 0.05 Age x CKD: p > 0.05	13.59 ± 1.80	12.84 ± 1.10	6.97 ± 1.00	8.48 ± 1.35	10.63 ± 1.86	8.12 ± 0.93
Displacement at Fracture (mm) Age: p > 0.05 CKD: p > 0.05 Age x CKD: p > 0.05	0.50 ± 0.10	0.41 ± 0.07	1.16 ± 0.20	0.66± 0.23 p = 0.010	0.64 ± 0.19	0.62 ± 0.12
Work to Fracture (mJ) Age: p > 0.05 ***CKD: p < 0.01*** Age x CKD: p > 0.05	6.40 ± 1.48	4.47 ± 0.74	9.45 ± 1.04	3.87 ± 1.22 p = 0.003	6.02 ± 1.96	4.53 ± 1.03

Data are presented as mean +/- standard error of the mean. P-values for main effects of age and CKD as well as their interaction are reported in the left column. P-values elsewhere are for comparisons between CKD and sham at the same age.

CKD significantly reduced stiffness, yield load, maximum load, energy at maximum load, and work to fracture. The effect of CKD on toughness was borderline significant, with p = 0.053. CKD and aging did not have significant interactions for any measures.

Comparisons between sham and CKD at each age (critical alpha = 0.05 / 3 = 0.0167) show that many measures are diminished with CKD at 18 months of age. Stiffness was reduced by 30.1% (p = 0.002) for CKD *vs* sham. Modulus, the geometry-independent analog of stiffness, was not significantly reduced with CKD at any age, but demonstrated a trend towards lower modulus for CKD *vs* sham at 18 months (-11.9%, p = 0.091). Post-yield displacement and displacement at fracture were also reduced at 18 months for CKD *vs* sham by 48.8% (p = 0.006) and 43.5% (p = 0.003), respectively. Work to fracture was lower at 18 months for CKD *vs* sham (-59.0%, p = 0.003). Toughness, the geometry-independent analog of work to fracture, was also significantly reduced at 18 months for CKD vs sham (-9.1%, p = 0.013). The only measure decreased for CKD *vs* sham at 24 months was maximum load, which was decreased by 26.9% (p = 0.006).

6.3.4 3D osteocyte lacunar geometries

Osteocyte lacunar geometries were segmented from 2D confocal z-stacks and reconstructed into 3D lacunae. Images included 53 – 194 lacunae. Osteocyte lacunar geometries changed with aging (Table 6-4, Figure 6-5). The main effect of age reduced lacunar volume and surface area, and increased lacunar sphericity. Closest center of mass and span theta did not change with age. There was not a main effect of CKD for any osteocyte lacunar geometric measure. However, aging and CKD had a significant interaction for lacunar sphericity.

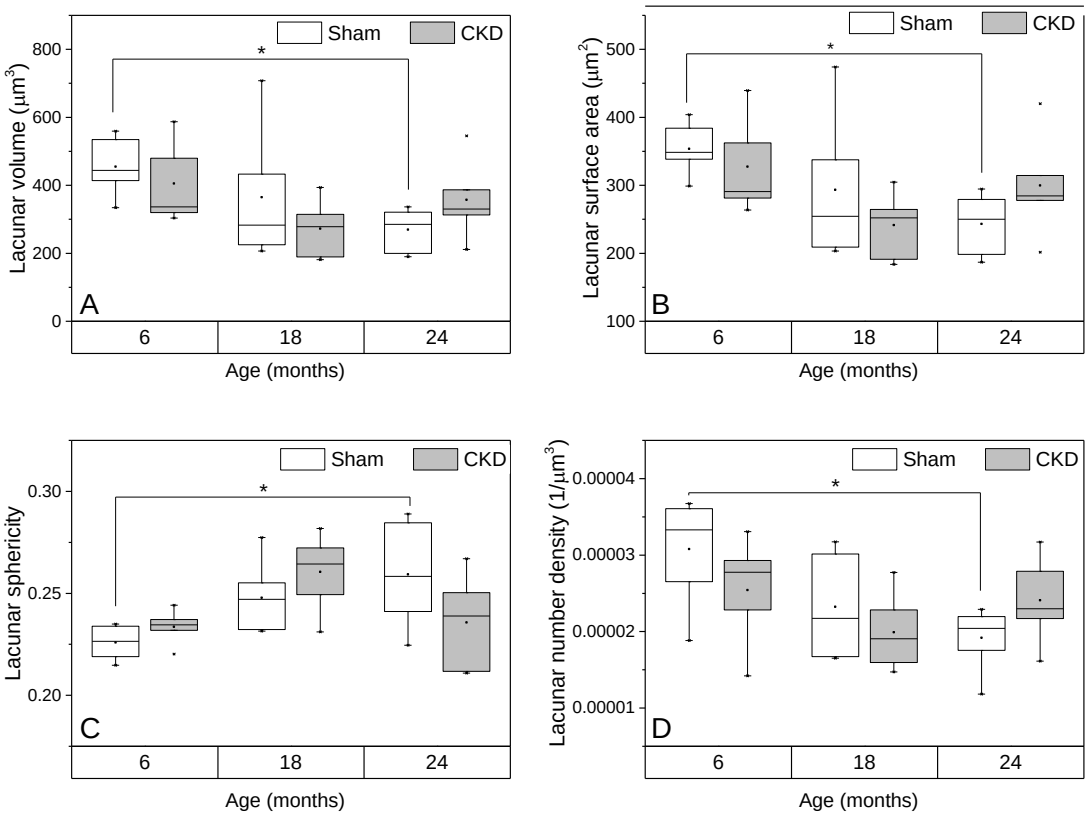

Figure 6-5: 3D osteocyte lacunar geometries change with age in sham but not CKD for mouse cortical bone. Osteocyte lacunae become smaller (A-B), more spherical (C), and sparser (D) with increasing age for sham mice. These age-related changes are not seen in CKD.

Table 6-4: 3D osteocyte lacunar geometries from confocal laser scanning microscopy

	6 mo		18 mo		24 mo	
	Sham	*CKD*	*Sham*	*CKD*	*Sham*	*CKD*
Lacunar volume (μm^3) ***Age: p = 0.023*** CKD: p > 0.001 Age x CKD: p > 0.05	454.9 ± 34.2	405.5 ± 55.2	365.1 ± 66.1	272.7 ± 33.4 p = 0.046[a]	269.7 ± 26.2 p = 0.007[a]	357.5 ± 54.9
Lacunar surface area (μm^2) ***Age: p = 0.016*** CKD: p > 0.05 Age x CKD: p > 0.05	353.7 ± 15.2	327.5 ± 32.6	293.5 ± 36.2 p = 0.033[a]	241.4 ± 19.2	243.3 ± 18.6 p = 0.006[a]	299.7 ± 39.4
Lacunar sphericity ***Age: p = 0.008*** CKD: p > 0.05 ***Age x CKD: p = 0.046***	0.23 ± 0.00	0.24 ± 0.00	0.25 ± 0.01 p = 0.024[a]	0.26 ± 0.01	0.26 ± 0.01 p = 0.004[a] p = 0.022[c]	0.24 ± 0.01 p = 0.036[b]
Closest center of mass (µm) Age: p > 0.05 CKD: p > 0.05 Age x CKD: p > 0.05	19.89 ± 0.37	20.27 ± 0.48	20.00 ± 0.50	20.02 ± 0.42	21.23 ± 0.54 p = 0.049[a]	20.52 ± 0.52
Span theta (degrees) Age: p > 0.05 CKD: p > 0.05 Age x CKD: p > 0.05	11.51 ± 1.73	11.18 ± 0.65	12.95 ± 1.43	12.00 ± 0.80	11.71 ± 0.97	13.84 ± 1.86
Lacunar number density ($1/\mu m^3$) ***Age: p = 0.022*** CKD: p > 0.05 Age x CKD: p > 0.05	3.06E-5 ± 0.28E-5	2.50E-5 ± 0.31E-5	2.32E-5 ± 0.24E-5	1.97E-5 ± 0.19E-5	1.92E-5 ± 0.16E-5 p = 0.002[a]	2.40E-5 ± 0.26E-5

Data are presented as mean +/- standard error of the mean. P-values with [a] subscript are for comparisons with 6 months within the same sham or CKD condition. P-values with a [b] subscript are between the sham and CKD at the same age. P-values with a [c] subscript are for comparisons with 18 months within the same sham or CKD or condition.

Simple effects comparisons were made between sham and CKD mice at the same age, and between ages within sham and CKD (critical alpha = 0.05/9 = 0.006). Sham mice had increasingly smaller and more spherical lacunae with age. Compared with 6 month sham mice, 24 month sham mice had decreased surface area (-31.2%, p = 0.006), decreased lacunar density (-37.7%, p =0.002), and increased sphericity (+14.8%, p = 0.004). There was also trend of decreased lacunar volume from 6 month sham to 24 month sham (-40.7%, p = 0.007). No comparisons between ages within CKD, or between sham and CKD within each age

were significant at less than p = 0.01. However, there was a trend of reduced lacunar volume from 6 months to 18 months for mice with CKD (-32.7%, p = 0.046). There was also a trend towards less sphericity (*i.e.,* more oblong shape) for 24 month old mice with CKD *vs* sham (-7.7%, p = 0.049).

6.3.5 Site-matched assessment of Raman chemistry and nanoindentation modulus

Reduced modulus from nanoindentation decreased with advancing age, but was not significantly different with CKD (Table 6-5, Figure 6-6). However, a trend was observed of reduced E_r in middle-age mice (-6.85%, p = 0.062). Microscale bone chemistry from Raman spectroscopy (mineral:matrix, carbonate:phosphate, crystallinity) did not significantly change with either age or CKD. While mean mineral:matrix is higher in CKD than sham at 18 months, and lower in CKD compared with sham at 24 months, fitted means from ANOVA models for these groups do not show significant differences between sham and CKD at either age.

Table 6-5: Mean microscale material properties from nanoindentation and Raman spectroscopy

	6 mo		18 mo		24 mo	
	Sham	*CKD*	*Sham*	*CKD*	*Sham*	*CKD*
E_r (GPa) ***Age: p = 0.006*** CKD: p > 0.05 Age x CKD: p > 0.05	29.16 ± 0.59	29.30 ± 0.58	28.99 ± 0.49	27.00 ± 0.87	26.46 ± 0.92	26.70 ± 0.96
ν_1 phosphate: (proline+hydroxyproline) Age: p > 0.05 CKD: p > 0.05 Age x CKD: p > 0.05	19.17 ± 3.69	17.04 ± 2.96	20.21 ± 1.74	28.04 ± 6.69	21.34 ± 3.71	14.38 ± 1.45
Carbonate:phosphate Age: p > 0.05 CKD: p > 0.05 Age x CKD: p > 0.05	0.09 ± 0.01	0.10 ± 0.01	0.10 ± 0.01	0.10 ± 0.01	0.11 ± 0.01	0.10 ± 0.01
Crystallinity Age: p > 0.05 CKD: p > 0.05 Age x CKD: p > 0.05	0.058 ± 0.001	0.058 ± 0.001	0.057 ± 0.000	0.058 ± 0.001	0.056 ± 0.000	0.058 ± 0.001

Data are presented as mean +/- standard error of the mean. P-values for main effects of age and CKD as well as their interaction are reported in the left column. P-values elsewhere are for comparisons between CKD and sham at the same age.

Microscale bone heterogeneity, as measured by standard deviation from each sample, changed with age and also CKD (Table 6-6, Figure 6-6). Heterogeneity of E_r was significantly increased with age. While there was not a significant main effect of CKD on E_r, 18 month old mice with CKD had significantly lower standard deviation of nanoindentation modulus (-19.7%, p = 0.013) compared with their sham counterparts. There was also a trend of diminished heterogeneity in crystallinity for 18 month old mice with CKD compared with sham (-28.1%, p = 0.040).

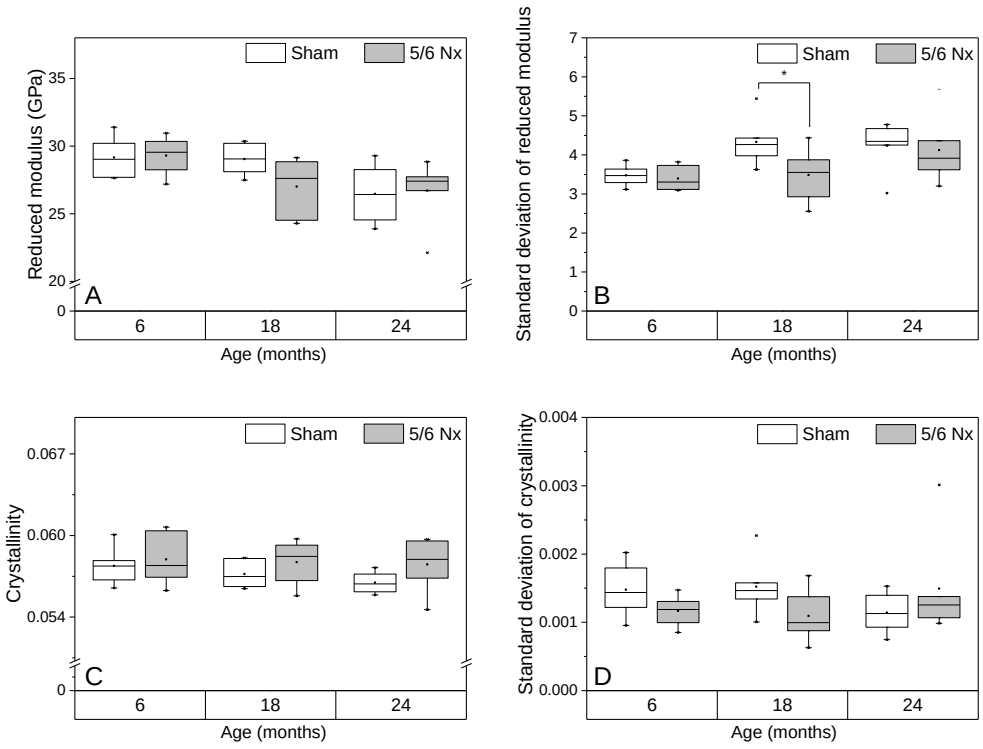

Figure 6-6: Microscale bone material changes in CKD. Microscale bone material properties change in CKD. A) Reduced modulus from nanoindentation may be lower in middle-age mice with CKD *vs* sham (p = 0.062). B) The heterogeneity of reduced modulus is significantly lower for middle-age mice with CKD *vs* sham. C) Mean crystallinity from Raman spectroscopy is not different between CKD and sham at any age, but D) heterogeneity of crystallinity may be reduced at middle-age for CKD *vs* sham (p = 0.040).

Table 6-6: Standard deviations of microscale material properties from nanoindentation and Raman spectroscopy

	6 mo		18 mo		24 mo	
	Sham	*CKD*	*Sham*	*CKD*	*Sham*	*CKD*
E_r (GPa) ***Age: p = 0.025*** CKD: p > 0.05 Age x CKD: p > 0.05	3.474 ± 0.108	3.395 ± 0.128	4.334 ± 0.252	3.482 ± 0.278 p = 0.014	4.235 ± 0.258	4.121 ± 0.359
v_1 phosphate: (proline+hydroxyproline) Age: p > 0.05 CKD: p > 0.05 Age x CKD: p > 0.05	10.79 ± 2.83	11.04 ± 3.38	8.87 ± 1.05	19.53 ± 6.73	15.46 ± 5.12	5.183 ± 0.819
Carbonate:phosphate Age: p > 0.05 ***CKD: p = 0.046*** Age x CKD: p > 0.05	0.011 ± 0.001	0.012 ± 0.001	0.009 ± 0.001	0.011 ± 0.002	0.0102± 0.001	0.013 ± 0.002
Crystallinity Age: p > 0.05 CKD: p > 0.05 Age x CKD: p > 0.05	0.0015 ± 0.0002	0.0012 ± 0.0001	0.0015 ± 0.0002	0.0011 ± 0.0002 p = 0.040	0.0011 ± 0.0001	0.0015 ± 0.0003

Data are presented as mean +/- standard error of the mean. P-values for main effects of age and CKD as well as their interaction are reported in the left column. P-values elsewhere are for comparisons between CKD and sham at the same age.

Multiple linear regression (MLR) was performed to assess whether changes to microscale material properties influence whole bone material properties (toughness, modulus, ultimate stress from three-point bending). The best-fit MLR model for toughness included nanoindentation modulus, standard deviation of crystallinity, CKD status, and the interaction of crystallinity and CKD status (r^2 adjusted = 30.4%; CKD: Toughness = 28.70 – 0.804*E_r – 517*stdev(crystallinity); Sham: Toughness = 22.10 – 0.805*E_r + 6872*stdev(crystallinity)). The best-fit MLR model for modulus included the terms of age, carbonate:phosphate, and the interaction of mineral:matrix and CKD (r^2 adjusted = 86.75%, CKD: Modulus = 7.530 – 0.1983*Age + 11.38*carbonate:phosphate – 0.00901*mineral:matrix; Sham: Modulus = 7.530 – 0.1983*Age + 11.38*carbonate:phosphate + 0.00901*mineral:matrix). The best-fit MLR model for ultimate stress included just age and crystallinity (r2 adjusted = 84.0%, Ultimate stress = 43.8 – 3.685*Age + 2366*crystallinity).

6.3.6 High performance liquid chromatography

One outlier (value greater than 3 standard deviations of the mean) was excluded from the 24 month old CKD group for the LP analysis. The crosslinks HP, LP, and pentosidine had higher means with increasing age (Table 6-7, Figure 6-7). However, the main effects of age and CKD were not significant for HP, LP, or pentosidine.

In comparing crosslink concentrations between sham and CKD at each age, there were no significant differences defined by a critical alpha of 0.0167. However, there were trends towards reduced HP for CKD *vs* sham at 24 months (-22.9%, p = 0.049), and reduced LP for CKD vs sham at 6 months (-20.7%, p = 0.056).

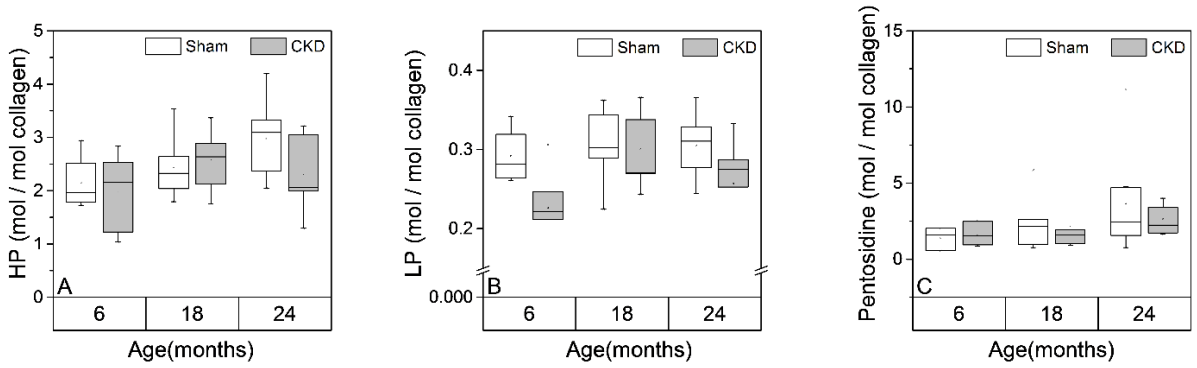

Figure 6-7: Enzymatic and non-enzymatic crosslinks are not significantly reduced by aging or CKD. Mature enzymatic crosslinks (HP and LP, A-B) and pentosidine (C) are not significantly altered by aging or CKD. However, there was a trend of lowered HP for 24 month old CKD *vs* sham (p = 0.049), as well as a trend of lowered LP for 6 month old CKD *vs* sham (p = 0.056).

Table 6-7: Collagen crosslinks from high performance liquid chromatography

	6 mo		18 mo		24 mo	
	Sham	*CKD*	*Sham*	*CKD*	*Sham*	*CKD*
HP (mol / mol collagen) Age: p > 0.05 CKD: p > 0.05 Age x CKD: p > 0.05	2.17 ± 0.39	2.15 ± 0.28	2.44 ± 0.25	2.57 ± 0.19	2.97 ± 0.25	2.29 ± 0.25 p = 0.049
LP (mol / mol collagen) Age: p > 0.05 CKD: p = 0.056 Age x CKD: p > 0.05	0.29 ± 0.02	0.23 ± 0.02	0.30 ± 0.02	0.30 ± 0.02	0.31 ± 0.01	0.28 ± 0.01
Pentosidine (mol / mol collagen) Age: p > 0.05 CKD: p > 0.05 Age x CKD: p > 0.05	1.39 ± 0.43	1.57 ± 0.26	2.42 ± 0.75	2.11 ± 0.53	2.59 ± 0.59	2.62 ± 0.35

Data are presented as mean +/- standard error of the mean. P-values for main effects of age and CKD as well as their interaction are reported in the left column. P-values elsewhere are for comparisons between CKD and sham at the same age.

6.4 Discussion

The purpose of this study was to evaluate how bone quality changes in CKD *via* 5/6 Nx alongside aging. We assessed changes to bone quality from the microscale to the whole bone. We also considered the effects of aging and CKD on mineral and collagen, as well as on the spatial heterogeneity of tissue-scale material properties. Our results demonstrate that bone quality is reduced with aging and also CKD, and that for most measures bone quality is lowest for the combination of old age and CKD.

Aging was expected to reduce cortical and trabecular microarchitecture, whole bone mechanical and material properties, and microscale material properties. The decreased cortical and trabecular microarchitecture with age was consistent with previous work characterizing bone loss with age in male C57Bl/6 mice [Halloran *et al.*, 2002]. Diminished whole-bone mechanical properties (*e.g.*, stiffness) with age were somewhat inconsistent with prior work [Ferguson *et al.*, 2003]. While both studies had similar results with respect to age for yield properties (*e.g.*, load at yield, energy at yield), there were discrepancies between the two studies with respect to properties at the maximum and fracture loads. In our study, maximum load, energy to maximum load, and stiffness were highest in 6 month old mice and decreased

with increasing age. Work to fracture was highest in 18 month old mice. In the earlier work, properties at max load and stiffness peaked at 12 months of age and decreased thereafter. Work to fracture was highest at approximately 6 months of age and then decreased [Ferguson *et al.,* 2003]. There are several possible reasons for discrepancies between these cohorts of mice. More than a decade of genetic drift could change bone properties for C57Bl/6 mice. More likely, however, is that the current study subjected mice to two sham surgeries, which would be expected to increase physiologic stress and lower physical activity. Thus, the peak bone properties reported in the earlier study with healthy mice that did not undergo experimental procedures may not correspond with our observations.

Our results for aging mice without CKD from microscale material assessments were in partial agreement with an earlier study of 5 month and 19 month male C57Bl/6 mice [Raghavan *et al.,* 2012]. Raghavan and coworkers reported that 19 month mice had higher mineral:matrix, carbonate:phosphate, and crystallinity than 5 month mice, but did not have changes to modulus from nanoindentation [Raghavan *et al.*, 2008]. In our study, we found that mean mineral:matrix and carbonate:phosphate increased with aging in sham mice, but we did not see increased crystallinity with age. We also found that reduced modulus from nanoindentation was lower with increased age. There were important differences between the two studies. Raghavan *et al* studied the surface of the mouse femur at five locations longitudinally, while our study performed maps spanning the midshaft cortical femur from endocortical to periosteal surfaces, surveying both mature and newly formed tissue. Lastly, we did not see changes to either enzymatic or non-enzymatic (pentosidine) crosslinking with age, as have been reported in other studies [Nyman *et al.,* 2006; Wang *et al.,* 2002]. Despite some differences from our work and previous studies, our results are generally in agreement with those of earlier efforts that bone quality at the whole bone and microscale are reduced with aging.

CKD was confirmed with increased serum BUN and phosphate, and decreased urine BUN and calcium. CKD was also seen to reduce bone quality. Cortical microarchitecture was diminished with CKD at either 6 months or 18 months for all measures. Meanwhile, most trabecular bone changes emerged at 24 months of age, with the exception of trabecular bone mineral density (vBMD), which was markedly

diminished at 18 months and 24 months. Our observation that bone microarchitecture was more affected in middle-age and old mice with CKD compared with young adult mice may reveal why previous work with young rodents do not consistently find diminished bone microarchitecture in CKD [Heveran *et al.,* 2016; Kadokawa *et al.,* 2011]. Specifically, the young study animals in the present study as well as previous works underwent skeletal maturation in the course of the study. Thus, the deleterious effects of CKD on microarchitecture may be masked by skeletal growth. It is possible that young mice experience CKD differently than middle-age or old mice. However, serum and urine indicators of kidney function were similar for all three ages, suggesting that the differences in microarchitecture for young mice are not explained by differences in disease severity.

CKD also affected whole bone mechanical and material properties from three-point bending. CKD reduced stiffness, max load, yield properties, and work to fracture. While whole bone material properties of modulus and ultimate stress did not change with CKD, there was a near-significant ($p = 0.053$) reduction in toughness as a main effect of CKD. Middle-age mice with CKD had significantly lower toughness than their sham counterparts. Reductions to microarchitecture and whole bone mechanical and material properties with aging and CKD were generally additive as opposed to interactive, such that old mice with CKD had the worst outcomes.

CKD was found to alter collagen as well as mineral. HP and LP, which are indicative of mature skeletal crosslinks, may be lower for 24 month old mice with CKD compared with sham. Pentosidine and was not seen to change with CKD. These findings contrast findings by Allen and coworkers that pentosidine is increased with CKD; however, their model involved a polycystic model of CKD in rats with severe disease [Allen *et al.,* 2008]. CKD was seen to alter mineral properties from microCT. Significantly diminished mineral was observed for middle age and old mice for both cortical and trabecular compartments.

At the microscale, CKD diminished modulus from nanoindentation for middle-age mice compared with sham. Mineral:matrix was not significantly different. However, it was observed for middle-age and old rats that the proline and hydroxyproline matrix peaks were often extremely small, leading to a number

of observations with very high mineral:matrix. Greater changes were observed with CKD in regards to material heterogeneity. Middle-age mice with CKD had less variable modulus and potentially less variable crystallinity compared with their sham counterparts. Multiple linear regression models were employed to test the dependence of whole bone outcomes on microscale material means and variance to whole-bone outcomes. It was observed that modulus depended predominantly on age, carbonate:phosphate, and the interaction of mineral:matrix and CKD. This model suggests that increased mineral:matrix leads to higher modulus for sham mice, and lower modulus for mice with CKD. This is consistent with mineral:matrix predominantly increasing with mineral content in sham animals, but responding to diminished collagen in CKD. Ultimate stress was explained by age and crystallinity, and was not affected by CKD. Meanwhile, the best-fit model for toughness revealed dependency on reduced modulus, the standard deviation of crystallinity, CKD status, and the interaction of CKD and standard deviation of crystallinity. Model results indicate that bone toughness is increased with increased standard deviation of heterogeneity for sham mice, but that too high of heterogeneity is detrimental for toughness for CKD. Interestingly, even though bone from middle-age mice with CKD was less tough and also had diminished heterogeneity of both reduced modulus and crystallinity, toughness was only significantly influenced by the heterogeneity of crystallinity. In this study, reduced modulus and crystallinity were poorly correlated, such that the lack of dependence of toughness on modulus was not trivially produced by multicollinearity. Importantly, as the v_1 phosphate peak that crystallinity is measured from depends on tissue orientation for Raman systems without depolarizing optics such as ours, heterogeneity of crystallinity could correspond to both variance in crystallite size and orientation. Nonetheless, these results suggest that the bone-tissue composite may derive toughness in part from the spatial arrangement and size of mineral, which are in turn potentially disrupted in CKD.

We also evaluated osteocyte lacunar morphologies in 3D in this study. For sham mice, osteocyte lacunae became smaller and more spherical with age. Lacunar number density also decreased with age, consistent with previous reports [Lai *et al.,* 2015; Vashishth *et al.,* 2000]. These age-related changes were less present with CKD. Lacunar volume may be lower in 18 month old mice with CKD compared with 6

month old mice with CKD, but mean volume was not decreased from 18 to 24 months. At 24 months, lacunae may be less spherical for CKD *vs* sham. Osteocyte lacunae number densities also did not decreased with age in CKD, though there was not significantly greater density of lacunae at 24 months for CKD *vs* sham. Our results suggest that perilacunar remodeling may change with aging, and that relationships between aging and perilacunar remodeling could be altered in CKD. Perilacunar remodeling has been shown to contribute to maintenance of bone quality and fracture resistance through replacement of bone tissue local to osteocytes [Tang *et al.,* 2012; Gardinier *et al.,* 2016]. This mechanism is also important for systemic calcium homeostasis, as the surface area of bone accessible for calcium resorption through the lacunar-canalicular system is immense in comparison to the periosteal and endocortical surfaces [Schaffler *et al.,* 2014]. Changes in PLR with aging could occur for a number of reasons, including changing mineral metabolism with aging [Orwoll *et al.,* 2009, Tsai *et al.,* 1984], compensation for decreased structural competence of bone, or potentially osteocyte senescence, which increases prevalence with age and is associated with osteocytic expression of toxic factors [Farr *et al.,* 2016]. The similar osteocyte lacunae across ages in CKD suggests that systemic demand for calcium may influence perilacunar remodeling more than aging alone. The osteocyte is known to participate in the pathophysiology of CKD through FGF23 expression, which interacts with vitamin D and PTH to influence bone turnover and systemic mineral homeostasis [Stubbs *et al.,* 2014; Komaba *et al.,* 2010]. Thus, an active role for osteocytes in liberating local mineral in CKD and consequently changing bone material is plausible. Determination of why osteocyte lacunar geometries change differently in aging with and without CKD is beyond the scope of the present work, and requires additional mechanistic study. However, these results suggest that the osteocyte is differently participating in local bone quality regulation in health and CKD. Bone material changes occurring along the expansive lacunar-canalicular system can impact whole-bone structural integrity and fracture resistance, thus changes to perilacunar bone quality in CKD merits further investigation [Fowler *et al.,* 2016; Tang *et al.,* 2012].

There were several limitations to this study. Mice from this study did not receive fluorochrome labels and thus measurement of mineral apposition rate through quantitative histomorphometry was not

possible. Additionally, the systemic effects of 5/6 Nx at different ages in C57Bl/6 mice have not been fully described. Another limitation is that toughness was evaluated from unnotched femurs in three-point bending as the geometry-independent analog of work to fracture. Notched fracture testing prescribes the location of fracture, which reduces experimental variance, and provides an analytic solution for a fracture toughness value [Ritchie *et al.,* 2008]. However, unlike notched fracture toughness testing, where compliance is directly influenced by the notch geometry, conventional three-point bending allows calculation of elastic and yield properties.

In summary, we observed that aging and CKD together lower bone quality from the whole bone scale to the microscale, affecting both collagen and mineral. We also observed that changes to bone tissue heterogeneity at the microscale were predictive of changes to whole bone toughness. These observed changes with aging and CKD have implications for therapeutic interventions. Antiresorptive bisphosphonate therapies have been considered for use in CKD to potentially mitigate bone loss through reduction of osteoclast resorption [Allen *et al.,* 2017]. The diminished cortical and trabecular microarchitecture, decreased mature collagen crosslinks, lower cortical and trabecular mineral densities, and lowered tissue-scale material heterogeneity observed with CKD in this study are consistent with abnormalities caused by high-turnover renal osteodystrophy, and could plausible improve by reducing osteoclast-mediated turnover with bisphosphonate therapy. However, there are several potentially serious problems with administering bisphosphonates for treatment of bone quality loss in CKD. First, bisphosphonates can alter bone tissue composition and lower heterogeneity, potentially contributing to fracture-prone adynamic bone [Gourion-Arsiquaud *et al.,* 2010; Allen *et al.,* 2008; Mashiba *et al.,* 2000]. Second, bisphosphonates may not be able to correct loss of bone fracture resistance attributed to altered perilacunar remodeling in CKD. Previous work evaluated the ability of bisphosphonates to improve bone quality. Rats with high-turnover genetic polycystic kidney disease responded to treatment with zoledronic acid with lowered bone turnover and improved trabecular microarchitecture, consistent with the expected effects of an antiresorptive therapy [Moe *et al.,* 2014; Allen *et al.,* 2017]. However, cortical bone mechanical properties assessed by three-point bending were only partially improved with bisphosphonate

therapy [Moe *et al.*, 2014]. It is possible that cortical bone material experiences disruptions to perilacunar remodeling with CKD that diminishes material properties. These osteocyte-mediated bone quality changes would not be expected to change with bisphosphonate therapies, which primarily target the osteocyte. The role of the osteocyte in mediating bone quality changes in CKD is intriguing, as the osteocyte may provide new targets for therapeutic interventions aimed at maintaining fracture resistance.

Acknowledgements:

We would like to thank William Schroeder for excellent care of study animals, and William Schroeder and Ryan Clark for serum chemistry analyses.

6.5 References

1. Nickolas, T. L., Leonard, M. B., & Shane, E. (2008). Chronic kidney disease and bone fracture: a growing concern. *Kidney international*, *74*(6), 721-731.
2. Naylor, K. L., McArthur, E., Leslie, W. D., Fraser, L. A., Jamal, S. A., Cadarette, S. M., ... & Garg, A. X. (2014). The three-year incidence of fracture in chronic kidney disease. *Kidney international*, *86*(4), 810-818.
3. Heveran, C. M., Ortega, A. M., Cureton, A., Clark, R., Livingston, E. W., Bateman, T. A., ... & Ferguson, V. L. (2016). Moderate chronic kidney disease impairs bone quality in C57Bl/6J mice. *Bone*, *86*, 1-9.
4. Iwasaki, Y., Kazama, J. J., Yamato, H., Matsugaki, A., Nakano, T., & Fukagawa, M. (2015). Altered material properties are responsible for bone fragility in rats with chronic kidney injury. *Bone*, *81*, 247-254.
5. Allen, M. R., Newman, C. L., Chen, N., Granke, M., Nyman, J. S., & Moe, S. M. (2015). Changes in skeletal collagen cross-links and matrix hydration in high-and low-turnover chronic kidney disease. *Osteoporosis International*,*26*(3), 977-985.
6. Kadokawa, S., Matsumoto, T., Naito, H., & Tanaka, M. (2011). Assessment of trabecular bone architecture and intrinsic properties of cortical bone tissue in a mouse model of chronic kidney disease. *Journal of Hard Tissue Biology*,*20*(2), 79-86.
7. Boskey, A. L. (2002). Variations in bone mineral properties with age and disease. *JOURNAL OF MUSCULOSKELETAL AND NEURONAL INTERACTIONS*, *2*(6), 532-534.
8. Boskey, A. L., & Coleman, R. (2010). Aging and bone. *Journal of dental research*, *89*(12), 1333-1348.
9. Akkus, O., Polyakova-Akkus, A., Adar, F., & Schaffler, M. B. (2003). Aging of microstructural compartments in human compact bone. *Journal of Bone and Mineral Research*, *18*(6), 1012-1019.
10. Schaffler, M. B., Choi, K., & Milgrom, C. (1995). Aging and matrix microdamage accumulation in human compact bone. *Bone*, *17*(6), 521-525.
11. Wang, X., Shen, X., Li, X., & Agrawal, C. M. (2002). Age-related changes in the collagen network and toughness of bone. *Bone*, *31*(1), 1-7.
12. Riggs, B. L., Melton, L. J., Robb, R. A., Camp, J. J., Atkinson, E. J., Peterson, J. M., ... & Khosla, S. (2004). Population-based study of age and sex differences in bone volumetric density, size, geometry, and structure at different skeletal sites. *Journal of Bone and Mineral Research*, *19*(12), 1945-1954.
13. Roschger, P., Paschalis, E. P., Fratzl, P., & Klaushofer, K. (2008). Bone mineralization density distribution in health and disease. *Bone*, *42*(3), 456-466.
14. Tai, K., Dao, M., Suresh, S., Palazoglu, A., & Ortiz, C. (2007). Nanoscale heterogeneity promotes energy dissipation in bone. *Nature materials*, *6*(6), 454-462.
15. Yao, H., Dao, M., Carnelli, D., Tai, K., & Ortiz, C. (2011). Size-dependent heterogeneity benefits the mechanical performance of bone. *Journal of the Mechanics and Physics of Solids*, *59*(1), 64-74.
16. Gourion-Arsiquaud, S., Allen, M. R., Burr, D. B., Vashishth, D., Tang, S. Y., & Boskey, A. L. (2010). Bisphosphonate treatment modifies canine bone mineral and matrix properties and their heterogeneity. *Bone*, *46*(3), 666-672.
17. Allen, M. R., Gineyts, E., Leeming, D. J., Burr, D. B., & Delmas, P. D. (2008). Bisphosphonates alter trabecular bone collagen cross-linking and isomerization in beagle dog vertebra. *Osteoporosis international*, *19*(3), 329-337.

18. Mashiba, T., Hirano, T., Turner, C. H., Forwood, M. R., Johnston, C. C., & Burr, D. B. (2000). Suppressed bone turnover by bisphosphonates increases microdamage accumulation and reduces some biomechanical properties in dog rib. *Journal of Bone and Mineral Research*, *15*(4), 613-620.

19. Bouxsein, M. L., Boyd, S. K., Christiansen, B. A., Guldberg, R. E., Jepsen, K. J., & Müller, R. (2010). Guidelines for assessment of bone microstructure in rodents using micro–computed tomography. Journal of Bone and Mineral Research, 25(7), 1468-1486.

20. Jepsen, K. J., Goldstein, S. A., Kuhn, J. L., Schaffler, M. B., & Bonadio, J. (1996). Type-I collagen mutation compromises the post-yield behavior of Mov13 long bone. Journal of orthopaedic research, 14(3), 493-499.

21. Turner, C. H., & Burr, D. B. (1993). Basic biomechanical measurements of bone: a tutorial. Bone, 14(4), 595-608.

22. Burr, D. B., & Hooser, M. (1995). Alterations to the en bloc basic fuchsin staining protocol for the demonstration of microdamage produced in vivo. *Bone*, *17*(4), 431-433.

23. Bushby, A. J., Ferguson, V. L., & Boyde, A. (2004). Nanoindentation of bone: comparison of specimens tested in liquid and embedded in polymethylmethacrylate. Journal of Materials Research, 19(01), 249-259.

24. Boyde, A., Travers, R., Glorieux, F. H., & Jones, S. J. (1999). The mineralization density of iliac crest bone from children with osteogenesis imperfecta. Calcified tissue international, 64(3), 185-190.

25. Campbell, S. E., Geiss, R. H., Feller, S. A., & Ferguson, V. L. (2012). Tunable glass reference materials for quantitative backscattered electron imaging of mineralized tissues. Journal of Materials Research, 27(19), 2568-2577.

26. Rasband, W.S., ImageJ, U. S. National Institutes of Health, Bethesda, Maryland, USA, http://imagej.nih.gov/ij/, 1997-201.

27. Bank, R. A., Beekman, B., Verzijl, N., de Roos, J. A., Sakkee, A. N., & TeKoppele, J. M. (1997). Sensitive fluorimetric quantitation of pyridinium and pentosidine crosslinks in biological samples in a single high-performance liquid chromatographic run. *Journal of Chromatography B: Biomedical Sciences and Applications*, *703*(1), 37-44.

28. Oren, T. W., Botolin, S., Williams, A., Bucknell, A., & King, K. B. (2011). Arthroplasty in veterans: analysis of cartilage, bone, serum, and synovial fluid reveals differences and similarities in osteoarthritis with and without comorbid diabetes. *Journal of rehabilitation research and development*, *48*(10), 1195.

29. Bank, R. A., Jansen, E. J., Beekman, B., & te Koppele, J. M. (1996). Amino acid analysis by reverse-phase high-performance liquid chromatography: improved derivatization and detection conditions with 9-fluorenylmethyl chloroformate. *Analytical biochemistry*, *240*(2), 167-176.

30. Halloran, B. P., Ferguson, V. L., Simske, S. J., Burghardt, A., Venton, L. L., & Majumdar, S. (2002). Changes in bone structure and mass with advancing age in the male C57BL/6J mouse. *Journal of Bone and Mineral Research*, *17*(6), 1044-1050.

31. Ferguson, V. L., Ayers, R. A., Bateman, T. A., & Simske, S. J. (2003). Bone development and age-related bone loss in male C57BL/6J mice. *Bone*, *33*(3), 387-398.

32. Nyman, J. S., Roy, A., Acuna, R. L., Gayle, H. J., Reyes, M. J., Tyler, J. H., ... & Wang, X. (2006). Age-related effect on the concentration of collagen crosslinks in human osteonal and interstitial bone tissue. *Bone*, *39*(6), 1210-1217.

33. Raghavan, M., Sahar, N. D., Kohn, D. H., & Morris, M. D. (2012). Age-specific profiles of tissue-level composition and mechanical properties in murine cortical bone. *Bone*, *50*(4), 942-953.

34. Lai, X., Price, C., Modla, S., Thompson, W. R., Caplan, J., Kirn-Safran, C. B., & Wang, L. (2015). The dependences of osteocyte network on bone compartment, age, and disease. *Bone research*, *3*.

35. Vashishth, D., Verborgt, O., Divine, G., Schaffler, M. B., & Fyhrie, D. P. (2000). Decline in osteocyte lacunar density in human cortical bone is associated with accumulation of microcracks with age. *Bone*, *26*(4), 375-380.

36. Tang, S. Y., Herber, R. P., Ho, S. P., & Alliston, T. (2012). Matrix metalloproteinase–13 is required for osteocytic perilacunar remodeling and maintains bone fracture resistance. *Journal of Bone and Mineral Research*, *27*(9), 1936-1950

37. Gardinier, J. D., Al-Omaishi, S., Morris, M. D., & Kohn, D. H. (2016). PTH signaling mediates perilacunar remodeling during exercise. *Matrix Biology*, *52*, 162-175.

38. Schaffler, M. B., Cheung, W. Y., Majeska, R., & Kennedy, O. (2014). Osteocytes: master orchestrators of bone. *Calcified tissue international*, *94*(1), 5-24.

39. ORWOLL, E. S., & MEIER, D. E. (1986). Alterations in calcium, vitamin D, and parathyroid hormone physiology in normal men with aging: relationship to the development of senile osteopenia. *The Journal of Clinical Endocrinology & Metabolism*, *63*(6), 1262-1269.

40. Tsai, K. S., Heath 3rd, H., Kumar, R., & Riggs, B. L. (1984). Impaired vitamin D metabolism with aging in women. Possible role in pathogenesis of senile osteoporosis. *Journal of Clinical Investigation*, *73*(6), 1668.

41. Farr, J. N., Fraser, D. G., Wang, H., Jaehn, K., Ogrodnik, M. B., Weivoda, M. M., ... & Bonewald, L. F. (2016). Identification of senescent cells in the bone microenvironment. *Journal of Bone and Mineral Research*, *31*(11), 1920-1929.

42. Stubbs, J., Liu, S., & Quarles, L. D. (2006, December). Role of fibroblast growth factor 23 in phosphate homeostasis and pathogenesis of disordered mineral metabolism in chronic kidney disease. In *Seminars in dialysis* (Vol. 20, No. 4, pp. 302-308).

43. Komaba, H., & Fukagawa, M. (2010). FGF23–parathyroid interaction: implications in chronic kidney disease. *Kidney international*, *77*(4), 292-298.

44. Ritchie, R. O., Koester, K. J., Ionova, S., Yao, W., Lane, N. E., & Ager, J. W. (2008). Measurement of the toughness of bone: a tutorial with special reference to small animal studies. *Bone*, *43*(5), 798-812.

45. Allen, M. R., & Aref, M. W. (2017). What Animal Models Have Taught Us About the Safety and Efficacy of Bisphosphonates in Chronic Kidney Disease. *Current Osteoporosis Reports*, 1-7.

46. Moe, S. M., Chen, N. X., Newman, C. L., Gattone, V. H., Organ, J. M., Chen, X., & Allen, M. R. (2014). A comparison of calcium to zoledronic acid for improvement of cortical bone in an animal model of CKD. *Journal of Bone and Mineral Research*, *29*(4), 902-910.

7. The role of cortical bone microscale material heterogeneity in determining bone fracture toughness

Abstract

Bone fracture resistance depends on tissue-scale toughening mechanisms that resist crack formation and propagation. Bone toughness has been shown to be influenced by structural features, but the material contributions to toughness are not fully understood. Notably, observational studies report altered microscale bone tissue heterogeneity in biopsies from patients with fragility fractures compared with age-matched controls. Yet experimental evidence for relationships between whole bone fracture toughness and microscale material heterogeneity is lacking. The purpose of this study was to evaluate whether microscale heterogeneity in mechanical properties and bone chemistry is predictive of fracture toughness in a rat model of exercise and obesity. Male rats were fed a high fat diet and stratified into lean and obese groups. Within these groups, rats were randomized to exercised or sedentary conditions. Fracture toughness was evaluated for the femur. Microscale material properties, including bone chemistry from Raman spectroscopy, and reduced modulus from nanoindentation, were assessed for both lamellar and woven bone for each previously-fractured femur. Exercised rats had significantly higher fracture toughness values than sedentary rats, but obese and lean rats had similar fracture toughness values. Multiple linear regression revealed that the heterogeneity of reduced modulus from nanoindentation and mean mineral:matrix from Raman spectroscopy contribute to fracture toughness regardless of exercise or obesity status. Importantly, both of these predictive relationships with fracture toughness have a negative quadratic form, implying that moderate mineral content and moderate variance in microscale modulus are beneficial for fracture toughness.

7.1 Introduction

Bone is hierarchically structured and dynamically remodels, leading to a characteristically heterogeneous bone tissue composite. Bone structure at the microscale is known to be important to bone fracture toughness; a known toughening mechanism in bone is for cracks to deflect along relatively compliant osteonal cement lines [Koester *et al.*, 2008]. Bone material properties and their microscale spatial heterogeneity are widely thought to also be important to bone toughness, but the work supporting this theory

has been largely observational [Lloyd *et al.,* 2016]. Backscatter scanning electron microscopy studies comparing bone samples with and without fragility fractures have reported that fragile bone can have abnormal mean or variance in mineral content. Interestingly, fragile bone can have either too-low or too-high variance in microscale mineral content compared with controls. For instance, the coefficient of variance of bone mineralization was lower in iliac crest biopsies from women with vertebral fractures compared with healthy cadaveric controls [Ciarelli *et al.,* 2009]. Yet in another study of bone mineralization at the iliac crest, cadaveric trabeculae from women with osteoporotic vertebral fractures had a widen distribution of bone mineral content than healthy trabeculae [Busse *et al.,* 2009]. Increased heterogeneity in mineralization has also been reported in both trabecular and cortical bone for fracture-prone children [Tamminen *et al.,* 2014]. Though these observations suggest intriguing dependencies of bone fracture resistance on microscale material heterogeneity, the specific relationships linking tissue-scale bone variance and whole bone fracture toughness are not understood.

Limited work has evaluated how fracture toughness may depend on microscale bone material properties. Makowski and coworkers considered how bone chemistry measured from Raman spectroscopy contributes to fracture toughness in human cortical bone spanning a range of ages [Makowski *et al.,* 2015]. Heterogeneity of bone chemistry measures *(e.g.,* mineral:matrix and crystallinity) had poor correlations with fracture toughness, though principal component analysis revealed components from whole spectra that moderately predicted fracture toughness. However, fracture toughness may also depend on heterogeneity in microscale material response to loading (*e.g.,* modulus and plastic work from nanoindentation). Finite element models suggest that variance in microscale bone tissue modulus encourages energy dissipation and potentially promotes fracture toughness [Tai *et al.,* 2007; Yao *et al.,* 2011]. Yet it is not known how microscale bone mechanical properties and chemistry together influence fracture toughness. Thus, it is currently difficult to interpret how altered heterogeneity in material properties that can occur in response to age, disease, or interventions may be expected to influence bone fracture properties. The purpose of this study was to experimentally assess how fracture toughness depends on microscale bone material properties for cortical rat bone.

7.2 Methods

7.2.1 Animal model

To evaluate the contributions of material heterogeneity on fracture toughness, notched fracture toughness testing was conducted on rat femurs from a study of obesity and exercise [Song *et al.*, 2016]. Male Wistar rats were fed an ad libitum high fat diet (HFD) for 10 weeks, starting at 5 weeks of age. Within sex, obese and lean groups were defined as the highest and lowest tertiles of weight and fat gain. Obese and lean rats were randomized to exercise or sedentary controls for the last 4 weeks of HFD (n = 8 / group; N = 32). Exercised rats were treadmill running at 15 m/min, 60 min/day for 5 days/week.

7.2.2 Fracture toughness

Fracture toughness (K_c) was evaluated for notched femurs in three-point bending [Ritchie *et al.*, 2008]. Briefly, femurs were cleaned of non-osseous tissue, and both the condyles and bone proximal to the lesser trochanter were trimmed off to ensure consistent notching conditions for all bones. A custom apparatus was used to notch femurs on the posterior aspect to nominally 30% of the anterior-posterior width at the cortical midshaft. A single pass with a feather blade lubricated with 1 μm alumina slurry polish sharpened the notch. Notched femurs were sonicated to remove polishing media and then maintained in phosphate buffered saline – dampened gauze before testing.

Notched femurs were placed on a span for three-point bending such that the anterior aspect of the femur was placed up (in compression) and the notched posterior surface was placed down (in tension). The span for notched fracture testing in three-point bending should be four times the anterior-posterior width. Femur widths for this study were stratified into quintiles, and the mean of each quintile used for span length determination. Consistent with the protocol described by Ritchie *et al*, femurs were loaded at a rate of 0.001 mm/s until fracture [Ritchie *et al.*, 2008]. Following testing, the proximal half of the fractured femur was air dried and imaged *via* variable pressure SEM to identify the notch angle (Figure 7-1). The max load and initial notch angle were used to calculate the max fracture toughness [Ritchie *et al.*, 2008].

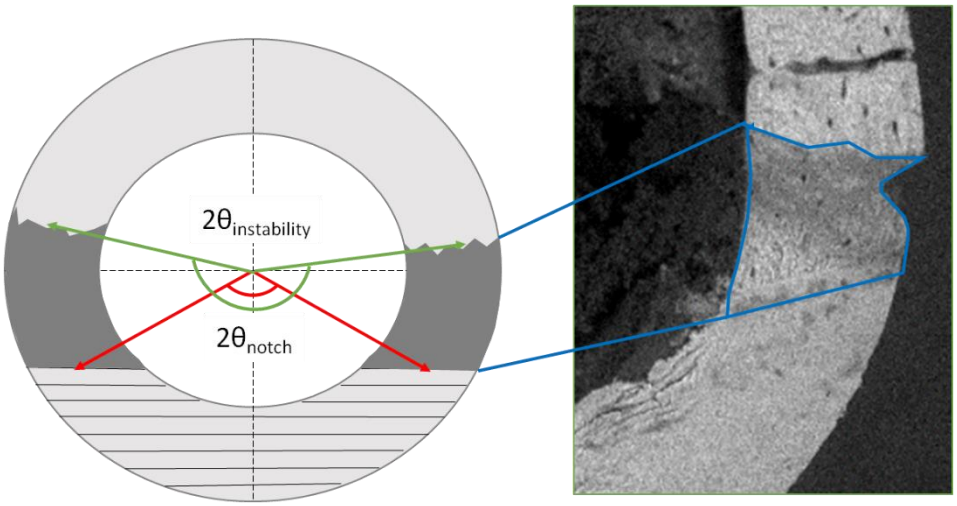

Figure 7-1: Evaluation of notch and instability angles from SEM. The SEM image on right collected by Chelsea Heveran. Figure adapted from Ritchie *et al*., Bone, 2008

7.2.3. Assessment of microscale bone heterogeneity

Following notched fracture testing, the distal half of the fractured femurs were histologically dehydrated and embedded in poly(methyl)methacrylate. The embedded transverse sections were polished to 0.1 µm finish, taking care to polish just beyond the relief of the notched surface. Samples were sonicated between polishing steps, and again after the final polishing step.

Material property heterogeneity was assessed with maps of microscale modulus from nanoindentation (Hysitron TI950). Maps of 25 points (spacing: 20 µm in x and y directions) were placed in lamellar bone and also woven bone on the medial aspect of each sample. Bone type was identified with indentation optics before mechanical testing; for each sample, lamellar bone was found on the endocortical surface while woven bone was located midway between the endocortical and periosteal surfaces. An initial parameter study revealed that variability in nanoindentation modulus was highest for indents of 300 nm in depth or less. As the root mean square error of surface roughness of a representative final polished surface was measured to be 31 nm, 300 nm was chosen as an indentation depth that both avoids surface roughness and minimizes volume averaging the measured modulus [Greenwood *et al*., 1984]. A 5 µm radius tip was thus employed to indent bone to 300 nm in depth-controlled tests, with a load function of 30s loading, 120s hold to dissipate viscoelastic energy, and 30s unload.

Bone chemistry heterogeneity was evaluated *via* Raman spectroscopy (Renishaw inVia, 785 nm laser). As with nanoindentation, maps of 25 points (spacing: 20 μm in x and y directions) were placed in lamellar and also woven bone. Raman maps were placed adjacent to previous arrays from nanoindentation, but did not spatially overlap. Raman spectra were analyzed for peak areas of v_1 phosphate (920 – 990 cm^{-1}), v_2 phosphate (410 – 480 cm^{-1}), amide III (1220 – 1295 cm^{-1}), and carbonate (1045-1110 cm^{-1}) using custom Matlab code. Mineral:matrix was evaluated as v_2 phosphate / amide III, which has been demonstrated by others to be phase-matched and thus polarization insensitive [Gamsjaeger *et al.*, 2010]. Carbonate:phosphate was assessed from carbonate / v_1 phosphate. Crystallinity, which relates to crystal size, was defined as the inverse of the full width at half-maximum intensity of the v_1 phosphate peak.

7.2.4 Data analysis

Differences between means and standard deviations of microscale properties from nanoindentation and Raman spectroscopy were evaluated with respect to the factors of bone type, obesity status, exercise status, as well as all interactions between these factors, were evaluated with ANOVA. Residuals were checked for normality and homoscedasticity. ANOVA was also employed to evaluate the effect of obesity and exercise status, as well as the interaction of obesity and exercise, on fracture toughness.

Multiple linear regression was used to assess the contributions of microscale bone properties on fracture toughness. Separate models were established for lamellar and woven bone types. Pearson's R was first checked for all variables such that highly intercorrelated terms ($R > 0.6$) were not both entered into the model. Models included second order terms of each proposed explanatory variable, as well as the interactions of each term with exercise and obesity factors. Term elimination was accomplished with a stepwise procedure. Terms were introduced back into the final model to ensure hierarchical structure. Final models were evaluated using criteria of highest adjusted correlation coefficient and lowest error.

7.3 Results

Fracture toughness (K_c) for rats fed a high-fat diet was highly variable, ranging from 5.34 MPa √m to 9.88 MPa √m. There was a significant main effect of exercise but not obesity on fracture toughness

(Table 7-1). Exercised rats had +12.0% tougher femurs than sedentary rats ($p = 0.046$). There was not a significant interaction between the factors of exercise and obesity.

Table 7.1: Fracture toughness from notched fracture testing.

	Lean		Obese	
	Exercise	*Sedentary*	*Exercise*	*Sedentary*
Fracture toughness (Kc) (MPa √m)	7.43 ± 0.36	6.71 ± 0.39	7.97 ± 0.43	7.05 ± 0.40

ObS: $p > 0.05$
ExS: $p = 0.046$
ObS x ExS: $p > 0.05$

Data are presented as mean +/- standard error of the mean. P-values for main effects of obesity status (ObS), exercise status (ExS), as well as their interaction (OSb x ExS) are reported in the left column.

Mean microscale material properties from Raman spectroscopy and nanoindentation were all significantly affected by bone type (*i.e.*, lamellar *vs* woven) (Table 7-2). Mineral:matrix was +14.4% higher ($p < 0.001$) for woven than lamellar bone. Carbonate:phosphate and crystallinity were +6.2% ($p < 0.001$) and +2.0% ($p < 0.001$) higher for lamellar compared to woven bone, respectively. Reduced modulus and plastic work were not significantly different between bone types.

Table 7.2: Mean microscale material properties for lamellar and woven bone.

	Lamellar				Woven			
	Lean		*Obese*		*Lean*		*Obese*	
	Ex	*Sed*	*Ex*	*Sed*	*Ex*	*Sed*	*Ex*	*Sed*
ν_2 phosphate : amide III **Type: p < 0.001** **ObS: p = 0.004** ExS: p > 0.05 Type x ObS: p > 0.05 Type x ExS: p > 0.05 ObS x ExS: p > 0.05 Type x ObS x ExS: p > 0.05	1.11 ± 0.04	1.06 ± 0.04	1.01 ± 0.05	0.99 ± 0.04	1.26 ± 0.03	1.22 ± 0.04	1.13 ± 0.06	1.15 ± 0.04
Carbonate : phosphate (x 10^{-2}) **Type: p < 0.001** ObS: p > 0.05 ExS: p > 0.05 **Type x ObS: p = 0.014** Type x ExS: p > 0.05 Ob x ExS: p > 0.05 Type x ObS x ExS: p > 0.05	17.78 ± 0.23	18.02 ± 0.35	17.33 ± 0.14	17.53 ± 0.38	16.36 ± 0.20	16.46 ± 0.25	16.98 ± 0.17	16.70 ± 0.20
Crystallinity (x 10^{-2}) **Type: p < 0.001** ObS: p > 0.05 ExS: p > 0.05 Type x ObS: p > 0.05 Type x ExS: p > 0.05 ObS x ExS: p > 0.05 Type x ObS x ExS: p > 0.05	5.74 ± 0.02	5.78 ± 0.02	5.77 ± 0.03	5.76 ± 0.02	5.66 ± 0.02	5.61 ± 0.02	5.66 ± 0.04	5.66 ± 0.02
Reduced modulus (GPa) Type: p > 0.05 ObS: p > 0.05 ExS: p > 0.05 Type x ObS: p > 0.05 Type x ExS: p = .081 ObS x ExS: p > 0.05 Type x ObS x ExS: p > 0.05	31.47 ± 1.70	34.15 ± 1.72	32.67 ± 1.15	31.54 ± 1.51	33.65 ± 1.98	31.10 ± 1.64	36.14 ± 1.72	32.28 ± 1.01
Plastic work (J x 10^{-11}) Type: p > 0.05 ObS: p > 0.05 ExS: p > 0.05 Type x ObS: p > 0.05 Type x ExS: p > 0.05 ObS x ExS: p > 0.05	16.16 ± 1.45	15.55 ± 0.67	15.99 ± 1.31	16.45 ± 1.32	15.24 ± 1.66	13.77 ± 0.87	15.33 ± 1.37	14.09 ± 1.60

Type x ObS x ExS:	p > 0.05

Data are presented as mean +/- standard error of the mean. P-values for main effects of bone type, obesity status (ObS), exercise status (ExS), as well as their interactions are reported in the left column.

Standard deviations were also affected by type of bone (Table 7-3). The standard deviation of mineral:matrix was +53.0% higher ($p < 0.001$) for woven versus lamellar bone. Standard deviations of carbonate:phosphate and crystallinity were +32.7% ($p < 0.001$) and +68.9% ($p < 0.001$) higher for woven versus lamellar bone, respectively. The standard deviations of reduced modulus and plastic work also significantly differed for bone type. The standard deviations of reduced modulus and plastic work were +16.3% ($p = 0.044$) and +13.4% ($p = 0.046$) more variable for woven than lamellar bone.

Table 7.3: Standard deviation in microscale material properties for lamellar and woven bone.

	Lamellar				Woven			
	Lean		*Obese*		*Lean*		*Obese*	
	Ex	*Sed*	*Ex*	*Sed*	*Ex*	*Sed*	*Ex*	*Sed*
ν_2 phosphate : amide III (x 10^{-2}) **Type: p < 0.001** ObS: p > 0.05 ExS: p > 0.05 Type x ObS: p > 0.05 Type x ExS: p > 0.05 ObS x ExS: p > 0.05 Type x ObS x ExS: p > 0.05	13.97 ± 1.44	11.49 ± 1.28	10.98 ± 0.85	19.36 ± 8.37	18.97 ± 1.33	23.00 ± 2.44	17.34 ± 2.94	19.12 ± 3.22
Carbonate : phosphate (x 10^{-4}) **Type: p < 0.001** ObS: p > 0.05 ExS: p > 0.05 Type x ObS: p > 0.05 Type x ExS: p > 0.05 ObS x ExS: p > 0.05 Type x ObS x ExS: p = 0.070	83.31 ± 7.69	71.82 ± 5.96	78.62 ± 4.55	146.20 ± 61.90	109.7 ± 10.5	113.0 ± 9.7	112.6 ± 7.0	100.5 ± 9.8
Crystallinity (x 10^{-4}) **Type: p < 0.001** ObS: p > 0.05 ExS: p > 0.05 Type x ObS: p > 0.05 Type x ExS: p > 0.05 ObS x ExS: p > 0.05 Type x ObS x ExS: p > 0.05	8.23 ± 0.83	5.37 ± 0.83	9.37 ± 2.09	9.47 ± 1.94	13.62 ± 1.26	13.21 ± 1.05	13.16 ± 1.46	12.34 ± 1.86
Reduced modulus (GPa) **Type: p = 0.044** ObS: p > 0.05 ExS: p > 0.05 Type x ObS: p > 0.05 Type x ExS: p > 0.05 ObS x ExS: p > 0.05 Type x ObS x ExS: p > 0.05	4.10 ± 0.62	4.53 ± 0.36	4.81 ± 0.45	3.90 ± 0.53	5.28 ± 0.62	5.17 ± 0.33	4.73 ± 0.35	4.99 ± 0.52
Plastic work (J x 10^{-12}) **Type: p = 0.046** ObS: p > 0.05 ExS: p > 0.05 Type x ObS: p > 0.05 Type x ExS: p > 0.05 ObS x ExS: p > 0.05	22.45 ± 1.22	25.21 ± 2.66	22.35 ± 2.02	24.58 ± 2.23	27.36 ± 2.65	27.39 ± 1.28	24.28 ± 1.57	28.22 ± 3.13

Type x ObS x ExS: $p > 0.05$

Data are presented as mean +/- standard error of the mean. P-values for main effects of bone type, obesity status (ObS), exercise status (ExS), as well as their interactions are reported in the left column.

Exercise did not significantly affect mean or standard deviation of microscale material properties. Obesity affected some measures. Mineral:matrix was +10.3% higher ($p = 0.004$) for lean compared with obese bone. There was a significant interaction between bone type and obesity for carbonate:phosphate ($p = 0.014$). Obese rats had +3.5% greater carbonate:phosphate ($p = 0.024$) in lamellar as compared to woven bone while for lean rats this difference was +9.1% ($p < 0.001$).

Multiple linear regression models were generated for lamellar and woven bone types (Table 7-4). For lamellar bone, K_c was significantly affected by exercise, obesity, mineral:matrix (first and second order terms from regression analysis), carbonate:phosphate (second order term), standard deviation of carbonate:phosphate, standard deviation of crystallinity, standard deviation of E_r (first and second order terms), as well as the interactions of crystallinity and exercise, standard deviation of carbonate:phosphate and exercise, and the standard deviation of crystallinity and exercise. For woven bone, K_c was significantly affected by exercise, as well as the interactions of crystallinity and exercise, standard deviation of crystallinity and exercise, plastic work and exercise, plastic work and obesity, standard deviation of plastic work and obesity, and exercise and obesity.

Table 7.4: Best-fit multiple linear regression models.

		Lean		Obese	
		Ex	*Sed*	*Ex*	*Sed*
Lamellar					
r^2a = 65.3%					
parameter	**p value**				
min:mat	0 .001	K_c = 37.4 + 62.1**min:mat* – 27.5**carb:phos* – 1115 *crystallinity* + 373 stdev (*carb:phos*) - 2844 stdev(*crystallinity*) + 2.933 * *Er* – 29.56 (min:mat^2) – 0.3154 (*Er*^{2})	K_c = -91.9 + 62.1**min:mat* + 55.7**carb:phos* +858 *crystallinity* – 50.6 stdev (*carb:phos*) + 1224 stdev(*crystallinity*) + 2.933 * *Er* – 29.56 (*min:mat*^{2}) – 0.3154 (*Er*^{2})	K_c = 38.6 + 62.1**min:mat* – 27.5**carb:phos* – 1115 *crystallinity* + 373 stdev (*carb:phos*) - 2844 *stdev(crystallinity*) + 2.933 * *Er* – 29.56 (*min:mat*^{2}) – 0.3154 (*Er*^{2})	K_c = -90.9 + 62.1**min:mat* + 55.7**carb:phos* +858 *crystallinity* – 50.6 stdev (*carb:phos*) + 1224 stdev(*crystallinity*) + 2.933 * *Er* – 29.56 (*min:mat*^{2}) – 0.3154 (*Er*^{2})
crystallinity	> 0.05				
stdev(*carb:phos*)	0.003				
stdev(*Er*)	0.001				
ExS	0.003				
ObS	0.001				
min:mat^2	0.001				
carb:phos^2	0.022				
stdev(*Er*^{2})	0.001				
crystallinity x ExS	0.003				
stdev(*carb:phos*) x ExS	0.001				
stdev(*crystallinity*)*ExS	0.001				
Woven					
r^2a = 61.87%					
parameter	**p value**				
ExS	0.012	K_c = 40.1 – 626**crystallinity* + 726 stdev(*crystallinity*) – 0.000112*stdev(*PW*) + 0.000031**PW*	K_c = -25.5+ 626**crystallinity* + 726 stdev(*crystallinity*) – 0.000112*stdev(*PW*) - 0.000005**PW*	K_c = 40.8 – 626**crystallinity* - 726 stdev(*crystallinity*) + 0.000112*stdev(*PW*) + 0.000005**PW*	K_c = -26.2+– 626**crystallinity* - 726 stdev(*crystallinity*) + 0.000112*stdev(*PW*) + 0.000031**PW*
crystallinity x ExS	0.009				
stdev(*crystallinity*) x ObS	0.016				
PW x ExS	0.001				
PW x ObS	0.002				
stdev(*PW*) x ObS	0.001				
ExS x ObS					
0.019					

Multiple linear regression model parameters and associated p-values for models including the factors of exercise status (ExS), obesity status (ObS), and means and standard deviations of microscale material properties: plastic work (*PW*), reduced modulus (*Er*), mineral:matrix (*min:mat*), carbonate:phosphate (*carb:phos*), and *crystallinity*.

7.4 Discussion

The purpose of this study was to evaluate how fracture toughness depends on microscale cortical bone material heterogeneity, including bone chemistry and mechanical properties. Our rat model, which utilized outbred male rats fed a high-fat diet and included factors of exercise and obesity, achieved wide variability in fracture toughness.

Fracture toughness of the femur depended on exercise such that rats who were exercised had tougher bone than those who were sedentary. There was not an interaction with obesity, suggesting that exercise increases fracture toughness similarly for both lean and obese rats.

Microscale material properties were evaluated for lamellar and woven cortical bone for each fractured rat femur. Material properties different with bone type. Compared with lamellar bone, woven bone had greater mineral:matrix and otherwise had smaller bone crystal, less carbonate:phosphate, and higher variability in all bone chemistry parameters. These observations are consistent with woven bone having less organization and maturity than lamellar bone. The higher mineral:matrix of woven bone is not inconsistent with this general observation, as this ratio increases with immature collagen. Microscale material properties were not different with exercise, but did differ with obesity. Obese rats had lower mineral:matrix and had less difference in carbonate:phosphate between lamellar and woven bone compared with their lean rat counterparts.

Multiple linear regression (MLR) models suggest that fracture toughness depends on several microscale material properties, including heterogeneity. The best-fit MLR model for lamellar bone featured standard deviations of carbonate:phosphate, crystallinity, and reduced modulus from nanoindentation. Interestingly, K_c had a significant dependence on the square of several terms, including the standard deviation of reduced modulus. This implies a non-linear relationship between fracture toughness and variation in microscale mechanical properties. Indeed, the negative quadratic fit indicates that there is a "sweet spot" of variability in modulus, where too-low and too-high variability have deleterious effects on fracture toughness. Fracture toughness for woven bone also depends on heterogeneity, notably on the standard deviations of crystallinity and plastic work. Second-order terms were not featured in the woven

bone MLR model, suggesting that predominantly linear relationships exist between microscale measures and fracture toughness.

MLR models demonstrate significant interactions with exercise (lamellar bone) and both exercise and obesity (woven bone), implying that the influence of microscale bone characteristics on fracture toughness depends considerably on the context of these experimental factors. For instance, in lamellar bone, fracture toughness for sedentary rats is improved when bone is more mature (increased crystallinity, decreased standard deviation of carbonate:phosphate), while the reverse is observed for exercised rats. One possible interpretation of this effect may be that sedentary rats benefit from bone tissue maturity, while exercised rats benefit from newer tissue that possesses less microdamage. However, this explanation for the interactive nature of bone maturity and exercise for lamellar bone in this study is speculative and requires further confirmation. Notably, both sedentary and exercised rats have the same quadratic relationships between fracture toughness and lamellar bone mineral:matrix and standard deviation of reduced modulus, suggesting that a "sweet spot" for mineral content and variability in modulus is generalizable across the experimental factors of exercise and obesity. The MLR model for woven bone is characterized by many interactions between exercise and obesity and material properties and is therefore especially challenging to interpret. No one factor was generalizable across exercise and obesity conditions.

Increased standard deviation of reduced modulus for lamellar bone was found to contribute to fracture toughness regardless of exercise or obesity status. The tissue-scale stiffness of bone in part depends on bone chemistry, and so correlations were assessed between standard deviation of reduced modulus and parameters measured from Raman spectroscopy (Table 7-5). Correlations were generally poor between means and standard deviations of Raman measures and the standard deviation of reduced modulus. The strongest correlation was with mean mineral:matrix (+0.210). Though mineral:matrix and other aspects of bone chemistry contribute to tissue-scale stiffness and its variability, other measures, such as microdamage and collagen crosslinks, are also important and were not assessed in this study.

Table 7.5: Correlations between standard deviation of reduced modulus from nanoindentation and measures of microscale bone chemistry from Raman spectroscopy.

Measures from Raman spectroscopy	Correlation with standard deviation of reduced modulus
Mineral:matrix	+0.210
Carbonate:phosphate	+0.155
Crystallinity	+0.108
Standard deviation (mineral:matrix)	-0.114
Standard deviation (carbonate:phosphate)	-0.078
Standard deviation (crystallinity)	-0.035

We report herein that heterogeneity of microscale cortical bone material properties affects fracture toughness of the whole bone. Though relationships between fracture toughness and microscale material properties are complex and depend at least on bone type, exercise status, and, for woven bone, obesity, there are several ways that the current data contribute to knowledge about determinants of bone fragility. First, negative quadratic relationships are observed between fracture toughness and both standard deviation of reduced modulus and mean mineral:matrix for lamellar bone. Our findings are consistent with observations from backscattered SEM studies of biopsied bone from patients with fragility fractures, where mean and standard deviation of mineral content are disrupted by disease to values either higher *or* lower than those from healthy bone tissue [Ciarelli *et al.,* 2009; Busse *et al.,* 2009; Tamminen *et al.,* 2014]. Yet these observational works have not directly addressed whether disrupted mineral content or heterogeneity deleteriously affect fracture toughness. Indeed, we do not find a strong relationship between fracture toughness and standard deviation of mineral:matrix. However, we find that standard deviation of bone chemistry (crystallinity and carbonate:phosphate) and particularly standard deviation of microscale mechanical properties have a significant influence on fracture toughness. Our finding that standard deviation of reduced modulus (lamellar bone) and standard deviation of plastic work (woven bone) influence fracture toughness also lends experimental support to computational works by Tai *et al.* and Yao

et al., although the present work is the first to suggest a non-linear relationship between fracture toughness and variance in mechanical properties [Tai *et al.*, 2007, Yao *et al.*, 2011].

This work has several limitations. All rats in this study were fed a high-fat diet, and thus further work is required to confirm relationships between fracture toughness and microscale bone material properties for rodents receiving standard diets. Next, our survey of microscale bone quality is by no means exhaustive. Collagen crosslinking, microdamage, bound and free water, and other parameters that were not assessed in the current work may contribute to fracture toughness. Additionally, although mineral:matrix from Raman spectroscopy is sensitive to mineral content, the ratio is sensitive to collagen content and integrity and therefore delivers different information than a mineral content from SEM. Nonetheless, findings from this study provides experimental confirmation that fracture toughness indeed depends on microscale bone material heterogeneity, and that these relationships are often non-linear. This knowledge may aid efforts in determining how age, disease, and interventions may disrupt bone fracture resistance.

7.5 References

1. Koester, K. J., Ager, J. W., & Ritchie, R. O. (2008). The true toughness of human cortical bone measured with realistically short cracks. *Nature materials*, *7*(8), 672-677.
2. Lloyd, A. A., Wang, Z. X., & Donnelly, E. (2015). Multiscale contribution of bone tissue material property heterogeneity to trabecular bone mechanical behavior. *Journal of biomechanical engineering*, *137*(1), 010801.
3. Ciarelli, T. E., Tjhia, C., Rao, D. S., Qiu, S., Parfitt, A. M., & Fyhrie, D. P. (2009). Trabecular packet-level lamellar density patterns differ by fracture status and bone formation rate in white females. *Bone*, *45*(5), 903-908.
4. Busse, B., Hahn, M., Soltau, M., Zustin, J., Püschel, K., Duda, G. N., & Amling, M. (2009). Increased calcium content and inhomogeneity of mineralization render bone toughness in osteoporosis: mineralization, morphology and biomechanics of human single trabeculae. *Bone*, *45*(6), 1034-1043.
5. Tamminen, I. S., Misof, B. M., Roschger, P., Mäyränpää, M. K., Turunen, M. J., Isaksson, H., & Klaushofer, K. (2014). Increased heterogeneity of bone matrix mineralization in pediatric patients prone to fractures: a biopsy study. *Journal of Bone and Mineral Research*, *29*(5), 1110-1117.
6. Makowski, A. J., Granke, M., Uppuganti, S., Mahadevan-Jansen, A., & Nyman, J. S. (2015, February). Bone tissue heterogeneity is associated with fracture toughness: a polarization Raman spectroscopy study. In *SPIE BiOS* (pp. 930341-930341). International Society for Optics and Photonics.
7. Tai, K., Dao, M., Suresh, S., Palazoglu, A., & Ortiz, C. (2007). Nanoscale heterogeneity promotes energy dissipation in bone. *Nature materials*, *6*(6), 454-462.
8. Yao, H., Dao, M., Carnelli, D., Tai, K., & Ortiz, C. (2011). Size-dependent heterogeneity benefits the mechanical performance of bone. *Journal of the Mechanics and Physics of Solids*, *59*(1), 64-74.
9. Song, Z., Houck, J. A., Sherk, V., Foright, R., Presby, D., Giles, E., ... & MacLean, P. S. (2016). Exercise Counters the Changes in Nutrient Sensing Gene Expression after Caloric Restriction and the Loss of Ovarian Function in Obesity-prone Rats. *The FASEB Journal*, *30*(1 Supplement), 1293-8.
10. Ritchie, R. O., Koester, K. J., Ionova, S., Yao, W., Lane, N. E., & Ager, J. W. (2008). Measurement of the toughness of bone: a tutorial with special reference to small animal studies. *Bone*, *43*(5), 798-812.
11. Greenwood, J. A., Johnson, K. L., & Matsubara, E. (1984). A surface roughness parameter in Hertz contact. *Wear*, *100*(1-3), 47-57.
12. Gamsjaeger, S., Masic, A., Roschger, P., Kazanci, M., Dunlop, J. W. C., Klaushofer, K., ... & Fratzl, P. (2010). Cortical bone composition and orientation as a function of animal and tissue age in mice by Raman spectroscopy. *Bone*, *47*(2), 392-399.

8. Discussion of changes to fracture resistance-determining bone quality in CKD

8.1 Summary of dissertation findings

The primary question motivating this dissertation research was how CKD produces clinically-observed bone fragility. In this work, bone quality measurements were employed from the whole bone to the microscale to assess how fracture resistance-determining bone quality is diminished with CKD. Chapter 4 established that microscale bone material quality is diminished for bone formed during moderate, high-turnover CKD for young, skeletally mature mice. Chapter 5 demonstrated that osteocyte lacunae can be conveniently and efficiently visualized and analyzed in 3D from images generated by confocal laser scanning microscopy. 3D analyses showed that osteocyte lacunae become smaller, more spherical, and more sparsely populated with increasing mouse age. Chapter 6 described how aging and CKD together reduce bone quality. Deleterious changes to bone microarchitecture as well as whole bone and microscale material properties occurred with CKD and generally emerged with increasing age. Chapter 7 explored how fracture toughness of the whole bone depends on heterogeneity of microscale cortical bone material properties. It was observed that fracture toughness depends on heterogeneity of microscale properties most generally including reduced modulus from nanoindentation, and that this negative quadratic relationship has a fracture toughness maximum at mid-range values of variability for reduced modulus.

8.2 Major conclusions

- Bone material properties are diminished in CKD. In Chapter 4, it was found that microscale bone material properties are reduced in bone formed during high-turnover moderate CKD. Specifically, nanoindentation modulus and mineral volume fraction were diminished for mice with CKD induced *via* 5/6 Nx compared with sham. In Chapter 6, microscale modulus measured from maps spanning the cortical thickness of the femur was lower with CKD from 5/6 Nx in middle-age mice compared with sham. Whole bone toughness was also lower in middle-age mice with CKD *vs* sham. Thus, changes to bone material properties with CKD potentially contribute to fragility.

- Aging and CKD together deleteriously affect bone quality. As seen in Chapter 4, microscale material properties were diminished in young adult mice for bone formed during CKD, while cortical and trabecular microarchitecture and whole bone properties were not affected. In Chapter 6, it was found that the influence of CKD on bone quality increases with advanced age. Changes to bone in young adult mice were constrained to few changes in cortical microarchitecture. By middle-age, mice with CKD had diminished cortical microarchitecture, whole bone mechanical and material properties, and microscale material properties. At old age, mice with CKD had diminished trabecular and cortical microarchitecture, whole bone mechanical properties, and collagen crosslinks. These results suggest that aging and CKD together diminish bone quality such that fracture-resistance determining bone quality is worst in old mice with CKD.
- CKD deleteriously affects both collagen and mineral. In Chapter 4, mineral volume fraction was reduced for bone formed during CKD, and cortical total mineral density was lower for CKD *vs* sham. In Chapter 6, cortical total mineral density was reduced in young, middle-age, and old mice, while trabecular volumetric mineral density was diminished for CKD *vs* sham in middle-age and old mice. Crystallinity was potentially less variable in middle-age mice with CKD compared with sham. Mature skeletal crosslinks were reduced for old mice with CKD *vs* sham. These changes to both collagen and mineral components of bone quality potentially contribute to increased fragility in CKD.
- 3D analysis of osteocyte lacunae does not deliver the same information as 2D geometries from images acquired *via* confocal laser scanning microscopy. Chapter 5 presents a facile, open-source method to automatically segment and analyze geometries of osteocyte lacunae from confocal laser scanning microscopy z-stacks. Unlike 2D, the 3D measurements allow determination of the size and orientation of lacunae regardless of sectioning plane, and also permit exclusion of non-osteocyte objects (*e.g.*, vasculature).

- Osteocyte geometries change with aging in sham mice to become smaller, more spherical, and more sparsely populated (Chapter 5). These age-dependent changes to osteocyte geometries are not present in CKD, suggesting that altered perilacunar remodeling may have a role in bone quality changes in CKD (Chapter 6).
- CKD alters bone material heterogeneity. These changes to bone tissue heterogeneity may deleteriously affect whole bone toughness. In Chapter 4, new bone formed during CKD had less variable nanoindentation modulus and more variable mineral volume fraction than sham. In Chapter 6, middle-age mice with CKD had less variable nanoindentation modulus and potentially less variable crystallinity compared with sham. Heterogeneity of crystallinity was observed from multiple linear regression modeling to predict toughness from three-point bending. Thus, changes with CKD to bone tissue heterogeneity may diminish bone fracture resistance.
- Whole bone fracture toughness may depend on heterogeneity of microscale material properties. In Chapter 7, fracture toughness was found to depend on microscale material properties and their spatial variation in a model of male rats fed a high-fat diet with factors of obesity and exercise. In particular, mean mineral:matrix and standard deviation of reduced modulus in lamellar bone were predictive of fracture toughness across the model. It was also observed that some aspects of bone heterogeneity can have differing meaning depending on other factors. For example, and increase in standard deviation of crystallinity in lamellar bone predicts an increase in fracture toughness for an exercised rat and yet predicts a decrease in fracture toughness for a sedentary rat.

8.3 Significance of work

The body of work described in this dissertation provides evidence that CKD alters bone material from the whole bone to the tissue-scale, including material properties and heterogeneity. Previous efforts to characterize skeletal outcomes in CKD have inconsistent findings about whether bone material is diminished with kidney dysfunction [Iwasaki *et al.,* 2011; Kadokawa *et al.,* 2012; Iwasaki *et al.,* 2015; Newman *et al.,* 2014]. The uncertainty about whether material properties are affected by CKD was likely

a consequence of measurement methods as well as study animal age. Other studies typically surveyed microscale material quality with a smaller number of measurements, either on the periosteal surface or in the center of transversely sectioned cortical bone. These studies also involved young adult mice or rats [Iwasaki *et al.,* 2011; Kadokawa *et al.,* 2012; Iwasaki *et al.,* 2015; Newman *et al.,* 2014]. The work described in this dissertation was unique in mapping the cortical thickness from endocortical to periosteal surfaces, and was therefore more likely to detect bone material changes in tissue accrued during CKD. It was also found that changes to bone quality with CKD, including material properties, were more pronounced for middle-age than young mice.

Work presented in this dissertation adds to the knowledge of how CKD affects bone quality. In addition to demonstrating that material properties are diminished in CKD, it was shown here that both collagen and mineral are deleteriously affected by kidney dysfunction. Contrasting other work, we found that levels of mature collagen crosslinks were reduced in CKD, but non-enzymatic crosslinks (pentosidine) were not affected [Allen *et al.,* 2008]. However, there may be differences between our studies because of disease severity. Specifically, the 5/6 Nx model produces moderate CKD while rats studied by Allen *et al.* had relatively severe disease induced by genetic polycystic kidney disease. In earlier work with the same rat model, younger rats with less severe disease did not have changes to non-enzymatic crosslinks compared with wild type littermates [Newman *et al.,* 2014]. Meanwhile, the mineral changes that we have observed are consistent with findings by Iwasaki and coworkers, where mineral:matrix and crystallinity were diminished in 16 week old male Sprague-Dawley rats that underwent 5/6 Nx at 12 weeks [Iwasaki *et al.,* 2015]. The mineral and collagen changes seen in this work and the work of others is consistent with high-turnover renal osteodystrophy, where the average tissue age and maturation are lower from abnormally high rate of bone tissue resorption and deposition. Indeed, in low-turnover CKD, such as produced with 5/6 Nx and thyro-parathyroidectomy, mineral:matrix is abnormally high [Iwasaki *et al.,* 2011; Iwasaki *et al.,* 2015]. The altered heterogeneity observed in the current work for CKD is also consistent with abnormally immature tissue. Specifically, less variable nanoindentation modulus and more variable crystallinity would be expected in newly deposited, maturing tissue. Because bone material quality changes occurring with

CKD appear well-aligned with bone turnover abnormality, it is clinically-relevant to question if anti-resorptive medications (*i.e.*, bisphosphonates) might have a role in the management of bone fragility in CKD. However, as discussed in 8.3 and 8.4, anti-resorptive therapies may have serious limitations for treatment of CKD, and additional therapeutic interventions, such as those that target the osteocyte, should also be evaluated.

This dissertation also contributes to the field by describing differences to bone quality with CKD together with aging. Though most individuals with CKD are elderly, previous studies of rodent models of CKD have only involved young rats or mice [Iwasaki *et al.*, 2011; Iwasaki *et al.*, 2015; Kadokawa *et al.*, 2011; Moe *et al.*, 2014; Allen *et al*, 2008; Newman *et al.*, 2014]. In Chapter 6, it was found that the influence of CKD on bone quality increases with age. Young mice with CKD had few changes to cortical microarchitecture. Middle-age mice with CKD had diminished cortical microarchitecture, whole bone mechanical and material properties, and microscale material properties. At old age, mice with CKD had diminished trabecular and cortical microarchitecture, whole bone mechanical properties, and collagen crosslinks. The combined influences of aging and CKD are important for understanding loss of bone fracture resistance with kidney dysfunction. Studies in young mice, including the work presented in Chapter 4, do not consistently observe changes to bone microarchitecture and, not surprisingly, draw disparate conclusions about whether changes to bone material or microarchitecture drive bone fragility in CKD [Kadokawa *et al.*, 2011; Iwasaki *et al.*, 2015; Newman *et al.*, 2014]. Measurement of bone microarchitecture in CKD for young rodents is likely confounded by study animals undergoing skeletal maturation during the course of the study. It is possible that skeletal growth may mask loss of bone microarchitecture from CKD. The findings for mice that were skeletally mature throughout the study that bone material and microarchitecture are both affected by CKD suggests that high-turnover CKD broadly reduces bone quality. Further, there were aging-related differences in when particular aspects of bone quality were diminished with CKD. For instance, bone material properties were most reduced in CKD for middle-age mice, while trabecular microarchitecture and collagen crosslinks were diminished by CKD in old mice. There may be differences in disease severity resulting from how young, middle-age, and old mice

respond to 5/6 Nx. However, aging is also seen to reduce bone material and microarchitecture, and thus the effects of aging and CKD appear to be additive. These findings may be important for understanding why patients with CKD demonstrate increasing prevalence of bone fragility with age [Naylor *et al.*, 2014].

This work provides the first description that aging changes osteocyte geometries in cortical bone. Previous work has suggested that 2D osteocyte lacunae may become smaller with aging in trabecular but not cortical bone for C57Bl/6 mice [Lai *et al.*, 2015]. The results of Chapter 5 demonstrate that osteocyte lacunae become smaller, more spherical, and less populated in aging for cortical bone from C57Bl/6 mice. Importantly, we observe these changes in 3D and not in 2D, potentially explaining why these results have not been previously observed by other researchers. Findings that age-related changes to osteocyte lacunae do not occur in CKD are also novel, suggesting that perilacunar remodeling may have a role in bone quality changes in CKD. As considered in the following 'Future Directions', the role of the osteocyte in mediating local bone quality changes in aging and CKD is intriguing. A number of therapeutic agents (*e.g.*, TGF-β inhibitors, PTH, glucocorticoids) act on the osteocyte and can regulate perilacunar remodeling to affect bone material quality.

Another purpose of Chapter 5 was to share a method with the orthopaedic research community to conveniently and efficiently assess 3D osteocyte lacunae. This method allows use of common confocal laser scanning microscopy and Matlab-based segmentation to visualize and analyze 3D osteocyte lacunar geometries. This work demonstrated that 3D metrics are not well approximated by 2D analogs. It is anticipated that this method will be useful for understanding the role of the osteocyte and perilacunar remodeling for many physiological states (*e.g.*, lactation, hibernation), diseases (*e.g.*, CKD and other metabolic diseases), and therapeutic interventions (*e.g.*, glucocorticoid therapy, TGF-β inhibitors).

This dissertation work has a substantial focus on bone material heterogeneity. The work is unique in exploring whether heterogeneity in material is affected by CKD. Site-matched microscale material property assessment in arrays spanning the cortical thickness allowed evaluation of heterogeneity of microscale material properties in Chapter 4 and Chapter 6. It was observed in both studies that CKD altered bone microscale material heterogeneity. Furthermore, in Chapter 6, toughness of the whole bone depended

on heterogeneity of crystallinity. This altered heterogeneity is part of the constellation of bone quality effects from CKD. Therefore, restoring normal heterogeneity may be considered a therapeutic outcome.

This work is not alone in considering that properties related to toughness may be influenced by heterogeneity. Makowski and coworkers evaluated how heterogeneity in Raman chemistry explained fracture toughness in aging human cortical bone [Makowski *et al.,* 2015]. However, heterogeneity in individual measures (*e.g.,* mineral:matrix, carbonate:phosphate, crystallinity) did not explain more than 11% of the variance in fracture toughness. Principal components analysis from whole spectra provided a somewhat better prediction of fracture toughness [Makowski *et al.,* 2015]. Granke and coworkers used NMR and reference point indentation (RPI) to search for meaningful predictors of fracture toughness [Granke *et al.,* 2015]. Multiple linear regression models including pore water and RPI stiffness were most predictive of crack initiation toughness. Another model, including total mineral density from microCT, pentosidine measured by HPLC, and cortical porosity was also predictive of fracture toughness [Granke *et al.*, 2015]. Importantly, neither of these efforts extended measurements of microscale heterogeneity to both bone chemistry (*e.g.,* Raman mineral:matrix, crystallinity) and material response to mechanical loading (*e.g.,* nanoindentation modulus). This gap in the knowledge is critical because the tissue-scale bone toughening mechanisms could be affected by size, organization, structure, and content of mineral, as well as domains of differing modulus that are determined in part by these chemical and compositional features. The current work approached these questions through mapping measures of microscale material heterogeneity including bone chemistry and nanoindentation modulus on femurs for which notched fracture toughness values were obtained. The negative quadratic relationships seen between the standard deviation of reduced modulus and mean mineral:matrix with fracture toughness in lamellar bone suggests that tough bone has a "sweet spot" of microscale material properties that can be potentially be disrupted by age, disease, or interventions. Interestingly, heterogeneity of other measures, such as crystallinity, were predictive of fracture toughness but the direction of the effect depended on whether rats were exercised or sedentary. These findings support previous observational and computational efforts that suggested fracture toughness depends on microscale heterogeneity, and adds to this understanding through describing

relationships between fracture toughness and specific material properties as well as their dependencies on exercise and obesity.

8.4 Future directions

8.4.1 *Treatment of bone quality loss in CKD*

An important future direction is to assess how bone quality loss in CKD responds to therapeutic treatment. In Chapter 4, it was observed that young mice with CKD induced *via* 5/6 Nx have loss of bone material quality (lower nanoindentation modulus and mineral content) in bone formed during CKD. Then, in Chapter 6, it was observed that diminished cortical and trabecular microarchitecture, microscale material properties, and collagen crosslinking emerge with advancing age. Altered microscale bone material heterogeneity was also observed for young mice in Chapter 4 and middle-age mice in Chapter 6. Bisphosphonate treatment has been considered for patients with CKD [Allen *et al.,* 2017]. This treatment is conventionally used for management of loss of bone mass in osteoporosis through reduction of osteoclast-mediated bone turnover. It is possible that the diminished microarchitecture observed with high turnover CKD in the work presented herein could benefit from reduction of turnover with bisphosphonate therapy. However, by reducing bone turnover, bisphosphonates can also lead to adynamic bone and associated bone fragility [Gourion-Arsiquaud *et al.,* 2010; Allen *et al.,* 2008; Mashiba *et al.,* 2000]. Some work has been conducted on the efficacy of bisphosphonates in preventing bone quality loss in CKD. In a polycystic model of CKD in rats, bisphosphonate therapy restored trabecular microarchitecture, but did not restore whole bone mechanical properties of cortical bone [Moe *et al.,* 2014]. Given that bisphosphonates may have consequences to systemic mineral homeostasis and may burden failing kidneys, further evaluation of bisphosphonates on short- and longer-term bone outcomes including bone material quality is necessary. Other therapeutic interventions, such as may target the osteocyte and are discussed in the next points, should also be considered.

8.4.2 *Influence of aging on osteocyte perilacunar remodeling*

In Chapter 5, it was observed that osteocyte lacunae become smaller, more spherical, and more sparsely populated with increased age in male C57Bl/6 mice. This observation suggests that osteocyte

perilacunar remodeling may change in the aging process. It is not clear why osteocyte morphologies change with aging. Candidate explanations include compensation for loss of bone structural integrity with aging, response to changing in aging to mineral homeostasis, or perhaps consequence of osteocyte senescence. In these possibilities, changes to perilacunar remodeling could be compensatory and improve bone quality local to the osteocyte, or deleterious and worsen local bone quality. Further work is necessary to identify how changes in osteocyte lacunar geometries with age correspond with bone material quality and whole bone fracture toughness. Perilacunar remodeling requires TGF-β and downstream targets (*e.g.*, MMP13), and has been seen to be mediated by PTH signaling in exercise [Alliston *et al.*, 2004; Gardinier *et al.*, 2016]. Thus, in identifying the role of perilacunar remodeling in bone quality changes in aging, new therapeutic targets that act on the osteocyte may be revealed.

8.4.3 *Influence of CKD on osteocyte perilacunar remodeling*

The changes to 3D osteocyte lacunar geometries with increasing age in sham mice were not observed for aging mice with CKD. Accordingly, it is of interest whether perilacunar remodeling is affected by CKD. The osteocyte is known to participate in systemic mineral homeostasis in CKD through elevated expression of FGF-23 [Stubbs *et al.*, 2006]. If the osteocyte participates directly in liberating mineral from surrounding bone matrix, high-turnover type changes to bone quality (*e.g.*, immature, hypomineralized, and less stiff tissue) could occur outside of osteoclast - and osteoblast - mediated remodeling. This hypothesis is consistent with the observation of Moe and coworkers that cortical bone properties were not restored with bisphosphonate treatment in a rat model of CKD [Moe *et al.*, 2014]. Further work is needed to identify how material properties local to osteocyte lacunae change in CKD. As discussed in 8.4.2, osteocytic perilacunar remodeling is sensitive to TGF-β, the availability of MMP-family proteases, and PTH, which could serve as attractive targets.

8.4.4 *Mechanistic determination material heterogeneity contributions to bone toughening mechanisms*

In work presented in this dissertation, heterogeneity of bone material was seen to influence whole-bone measures of toughness. In Chapter 4, newly formed bone in CKD had lower standard deviation of microscale modulus from nanoindentation and higher standard deviation of mineral volume fraction

compared with the same regions in sham mice. In Chapter 6, middle-age mice with CKD had lower whole-bone toughness from three-point bending, and also had lower standard deviation of microscale modulus and possible less variable crystallinity. In multiple linear regression modeling, heterogeneity of crystallinity was predictive of whole-bone toughness. Then, in Chapter 7, heterogeneity of reduced modulus from lamellar bone was generally predictive of fracture toughness, while heterogeneity of other terms *(e.g.*, crystallinity) depended on experimental factors such as exercise. A compelling next question is how small-scale toughening mechanisms are specifically affected by heterogeneity of material. Bone is known to have a rising r-curve; cracks propagate with lower resistance before ~ 100 μm in size, and then encountering structural features (*e.g.*, osteons, lamellar boundaries, and vasculature) that cause crack deflection and toughen bone [Koester *et al.*, 2008]. Yet it is not known at the micrometer to nanometer length scales how heterogeneity of mineralized collagen fibrils (*i.e.*, variance in mineral size and orientation, as well as collagen crosslinking) influences energy dissipation at the crack tip or crack wake. This question may be best explored with computational methods, where collagen and mineral components are systematically varied. Experimental work may allow high resolution imaging of cracks within the mineralized tissue composite, but it is challenging to obtain appropriately high resolutions in environmental SEMs to measure mineralized collagen fibrils without dehydrating bone and potentially altering crack morphologies. The impact of this question is to further understand how heterogeneity specifically affects fracture toughness so that the roles of aging, disease, exercise, and therapeutics on bone quality can be more completely understood.

8.5 References

1. Iwasaki, Y., Kazama, J. J., Yamato, H., & Fukagawa, M. (2011). Changes in chemical composition of cortical bone associated with bone fragility in rat model with chronic kidney disease. *Bone*, *48*(6), 1260-1267.

2. Kadokawa, S., Matsumoto, T., Naito, H., & Tanaka, M. (2011). Assessment of trabecular bone architecture and intrinsic properties of cortical bone tissue in a mouse model of chronic kidney disease. *Journal of Hard Tissue Biology*,*20*(2), 79-86.

3. Iwasaki, Y., Kazama, J. J., Yamato, H., Matsugaki, A., Nakano, T., & Fukagawa, M. (2015). Altered material properties are responsible for bone fragility in rats with chronic kidney injury. *Bone*, *81*, 247-254.

4. Newman, C. L., Moe, S. M., Chen, N. X., Hammond, M. A., Wallace, J. M., Nyman, J. S., & Allen, M. R. (2014). Cortical bone mechanical properties are altered in an animal model of progressive chronic kidney disease. *PLoS One*, *9*(6), e99262.

5. Allen, M. R., Newman, C. L., Chen, N., Granke, M., Nyman, J. S., & Moe, S. M. (2015). Changes in skeletal collagen cross-links and matrix hydration in high-and low-turnover chronic kidney disease. *Osteoporosis International*,*26*(3), 977-985.

6. Moe, S. M., Chen, N. X., Newman, C. L., Gattone, V. H., Organ, J. M., Chen, X., & Allen, M. R. (2014). A comparison of calcium to zoledronic acid for improvement of cortical bone in an animal model of CKD. *Journal of Bone and Mineral Research*, *29*(4), 902-910.

7. Naylor, K. L., McArthur, E., Leslie, W. D., Fraser, L. A., Jamal, S. A., Cadarette, S. M., ... & Garg, A. X. (2014). The three-year incidence of fracture in chronic kidney disease. *Kidney international*, *86*(4), 810-818.

8. Lai, X., Price, C., Modla, S., Thompson, W. R., Caplan, J., Kirn-Safran, C. B., & Wang, L. (2015). The dependences of osteocyte network on bone compartment, age, and disease. *Bone research*, *3*.

9. Makowski, A. J., Granke, M., Uppuganti, S., Mahadevan-Jansen, A., & Nyman, J. S. (2015, February). Bone tissue heterogeneity is associated with fracture toughness: a polarization Raman spectroscopy study. In *SPIE BiOS* (pp. 930341-930341). International Society for Optics and Photonics.

10. Granke, M., Makowski, A. J., Uppuganti, S., Does, M. D., & Nyman, J. S. (2015). Identifying novel clinical surrogates to assess human bone fracture toughness. *Journal of Bone and Mineral Research*, *30*(7), 1290-1300.

11. Allen, M. R., & Aref, M. W. (2017). What Animal Models Have Taught Us About the Safety and Efficacy of Bisphosphonates in Chronic Kidney Disease. *Current Osteoporosis Reports*, 1-7.

12. Gourion-Arsiquaud, S., Allen, M. R., Burr, D. B., Vashishth, D., Tang, S. Y., & Boskey, A. L. (2010). Bisphosphonate treatment modifies canine bone mineral and matrix properties and their heterogeneity. *Bone*, *46*(3), 666-672.

13. Allen, M. R., Gineyts, E., Leeming, D. J., Burr, D. B., & Delmas, P. D. (2008). Bisphosphonates alter trabecular bone collagen cross-linking and isomerization in beagle dog vertebra. *Osteoporosis international*, *19*(3), 329-337.

14. Mashiba, T., Hirano, T., Turner, C. H., Forwood, M. R., Johnston, C. C., & Burr, D. B. (2000). Suppressed bone turnover by bisphosphonates increases microdamage accumulation and reduces some biomechanical properties in dog rib. *Journal of Bone and Mineral Research*, *15*(4), 613-620.

15. Alliston, T. (2014). Biological regulation of bone quality. *Current osteoporosis reports*, *12*(3), 366-375.

16. Gardinier, J. D., Al-Omaishi, S., Morris, M. D., & Kohn, D. H. (2016). PTH signaling mediates perilacunar remodeling during exercise. *Matrix Biology*, *52*, 162-175.

17. Stubbs, J., Liu, S., & Quarles, L. D. (2006, December). Role of fibroblast growth factor 23 in phosphate homeostasis and pathogenesis of disordered mineral metabolism in chronic kidney disease. In *Seminars in dialysis* (Vol. 20, No. 4, pp. 302-308)

18. Koester, K.J., Ager, J.W., & Ritchie, R.O. (2008). The true toughness of human cortical bone measured with realistically short cracks. *Nature materials*, *7*(8), 672-677.